FINAL REPORT

Reduced Iron Sulfide Systems for Removal of Heavy Metal Ions from Groundwater

SERDP Project ER-1375

JULY 2009

Kim F. Hayes
Peter Adriaens
Avery H. Demond
Terese Olson
University of Michigan

Linda M. Abriola
Tufts University

This document has been approved for public release.

Strategic Environmental Research and Development Program

This report was prepared under contract to the Department of Defense Strategic Environmental Research and Development Program (SERDP). The publication of this report does not indicate endorsement by the Department of Defense, nor should the contents be construed as reflecting the official policy or position of the Department of Defense. Reference herein to any specific commercial product, process, or service by trade name, trademark, manufacturer, or otherwise, does not necessarily constitute or imply its endorsement, recommendation, or favoring by the Department of Defense.

Table of Contents

Cover Page.....i
Table of Contents.....ii
List of Tables.....iii
List of Figures.....iv
List of Acronyms.....x
Keywords.....xii
Acknowledgements.....xiii
Abstract.....xiv
Executive Summary.....1
Background.....3
Project Objectives.....7
Task 1. Characterization of FeS Reactivity for Cd and As Removal in PRB Applications..13
Subtask 1.1. Preparation of Reactive FeS.....13
Subtask 1.2. Sorption Capacity Determination of FeS.....26
Subtask 1.3. Uptake Mechanism of As and Cd by FeS and As by FeS-Coated Sand.....31
Subtask 1.4. Sorption Behavior of As and Cd by Nanoscale FeS and FeS-Coated Sand.....55
Subtask 1.5. Impact of Oxygen on the Mobilization of As Sorbed by FeS.....77
Subtask 1.6. Column Study of As(III) Uptake by FeS-Coated Sand.....96
Task 2. Evaluation of Microbial Methods for Regeneration of FeS PRBs.....112
Subtask 2.1. Biogenic Formation of FeS by SRB.....116
Subtask 2.2. Sorption Behavior of As and Cd by Biogenic FeS.....124
Task 3. Optimization of Colloidal Injection Methods for the Effective Introduction and Dispersal of Nanoscale FeS into Porous Media.....132
Subtask 3.1. Chemical Optimization of Deposition with Colloidal FeS.....132
Subtask 3.2. FeS Release Evaluation.....141
Task 4. Investigation of Suitable Methods of Emplacement of *FeS* in Mixed Porous Media for Plugging Avoidance.....146
Subtask 4.1. Development of the Optimal Particle-Size Distributions of PRB Media for Limiting the Reduction in Permeability.....146
Subtask 4.2. Analyze and Measure the Patterns of Permeability and Porosity Reduction...169
Task 5. Development and Laboratory-Validation of a Multi-Component Reactive Transport Model for PRB Performance Predictions and Field-Scale Design Applications.....183
Subtask 5.1. Conceptual Reaction Model Development and Validation.....183
Subtask 5.2. Investigation of Rate-limited Processes in Transport Systems.....192
Subtask 5.3. Field-scale Simulation for Long-term Performance Evaluation of FeS-coated Sand Based PRBs.....198

Appendix A. Supporting Data.....204
Appendix B. List of Scientific/Technical Publications.....205
Appendix C. Other Supporting Material.....209

List of Tables

Table 1.1 Unit cell parameters for synthetic mackinawite
Table 1.2. Particle size and SSA_{ext} values of synthetic mackinawite by different methods
Table 1.3. Binding energies (BE), peak full width at half maximums (FWHM) and peak areas for Fe $2p_{3/2}$, and O 1*s* X-ray photoelectron spectra of FeS (mackinawite), FeS-coated sand, Wedron sand and acid-washed Wedron
Table 1.4. Arsenic local structure for mackinawite samples reacted at pH 5, 7 and 9 with initial concentrations of 5.0×10^{-5} M and 5.0×10^{-4} M As(III).
Table 1.5. EXAFS data fits and model compound crystallographic information.
Table 1.6. Structural parameters of model compounds extracted from Cd EXAFS data (*CN*: coordination number, *R*: inter-atomic distance, σ^2: Debye-Waller factor).
Table 1.7. Structural parameters of Cd sorbed by synthetic mackinawite extracted from Cd EXAFS data (*CN*: coordination number, *R*: inter-atomic distance, σ^2: Debye-Waller factor).
Table 1.8. EXAFS fit results for pH 5 and 9 FeS-coated sand As reacted samples and As reference model compounds.
Table 1.9. Fitting parameters for XPS As 3d for arsenic reference compounds.
Table 1.10. XPS fits showing relative contributions of As species in spectra.
Table 1.11. EXAFS fit results and crystallographic data for reference compounds.
Table 1.12. EXAFS fit results for samples oxidized at pH 4.9.
Table 1.13. EXAFS fit results for samples oxidized at pH 7.1.
Table 1.14. EXAFS fit results for samples oxidized at pH 9.1.
Table 1.15. Column experimental conditions.
Table 1.16. Comparison As(III) removal capacity between column and batch reactor results.

Table. 2.1. General metabolic characteristics of SRB used in this study
Table 2.2. Biogenic FeS production by *D. vulgaris* in terms of protein concentration.
Table 2.3. Sulfate depletion rates (*1/d*) of various incubations in presence of sulfate reducing bacteria.
Table 2.4. Iron sulfide production and Fe conversion efficiency in the presence of different iron solid phases.
Table 2.5. Sulfate reducing bacterial protein concentrations, growth yields, and amount of sulfide produced per g of cells (dry weight) during 10-day incubation with HFO.

Table 3.1. Summary of deposited FeS concentrations at varying pH and ionic strength.

Table 4.1. ZVI PRBs analyzed for correlations between geochemical parameters and performance.
Table 4.2. Reported geochemical data for ZVI PRBs.
Table 4.3. Calculated geochemical data for ZVI PRBs.
Table 4.4. Logistic regression and odds ratio maximization results.
Table 4.5. Summary of column experiments.

Table 5.1. Important chemical reactions in the FeS-coated sand-As(III) system.
Table 5.2. Dispersivities in column experiments.

List of Figures

Figure 1.1. X-ray diffraction patterns for the magnetic portion (B) and the non-magnetic portion (A) of synthetic mackinawite. In part (B), the diffraction data for reference minerals are obtained from JADE7 (Materials Data Inc.). In part (B), the diffraction peaks are indexed for mackinawite.

Figure 1.2. TEM images of the four-day mackinawite (A) 50,000 magnification, (B) 80,000 magnification (C) 500,000 x magnification.

Figure 1.3. SEM images of (A) natural Wedron silica sand and (B) FeS-coated sand with 1.2 mg FeS/g-coated sand, (C) 2.4 mg FeS/g-coated sand and (D) 4 mg FeS/g-coated sand. FeS deposits as patches on the sand with some areas of the surface appearing uncoated and exposed.

Figure 1.4. Sorption isotherm results at pH 5, 7 and 9 plotted as the amount removed versus the solution concentration of As after 2 days equlibration time with FeS (A) and FeS-coated sand (B). (● pH 5, ◇ pH 7, and ▲ pH 9, Error bars: standard deviation).

Figure 1.5. Plot of dissolved concentration of Cd versus pH illustrating that nearly quantitatively removal of Cd occurs at Cd intial concentrations of 0.015 M and 0.0005 M for 10 g/L FeS (0.11 M FeS). Dotted line shows the MCL of 5 ppb (4.5×10^{-8} M) Cd.

Figure 1.6. HAADF-STEM image of FeS reacted with As(III) at pH 5.

Figure 1.7. HAADF-STEM with EDX mapping of FeS reacted with As(III) at pH 5. The box in the image shows the region of EDS elemental mapping. EDXS maps specific to As, S, and Fe are shown to the right of the image and confirm the presence of discrete arsenic sulfide phases.

Figure 1.8. HAADF-STEM with EDXS mapping of FeS reacted with As(III) at pH 9. EDXS maps specific to As, S, and Fe are shown to the right of the image and show a homogeneous distribution of As among the FeS aggregates.

Figure 1.9. XANES spectra of As reacted with FeS.

Figure 1.10. EXAFS spectra and radial distribution functions for As sorption and models.

Figure 1.11. XRD spectra for mackinawite samples reacted (a) without As(III) and (b) with 1×10^{-2} M As(III) at pH 5. Reference spectra for mackinawite, halite, realgar polymorphs (α- and ω-As_4S_4), orpiment (As_2S_3) and arsenopyrite (FeAsS) are shown as solid lines at the bottom of the figure. Spectra labels are defined as follows: M=mackinawite, G=greigite, H=halite, R=realgar.

Figure 1.12. EXAFS data and corresponding Fourier transforms of Cd model compounds.

Figure 1.13. EXAFS data and corresponding Fourier transforms of Cd loaded on mackinawite under different pH conditions: ΣCd = 0.025M, I = 0.2M NaCl, 10 g/L mackinawite.

Figure 1.14. EXAFS data and corresponding Fourier transforms of Cd loaded on mackinawite under different pH conditions: ΣCd = 10^{-4} M, I = 0.01M NaCl, 1 g/L mackinawite, dry powder sample.

Figure 1.15. XRD characterization of Cd reacted with FeS vs. pH.

Figure 1.16. Arsenic K-edge XANES spectra for FeS-coated sand reacted with at pH 5 (e) and pH 9 (f), which are enveloped by reference compounds: aqueous As(V) (h), aqueous As(III) (g), disordered As_2S_3 (d), disordered AsS (c), arsenopyrite (b), and As(0) (a). The mark on the absorption edges corresponds to the first derivative maxima of XANES spectra.

Figure 1.17. k^3-weighted arsenic K-edge EXAFS spectra ($k^3\chi(k)$) (**Left**) and corresponding Fourier transforms (**right**) for FeS-coated samples and reference compounds. Solid lines are the experimental data; dashed lines are the numerical fits. The 416 g/L FeS-coated sand reacted with 1.33×10^{-3} M As(III) at pH 5 (e) and pH 9 (f), which are enveloped by reference compounds: aqueous As(V) (h), aqueous As(III) (g), disordered As_2S_3 (d), disordered AsS (c), arsenopyrite (b), and As(0) (a).

Figure 1.18. XPS As 3d peak spectra for As(III) reacted with FeS coated sand at pH 5 and 9 using a high pass energy of 160 eV.

Figure 1.19. pH edges measured at varying solid FeS:solution ratios for initial As(III) concentration of $1.3\text{x}10^{-5}$ M (1 mg/L) and ionic strength of 0.015M.

Figure 1.20. Total iron concentrations measured in 0.1, 0.5, 1, and 10 g/L FeS after equilibration with 1.3×10^{-5} M As(III) and in the absence of arsenite (1g/L system only).

Figure 1.21. Cd(II) uptake in 10 g/L FeS as function of (A) pH at two different initial Cd(II) concentrations (Cd0), and (B) Dissolved Fe concentration (FeDiss) as a function of pH at various initial Cd(II) concentrations (Cd0).

Figure 1.22. Exchanged Fe(II) concentration (Feexch) versus sorbed Cd(II) concentration (Cdsorb) at pH 5.5 ~ 6.0 where precipitation of Fe (hydr)oxides is avoided.

Figure 1.23. Percent removed of 1.33 x 10^{-5} M (1 mg/L) As(III) (left) as a function of pH for 100 g FeS-coated sand (0.124 g FeS) and uncoated 100g Wedron sand/L in 0.1M NaCl aqueous solutions.

Figure 1.24. Dissolved Fe concentration as a function of pH for 100 g FeS-coated sand/L in 0.01 M NaCl. Also shown is the percentage of total iron removed from the sand.

Figure 1.25. Dissolved silica concentration as a function of pH in 100 g FeS-coated sand/L of water.

Figure 1.26. Effect of dissolved silicate on As(III) uptake by nanoscale FeS at pH 5, 7 and 9.

Figure 1.27. Effect of dissolved silicate on As(III) uptake by FeS-coated sand at pH 5, 7 and 9. The circled area is enlarged for better viewing.

Figure 1.28. Profiles of pH (A) and redox potential (B) during mackinawite (FeS) oxidation. The redox potentials measured using a Ag/AgCl ORP combination electrode were corrected for the stand hydrogen electrode (SHE).

Figure 1.29. Dissolved Fe concentrations Fe_{diss} (A), dissolved sulfate concentrations $(SO_4^{2-})_{diss}$ (B), dissolved arsenic concentrations As_{diss} (C), and dissolved As(III) concentrations $As(III)_{diss}$ (D) during mackinawite (FeS) oxidation. Error bars correspond to one standard deviation. Arrows inserted in parts (A) and (C) guide which y-axis the data can be read from.

Figure 1.30. Diffraction patterns of the samples oxidized at pH 4.9 (A), 7.1 (B), and 9.1 (C). Oxidation times are indicated in the diffractograms. Reflection peaks are labeled for mackinawite (M), goethite (G), lepidocrocite (L), sulfur (S), and halite (H).

Figure 1.31. Change of Fe crystalline minerals during mackinawite (FeS) oxidation.

Figure 1.32. Comparison of dissolved Fe concentrations Fe_{diss} (A) and dissolved sulfate concentrations $(SO_4^{2-})_{diss}$ (B) between 0.1 M CHES buffer and 0.1 M TAPS buffer. The solution pH in both buffer systems was 9.1 ± 0.2.

Figure 1.33. Arsenic K-edge XANES spectra for the samples oxidized at pH 4.9 (A), 7.1 (B), and 9.1 (C) as well as reference compounds. The samples oxidized for 0, 1, 2, 4, and 192 h (all black) are arranged from the bottom to the top, which are enveloped by reference compounds: aqueous As(V) (red), aqueous As(III) (orange), disordered As_2S_3 (pink),

disordered AsS (blue), arsenopyrite (green), and As(0) (grey). The absorption edges correspond to the first derivative maxima of XANES spectra.

Figure 1.34. k^3-weighted arsenic K-edge EXAFS spectra ($k^3\chi(k)$) and corresponding Fourier transforms for the samples oxidized at pH 4.9 (A), 7.1 (B), and 9.1 (C) as well as reference compounds. Solid lines are the experimental data; dashed lines are the numerical fits. The samples oxidized for 0, 1, 2, 4, and 192 h (all black) are arranged from the bottom to the top, which are enveloped by reference compounds: aqueous As(V) (red), aqueous As(III) (orange), disordered As_2S_3 (pink), disordered AsS (blue), arsenopyrite (green), and As(0) (grey).

Figure 1.35. Column breakthrough curve at pH 5 (**bottom**) of FeS-coated sand column and concentration of dissolved Fe measured in effluent (**top**). (Influent: 0.1 M buffered solution with 0.013 mM (1 ppm) As(III) and 10 mM bromide with an average pore water velocity of 4.59 cm/hr).

Figure 1.36. Column breakthrough curve at pH 7 of FeS-coated sand column. (Influent: 0.1 M buffered solution with 0.013 mM (1 ppm) As(III) and 10 mM bromide with an average pore water velocity of 4.59 cm/hr).

Figure 1.37. Column breakthrough curve at pH 9 of FeS-coated sand column. (Influent: 0.1 M buffered solution with 0.013 mM (1 ppm) As(III) and 10 mM bromide with an average pore water velocity of 4.59 cm/hr).

Figure 1.38. Linearlized Langmuir sorption isotherm result at pH 5, 7 and 9 (**top**) and estimated retardation factor (**bottom**) with varying equilibrium arsenic concentration in solution at pH 5, 7 and 9. The vertical dotted line marks the As(III) concentration=1ppm and the horizontal dotted line shows that R approaches to 1 when the As(III) concentration increases.

Figure 1.39. Sorption isotherm of As(III) as a function of solid/solution ratio of FeS-coated sand suspension at (a) pH 5 and (b) pH 9. The effect of SSR is strongly shown at pH 9 condition.

Figure 1.40. SSR dependent Fe dissolution concentration (**left**) and the measured pe (**right**) at pH 5 FeS-coated sand batch. The x-axis number means the g mass of sand per 1000 mL solution. The marked point in the right plot shows the equilibrium pe value measured in the column from the continuous monitoring using a closed effluent chamber which was attached to the right next to the column end.

Figure 1.41. As(III) breakthrough curve with different column experimental conditions for (a) pH 5 and (b) pH 9 column influent with 1.3×10-5 M (1 ppm) As(III). The solute retention (travel) time for each column is 3.37 hr (Col #1), 1.16 hr (Col #4), 3.31 hr (Col #3), 1.16 hr (Col #5) and 3.44 hr (Col #6).

Figure 2.1. Loss of sulfate in biogenic production of FeS by *D. vulgaris* in terms of protein concentration. The lactate:sulfate ratio 2:1. The reaction solution was buffered to pH 7.2 by 50 mM HEPES.

Figure 2.2. pH changes during the biogenesis of ferrous sulfide minerals in presence of sulfate reducing bacteria.

Figure 2.3. Measurement of sulfate during the biogenesis of ferrous sulfide minerals in presence of sulfate reducing bacteria.

Figure 2.4. Measurement of sulfide concentrations during the biogenesis of ferrous sulfide minerals in presence of sulfate reducing bacteria.

Figure 2.5. XRD spectra of (a) *D.vulgaris* and (b) *D. autotrophicum*; Experiments conducted in presence of HFO; lactate:sulfate ratio 2:1.

Figure 2.6. Scanning electron micrographs of biogenically produced minerals; Minerals generated by (a) *D. vulgaris* and (b) *D. acetoxidans*.
Figure 2.7. pH edges measured at different biogenic FeS concentrations. Initial As(III) concentration was 13.4 μM; ionic strength 0.015M.
Figure 2.8. Effect of equilibration time on As(III) uptake by biogenic FeS and synthetic mackinawite; (a) pH 5.0; (b) pH 7.0; (c) pH 9.0. FeS concentration 1 g/L; pH adjusted with 0.1 N HCl or 0.1 N NaOH; initial As (III) concentration 6.4 mM.
Figure 2.9. Sorption isotherms of As(III) ion by biogenic FeS at constant pH with (a) higher and (b) lower initial concentrations. FeS concentration 1 g/L; pH adjusted with 0.1 N HCl or 0.1 N NaOH; ionic strength 0.015M.
Figure 2.10. pH edge experiments at different biogenic FeS concentrations; Cd (II) initial concentration 13.4 μM; Ionic strength 0.015 M NaCl.
Figure 2.11. Sorption isotherms of Cd(II) by biogenic FeS at different pH; Cd initial conc. 0.02 mM to 0.2 mM; FeS concentration 1 g/L; pH adjusted with 0.1 N HCl or 0.1 N NaOH; ionic strength 0.015M.
Figure 2.12. Sorption isotherms of Cd(II) by biogenic FeS at different pH; FeS concentration 1 g/L; pH adjusted with 0.1 N HCl or 0.1 N NaOH; ionic strength 0.015M.

Figure 3.1. Initial aggregation rates of nanoparticulate FeS suspensions at varying pH and constant ionic strength, 0.05 M. Particle diameters were measured by PCS.
Figure 3.2. Stability ratio dependence on pH with and without pH buffers. Error bars represent one standard deviation, and are obscured by the symbols in some cases.
Figure 3.3 FeS stability ratios as a function of buffer concentration at fixed ionic strength. (a) MOPS buffer at pH 7.0, (b) borate at pH 8.3.
Figure 3.4 Semi-logarithmic plot of FeS stability ratios as a function of ionic strength at pH 8.3 and 0.01 M borate buffer.
Figure 3.5 Deposition experiments of 1 g/L FeS suspensions in sand columns at varying pH and fixed ionic strength (0.025 M). (a) deposited FeS concentration profiles after 10 pore volumes (b) effluent breakthrough curves.
Figure 3.6. Eluted dissolved iron as a function of pH in FeS coated sand column. I = 0.01 M, Darcy velocity = 0.024 cm/s. Purple horizontal line indicates MINEQL+ prediction of saturation iron concentration with respect to FeS at pH 5.5.
Figure 3.7. Comparison of total and dissolved iron concentrations at pH 5.4-5.5 eluted from FeS-coated sand column. Filled markers are total iron concentrations, unfilled symbols are dissolved iron concentrations. Circles and triangles correspond to ionic strength conditions of 0.01 and 0.1 M, respectively.
Figure 3.8. pH dependence of particulate Fe release from FeS-coated sand columns. I = 0.01 M, Darcy velocity = 0.024 cm/s.
Figure 3.9 Effect of flow rate on total and dissolved iron elution from FeS-coated sand column at pH 5.5, I = 0.01 M. Numeric values next to curves are steady-state iron concentrations. Unfilled markers are particulate iron concentrations, filled markers are total Fe concentrations.

Figure 4.1. Matrix plot of selected variables for analysis of PRB geochemistry. "At risk" PRBs are indicated by green diamonds; "not at risk" by blue circles. (See Table 4.4 for units of measure).

Figure 4.2. MINEQL+ simulations of the final pH in the FeS system as a function initial pH, carbonate and calcium concentrations. Increasing carbonate provides buffering (increasing values on the x axis) and prevents pH increase (values of final pH are close to initial pH), and thus precipitation is expected only with initial pH >7 and carbonate > 1 x 10^{-3} mole/L.
Figure 4.3. Stability diagram for ZVI and FeS system, assuming FeT = 10^{-5} M, ST = 10^{-3} M, and CO3T = 10^{-2} M.
Figure 4.4. PHREEQC equilibrium simulation of addition of reactive media to pure water indicates the pH increase and pe decrease due to ZVI is greater than that due to FeS.
Figure 4.5. PHREEQC simulations indicate that carbonate mitigates the pH and pe changes caused by the presence of ZVI or FeS reactive media.
Figure 4.6. PHREEQC simulations showing the solids production due to the presence of 5 mmol/L of reactive media and calcium and carbonate in varying concentrations.
Figure 4.7. PHREEQC simulations showing mass and volume production of solids for the ZVI and FeS systems; ZVI consistently results in more solids mass and volume than FeS.
Figure 4.8. PHREEQC simulations with 5 mmol/L reactive media and 1.6mmol/L nitrate show that nitrate increases the equilibrium pH, and that the ZVI pH is consistently higher than the FeS system pH.
Figure 4.9. PHREEQC simulation show speciation of solids formed for the ZVI and FeS systems (5 mmol/L of reactive media) with 1.6mmol/L nitrate; ZVI consistently results in more solids mass and volume than FeS.
Figure 4.10. PHREEQC simulations showing mass and volume production of solids for the ZVI and FeS systems (5 mmol/L of reactive media) with 1.6mmol/L nitrate; ZVI consistently results in more solids mass and volume than FeS.
Figure 4.11. Porosity of mixtures of sand and ZVI is shown to vary linearly by mass fraction.
Figure 4.12. A) uneven flow distribution across the cross-sectional area of the column, and B) 1-D flow created by proper column packing and fitting assembly.
Figure 4.13. Increasing pressure to maintain flow caused by permeability loss in the ZVI-oxygen column.
Figure 4.14. SEM of ZVI-oxygen grains shows precipitation. ZVI particles are lower left and upper right; precipitates are seen in the pore space running from upper left to lower right.
Figure 4.15. Needle structure of precipitates in the ZVI-oxygen column.
Figure 4.16. FeS-oxygen column changes color as it is oxidized.
Figure 4.17. Change in color in the ZVI column influent end (bottom) relative to effluent end suggests accumulation of calcium carbonate.
Figure 4.18. pH and calcium data for both the FeS-fine and FeS-coarse columns; minimal changes in either parameter are observed.
Figure 4.19. The appearance of the FeS-fine column changed with time, moving from the influent (bottom end) to the effluent.
Figure 4.20. Sections taken from the coarse FeS column indicate dissolution of FeS, but no preferential flow paths. Each section is 2.5 cm thick, and section 1 is the influent end of the column.
Figure 4.21. pH increase in ZVI-nitrate column; minimal increase in FeS-nitrate column.
Figure 4.22. Calcium removal in ZVI-nitrate column; no removal in FeS-nitrate column.

Figure 5.1. Conceptual reaction model of FeS-coated sand–As(III) system.

Figure 5.2. Distribution of iron in different phases in batch systems (1g FeS-coated sand in 10 ml solution).
Figure 5.3A. Comparison of model predictions with measured pH data in the FeS-coated sand acid/base titration experiments (1g FeS-coated sand in 10 ml solution with no As(III) added).
Figure 5.3B. Comparison of model predictions with measured dissolved Fe concentration data in the FeS-coated sand acid/base titration experiments (1g FeS-coated sand in 10 ml solution with no As(III) added).
Figure 5.4. Model predicted pH-dependent speciation of surface sites associated with mackinawite and magnetite on the FeS-coated sand surface (1g FeS-coated sand in 10 ml solution with no As(III) added).
Figure 5.5. Comparison of model predictions with measured As concentration data in the FeS-coated sand acid/base titration experiments (1g FeS-coated sand in 10 ml solution with 1 ppm As(III) added).
Figure 5.6. Model predictions of pH-dependent As distribution in different phases (1g FeS-coated sand in 10 ml solution with 1 ppm As(III) added).
Figure 5.7. Reaction part of the reactive transport model for columns.
Figure 5.8. Comparison of As(III) breakthrough data with model predictions in Col#5.
Figure 5.9. Figure 5.9. Comparison of As(III) breakthrough data with model predictions in Col#4.
Figure 5.10. Flowchart of PHAST algorithm and modifications.
Figure 5.11. 1-D Simulation using data from a field ZVI PRB Site (Moffett Federal Airfield in Mountain View, CA) using a mixed equilibrium and kinetic reaction model for iron corrosion and subsequent mineral precipitation.
Figure 5.12. Comparisons of model predictions with measured trichloroethylene profiles in a ZVI column experiment conducted by Jeen et al. (2007).

List of Acronyms

ADE: advection-diffusion equation
BE: binding energy
BET: Brunauer, Emmett, and Teller surface area estimation method
BTC: break-through curve
CHES: 2-(cyclohexylamino) ethanesulfonic acid
CPU: central processing unit
CXTFIT: A code for estimating transport parameters from laboratory or field tracer experiments
DI: deionized
DLCA: diffusion limited colloid aggregation
DLVO: Derjaguin Landau Verwey Overbeek
DO: dissolved oxygen
DOD: Department of Defense
EDXS: energy dispersive x-ray spectroscopy
EGME: ethylene glycol monoethyl ether
EXAFS: extended x-ray absorption fine structure
FWHM: full width at half maximum
GNU: a recursive acronym that stands for "GNUs Not Unix" operating system
HAADF: high-angle annular dark field
HDF: hierarchical data format
HFO: hydrous ferric oxide
HPLC: high performance liquid chromatography
HST3D: non-iterative operator-splitting scheme to solve reactive transport problems by coupling
IB: integral breadth
ICP-MS: inductively coupled plasma-mass spectrometry
ICP-OES: inductively coupled plasma-optical emission spectroscopy
MCL: maximum contaminant level
MINTEQA2: A geochemical assessment model for environmental systems
MIN3P: a fully-implicit reactive transport code
MOM: The method of moment
MOPS: 3-(N-morpholino)-propanesulfonic acid
MPI: message passing interface
MW: molecular weight
NAPL: non-aqueous phase liquid
PCS: photon correlation spectroscopy
PEST: A nonlinear parameter estimation package
PHAST: ground water flow and solute transport simulator for 3D saturated ground water systems
PHREEQC: A computer program for speciation, batch-reaction, one-dimensional transport, and inverse geochemical calculations
PRB: permeable reactive barrier
PTZ: pre-treatment zone
PZC: point of zero charge
RDF: radial distribution function
RT3D: an all-kinetic modeling approach to simulate reactive transport in groundwater systems
SCM: Surface Complexation Model

SEM: scanning electron microscopy
SRB: sulfate reducing bacteria
SSA_{ext}: external specific surface area
SSR: solid solution ratio
STEM: scanning transmission electron microscopy
SON: statement of need
TEM: transmission electron microscopy
XANES: x-ray absorption near edge structure
XAS: x-ray absorption spectroscopy
XPS: x-ray photoelectron spectroscopy
XRD: x-ray diffraction
ZVI: zero valent iron

Keywords

groundwater contamination, *in situ* groundwater treatement, anoxic conditions, anaerobic conditions, arsenic, cadmium, realgar, orpiment, cadmium sulfide, mackinwate, pyrrhotite, nanoscale iron sulfide, iron-sulfide coated sand, zero valent iron, sulfate reducing bacteria, biogenic formation of iron sulfide, precipitation, adsorption, surface precipitation, permeable reactive barriers, colloidal emplacement, colloidal deposition, PRB failure modes, pore plugging mechanisms, 1D and 2D reactive transport modeling, porosity and permeability reduction modeling.

Acknowledgements

This production of this report and the experimental work reported herein were the result of the effort of the project's research team. This includes, in addition to the PI/PD (Kim F. Hayes) and co-PIs (Peter Adriaens, Avery H. Demond, Terese M. Olson, and Linda M. Abriola-Tufts University), the contributions of Drs. Tanya J. Gallegos, Hoon Young Jeong, Sung Pil Hyun, Jun Hee Lee, and Raveender Vannela; Ph.D. graduate students Young Soo Han, Andrew Henderson, Monica Higgins, Li Wang (Tufts University) and Devon Renock (and his Ph.D. advisers Drs. Udo Becker and Rodney Ewing); and undergraduate students Kate Baldwin, Alicia Lane, and Anthony Martus. We thank Thomas Yavaraski, Laboratory Manager in the Environmental and Water Resources Engineering Program in the Department of Civil and Environmental Engineering at the University of Michigan, for his technical support of this project. Funding for this work was provided by the Department of the Army, Strategic Environmental Research and Development Program (SERDP contract# W912HQ-04-C-0035) for this project, referenced as SERDP ER-1375. Portions of this research were carried out at the Stanford Synchrotron Radiation Light source, a national user facility operated by Stanford University on behalf of the U.S. Department of Energy, Office of Basic Energy Sciences. The SSRL Structural Molecular Biology Program is supported by the Department of Energy, Office of Biological and Environmental Research, and by the National Institutes of Health, National Center for Research Resources, Biomedical Technology Program.

Abstract

In this research, we have evaluated iron sulfide for treating heavy metal contaminated groundwater plumes for PRB systems. Our approach was to test the effectiveness of reduced iron sulfide (FeS) as both a sorbent and reducing agent in PRB applications for long-term sequestration of heavy metal ions. Cadmium (Cd) and Arsenic (As) were the targeted contaminants. Mechanistic information on the metal removal mechanisms was obtained by molecular-scale surface techniques including synchrotron-based XAS and XRD, and microscopic tools such as HRTEM and SEM-EDS. FeS performance under various geochemical conditions was investigated using batch and column reactor systems. Two different forms of reactive sorbent media were prepared, nanoscale FeS and FeS-coated sand for two emplacement methods, colloidal injection and physical packing of porous media, respectively. Rejuvenation of FeS using sulfate reducing micro-organisms for biogenic formation of FeS from iron oxidation products was examined and shown to be feasible. Finally, a reactive transport model was developed using batch isotherm and column arsenic breakthrough data. The overall results provide tools needed to design and apply the FeS PRB media for effective long-term treatment of mixed-metal ion plumes at contaminated groundwater DOD sites.

Executive Summary

In situ abiotic/biotic permeable reactive barrier (PRB) systems offer great potential for the cost-effective removal of heavy metal ions from contaminated groundwater supplies. In these systems, reactive material is introduced into a "permeable wall" placed in the groundwater flow path to remove targeted contaminants. Of interest in this project is the use of particulate iron sulfide (FeS) in PRB applications. FeS has a high capacity for non-redox active metals such Cd(II) in which highly insoluble cadmium sulfides (CdS(s)) form by favorably exchanging for Fe in FeS. For redox-active metals such as arsenic (As), FeS serves as an effective reductant, converting oxidized forms of As(V) to the more reduced forms of As(III) and subsequently removing it by adsorption or formation of mixed-metal sulfide phases. Concerns remain, however, related to the longevity of materials in PRBs and the impact of changing geochemical conditions (e.g., pH and redox) on long-term sequestration properties. A natural consequence of redox reactions and introduction of oxygenated water is the formation of more oxidized forms of FeS. In situ microbiological processes could provide a cost-effective way to rejuvenate FeS for long-term use and reuse and to maintain reducing conditions. Also, the successful design and performance evaluation of FeS PRBs will require the application of reactive transport models, based on a clear understanding of the metal ion sequestration mechanisms (e.g., reduction, sorption and precipitation) and their impact on transport properties (e.g., porosity and hydraulic conductivity) under realistic geochemical conditions.

In recognition of the potential of FeS for treating contaminated groundwater, in this research, two different forms of FeS have been developed for treating heavy metal contaminated groundwater plumes in PRB systems, a nanoscale form of FeS for direct injection and FeS-coated sand for emplacement in PRB walls. To test the effectiveness of reduced iron sulfide (FeS) for long-term sequestration of heavy metal ions and oxyacids, cadmium (Cd) and arsenic (As) were selected. FeS performance has been investigated using batch reactor and column reactor systems under various geochemical conditions. Using molecular-scale surface techniques including synchrotron-based x-ray absorption spectroscopy (XAS), x-ray diffraction (XRD), x-ray photoelectron spectroscopy (XPS), and microscopic tools such as transmission electron microscopy (TEM) and scanning electron microscopy (SEM) with energy dispersive x-ray spectroscopy (EDXS), information of the properties of FeS an dmechanistic information on the removal mechanisms by FeS of both As and Cd has been obtained. Two emplacement methods, colloidal injection and physical packing of FeS-coated sand in porous media, were also evaluated. We also assessed the ability to rejuvenate FeS from oxidized forms of iron that were expected to be representative of reacted FeS using a variety of sulfate reducing microorganisms. Finally, a reactive transport model was developed using batch uptake and column breakthrough data for calibration along with the mechanistic information obtained. The model is expected to useful for designing and apply the FeS media in a PRB application for effective long-term treatment of an arsenic contaminated plume at an appropriate Department of Defense (DOD) site.

Achievements of this work include the successful development of two forms of reactive FeS media for field-scale application, a nanoscale FeS for direct colloidal injection into the subsurface at a contaminated site and FeS-coated sand for a trench and fill PRB application. The colloidal form was tested and the conditions established for optimal effective dispersal and coating of packed column of cleaned sand. An extension for establishing the appropriate conditions for natural sand will require applying the protocols developed for site specific

materials. The results indicate, in general, that by changing solution conditions (pH and ionic strength) it is possible to optimize the process for effective distribution of the material in sandy porous media without clogging the formation. Likewise a procedure to effectively coat sand with FeS was developed. Reactivity studies with both nano-scale FeS and FeS-coated sand indicate that these materials will be effective for removing arsenic from contaminated groundwater in PRB applications.

As a benchmark, the pore plugging of FeS-coated materials was compared with zero valent iron (ZVI), a commonly used material in many current PRB systems. Columns packed with FeS-coated sand indicated much less pore plugging compared to columns packed with ZVI reactive media. This is due to the lower potential for FeS-coated sand to undergo anaerobic corrosion by water and the lack of pH change in carbonate buffered water systems representative of groundwater. In contrast, the pH changed more than two pH units in ZVI media from anaerobic corrosion, which can lead to excessive build-up of iron hydroxide corrosion and precipitation of $CaCO_3$(s) products in ZVI packed columns. The pore plugging studies also indicate that the main failure mode for FeS-based PRBs, if it occurs at all, would be more likely from pore plugging caused by precipitation of $CaCO_3$(s), depending on groundwater pH, alkalinity and Ca concentrations, rather than from corrosion or loss of FeS media reactivity from treated targeted contaminants.

Several sulfate reducing bacteria (SRB) were shown to be capable of rejuvenating *FeS* should it become oxidized or converted to iron hydroxide or oxide forms from treating contaminants or through oxidation reactions with the background water. *FeS* was biogenically produced by SRB from a variety of different forms of iron including (ferric hydroxide, mixed ferric-ferrous green rusts and soluble ferrous salt). Three Gram negative strains of SRB (*Desulfovibrio desulfuricans, Desulfovibrio vulgaris,* or *Desulfobacter autotrophicum*) and two strains of gram positive SRB (*Desulfotomaculum acetoxidans* or *Desulfotomaculum nigrificans*) were found to form FeS. In this work, the biogenically formed FeS by *Desulfovibrio vulgari* using HFO as an iron source has been demonstrated to have similar reactivity and capacity to the synthetic form of FeS for arsenic and cadmium removal from water.

Mechanistic information obtained during this investigation has established that arsenic is removed at lower pH (e.g., pH 5) by FeS primarily from the formation of AsS(s) (realgar) or orpiment (As_2S_3), depending on the reducing conditions as measured by E_H. The removal capacity at pH 5 is relatively high and apparently limited only by the accessibility of the molar amount of sulfide available in the FeS for this precipitation. At higher pH (7 and 9), the removal of arsenic occurs by both precipitation and surface-limited adsorption on the FeS surface and/or the iron oxides or hydroxides that may form upon the replacement of Fe by As during the formation of AsS(s) or As_2S_3(s) or as a result of the preparation and aging of FeS. The capacity of FeS is significantly less at the higher pH values indicating that optimal removal of As is best at pH less than 7. Cd removal mechanistic studies indicate that FeS is effective and also removes Cd by the precipitation of CdS(s) or adsorption. The removal of Cd as CdS(s) solid appears to be the primary removal mechanism over the entire range of pH from 5 – 9.

In general, the removal mechanistic established for the systems containing suspensions of nanoscale FeS and arsenic were also found to be operating for the FeS-coated sand materials developed for PRB applications. However, a few differences were noted. Whereas at pH 5, arsenic removal upon reaction with FeS was primarily found result from the formation of AsS(s), in the case of FeS-coated sand, the precipitated solid was As_2S_3. This was postulated to result from the higher E_H conditions measured for the FeS-coated sand leading to the favorability of the

less reduced form of arsenic sulfide. Also in the FeS-coated sand system, the presence of dissolved silica had an inhibiting effect of As uptake at higher pH of 9, where the removal of arsenic was primarily due to sorption of arsenic on iron oxyhydroxides that formed or were originally present on the sand used that were coated for these studies. Finally, at pH 5 and 7 the removal capacity of FeS-coated sand was less than the nanoscale FeS material but slightly greater at pH 9. The capacity differences were attributed to partial conversion of FeS to iron oxyhydroxides and less reactive forms of FeS during the coating procedure. In general, the FeS-coated sand material was found to be effective at removing arsenic with a capacity that is comparable to other coated-sand materials that have been produced for arsenic from water. The primary advantage of FeS over these other materials is that it is applicable to anoxic systems whereas most other materials release arsenic (or other sorbed heavy metals) through reductive dissolution processes when subjected to reducing conditions.

Finally, a 1D transport module in PHREEQC was utilized in this project to incorporate the impact of pH, pe, and equilibrium and rate-limited dissolution and arsenic precipitation and adsorption to *FeS* to model the transport of *As* in *FeS*-coated sand columns using the mechanisms established for arsenic removal to guide the selection of appropriate relationships. The model was successful in simulating the breakthrough data for pH 5 and 9. A modeling effort was also focused on improving and validating the numerical simulator PHAST to account for time-varying porosity and permeability so that the impact of precipitation on the longevity of PRBs can be evaluated. A ZVI reactivity model was been incorporated in PHAST to account for the reactivity reduction of ZVI due to surface passivation caused by iron corrosion products. Validation of this later code was accomplished using data from a field ZVI PRB site, and a ZVI column experiment using field groundwater at the site of Y-12 National Security Complex in Oak Ridge, TN. This code was also successful in modeling reactivity changes in ZVI column data reported in the literature.

Background

In situ abiotic/biotic PRBs offer great potential and cost savings advantages for removing heavy metal ions from contaminated groundwater supplies. In these systems, reactive material is introduced into a "permeable wall" placed in the groundwater flow path to remove targeted contaminants. Of particular interest in the context of this proposal is the use of particulate FeS in PRB applications. FeS has a high capacity for non-redox active metals such as Pb(II) and Cd(II) in which highly insoluble Cd or Pb sulfides form by favorably exchanging for Fe in FeS. For redox-active metals such as As or Cr, FeS serves as an effective reductant, converting oxidized forms (As(V) and Cr(VI)) to more reduced forms (As(III) and Cr(III)) and subsequently removing the metals by adsorption or formation of mixed-metal sulfide phases. Concerns remain, however, relating to the longevity of materials, such as FeS, in PRBs and the impact of changing geochemical conditions (e.g., pH and redox) on long-term sequestration properties. A natural consequence of redox reactions and introduction of oxygenated water is the formation of more oxidized forms of FeS. In situ microbiological processes could provide a potentially attractive and cost effective way to rejuvenate FeS for long term use and re-use and to maintain reducing conditions. Also, since FeS can be generated as a coating on other commonly prepared materials for PRB applications (such as iron-coated sands or zero valent iron), it may be feasible to produce reactive FeS economically in a whole range of sizes. This may facilitate the use of FeS in a variety of applications, ranging from constructed near-surface PRB walls to colloidal

injection of FeS into difficult to treat locations such as under buildings or into deep aquifers. The successful design and performance evaluation of FeS PRBs requires the application of reactive transport models, based upon a clear understanding of the metal ion sequestration mechanisms (e.g., reduction, sorption and precipitation) and their impact on transport properties (e.g. porosity and hydraulic conductivity) under realistic geochemical conditions.

FeS for Removing Cd and As from Groundwater. Materials that are effective at immobilizing and capturing metals and radionuclides include naturally occurring aluminum and iron oxyhydroxides (Jenne, 1968; 1998; McKenzie, 1980; Kinniburgh and Jackson, 1981), aluminosilicate clays (Zachara et al., 1992, 1993; Hayes and Chen, 1999), natural zeolites (Jenne, 1998), hydroxyappatites (Ma et al., 1993; 1994a,b; 1995) and iron sulfide minerals (Wildeman et al., 1994; Parkman et al., 1999; Moyes et al., 2000; 2002; Jeong et al., 2003) as well as synthetic materials including ion exchange resins (deRoy et al., 1992; Newman and Jones, 1998) and functionalized clays (Mercier and Pinnavaia, 1997; 1998). While most of these metal ion sorbents can reduce metal toxicity, bioavailabilty, and mobility by lowering the concentration through sorption under oxic conditions, many of these subsequently release metals when subjected to reducing conditions, and only a few are also capable of redox conversions of redox-active metals to less harmful or less mobile forms. Unlike these other materials, FeS has been shown capable of effective sequestration of both redox active and non-redox active metals. For example, FeS is capable of converting Cr(VI), a toxic and highly mobile form of Cr, to the very insoluble and less toxic Cr(III) solid form (Paterson et al., 1997; Bouriquot et al., 2002)). In the case of As, XAS (x-ray absorption spectroscopy) studies have illustrated that FeS (as mackinawite) reduces As(V) to As(III) with the formation of insoluble As_2S_3 or As(III) surface complexes depending on the surface coverage, relative concentrations, and the order in which the phases are contacted (Farquhar et al., 2002). Dissolved sulfide can also convert As(V) to As(III), with the formation of the orpiment (As_2S_3; Rochette et al., 2000). Although zero-valent iron (ZVI) can reductively convert Cr(VI) to Cr(III) hydroxide precipitate (Puls et al., 1995; Blowes et al., 1995, 1997; Powell et al., 1995) and has been used for this purpose in permeable barriers (Gavaskar et al., 1998; National Research Council; 1997), it is not, in general, a very effective trapping agent for metals nor has it been found effective at completely reducing As(V) to As(III) (Farrel et al., 2001) although As removal through sorption (presumably to more oxidized forms of iron) in ZVI systems has been reported (Su and Puls, 2001). FeS has been used to control the migration of toxic metals in acidic mine tailing groundwater plumes by promoting the formation of more insoluble metal sulfides with divalent cations (Herbert et al., 2000). FeS has also been shown to be an excellent material for removing divalent cations by forming very insoluble metal sulfides (e.g., HgS, Jeong et al., 2003; Cd, Billon et al., 2001), or by forming solid solutions with FeS (e.g., with Cd and Pb; Coles et al., 2000). With its excellent properties as both a reducing and a heavy metal ion trapping agent, FeS is an excellent candidate for the sequestration of Cd and As (and other heavy metal ions) particularly under reducing geochemical conditions, where other iron sorbents (e.g., ZVI and aluminum oxides) typically release these metals. As such, in this work, ***FeS* was investigated for efficacy in sequestering *Cd* and *As* under a reducing geochemical conditions over a range of pH conditions.**

Impact of oxidation process on FeS metal ion sequestration properties and methods of regeneration of FeS using sulfate reducing bacteria. A major issue with any PRB system is its capacity and long-term performance under changing geochemical conditions. Of particular

concern with PRB systems that use reduced material such as ZVI or FeS is the impact of oxidation/reduction reactions. Fortunately ample studies have been conducted with both ZVI and FeS to address the expected impacts of changing oxidation conditions on reactivity. Corrosion (oxidation) studies of ZVI by oxygen have shown that corrosion reactions convert the surface of ZVI to iron oxides of higher iron oxidation state, ranging from green rusts with predominantly Fe(II) to mixed Fe(II)/Fe(III) solids such as magnetite to Fe(III) oxyhydroxides such as ferrihydrate. In PRBs, oxidation of reactive ZVI by oxygen mainly occurs near the "edge" or "entrance" of the walls whereas anaerobic oxidation by other oxidants (e.g., targeted redox active contaminants) leads to formation of other iron minerals such as magnetite or siderite (Furwkawa et al., 2002). Similarly, oxidation of FeS by oxygen can produce Fe(III) oxides such as goethite (α–FeOOH) and mixed Fe(II)/Fe(III) oxides that also form from ZVI, as well as less reduced iron sulfide forms such as the mixed Fe(II)/Fe(III) iron sulfide greigite (Fe_3S_4) or pyrite (FeS_2) (Lennie et al., 1995). Interestingly, iron oxides formed from the oxidation of ZVI or FeS are also excellent sequestration agents for heavy metal cations and oxyacids (Jenne, 1967; Kinniburgh and Jackson, 1981; Hingston, 1981). Hence, even if reduced iron PRB materials are oxidized, the resulting solid phases can still provide a certain level of protection from metal cations (Furukawa et al., 2002) and oxyacids (Su and Puls, 2001). Although oxidation processes must be understood and can eventually deplete the reducing capacity of reduced materials, oxidizing conditions per say will not limit the effectiveness of FeS any more than they would ZVI walls, as long as the design capacity (i.e., emplaced material) is sufficient for the planned barrier life. That some of the first ZVI walls installed in the early 90s are still functioning is compelling evidence that reduced iron PRBs can remain effective for a very long time.

Recognizing that reducing capacity of FeS will eventually run out makes it desirable to find ways to "recharge" the system. Sulfate reducing bacteria can couple the oxidation of organic matter to the reduction of sulfate to sulfide, to produce FeS when reduced iron is also present (Watson et al., 2000; Matsuo et al., 2000; Herbert et al., 1998). Microbial formation of iron sulfides by SRB almost always produces a monosulfide, mackinawite-FeS type phase (Vaughan and Lennie, 1991). In general, both intracellular and extracellular iron sulfide biogenesis can produce FeS, with the later germane to this work. Extracellular iron sulfide biogenesis occurs in environments where biogenic sulfide and ferrous iron accumulate, the expected scenario for FeS PRB systems. Most studies of extracellular biogenic processes indicate that the bacteria act simply to generate sulfide (e.g., Herbert et al. 1998). The starting form of iron appears to play a role in dictating the form of biogenic iron sulfide formed. For example, using a sulfate reducing enrichment culture, Herbert et al. (1998) reported that poorly ordered mackinawite was the primary biogenic FeS formed when Fe(II) was provided in solution at ca 14 μM. Using hematite (α-Fe_2O_3) as the iron source and a pure culture of Desulfovibrio desulfuricans, Neal et al. (2001) reported that surface associated pyrrhotite, another form of FeS, was the principal biogenic product. FeS has been found to form under sulfate reducing conditions in a variety of field settings including acid mine tailings impoundments (Fortin and Beveridge 1997), reactive barriers specifically set up to generate FeS for treating acid mine drainage (Wildeman et al., 1994; Herbert et al., 2000) and ZVI PRBs (Gu et al., 1999), indicating that in situ formation of FeS under sulfidogenic conditions is possible and likely when iron is present. **SRB were investigated in this project for their potential to regenerate FeS from its iron oxidation products**.

Methods of Generating FeS. Reactive solid materials can be mixed in permeable reactive barrier systems in so-called "funnel and gate" configurations. Zero valent iron (ZVI) has been used most frequently in such applications (see, e.g., with pilot- and full-scale operations documented at more than a dozen sites (Gavaskar et al., 1998), particularly for reductive dechlorination of chlorinated solvents based on successful laboratory demonstrations (Gillham and O'Hannesin, 1994; Matheson and Tratnyek, 1994; Roberts et al., 1996; Johnson et al., 1996). While solid forms of FeS have not been used in such applications, it is equally feasible to do so. For such applications to be economically viable and acceptable in practice, however, FeS would ultimately need to be available in large quantities and size ranges. Past laboratory studies have established the feasibility of producing FeS from ZVI by reaction with soluble sulfide (Boursiquot et al. 2002). Another potential pathway for establishing a solid form of FeS in mixed-media barrier material applications is through the preparation of FeS-coated sands. FeS coated sands can be prepared using pre-cleaned quartz particles and procedures documented by Willard and Seward (2002). Both of these processes would need to be scaled-up for full commercial production. Nanoscale FeS can be prepared by direct precipitation of solid FeS (Jeong et al., 2008). **In this project, nanoscale FeS and FeS-coated sand media were evaluated for removal of arsenic and cadmium, and arsenic, respectively, from water and for use in PRB applications.**

Methods of Emplacing FeS in PRBs. In PRB applications involving FeS, effective sequestration must be balanced against maintaining a sufficiently high hydraulic conductivity through the treatment zone to allow for prolonged precipitation or sorption of the targeted metal ions (Gavaskar et al., 1998). Given that substantial precipitation can occur from unwanted side reactions between the PRB reactive material and groundwater near the entrance to PRBs (Yabusaki et al., 2001), it is imperative to design the barrier so that its performance will not be adversely impacted. In this research, the impact of various barrier configurations and FeS forms will be tested in column reactor systems to develop the understanding needed to establish optimal configurations of FeS and porous media to avoid unwanted pore plugging.

Alternatively, when constructed walls of FeS would be impractical, such as when contamination is under buildings or deep in the subsurface, injecting reactive slurries of colloidal FeS may be feasible. Prior work using colloidal ZVI particles shows that it is possible to effectively inject ZVI colloids evenly throughout a porous medium, but control of ionic strength and pH is important (Kaplan et al., 1994). Adjustments of particle concentration, fluid viscosity properties, and particle surface charge are also factors that enhance the stability of ZVI colloids and the effectiveness of delivery in such applications (Cantrell and Kaplan, 1997; Cantrell et al., 1997). Similarly, it should be equally possible to utilize nanoscale FeS for effective subsurface delivery. With a pH point of zero charge of below pH of 3 (Bebie et al., 1998), colloidal FeS particles, with a negative charged at typical groundwater pH values, should be amenable for effective dispersion throughout a porous medium of predominantly negatively charged particles, the case that would be encountered in many subsurface environments. The potential to adjust surface charge and colloidal stability through ionic strength adjustments also provides an opportunity to tailor colloidal FeS for any given application**. In this research, various emplacement methods of FeS materials (e.g. physical mixing or injection of colloids) were evaluated, and as needed, optimized to reduce their impact on hydraulic conductivities.**

Reactive Transport Modeling of Metal Ion Sequestration in FeS PRBs. A suitable reactive transport model is needed for effective design and evaluation of FeS PRB systems and for modeling the column reactors proposed for this research. Past experience in modeling ZVI PRB systems indicates that, to effectively simulate pH, uptake or transformation of targeted contaminants, and pore plugging potential from mineral precipitation, reactive transport models must incorporate oxidation (i.e., corrosion), precipitation, and adsorption reactions with the PRB material, as well as realistic solution chemistry (see e.g., Mayer et al., 2001; Yabusaki et al., 2001). A similar level of detail is needed to effectively model the reactions occurring in the FeS systems that were developed in this research. Important "background" solution components in groundwater include major cations such as Na^+ and Ca^{2+} and major anions such Cl^- and $HCO3^-$, with carbonate of particular importance for any realistic prediction of pH. Additionally, the solution chemistry of the targeted contaminants (e.g, Cd(II) and As (As(III) or As(V)) and their reactions with FeS must be included. For As and Cd, the main removal reactions under anoxic conditions are expected to be the precipitation of CdS(s) and AsS(s) or As_2S_3(s), respectively, with the potential for solid solution formation a secondary effect. Additional precipitation products in a simulated FeS/groundwater system would, at a minimum, include $CaCO_3$(s), $Fe(OH)_3$(am), $FeCO_3$(s), FeS, $Fe(OH)_2$ (am), $CdCO_3$(s), $Cd(OH)_2$(am), As_2O_3, and $FeAsO_4$, the simplest and primary minerals that might form. Redox reactions rates between FeS and the major redox couples present (As(III)/As(V), H_2O/H_2, and O_2/H_2O) may also need to be part of a transport model. Overall reaction stoichiometries that produce Fe(II) or Fe(III) from coupling of the major redox reactions with FeS oxidation might need to be specified or assumed, similar to the approach presented by Mayer et al. (2001) for simulating ZVI PRB corrosion reactions. An appropriate sorption/desorption model may also be needed to assess the potential importance of surface sorption reactions. Surface complexation models have been found to be effective in modeling the pH, ionic strength, and competitive sorption behavior of metal cations and oxyacid in the presence of iron oxide minerals (see, e.g., Hayes and Katz, 1996; Dzombak and Morel, 1990). Model validation requires simulating breakthrough data, including pH and the concentrations of major anions, cations, and targeted metals, over a range of solution conditions. The reactive transport model PHREEQC (Parkhurst and Appelo, 1999) can be adapted to predict PRB performance as a functional of geochemical conditions. As currently configured, this code can model solution speciation in batch reactors and one dimensional transport in column reactors, using equations involving several types of reversible (e.g., acid-base and precipitation reactions) and irreversible solution reactions (e.g., redox reactions). The model also incorporates surface complexation subroutines for predicting sorption/desorption reactions of metals and oxyacids with iron oxides. **A 1D reactive transport code was developed and laboratory-validated in this research effort and applied in a 2D/3D version for prediction of FeS barrier performance and field-scale barrier design applications.**

Project Objectives

Arsenic (As) and Cadmium (Cd) have known toxic and carcinogenic properties and have been identified as high priority pollutants in the SERDP Statement of Need (SON). Cd, a non-redox divalent metal cation represents a class of common heavy metal ion contaminants that includes metals such as Pb, Hg, Ni and Zn. As, a redox active oxyacid represents a class of difficult to treat metals that include Cr and Se. As concentration in groundwater at DOD sites often exceeds 30 μg/L, with concentrationsin excess of 200,000 μg/L noted at some sites. These high

concentrations result from the high solubility of As in the form of oxyacids that predominate in aqueous systems. Cd, a divalent cation (Cd^{2+}), is less soluble than As due to the relatively lower solubility of Cd in common mineral forms. Cd, however, can be found in concentrations up to 100-1000 ug/L (its solubility in $CdCO_3$(s) near neutral pH, depending on how carbonate concentration is controlled) and at even higher concentrations if chelating agents are present that are common in mixed wastes. Maximum Contaminant Levels (MCLs) for As and Cd, 10 and 5 μg/L respectively, present an exceptional challenge for achieving safe levels at contaminated DOD sites. Fortunately, evidence suggests that both As and Cd can be effectively treated with FeS systems to produce highly insoluble sulfide phases and reduce concentrations well below MCL levels under anoxic conditions. In addition, ample evidence exists that metal sulfide phases are resistant to reductive and oxidative leaching and further that oxidized forms of FeS can also can effectively sequester metals such as Cd and As. Hence, this research focused on the mechanisms of removal and the long-term effectiveness of FeS PRB systems for removal of As and Cd under anoxic conditions and under changing geochemical pH and redox conditions that may occur during long-term operation. Given that the impact of changing geochemical conditions at heavy metal contaminated sites was cited as a major concern in the SON for treatment systems which sequester metal ions in place, this work investigated another major SON of SERDP. Further, since longevity is often cited as a major concern for in-place PRBs, this work also investigated the potential for re-activating FeS in PRB systems by using an in situ microbiological rejuvenation processes to convert oxidized iron phases produced or present during treatment or exposure to oxidizing conditions back to reactive FeS. These microbiological processes could be used for both of the FeS-based systems studied here, but also could be applied to currently operating PRBs that use reduced iron media. Finally, the development of effective FeS emplacement methods and a reactive transport model were also developed in this project for moving the laboratory-scale investigations to the field.

Given the above research needs of SERDP, the overall objective of this project was to evaluate the effectiveness of FeS materials for sequestration of a targeted oxyacid, As, and heavy metal cation, Cd, under anoxic conditions in PRB applications. Consistent with this overall objective, five major research tasks were undertaken, viz., to: 1) characterize FeS reactivity and reaction mechanisms for As and Cd removal, 2) evaluate microbial methods for regeneration of FeS, 3) optimize colloidal injection methods for the effective dispersal of nanoscale FeS into porous media, 4) investigate suitable methods of emplacement of FeS in mixed porous media for plugging avoidance, and 5) develop and laboratory-validate a multi-component reactive transport model for PRB performance predictions and field-scale design applications.

The working hypotheses were that:

1. *effective forms of FeS (e.g., colloidal FeS and FeS-coated sand) could be developed for in situ PRB applications,*

2. *FeS materials would be effective for removal of As and Cd under anoxic conditions over a range of pH values,*

3. *FeS materials could be optimized for colloidal injection and mixed porous media emplacement,*

4. *sulfate reducing bacteria could be used to convert oxidized forms of iron back to a reactive form of FeS, and*

5. *a reactive transport model would be useful for evaluating FeS performance.*

For each major task undertaken, the specific task objectives, background, material and methods, results and discussion, and conclusions and implications for future research/implementation are described below in this report.

Literature Cited

Bebie, J., A.A.M. Schoonen, M. Furhrmann, D.R. Strongin, 1998. Surface charge development on transition metal sulfides: An electrokinetic study. *Geochimica Cosmochimica Acta*, **62**, 633-642.

Billon G., B. Ouddane B, J. Laureyns A. Boughriet, 2001. Chemistry of metal sulfides in anoxic sediments. *Physical Chemistry Chemical Physics* **3**, 3586-3592.

Blowes, D.W., C.J. Ptacek, C.J. Hanton-Fong, J.L. Jambor, 1995. In Situ remediation of chromium contaminated groundwater using zero valent iron," Preprints of 209th American Chemical Society National Meeting, Anaheim, CA, April 2-7.

Blowes, D., C. Ptacek, C., J. Jambor, 1997. In-situ remediation of Cr(VI)-contaminated groundwater using permeable reactive walls: Laboratory studies. *Environ. Sci. Technol*., **31**, 3348-3357.

Boursiquot, S., M. Mullet, M. J.J. Ehrhardt, 2002. XPS study of the reaction of chromium (VI) with mackinawite (FeS). *Surfaces and Interfaces*, **34**, 293-297.

Cantrell, K. J., D. I. Kaplan and T. J Gilmore, 1997. Injection of Colloidal Size Particles of Fe(0) in Porous Media with Shear-thining Fluids as a Method to Emplace a Permeable Reactive Zone. *Land Contaminaton & Reclamation* **5**, 253-257.

Cantrell, K. J., and D. I. Kaplan, 1997a. Zero-valent iron colloid emplacement in sand columns. *J. Environ. Eng.* **123**, 499-505.

Cantrell, K. J., and D. I. Kaplan, 1997b. Injection of Colloidal Fe0 Paricles in Sand Columns with Shearthining Fluids. *J. Environ. Eng.* **123**, 786-791.

Coles, C.A., S.R. Rao, and R.N. Yong, 2000. Lead and Cadmium interactions with mackinawite: Retention mechanisms and the role of pH. *Environ. Sci. Technol*. **34**, 996-1000.

DeRoy, A., C. Forano, K.E. Malki, J.P. Besse, 1992. in Synthesis of Microporous Materials, Vol. 2, Van Nostrand Reinhold, New York, pp108-169.

Farrell, J., J.P. Wang, P. O'Day, and M. Conklin, 2001. Electrochemical and spectroscopic study of arsenate removal from water using zero-valent iron media. *Environ. Sci. Technol*. **35**, 2026-2032.

Farquhar, M.L., J.M. Charnock, F.R. Livens, and D.J. Vaughan, 2002. Mechanisms of arsenic uptake from aqueous solution by interaction with goethite, lepidocrocite, mackinawite, and pyrite: An X-ray absorption spectroscopy study. *Environ. Sci. Technol*. **36**, 1757-1762.

Fortin, D., and T.J. Beveridge, 1997. Microbial sulfate reduction within sulfidic mine tailings: Formation of diagenetic Fe sulfides. *Geomicrobiology Journal* **14**, 1-21.

Fryar A.E. and F.W. Schwartz, 1994. Modeling the Removal of Metals from Groundwater by a Reactive Barrier – Experimental results. *Water Resources Research* **30**, 3455-3469.

Furukawa, Y., J.W. Kim, J. Watkins, R.T. Wilkins, 2002. Formation of ferrihydrite and associated iron corrosion products in permeable reactive barriers of zero valent iron. *Environ. Sci. Technol.* **36**, 5469-5475.

Gavaskar, A.R., N. Gupta, B.M. Sass, R.J. Janosy, D. O'Sullivan, 1998. Permeable Barriers for Groundwater Remediation, Battelle Press, Columbus, OH, pp176.

Gillham, R.W., and S.F. Hannesin, 1994. Enhanced degradation of halogenated aliphatics by zero-valent iron. *Ground Water* **32**, 958-967.

Gu, B., T.J. Phelps, L. Liang, L., M.J. Dickey, Y. Roy, B.L. Kinsall, A.V. Palumbo, and G.K. Jacobs, 1999. Biogeochemical dynamics in zero valent iron columns: Implications for permeable reactive barriers. *Environ. Sci. Technol.* **33**, 2170-2177.

Herbert, R.B., S.G. Benner, and D.W. Blowes, 2000. Solid phase iron-sulfur geochemistry of a reactive barrier for treatment of mine drainage. *Applied Geochemistry* **15**, 1331-1343.

Herbert, R.B., Jr,. S.G. Benner, A.R. Pratt, and D.W. Blowes, 1998. Surface Chemistry and Morphology of Poorly Crystalline Iron Sulfides Precipitated in Media Containing Sulfate Reducing Bacteria. *Chemical Geology* **144**, 87-97.

Hayes, K.F., and L.E. Katz, 1996. Application of X-ray absorption spectroscopy for surface complexation modeling of metal ion sorption. in Physics and Chemistry of Mineral Surfaces (P.V. Brady, Ed.), CRC Press, New York.

Hingston, F.J., 1918. A review of anion adsorption, In Adsorption of Inorganics at Solid-Water Interfaces, (ed., M.A. Anderson and A.J. Rubin), Ann Arbor Science, Ann Arbor MI, pp51-90.

Jenne, E.A., 1967. Controls of Mn, Fe, Co, Ni, Cu, and Zn concentrations in soils and water-The significant role of hydrous Mn and Fe oxides. *Adv. Chem.* No. 73, pp337-387, American Chemical Society, Washington D.C.

Jenne, E.A. (ed.), 1998. Adsorption of metals by geomedia: variables, mechanisms, and model applications, Academic Press, New York, pp583.

Jeong, H.Y., B. Klaue, J.D. Blum, K.F. Hayes, 2007. Sorption of Mercuric Ion Hg(II) by Iron Sulfide. *Environ. Sci. Technol.* **41**, 7699-7705.

Johnson, T.M., M.M. Scherer, and P.G. Tratnyek, 1996. Kinetics of halogenated organic compound degradation by iron metal. *Environ. Sci. Technol*. **30**, 2634-2640.

Kaplan, D.I., Cantrell, K.J., Wietsma, T.W., and Potter, M.A., 1996. Retention of zero-valent iron colloids by sand columns: Application to chemical barrier formation. *J. Environ. Qual.* **25**, 1086-1094.

Kinniburgh, D.G., and M.L. Jackson, "Cation adsorption by hydrous metal oxides and clays," In Adsorption of Inorganics at Solid-Water Interfaces, (ed., M.A. Anderson and A.J. Rubin), Ann Arbor Science, Ann Arbor MI, 91-160, 1981.

Kinniburgh, D.G., and M.L. Jackson, "Adsorption of alkaline earth, transition, and heavy metal cations by hydrous oxide gels of iron and aluminum," *Soil Sci. Soc. Am. J.* 40, 796-799, 1981.

Lennie, A.R., S.A.T. Redfern, P.E. Champness, C.P. Stoddart, P.F. Schofield, and D.J. Vaughan, "Transformation of mackinawite to greigite: An in situ X-ray powder diffraction and transmission electron microscopy study," *American Mineralogist*, 82, 302-309, 1995.

Ma, Q.Y., S.J. Traina, and T.J. Logan, "In situ Pb immobilization by apatite," *Environ. Sci. Technol*. 27, 1803-1810, 1993.

Ma, Q.Y., T.J. Logan, and S.J. Traina, "Effects of NO_3^-, Cl^-, F^-, SO_4^{2-}, and CO_3^{2-} on Pb^{2+} immobilization by hydroxyapatite," *Environ. Sci. Technol*. 28, 408-419, 1994a.

Ma, Q.Y., S.J. Traina, and T.J. Logan, “Effects of Al, Cd, Cu Fe(II), Ni, and Zn on Pb immobilization by hydroxyapatite,” *Environ. Sci. Technol*. 27, 12190-1228-1810, 1994b.

Ma, Q.Y., T.J. Logan, and S.J. Traina, “Lead immobilization from aqueous solutions and contaminated soils using phosphate rock,” *Environ. Sci. Technol*. 29, 1118-1126, 1995.

Matheson, L.J., and P.G. Tratnyek, "Reductive dechlorination of chlorinated methanes by iron metal," *Environ. Sci. Technol*., 28, 2045-2053, 1994.

Matsuo, M., M. Kawakami,, and K. Sugimori, “Mossbauer spectroscopic study on the chemical changes of iron compounds with the aid of sulfate reducing bacteria,” *Hyperfine Interactions*, 126, 53-58, 2000.

Mayer, K.U., D.W. Blowes, and E.O. Frind, “Reactive transport modeling of an in situ reactive barrier for the treatment of hexavalent chromium and trichloroethylene in groundwater,” *Water Resources Research*, 37, 3091-3103, 2001.

McKenzie, R.M., "The adsorption of lead and other heavy metals on oxides of manganese and iron," *Aust. J. Soil Res.,* 18, 61-73, 1980.

Mercier, L., and T.J. Pinnavaia, "Access in mesoporous materials: Advantages of a uniform pore structure in the design of heavy metal ion adsorbents for environmental remediation," Adv. Mater., 9, 500-503, 1997.

Mercier, L., and T.J. Pinnavaia, "Heavy metal ion adsorbents formed by the grafting of a thiol functionality to mesoporous silica molecular sieves: factors affecting Hg(II) uptake," *Environ. Sci. Technol.,* 32, 1998.

Moyes L.N., Jones M.J., Reed W.A., Livens F.R., Charnock J.M., Mosselmans J.F.W., Hennig C., Vaughan D.J., Pattrick R.A.D., “An X-ray absorption spectroscopy study of neptunium(V) reactions with mackinawite (FeS),” Environ. Sci. Technol. 36, 179-183, 2002.

National Research Council, "Innovations in Groundwater and Soil Cleanup: from concept to commercialization," pp292, National Academy Press, Washington, D.C., 1997.

Neal, A.L., S. Techkarnjanaruk, A. Dohnalkova, D. McCready, B.M. Peyton, and G.G. Geesy, “Iron sulfides and sulfur species produced at hematite surfaces in the presence of sulfate-reducing bacteria,” *Geochimica et Cosmochimica Acta,* 65, 223-235, 2001.

Newman, S.D., and W. Jones, "Synthesis, characterization, and applications of layered double hydroxides containing organic guests," New J. Chem., 22, 105-115, 1998.

Parkhurst, D.L. and C.A.J. Appelo, “User’s guide to PREEEQC (Version 2): A computer program for speciation, batch reactions, one-dimensional transport, and inverse geochemical calculations,” *U.S Geol. Surv., Wat Resour. Invest*. Rep., WRI-99-4259, 312 pp, 1999.

Parkman, R.H., J.M. Charnock, N.D. Bryan, F.R. Livens, and D.J. Vaughan, "Reactions of copper and cadmium ions in aqueous solution with goethite, lepidocrocite, mackinawite, and pyrite," American Mineralogist, 84, 407-419, 1999.

Patterson, R. R., Fendorf, S. and Fendorf, M., "Reduction of Hexavalent Chromium by Amorphous Iron Sulfide", *Environ. Sci. Technol.,* 31, 2039-2044, 1997.

Powell R.M., R.W. Puls, S.K Hightower D.A. Sabatini, “Coupled iron corroision and chromate reduction-Mechanisms for subsurface remediation,” Environ. Sci. Technol., 29 (8): 1913-1922, 1995.

Puls, R.W., and R.M. Powell, and C.J. Paul, "In situ remediation of ground water contaminated with chromate and chlorinated solvents using zero-valent iron, A field study," Preprints of 209th American Chemical Society National Meeting, Anaheim, Division of Environmental Chemistry, ACS, Washington D.C., CA, April 2-7, 1995.

Roberts, A.L., L.A. Totten, W.A. Arnold, D.R. Burris, and T.J. Campbell, "Reductive elimination of chlorinated ethylenes by zero-valent metals," *Environ. Sci. Technol*., 30, 2654-2659, 1996.

Rochette, E.A., B.C. Bostick, G. Li, and S. Fendorf, "Kinetics of Arsenate Reduction by Dissolved Sulfide," *Environ. Sci. Technol*., 34, 4714-4720, 2000.

Su, C. and L. R.W. Puls, "Arsenate and Arsenite Removal by Zerovalent Iron: Kinetics, Redox, Transformations, and Implications for in Situ Groundwater Remediation," *Environ. Sci. Technol*., 35, 1487-1492, 2001.

Vaughan, D.J., and A.R. Lennie, "The iron sulfide minerals-Their chemistry and role in nature," *Science Progress*, 75 (298): 371-388, Part 3-4, 1991.

Watson, J.H.P., B.A. Cressey, A.P. Roberts, D.C. Ellwood, J.M Charnock, and A.K. Soper, "Structural and magnetic studies on heavy-metal-adsorbing iron sulfide nanoparticles produced by sulfate-reducing bacteria," *J. Magnetism and Magnetic Materials*, 214, 13-30, 2000.

Wildeman, T.R., D.M. Updegraff, J.S. Reynolds, and J.L. Bolis, "Passive bioremediation of metals from using reactors and constructed wetlands," in *Emerging Technology for Bioremediation of Metals*, J.L Means and R.E. Hinchee, eds., Ann Arbor Lewis Publishers, pp13-25, 1994.

Willard, A.M. and T.M. Seward, "The adsorption of gold(I) hydrosulfide complexes by iron sulfide surfaces, Geochim. Cosmo. Acta, 66, 383-402, 2002.

Yabusaki, S., K. Cantrell, B. Sass, amd C. Steefel, "Multicomponent reactive transport in an in situ zero-valent iron cell," *Environ. Sci. Technol*., 35, 1493-1503, 2001.

Task 1. CHARACTERIZATION OF FeS REACTIVITY AND REACTION MECHANISMS FOR Cd AND As REMOVAL (Hayes)

In this task a series of experiments were performed to develop and test iron sulfide materials for the removal of arsenic (As) and cadmium (Cd) from groundwater under anoxic conditions. Based on the Statement of Need (SON) to which this proposal responded, both As and Cd were listed as contaminants of interest. In addition, the SON requested research related to the impact of metal speciation on removal and/or sequestration techniques. Therefore this task also addressed the mechanism of As and Cd uptake by the FeS-based materials over a range of geochemical solution conditions including pH, FeS(s), and As and Cd concentrations. The reporting for Task 1 is divided into subtask sections on: (i) preparation of FeS, (ii) sorption capacity of FeS, (iii) mechanism of uptake of Cd and As by FeS, (iv) impact of solution conditions on Cd and As uptake by FeS, (vi) reactive transport of Cd and As in columns of packed with reactive FeS. All these studies aforementioned studies were performed under anoxic conditions. To address the potential of remobilization of sequestered metals by intrusion of oxygen, an additional subtask reports on: (v) impact of oxygen on the stability of As removal by FeS. This later subtask addressed a key SON on the long term stability of remedial method.

Subtask 1.1. Preparation of Reactive FeS

Objective

The overarching goal of this subtask was to develop methods for synthesizing reactive nanoscale FeS and FeS-coated sand with reasonably reproducible particle properties for eventual use in PRB applications.

Background

Previous mackinawite synthesis methods have resulted in a broad range of values in surface area (e.g., Jeong et al., 2008), particle size (Jeong et al., 2008), and solubility (Wolthers et al. 2005, Richard, 2006). Such variable of properties has been attributed to synthesis reaction conditions. For example, three synthesis methods have typically been used to produce mackinawite: (1) reaction of a sulfide solution with metallic iron (Berner, 1964), (2) reaction of sulfide solution with ferrous iron solutions (Rickard, 1969), and (3) using sulfate-reducing bacteria (Watson et al., 2000). The first approach leads to more crystalline form of mackinawite (Lennie and Vaughan, 1996; Mullet et al., 2002). In contrast, the other two methods lead to less crystalline FeS phases that are more similar to those found in natural environments (Berner, 1967b; Spadini et al., 2003; Wolthers et al., 2003). Given our desire to form less crystalline and more reactive mackinawite (hereafter referred to as FeS), and our previous experience with this method, a version of the second approach, in which a sulfide solution is reacted with a ferrous iron solution, was utilized in this work to produce nanoscale FeS. However, even with this method, the initial amorphous FeS or disordered mackinawite that forms (Rickard et al., 1995; Wolthers et al., 2003) has been found to form a more crystalline phase within days (Rickard, 1995; Wilkin and Barnes, 1996), although the complete transformation to well-crystalline mackinawite may require up to two years at room temperature (Rickard, 1995). Given this, aging time was identified as a potentially important parameter to consider in the synthesis of FeS.

In addition, it was desired to develop an FeS material for emplacement in a trench-and-fill constructed PRB (e.g., see Task 4). For this purpose, a method of coating mackinawite on sands (hereafter referred to as FeS-coated sand) was desired. Although nanosized mackinawite is highly reactive, it may not be suitable for trench and fill PRB applications due to its potential to create low permeability zones and short circuiting within a PRB. To eliminate the possibility of permeability reduction by nanoscale particles, past efforts have been devoted to coating sand with reactive iron materials such as $FeOOH/Fe(OH)_3$ (Appelo and Postma, 2005, Herbel and Fendorf, 2006, Thirunavukkarasu et al., 2003), MnO_2 (Guha et al., 2001), red mud (Genc-Fuhraman and Gencfuhrman, 2005) and humic acid, ferrihydrite and aluminosilicate (Jerez and Flury, 2006). For obtaining optimal mineral coatings, conditions have been varied such as temperature, aging time, pH and particle size (Coston et al., 1995, Kuan et al., 1998, Lo et al., 1997, Scheidegger et al., 1993, Xu and Axe, 2005). However, FeS is highly sensitive to oxygen and temperature change. Therefore, in this study, a coating procedure of mackinawite on a natural silica sand at room temperature and under anoxic conditions was undertaken.

Materials and Methods

Preparation of Nanoscale FeS. FeS was synthesized inside an anaerobic chamber maintained in a 5% H_2/95% N_2 atmosphere in which 2.0 L of a 0.57 M $FeCl_2$ solution was mixed with 1.2 L of 1.1 M Na_2S solution (Butler and Hayes, 1998). The mixture was mechanically stirred for 3 days with a magnetic stirrer and then centrifuged at 10,000 rpm for 15 minutes to separate the solid from liquid. After decanting the supernatant liquid, the solid was rinsed with Milli-Q water multiple times until the electrical conductivity of rinsing solution was below 1 mS/cm (typically within 5 rinses). After freeze-drying, the FeS solids were sealed in glass vials capped with Teflon-coated butyl rubber septa and stored inside the anaerobic chamber until used. The detailed physical properties of mackinawite prepared in this fashion including specific surface area and particle size have been recently reported by Jeong et al. (2008).

Preparation of FeS-coated Sand. All the coating procedures were performed in anoxic glovebox. The quartz sand for FeS coating was Wedron 510 silica sand (Wedron Silica Co., Wedron, IL) which was sieved to obtain a geometric mean size of 0.15-0.22 mm (Seive #70/#100), washed with Milli-Q water, and then dried at ambient temperature. This sand has 2.2×10^{-6} mol Fe/g sand (standard error: 3.0×10^{-7} mol Fe/g sand) of naturally existing which enhanced the FeS coating on sand surface compared to acid cleaned sand (Han et al. 2009). The 2 g/L FeS suspension pH was adjusted to 5.5 with 0.8 N HCl for the FeS sand coating. Then, 32.5 mL of the 2 g/L FeS solution was mixed with 32.5 mL of natural Wedron sand (1:1 mixture of sand and FeS suspension) in a 50 mL batch and the mixture was then completely mixed with an end-over-end rotator (Thermo Scientific Labquake ®) for 3 days. After the 3 days of aging, the supernatant was discarded and the remaining paste dried without rinsing. Drying was done inside a glove box to insure no oxygen contact. The completely dried FeS-coated sand then was stored in an air-tight container in the glovebox until needed. The amount of FeS coated on the sand using this procedure was found to be 1.4×10^{-5} mol FeS/g sand using an acid extraction procedure. The full details of the sand preparation, optimization of the coating procedure, spectroscopic characterization of the coating, and acid extraction method for measuring the amount of FeS coating are described elsewhere (Han et al., 2009).

Characterization of FeS. Nanoscale FeS was characterized for mineralogy, surface area, and particle size distribution using X-ray diffraction (XRD), transmission electron microscopy

analysis (TEM), Ethylene Glycol Monoethyl Ether (EGME) method, and Photon Correlation Spectroscopy (PCS), respectively (Jeong et al., 2008). XRD spectra of mackinawite powder were obtained from a Rigaku 12 kW rotating anode generator at 40 kV and 100 mV with Cu-K_α radiation, and analyzed using JADE7. Prior to the XRD data collection, the synthetic mackinawite was divided into magnetic and non-magnetic portions by a hand magnet inside the anaerobic chamber. For TEM analysis, ethanolic mackinawite suspension was applied to an ultrathin carbon film on a copper grid. Subsequently, the sample was dried under vacuum prior to the analysis. TEM images were collected with a JEOL 2010F analytical electron microscope operating at 200 kV. The EGME method (Carter et al., 1965) used to measure the surface area of synthetic mackinawite involved wetting the mackinawite powder with EGME (a polar liquid), equilibrating, and removing the excess liquid by evacuation. For PCS measurement, aqueous suspensions of synthetic mackinawite were analyzed using a Sub-Micron Particle Analyzer N4 MD (Coulter Electron, Inc., Hialeah, FL) at $\lambda = 632.8$ nm and $\theta = 90^o$ as described by Quirantes et al. (1996).

Characterization of FeS-Coated Sand. FeS-coated was characterized for surface morphology and chemical composition using SEM and XPS, respectively (Han et al., 2009). These methods have been commonly applied to characterize iron oxide coatings on sands and other oxide mineral phases (Jerez and Flury, 2006, Scheidegger et al., 1993, Xu and Axe, 2005). Given the sensitivity of FeS to transformations by oxidation or heat and the thin layer of coated-FeS on the sand, characterization was limited to surface sensitive methods in which exposure to heat or oxygen was minimized. Because the highest amount of FeS coating obtained was just 0.4% of the mass of silica sand, and that aggregated nanoscale FeS particles on the silica surface give only weak diffraction peaks, XRD was ineffective for confirming the presence of mackinawite on the sand surface. Also the widely used BET (Brunauer, Emmett, and Teller) surface area measuring method, in which samples are heated up to 300 °C, could not be applied with confidence given that FeS is easily transformed to greigite or pyrite in short time at a high temperature(Hunger and Benning, 2007). . For both the SEM and XPS tests, samples were prepared in the anaerobic glove box and transferred to the instruments using air-tight containers to minimize contact of the sample surface to oxygen. For collecting SEM images, a Philips XL30FEG instrument was used. For XPS, the chemical composition and oxidation state of Fe, S, O, Si and C on the surface of the FeS-coated sand were examined using a Kratos Axis Ultra X-ray photoelectron spectrometer a the Al-K_α line (1486.6 eV) as radiation source.

Results and Discussion

Nanoscale FeS

Nanoscale FeS Mineralogy. By XRD analysis combined with a magnet separation, mackinawite was found to be the major phase, with greigite accounting for at most a few percent by mass. Of the total mass produced, the magnetic portion accounted for 6%, with the remainder being non-magnetic. Fig. 1.1 shows the diffractograms of the magnetic portion (a) and the non-magnetic portion (b). In both diffractograms, the diffraction peaks are broad and weak, indicating a poor degree of crystallization or a small crystallite size. For the non-magnetic portion, the diffraction patterns are similar to those previously reported for synthetic mackinawite (Rickard, 1969; Wolthers et al., 2003). For the magnetic portion, the diffraction patterns correspond to those of

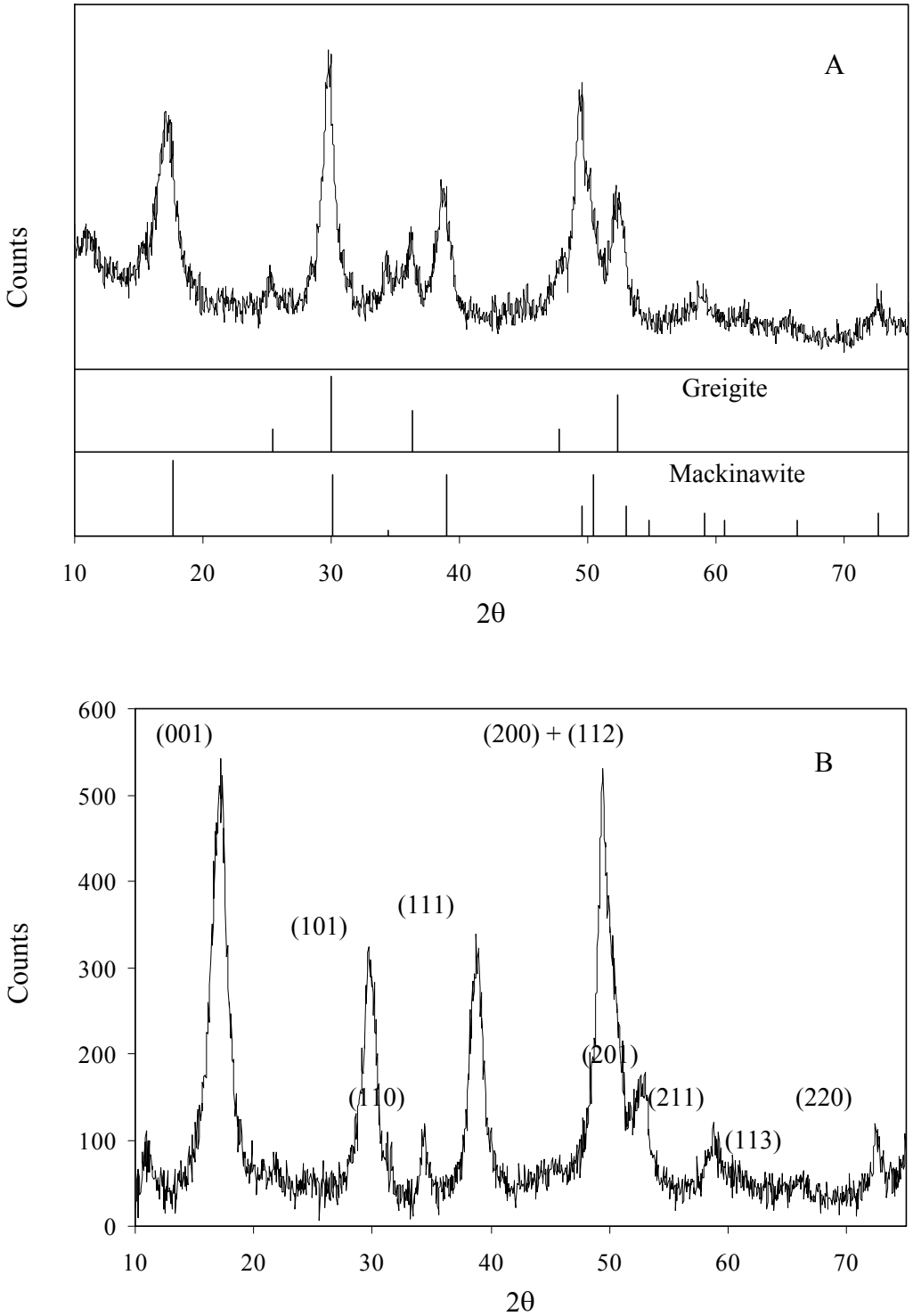

Figure 1.1. X-ray diffraction patterns for the magnetic portion (A) and the non-magnetic portion (B) of synthetic mackinawite. In part (A), the diffraction data for reference minerals are obtained from JADE7 (Materials Data Inc.). In part (B), the diffraction peaks are indexed for mackinawite (Jeong et al, 2008).

Table 1.1 Unit cell parameters for synthetic mackinawite (Jeong et al., 2008).

	$a = b$ (Å)	c (Å)
Synthetic Mk[a]	3.67	5.20
Synthetic MkA[b]	4.02	6.60
Synthetic MkB[b]	3.65	5.48
Crystalline Mk[c]	3.6735(4)	5.0328(7)

(a) Synthetic mackinawite aged for 3 days (Jeong et al., 2008).
(b) Synthetic mackinawite aged for < 0.5 h (Wolthers et al., 2003).
(c) Well-crystalline mackinawite (Lennie at al., 1995).

mackinawite and greigite. While greigite (cubic Fe_3S_4) exhibits a strong ferrimagnetism (Vaughan and Ridout, 1971), mackinawite is paramagnetic (Vaughan and Craig, 1978). Therefore, the detection of mackinawite in the magnetic portion (Fig. 1.1 A) suggests its close structural relationship with greigite. The lattice spacings were derived from the diffractogram of the non-magnetic portion (Fig. 1.1 B) and summarized in Table 1.1. The mackinawite phase prepared here exhibits significantly elongated lattice spacings compared with well-crystalline mackinawite (Lennie at al., 1995). The lattice expansion relative to well-crystalline mackinawite has been observed and attributed to both intercalation of water molecules between the layers of and lattice relaxation with decreasing crystallite size (Wolthers et al., 2003). Compared with the mackinawite prepared by Wolthers et al. (2003), the lattice spacings of synthetic mackinawite in this study are shorter. The 3-day aging in this study resulted in a higher degree of crystallization than the shorter aging in their study (< 0.5 h). The prior study also showed that the lattice spacings of mackinawite decreased with aging time.

TEM Images of Nanoscale FeS Particles. From a TEM image taken at 50,000x magnification, it appears that aggregates of the four-day mackinawite consist of needle-like nanoparticles as shown in Figure 1.2. TEM images taken at higher magnification show that the mackinawite nanoparticles are comprised of a disordered aggregation of platelets (shown on end allowing less light to pass through the sample). This is consistent with the "flake-like" description of high resolution TEM observations of 30-minute aged disordered mackinawite (Ohfuji and Rickard, 2006). Furthermore, this image taken at 80,000 times magnification in Figure 1.2 B also alludes to the horizontal stacking of the platy nanoparticles. Mackinawite crystal dimensions can be gleaned from higher magnification of these samples. Each set of lattice fringes represents a single crystal of mackinawite (Ohfuji and Ricard, 2006). The length of the crystal can be determined from the lateral extent of the fringes which averaged about 7.5 nm by 21.7 nm (Jeong et al. 2008).

Nanoscale FeS Particle Surface Area and Particle Size. Table 1.2 lists the particle size and external specific surface area (SSA_{ext}) of synthetic mackinawite by different methods. As shown in Table 1.2, a significant variation was observed for SSA_{ext} of synthetic mackinawite. The SSA_{ext} estimated by TEM analysis is the smallest, followed by the values obtained from XRD

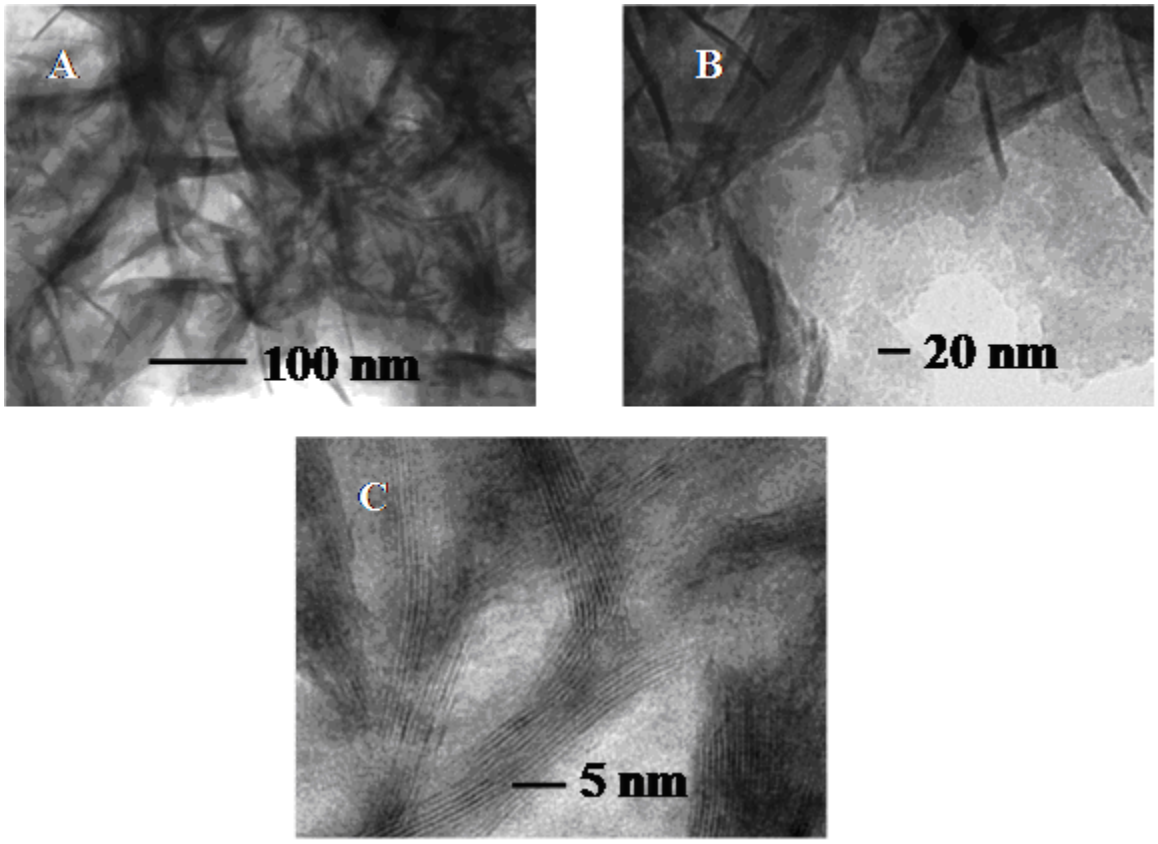

Figure 1.2. TEM images of the four-day mackinawite (A) 50,000 magnification, (B) 80,000 magnification (C) 500,000 x magnification.

Table 1.2. Particle size and SSA_{ext} values of synthetic mackinawite by different methods (Jeong et al., 2008).

Method	Particle dimensions[a]	SSA_{ext} (m^2/g)
XRD, FWHM (K = 0.9)	7.0 nm × 5.2 nm	219
XRD, IB (K = 1.05)	8.0 nm × 4.3 nm	220
XRD, FWHM (K = 0.5)	3.9 nm × 2.9 nm	392
TEM	21.7 nm × 7.5 nm	103
EGME		276[b], 294[c], 345[d]
PCS	3.5 nm	424 ± 130

(a) For single numbers, diameter is given; for paired numbers, length is followed by thickness.
(b) N_c is estimated by FWHM at K = 0.9.
(c) N_c is estimated by IB at K = 1.05.
(d) N_c is estimated by FWHM at K = 0.5.

analysis using both FWHM and IB approaches, EGME method, and PCS measurement. The observed variation in SSA_{ext} is caused by the limitations of each method, including underlying theoretical assumptions and experimental artifacts arising from sample handling and preparation. When a significant fraction of polycrystalline particles are present, the use of Scherrer equation will not yield accurate estimates of particle size and SSA_{ext} (Guinier, 1994). Another potential limitation of Scherrer equation comes from diffraction peak broadening by microstrain (Klug and Alexander, 1974). When non-uniform crystal defects are significant, the crystallite size will be underestimated by neglecting the microstrain component in Scherrer equation (van Berkum et al., 1994). Nonetheless, the microstrain broadening was not expected to be significant for the mackinawite prepared here. For example, the Rietveld refinement study of synthetic mackinawite (Lennie et al., 1995) showed that crystal defects such as sulfur vacancies and iron surplus were below the detection limit. Also, crystal defects such as edge dislocations and curvatures were shown to be limited along the grain boundaries of mackinawite. The choice of the Scherrer constant (K) is critical in the application of Scherrer equation. When crystallites vary significantly in size, a smaller K value than the one typically applied to a uniform size distribution should be used (Langford and Wilson, 1978). Due to a great variation in crystallite size, the use of K values close to unity (e.g., 0.9 by FWHM and 1.05 by IB) would significantly overestimate the crystallite size and thus underestimate the surface area. Notably, the SSA_{ext} by XRD analysis is much smaller than the values estimated by EGEM method and PCS measurement. The use of K = 0.5 in FWHM approach results in SSA_{ext} = 392 m^2/g, which is closer to those by these two methods.

TEM analysis. As shown in Table 1.2, TEM analysis yielded the smallest SSA_{ext} among the methods used. The lack of distinct particle boundaries due to significant particle overlapping may cause overestimation of the particle size and underestimation of SSA_{ext} by TEM analysis. The observed particle aggregation resulted from drying of mackinawite suspensions on the TEM grid under vacuum (Walther, 2003). Identification of fine particles with less than ~2 nm in size is likely to be hindered by insufficient diffraction intensity. When overlapping with larger particles, the fine particles are difficult to identify due to the poor contrast, implying that very fine particles are not resolved by TEM.

EGME Method. The surface area of the nanocrystalline mackinawite estimated by EGME method is much larger compared to those of amorphous materials such as hydrous ferric oxide (159–720 m^2/g; Dzombak and Morel, 1990) and amorphous silica (100–200 m^2/g; Dixit and van Cappellen, 2002), and even comparable to those of activated carbons with microporous structures (881–1,093 m^2/g; Nakai et al., 1993). This suggests that the area associated with both the external surfaces and interlayers can be measured by EGME method. Similar to its ability to wet the interlayers of swelling clays, the polar liquid, EGME may penetrate the interlayers of the nanocrystalline mackinawite. As noted by XRD analysis, however, its penetration between the interlayers apparently breaks apart the mackinawite structure rather than causing the lattice expansion along the *c*-axis. Although complete wetting of the interlayers was assumed to estimate the SSA_{ext} of synthetic mackinawite, a small fraction of the interlayers might not be completely wet by EGME. Under this circumstance, the assumption of complete wetting would underestimate the SSA_{ext} of the nanocrystalline mackinawite. This may explain the lower SSA_{ext} by EGME method compared with the PCS-based estimate (Table 1.2). Also, EGME method requires information on the number of unit cells along *c*-axis (N_c), which is independently assessed from XRD analysis. As shown in Table 1.2, the SSA_{ext} determined using N_c by FWHM

at K = 0.5 is larger than the other estimates based on different N_c values. This indicates that the uncertainty of N_c makes it difficult to accurately determine the SSA_{ext} of the nanocrystalline mackinawite using this approach. Nonetheless, EGME method is relatively simple and easy, and does not require expensive instrumentation. Most importantly, this method is not sensitive to particle aggregation state, which may lead to artifacts in the surface area estimates using TEM analysis or PCS measurement.

PCS measurement. The highest SSA_{ext} was obtained from PCS measurement. This may be explained by the tendency of other methods to underestimate the surface area due to non-uniform crystallites in XRD analysis, particle aggregation and low resolution of fine particles in TEM analysis, and incomplete wetability of EGME by the interlayers in EGME method. It should also be noted that PCS analysis is based on the assumption of spherical geometry. However, as indicated by both XRD and TEM analyses (Table 1.2), the mackinawite particles are longer along the *a*- and *b*-axes than the *c*-axis. In such a case, the simultaneous presence of both translational diffusion and rotational diffusion complicates the particle size determination by PCS (Quirantes et al., 1996). Nonetheless, PCS provides an easy in-situ method for particle size determination. Also, the particle size and SSA_{ext} of poorly crystalline or amorphous phases can be measured by PCS.

FeS-Coated Sand

SEM Images of FeS-Coated Sand. SEM images of FeS-coated sand illustrate patchwise coating and aggregated nanoparticles of FeS covering the sand surface (Figure 1.3). The indentations on the silica surface appear to be effective locations for the build-up of FeS aggregates. An increasingly thicker layer of FeS coating is visible as the coating amount increases from 1.2 to 4.0 mg FeS/g of coated sand (Figure 1.3, B - D)). This result demonstrates that self-aggregation between FeS particles is the primary mechanism leading to enhanced amounts of coating as the total amount of FeS in contact with the sand is increased.

XPS Analysis of FeS-Coated Sand. To characterize the surface of the coated sands, XPS spectra were obtained for FeS, FeS-coated sand, Wedron sand and acid-washed Wedron sand. The XPS survey scan of the FeS and FeS-coated sand (4 mg FeS/g sand) indicated the presence of O, C, Na, S, and Fe and the presence of O, C, S, Na, Fe and Si, respectively. The natural Wedron sand without acid washing showed the presence of O, C, Na, Al, Ca, Fe and Si, while the acid-washed Wedron sand survey scan consisted of only O, C and Si. The binding energies, FWHMs, and percentage of fitted species are listed in Table 1.3. The Fe(III)-O species is the sole contributor in Wedron sand sample but represents only 6.3±2.5% of the spectrum in the FeS. Relative to the FeS only sample, upon coating Wedron sand with FeS, the Fe(III)-O surface species contribution increases to 10.1±6.1%. At the same time, the Fe(II)-S species contributions in the FeS spectrum (36.0±1.3%) decrease (26.±3.3%) in the FeS-coated spectrum. These results suggest that upon coating a partial oxidation of the Fe(II) of FeS via a redox surface reaction occurs. The presence of significant contributions of Fe(III)-S in both the FeS (36.1±4.8%) and FeS-coated sand (37.9±7.3%) sand suggest that partial surface oxidation of FeS has resulted during the preparation of the samples. In the coating procedure, the FeS suspension was acidified to pH 5 with HCl. Acid addition may cause the oxidation of mackinawite to greigite (Fe_3S_4, e.g., $Fe^{II}Fe^{III}{}_2S_4$). The transformation of mackinawite to greigite was previously observed at pH 5

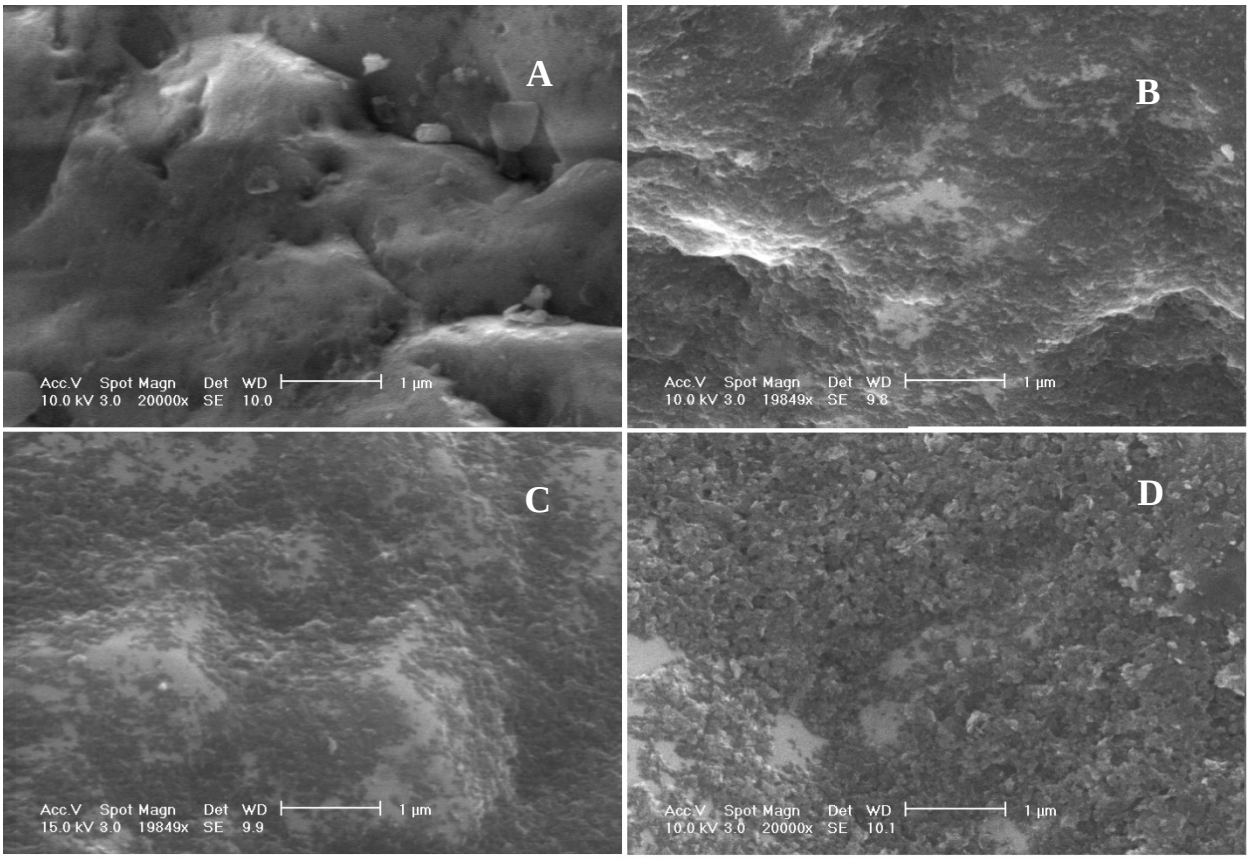

Figure 1.3. SEM images of (A) natural Wedron silica sand and (B) FeS-coated sand with 1.2 mg FeS/g-coated sand, (C) 2.4 mg FeS/g-coated sand and (D) 4 mg FeS/g-coated sand. FeS deposits as patches on the sand with some areas of the surface appearing uncoated and exposed.

based on XRD evidence (Gallegos et al., 2007). The formation of greigite can be explained as resulting from the following oxidation reaction with the proton:

$$4FeS + 2H^+ = H_2(g) + Fe_3S_4 + Fe^{2+} \quad (1.1)$$

It is also possible that oxidation of FeS by water could result in the formation of mixed iron oxides such as magnetite via anaerobic corrosion as follows:

$$3FeS + 4H_2O = Fe_3O_4 + H_2(g) + 3H_2S \quad (1.2)$$

However, given that the reaction of FeS suspensions with natural sand led to an increase in pH but not when FeS was reacted with acid washed sand (see discussion above), and that the contribution of the Fe(III)-S species remained unchanged during this reaction, suggests a redox reaction such as the following may have occurred:

$$FeS + 2FeOOH = Fe_3O_4 + H_2S \quad (1.3)$$

Table 1.3. Binding energies (BE), peak full width at half maximums (FWHM) and peak areas for Fe $2p_{3/2}$, and O 1*s* X-ray photoelectron spectra of FeS (mackinawite), FeS-coated sand, Wedron sand and acid-washed Wedron sand.

Chemical species	BE(eV)	FWHM (eV)	% area			
			FeS	FeS-coated sand	Wedron sand	Acid-washed Wedron sand
Fe $2p_{3/2}$						
Fe(II) -S	706.8	1.3	36.0±1.3	26.4±3.3	-	-
Fe(II)-O	707.9	1.5	21.5±6.3	25.7±6.5	-	-
Fe(III)-S	709.0 (709.4*)	1.5	36.1±4.8	37.9±7.3*	-	-
	710.1 (710.5*)	1.5				
	711.1 (711.5*)	1.5				
	712.1 (712.5*)	1.5				
Fe(III)-O	711.5	1.5	6.3±2.5	10.1±6.1	100	-
	712.6	1.5				
	713.6	1.5				
	714.6	1.5				
O 1*s*						
O^{2-}	529.5	1.5	9.9±1.3	10.6±2.1	1.9±0.1	-
OH^- or $>SiOH^0$	531.3	1.5	68.1±2.6	20.5±5.3	15.7±4.2	-
Adsorbed H_2O or $>SiO^-$	532.2	1.5	21.9±3.7	68.9±3.9	82.5±4.6	100

- * reperesents the binding energies applied to FeS-coated sand

At pH values less than 7, loss of the H_2S gas to the head space would lead to an increase in pH while producing magnetite. This would also explain the appearance of an increase of Fe(III)-O in FeS-coated sand relative to FeS upon FeS reaction with the natural sand and the decrease in the Fe(III)-O of the natural sand compared to the coated sand.

The identification of the iron mineralogy of the FeS-coated sand was not possible with XRD as mentioned previously. However, for further support of the above interpretation, thermodynamic calculations simulating the coating experiments were performed with the PHREEQC equilibrium modeling program (Parkhurst and Appelo, 1999). The results of the modeling (see Task 5) indicate that a majority of the FeS remains as mackinawite when reacted with iron oxides, but that some greigite may form as a result of FeS oxidation below pH 6 while a small portion of mackinawite is predicted to be transformed to greigite and magnetite above pH 6. This is consistent with the interpretation of the Fe 2p XPS data that the FeS-coated sand consists of at least two different surface iron phases, with the predominant form as mackinawite and a smaller amount of iron oxidation products such as greigite and magnetite.

Summary and Conclusions and Implications for Future Research/Implementation

Nanoscale FeS. This study showed the importance of aging and measurement methods for assessing nanoscale FeS mineralogical and surface area characteristics. It was shown that

mackinawite can be slowly transformed and subsequently associated with small fractions of griegite after only several days of aging in solution. Estimated particle size and external specific surface area (SSA_{ext}) of nanoscale FeS were shown to vary significantly with the measurement methods used. The use of Scherrer equation for measuring crystallite size based on XRD patterns is limited by uncertainty of the Scherrer constant (K) due to the presence of polydisperse particles. The presence of polycrystalline particles may also lead to inaccurate particle size estimation by Scherrer equation, given that crystallite and particle sizes are not equivalent. The TEM observation yielded the smallest SSA_{ext} of $103 m^2/g$. This measurement was not representative of dispersed particles due to particle aggregation from drying during sample preparation. In contrast, EGME method and PCS measurement yielded higher SSA_{ext} (276–345 m^2/g by EGME and 424±130 m^2/g by PCS). These data are in reasonable agreement with those previously measured by the methods insensitive to particle aggregation. These data indicate that the reactivity of nanoscale FeS particles may change with time and that monitoring these changes will be important for assessing the longevity of FeS particles in PRB applications, even when anoxic conditions are maintained.

FeS-Coated Sand. A procedure for coating FeS on a natural sand was developed and has been described. The following conclusions can be drawn from this study. Optimal coatings of FeS of sand results from using a coating pH of 5.5 and no rinsing following solid-liquid separation after a 3 day contact period between the FeS and the sand. Surface characterization by SEM and XPS show the FeS-coated sand has a patchwise coating that is predominantly comprised of FeS self-aggregrates along with a small fraction of oxidized magnetite or greigite phases and portions of uncoated sand exposed. In the context of PRB applications, the results are consistent with those for the nanoscale synthesized particles in that, even under anoxic conditions, the FeS coated on sand may age to produce either griegite or magnetite, depending on the pH conditions. Future work is needed to address the impact of these changes in the reactivity of FeS-coated sand from prolonged contact with water over time frames representative of the lifetime of a PRB. The data from this study indicate that aging processes are insignificant over the course of days to weeks, but it remains to be determined if longer aging of months to years will cause significant decrease in reactivity of FeS based PRB materials.

Literature Cited

Appelo, C.A.J. and Postma, D., 2005. Geochemistry, groundwater and pollution, A.A. Balkema Publishers

Berner, R. A. ,1967. Diagenesis of iron sulfide in recent marine sediments. In *Estuaries* (ed. G. H. Lauf). American Association for the Advancement of Science, Washington. pp. 268-272.

Berner, R. A., 1964. Iron sulfides formed from aqueous solution at low temperatures and atmospheric pressures. *J. Geol*. **72**, 293-306.

Butler, E. C. Hayes, K. F., 1998. Effects of solution composition and pH on the reductive dechlorination of hexachloroethane by iron sulfide. *Environ. Sci. Technol.* **32**, 1276-1284.

Carter D. L., Heilman M. D., and Gonzalez C. L., 1965. Ethylene glycol monoethyl ether for determining surface area of silicate minerals. *Soil Sci*. **100**, 356-360.

Coston, J. A., Fuller, C. C., Davis, J. A., 1995. Pb^{2+} and Zn^{2+} Adsorption by a Natural Aluminum-Bearing and Iron-Bearing Surface Coating on an Aquifer Sand. *Geochim. Cosmochim. Acta* **59**, 3535-3547.

Dixit S., van Cappellen, P., 2002. Surface chemistry and reactivity of biogenic silica. *Geochim. Cosmochim. Acta* **66**, 2559-2568.

Dzombak D. A., Morel F. M. M., 1990. *Surface Complexation Modeling, Hydrous Ferric Oxide*. John Wiley and Sons.

Gallegos, T. J., Hyun, S. P., Hayes, K. F., 2007. Spectroscopic investigation of the uptake of arsenite from solution by synthetic mackinawite. *Environ. Sci. Technol.* **41**, 7781-7786.

Genc-Fuhrman, H. and Gencfuhrman, 2005. Arsenate removal from water using sand-red mud columns. *Water Research* **39**(13), 2944-2954.

Guha, H., Saiers, J. E., Brooks, S., Jardine, P., Jayachandran, K., 2001. Chromium transport, oxidation, and adsorption in manganese-coated sand. *J. Cont. Hydro.***49**, 311-334.

Guinier A., 1994. *X-ray Diffraction in Crystals, Imperfect Crystals, and Amorphous Bodies*. Dover Publications, Inc.

Han, Y.-S., Gallegos, T.J., Demond, A.H., Hayes, K.F., 2009. FeS-Coated Sand for Removal of Arsenic(III) under Anaerobic Conditions: Coating Method and Characterization. *Water Research*, submitted.

Herbel, M. and Fendorf, S., 2006. Biogeochemical processes controlling the speciation and transport of arsenic within iron coated sands. *Chemical Geology* **228**(1-3), 16-32.

Hunger, S. and Benning, L.G., 2007. Greigite: a true intermediate on the polysulfide pathway to pyrite. *Geochemical Transactions* **8**.

Jeong, H. Y., Lee, J. L. Hayes, K. F., 2008. Characterization of synthetic nanocrystalline mackinawite: Crystal structure, particle size, and specific surface area. *Geochim. Cosmochim. Acta* **72**, 493-505.

Jerez, J. and Flury, M., 2006. Humic acid-, ferrihydrite-, and aluminosilicate-coated sands for column transport experiments. *Colloids and Surfaces a-Physicochemical and Engineering Aspects* **273**(1-3), 90-96.

Klug H. P. and Alexander L. E., 1974. *X-ray Diffraction Procedures: For Polycrystalline and Amorphous Materials, 2nd Edition*, John Wiley & Sons.

Kuan, W. H., Lo, S. L., Wang, M. K., Lin, C. F., 1998. Removal of Se(IV) and Se(VI) from water by aluminum-oxide-coated sand. *Wat. Res.* **32**, 915-923.

Langford J. I. and Wilson A. J. C., 1978. Scherrer after sixty years: a survey and some new results in the determination of crystallite size. *J. Appl. Cryst*. **11**, 102-113.

Lennie A. R. and Vaughan D. J., 1996. Spectroscopic studies of iron sulfide formation and phase relations at low temperatures. *Mineral Spectroscopy* **5**, 117-131.

Lo, S. L., Jeng, H. T., Lai, C. H., 1997. Characteristics and adsorption properties of iron-coated sand. *Wat. Sci. Tech.* **35**, 63-70.

Morse, J. W. Arakaki, T., 1993. Adsorption and Coprecipitation of Divalent Metals with Mackinawite (Fes). *Geochim. Cosmochim. Acta* **57**, 3635-3640.

Mullet, M., Boursiquot, S., Abdelmoula, M., Genin, J. M., Ehrhardt, J. J., 2002. Surface chemistry and structural properties of mackinawite prepared by reaction of sulfide ions with metallic iron. *Geochim. Cosmochim. Acta* **66**, 829-836.

Nakai K., Sonoda J., Kondo S., and Abe I., 1993. The analysis of surface and pores of the activated carbons by the adsorption of various gases. *Pure & Appl. Chem*. **65**, 2181-2187.

Ohfuji H. and Rickard D., 2006. High resolution transmission electron microscopic study of synthetic nanocrystalline mackinawite. *Earth and Planetary Science Letters* 241, 227-233.

Parkhurst, D.L., Appelo, C.A.J., 1999. User's guide to PREEEQC (Version 2): A computer program for speciation, batch reactions, one-dimensional transport, and inverse geochemical

calculation. *U.S Geol. Surv., Wat Resour. Invest*. Rep., WRI-99-4259.

Quirantes A., Ben-Taleb A., and Delgado A. V. (1996) Determination of size/shape of colloidal ellipsoids by photon correlation spectroscopy. *Colloids Surf. A* **119**, 73-80.

Rickard D., 1969. The chemistry of iron sulphide formation at low temperatures. Stockholm Contr. Geol. 26, 67-95.

Rickard D., 1995. Kinetics of FeS precipitation. Part I. competing reaction mechanisms. Geochim. Cosmochim. Acta 59, 4367-4379.

Rickard D., 2006. The solubility of FeS. Geochim. Cosmochim. Acta 70, 5779-5789.

Rickard D., Schoonen M. A. A., and Luther G. W., 1995. The chemistry of iron sulfides in sedimentary environments. In *Geochemical Transformations of Sedimentary Sulfur* (eds. M. A. Vairavamurthy and M. A. A. Schoonen). ACS Symposium Series 612. pp. 168-193.

Scheidegger, A., Borkovec, M. and Sticher, H., 1993. Coating of Silica Sand with Goethite - Preparation and Analytical Identification. *Geoderma* **58**(1-2), 43-65.

Scheidegger, A., Borkovec, M., Sticher, H., 1993. Coating of Silica Sand with Goethite - Preparation and Analytical Identification. *Geoderma* **58**, 43-65.

Spadini L., Bott M., Wehrli B., and Manceau A., 2003. Analysis of the major Fe bearing phases in recent lake sediments by EXAFS spectroscopy. *Aquat. Geochem*. **9**, 1-17.

Thirunavukkarasu, O. S., Viraraghavan, T., Subramanian, K. S., 2003. Arsenic removal from drinking water using iron oxide-coated sand. *Wat. Air and Soil Poll.* **142**, 95-111.

van Berkum J. G. M., Vermeulen A. C., Delhez R., de Keijser T. H., Mittemeijer E. J., 1994. Applicabilities of the Warren-Averbach analysis and an alternative analysis for separation of size and strain broadening. *J. Appl. Crystallogr*. **27**, 345-357.

Vaughan, D. J., Craig J. R., 1978. *Mineral Chemistry of Metal Sulfides*. Cambridge University Press.

Vaughan, D. J., Ridout M. S., 1971. Mössbauer studies of some sulphide minerals. *J. Inorg. Nucl. Chem*. **33**, 741-746.

Walther C., 2003. Comparison of colloid investigations by single particle analytical techniques-a case study on thorium-oxyhydroxides. *Colloid Surf. A* **217**, 81-92.

Watson J. H. P., Cressey B. A., Roberts A. P., Ellwood D. C., Charnock, J. M., Soper A. K., 2000. Structural and magnetic studies on heavy-metal-adsorbing iron sulphide nanoparticles produced by sulphate-reducing bacteria. *J. Magn. Magn. Materials* **214**, 13-30.

Wilkins, R.T. Acree, S.D., Beak, D.G., Ross, R.R., Lee, T.R., Paul, C.J., 2008. Field Application of a Permeable Reactive Barrier for Treatment of Arsenic in Groundwater. EPA Report: EPA 600/R-08/093. EPA Office of Research and Development, National Risk Management Research Laboratory, Ada, Oklahoma.

Wolthers, M., Charlet, L., C.H. van der Meijden, P.R. van der Linde, D. Rickard, 2005. Arsenic mobility in the ambient sulfidic environment: sorption of arsenic (V) and arsenic (III) onto dissordered mackinawite. *Geochim. Cosmochim. Acta* **69**, 3483-3492.

Wolthers, M., van der Gaast, S.J., Rickard, D. 2003. The structure of disordered mackinawite. *Am. Mineral.* **88**, 2007-2015.

Xu, Y. and Axe, L., 2005. Synthesis and characterization of iron oxide-coated silica and its effect on metal adsorption. *J. Colloid Interface Sci* **282**(1), 11-19.

Subtask 1.2. Sorption Capacity Determination of FeS

Objective

The overarching goal of this subtask was to assess the sorption capacity of nanoscale FeS for As and Cd and of FeS-coated sand for As.

Background

Ferric oxyhydroxide-based reactive materials have been found to be effective for removing arsenic from groundwater under aerobic conditions (for example, Hodi et al., 1995; Vaishya and Gupta, 2002; Thirunavukkarasu et al., 2003; and Kundu and Gupta, 2006) and have been suggested for permeable barrier applications (Scherer et al., 2000). However, these materials may not be suitable for long term sequestration of inorganic contaminants within a PRB operating under anoxic conditions. Under such conditions, reductive dissolution of ferric oxyhydroxide solids causes the release of sorbed contaminants back into solution (Masscheleyn et al., 1991, McGeehan and Naylor, 1994). Zero valent iron (ZVI) has also been proposed for PRB applications (Lackovic et al., 2000; Farrel et al., 2001; Su and Puls, 2001a,b; Manning et al., 2002; Su and Puls, 2003). However, it is generally thought that iron oxyhydroxide corrosion products that form on ZVI provide the reactive surface for the contaminant uptake (Furukawa et al., 2000; Manning et al., 2002) which too, may eventually dissolve and release contaminants back into solution over prolonged use under anoxic conditions (Tufano and Fendorf, 2008).

To overcome the limitations of iron oxyhydroxide based sorbents, FeS was considered in this work. FeS has been used to control the migration of toxic metals in acidic mine tailing groundwater plumes (Herbert et al., 2000). Laboratory studies have confirmed that FeS removes divalent cations from water by either forming very insoluble metal sulfides (e.g., HgS, Jeong et al., 2008; Cd, Billon et al., 2001) or by forming solid solutions with FeS (e.g., with Cd and Pb; Coles et al., 2000). Laboratory studies have also documented the effectiveness of iron sulfides for the removal of arsenic from anoxic water (Moore et al., 1998, Bostick and Fendorf, 2003, Wolthers et al., 2005). .

To confirm and quantify the effectiveness of the nanoscale FeS and FeS-coated sands produced in this work, their sorption capacity was evaluated as a function of pH range in this portion of the study.

Materials and Methods

Sorption Capacity for Arsenic. For As, sorption isotherm tests were performed on FeS and FeS-coated sand at pH 5, 7, and 9. The pH was buffered with 0.1N acetate (pH 5), 3-(N-morpholino)-propanesulfonic acid (MOPS, pH 7), and 2-(cyclohexylamino) ethanesulfonic acid (CHES, pH 9 for FeS coated sand) or 0.1N borate buffer (pH 9 for mackinawite). The As(III) removal capacity of FeS-coated sand was compared to suspensions of nanoparticulate FeS on a per gram of FeS weight basis. To perform the isotherm studies, mackinawite from a 50 g/L stock solution was added to each buffer solution to achieve 10 mL of a 1g/L mackinawite suspension in 15 mL polypropylene reactor tubes. Each tube was then spiked with varying amounts of $NaAsO_2$ stock solution to achieve a final concentration ranging from 6.7×10^{-7} M to 3.0×10^{-3} M As(III). Test tubes with 5 g of FeS-coated sand and 10 ml of buffer solutions were

spiked with As(III) stock solution to achieve a concentration range of 1.0×10^{-6} M to 6.7×10^{-4} M initial As(III) concentrations for pH 5, and 1.0×10^{-6} M to 2.6×10^{-4} M for pH 7 and 9. The reaction tubes were then mixed on an end-over-end rotator for 2 days. After 2 days, the supernatant in tubes was filtered through a 0.1 μm nylon filter, diluted, acidified with HNO_3 and then analyzed for arsenic by inductively coupled plasma-mass spectrometry (ICP-MS, Perkin Elmer). All the experimental steps except the supernatant acidifying step for ICP-MS analysis were performed in the anoxic chamber (H_2/N_2 = 5%/95%).

Sorption Capacity for Cadmium. For Cd, sorption experiments were conducted using 12 mL centrifuge tubes by reacting aqueous $CdCl_2$ solutions with FeS suspensions. The initial Cd(II) concentrations (Cd_0) used were 1.5×10^{-2}, and 5×10^{-4}, and an initial FeS concentrations ($[FeS]_0$) of 10 g/L. The equilibrium pH ranged over 4 to 11, and the total chloride concentration (Cl_T) was fixed at 0.2 M. The sorption batches were allowed to equilibrate for 48 hours on a shaker (Lab Industries, Berkeley, CA) at 25 ^oC. This was sufficient for completion of sorption reaction (Di Toro et al. 1992; Erdem and Özverdi 2006). At the end of reaction time, a portion of the supernatants was syringe-filtered using 0.2 μm polypropylene filter (Whatman). The filtrates were acidified with 10% (wt./wt.) nitric acid. Dissolved Cd in the acidified solutions was measured by inductively coupled plasma coupled with optical emission spectrometry (ICP-OES, Perkin-Elmer).

Results and Discussion

Sorption Capacity for Arsenic. As(III) removal capacities at pH 5, 7 and 9 were evaluated using synthesized FeS and FeS-coated sand and compared on an FeS unit mass basis. Removal capacities of FeS at pH 5, 7 and 9 were found to be on the order of 2×10^{-3}, 2×10^{-4} and 5×10^{-5} mol As removed/g FeS while FeS-coated sand removed on the order of 5×10^{-4}, 1.5×10^{-4} and 1.5×10^{-4} mol As/g FeS at pH 5, 7 and 9, respectively (Figure 1.4). Although Langmuir type sorption behavior was observed, As(III) removal mechanism is known to be caused by a combination of arsenic adsorption and bulk precipitation as arsenic sulfide over this pH range (Gallegos et al., 2007; 2008). Using the plateau values as the arsenic uptake capacity, it was found that the FeS-coated sand removed around 30%, 70% and 300% of the maximum capacity of FeS at pH 5, 7 and 9, respectively.

As shown in Figure 1.4, As(III) removal by FeS is highly pH-dependent and this trend is similar in FeS-coated sand system. At pH 5, bulk precipitation of realgar (AsS) from a reaction between dissolved sulfide and aqueous As(III) has been previously proposed as the primary mechanism for the high uptake (Gallegos et al., 2007 and 2008):

$$3FeS + H_3AsO_3 + 3H^+ = 1/2\ Fe_3S_4 + AsS + 3/2\ Fe^{2+} + 3H_2O \qquad (1.4)$$

However, at pH 5, using FeS-coated sand, the normalized amount of arsenic removed per g of FeS was 70% less after the coating process. This may be attributed to the change in the iron mineral composition based on XPS results above, or the possible reduction in accessibility of self-aggregated FeS particles on the sand surface.

As the pH is increased, the contribution of bulk precipitation of arsenic sulfide in As(III) removal decreases as the FeS solubility abruptly decreases above pH 6. Instead, a surface

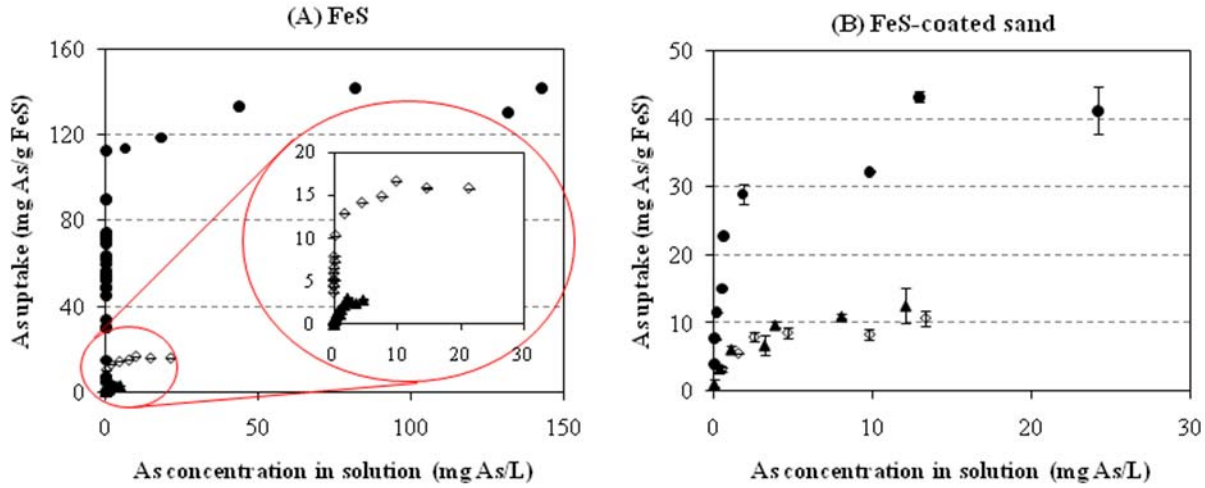

Figure 1.4. Sorption isotherm results at pH 5, 7 and 9 plotted as the amount removed versus the solution concentration of As after 2 days equlibration time with FeS (A) and FeS-coated sand (B). (● pH 5, ◇ pH 7, and ▲ pH 9, Error bars: standard deviation).

sorption mechanism is thought to become increasingly more important as pH increases above 6 (Gallegos et al., 2007) At pH 7, the FeS coated sand has about 70% of the capacity as FeS, perhaps resulting from less accessible FeS surface functional groups on the aggregatged FeS nanoparticles on the coated sand. Interestingly, at pH 9, the FeS-coated sand shows approximately three times more removal than FeS. This result may be attributed to the presence of other oxidized iron mineral phases such as the naturally existing metal (Fe and/or Al) oxide from uncoated sand surface or the presence of a secondary mineral phase from mackinawite oxidation. Recent work has shown that As(III) uptake is enhanced in the presence of magnetite, although this enhancement may only be temporary if prolonged exposure to reducing conditions prevails (Tufano and Fendorf, 2008) in the absence of sulfide. The maximum uptake capacity values for As(III) by FeS (at pH 5) of 2 mmol/g is similar to that obtained by hydrous ferric oxide (HFO) (at pH 8) (Dixit and Hering, 2003) .

The As(III) removal capacities (using Langmuir isotherm model) obtained in this study using FeS-coated sand, 41.6, 10.7 and 12.7 mg As/g FeS (0.052, 0.013, and 0.016 mg As/g FeS-coated sand) at pH 5, 7 and 9, respectively, are comparable to various other absorbents that have prepared for As(III) removal in PRB applications. For example, the adsorption capacity was 0.14 mg/g for a sulfate ($BaSO_4$) modified iron oxide-coated sand (d_{50} = 0.5 mm) (Vaishya and Gupta, 2002), and 0.041 mg/g (d = 0.6-0.8 mm) (Thirunavukkarasu et al. 2003) and 0.028 mg/g (d_{50} = 0.5 mm) (Gupta et al. 2005) for iron-oxide coated sands. For granular ZVI (d = 1-1.68 mm) pretreated with acid, a capacity of 0.3 mg/g was obtained for As(III) (Lackovic et al., 2000) while for a iron-oxide coated cement (d_{50} = 212μm) an even higher value of 0.67 mg/g (Kundu and Gupta, 2006) was found. The higher capacity for ZVI may result from the pitting/fracturing from acid pretreatment, while in the case of the porous cement, it may be due to accessible internal surface. Regardless, for either oxide-coated ZVI or ferric-coated material, under prolonged anoxic conditions, arsenic may ultimately be released by reductive dissolution under anoxic conditions (Tufano and Fendorf, 2008). Therefore, FeS-coated sands may provide an

attractive alternative for arsenic removal in PRB applications in which long-term reducing conditions prevail.

Sorption Capacity for Cadmium. In general, the mechanisms responsible for Cd(II) sorption by Fe sulfides are thought to include adsorption (Jean and Bancroft 1986; Kornicker and Morse 1991), surface Fe(II) exchange (Coles et al. 2000), and precipitation as CdS(s) (Bostick et al. 2000; Erdem and Özverdi 2006). These previous studies indicate that the principle sorption mechanisms for Cd(II) vary significantly with type of Fe sulfides and experimental conditions. However, in our study of capacity, we found that Cd was nearly quantitatively removed from solution regardless of pH as long as the ratio of Cd_0/FeS_0 was less than 1. As shown in Figure 1.5, below Cd was removed to below the MCL of 5 µg/L across the entire pH range for concentrations up to 0.015 M for 10 g/L FeS from pH 4-11. This indicates that the capacity of FeS for Cd can be as high as 1.5 mmol/g (168 mg Cd/g FeS). This high removal capacity is thought to be a result of the exchange of Cd for Fe in FeS(s) and the formation of the more insoluble CdS(s), particularly as the ratios of Cd_0/FeS_0 approach 1. Similarly, others also reported that precipitation of CdS(s) was the main mechanism for Cd(II) removal by FeS (Framson and Leckie 1978; Erdem and Özverdi 2006). This high capacity and type of behavior was also recently reported for Hg removal by FeS (Jeong et al., 2007).

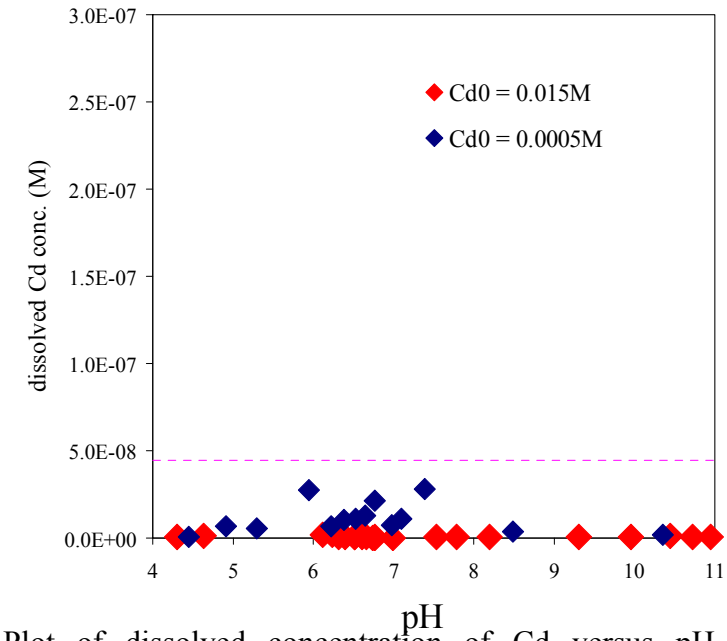

Figure 1.5. Plot of dissolved concentration of Cd versus pH illustrating that nearly quantitatively removal of Cd occurs at Cd intial concentrations of 0.015 M and 0.0005 M for 10 g/L FeS (0.11 M FeS). Dotted line shows the MCL of 5 ppb (4.5×10^{-8} M) Cd.

Summary and Conclusions and Implications for Future Research/Implementation

FeS is an effective sorbent for As(III) and Cd(II). In the case of As(III), the sorption capacity is highest (~$2x10^{-3}$ mol As/g FeS) at lower pH (over a pH range of 5-9) while for Cd, sorption capacity is high (~$2x10^{-3}$ mol Cd/g FeS) over the entire pH range investigated (pH 4-11). The high sorption capacity for As(III) and Cd(II) appears to be due to the precipitation of AsS(s) and

CdS(s), and limited only by the availability of sulfide from FeS. This capacity of FeS at pH 5 is similar to maximum capacity of HFO for As(III) at pH 8. At higher pH, the capacity drops off for As(III) as the mechanism of removal switches to from precipitation to a surface area-limited removal process. Cd removal of 1 mmol/g over the entire pH range is also similar to the maximum capacity observed for iron oxide based sorbents. In the case of FeS-coated sand, As(III) removal is 30%, 70% and 300% of the maximum capacity of FeS at pH 5, 7 and 9, respectively. As(III) uptake capacity by FeS-coated sand is comparable to other iron or aluminum oxide coated sand used for arsenic removal, with a maximum uptake capacity at pH 5 that decreases with pH. Under anoxic conditions, FeS-coated sand are expected to outperform other iron and aluminum oxides for As(III), given that these other sorbents are expected to release arsenic when reducing conditions prevail for long time periods. Although not tested, it is likely that Cd removal by FeS-coated sand would be comparable or better than iron and aluminum oxide materials, given the superior uptake capacity of FeS compared these other sorbents for Cd. These results suggest that FeS materials will be effective in PRB applications for the removal of arsenic and heavy metal cations such as Cd. The particular advantage of FeS compared to iron oxide based sorbents is, that in anoxic PRBs, FeS-based materials will not release sorbed contaminants back into solution by reductive dissolution.

Literature Cited

Billon G., B. Ouddane B, J. Laureyns A. Boughriet, 2001. Chemistry of metal sulfides in anoxic sediments. *Physical Chemistry Chemical Physics*, **3** (17), 3586-3592.

Bostick, B. C., S. Fendorf, 2003. Arsenite sorption on troilite (FeS) and pyrite (FeS2). *Geochim. Cosmochim. Acta* **67**, 909-921.

Bostick, B.C., S. Fendorf, and M. Fendorf, 2000. Disulfide disproportionation and CdS formation upon cadmium sorption on FeS2, Geochim. Cosmochim. Acta 64, 247-255.

Coles, C.A., S.R. Rao, and R.N. Yong, "Lead and Cadmium interactions with mackinawite: Retention mechanisms and the role of pH," *Environ. Sci. Technol*. **34**, 996-1000, 2000.

Dixit, S., J.G. Hering, 3003. Comparison of arsenic(V) and arsenic(III) sorption onto iron oxide minerals: implications for arsenic mobility. *Environ. Sci. Technol.* **37**, 4182-4189.

Erdem, M., A. Özverdi, 2006. Kinetics and thermodynamics of Cd(II) adsorption onto pyrite and synthetic iron sulphide. Separation and Purification Technology 51, 240-246.

Farrell, J. Wang, J., O'Day, P., Conklin, M. 2001. Electrochemical and spectroscopic study of arsenate removal from water using zero-valent iron media. *Env. Sci. Techl.* **35**, 2026-2032.

Furukawa, Y., J.W. Kim, J. Watkins, R.T. Wilkins, 2002. Formation of ferrihydrite and associated iron corrosion products in permeable reactive barriers of zero valent iron. *Environ. Sci. Technol.* **36**, 5469-5475, 2002.

Gallegos, T. J., S.P. Hyun, K.F. Hayes, 2007. Spectroscopic investigation of the uptake of arsenite from solution by synthetic mackinawite. *Environ. Sci. Technol.* **41**, 7781-7786.

Gallegos, T. J., Y.-S. Han, K.F. Hayes, 2008. Model precipitation by reaction of As(III) with synthetic mackinawite under anoxic conditions. *Environ. Sci. Technol.* **42**, 9338-9343.

Herbert, R.B., Benner, S.G. and Blowes, D.W., 2000. Solid phase iron-sulfur geochemistry of a reactive barrier for treatment of mine drainage. *Applied Geochemistry* **15**(9), 1331-1343.

Hodi, M., K. Polyak, K., J. Hlavay, 1995. Removal of pollutants from drinking water by combined ion exchange and adsorption methods. *Environ. Intern.* **21**, 325-331.

Jean, G.E., G.M. Bancroft, 1986. Heavy-metal adsorption by sulfide mineral surfaces. *Geochim. Cosmochim. Acta* **50**, 1455-1463.

Jeong, H.Y., B. Klaue, J.D. Blum, K.F. Hayes, 2007. Sorption of Mercuric Ion Hg(II) by Iron Sulfide. *Environ. Sci. Technol.*, 41, 7699-7705.

Kornicker, W.A., J.W. Morse, 1991. Interactions of divalent-cations with the surface of pyrite. *Geochim. Cosmochim. Acta* **55**, 2159-2171.

Kundu, S., A.K. Gupta, 2006. Arsenic adsorption onto iron oxide-coated cement (IOCC): regression analysis of equilibrium data with several isotherm models and their optimization. *Chem. Eng. J.* **112**, 93-106.

Lackovic, J.A., N.P. Nikolaidis, G.M. Dobbs, 2000. Inorganic Arsenic Removal by zero valent iron. *Environ. Eng. Sci.* **17**, 29-39.

Manning, B.A., M.L Hunt, C. Amrhein, J.A. Yarmoff, 2002. Arsenic (III) and Arsenic (V) reactions with zerovalent iron corrosion products. *Environ. Sci. Technol.* **36**, 5455-5461.

Masscheleyn, P. H., R.D. Delaune, W.H. Patrick, 1991. Arsenic and Selenium Chemistry as Affected by Sediment Redox Potential and pH. *J. Environ. Qual.* **20**, 522-527.

McGeehan, S. L. D.V. Naylor, 1994. Sorption and Redox Transformation of Arsenite and Arsenate in 2 Flooded Soils. *Soil Sci. Soc. Am. J.* **58**, 337-342.

Moore, J. N., W.H. Ficklin, C. Johns, 1988. Partitioning of Arsenic and Metals in Reducing Sulfidic Sediments. *Environ. Sci. Technol.* **22**, 432-437.

Scherer, M.M., S. Richter, R.L. Valentine, P.J.J. Alvarez, 2000. Chemistry and microbiology of permeable reactive barrier for in sute groundwater clean up. *Crit. Rev. Environ. Sci. Tech.* **30** (3), 363-411

Su, C., R.W. Puls, 2001a. Arsenate and arsenite removal by zerovalent iron: Kinetics, redox transformation, and implications for in situ groundwater remediation. *Environ. Sci. Technol.* **35**, 1487-1492.

Thirunavukkarasu, O.S., T. Viraghavan, T., K.S. Suramanian, 2003. Arsenic removal from drinking water using iron-oxide coated sand, *Water Air Soil Pollut.* **142**, 95-111.

Tufano, K.J., S. Fendorf, 2008. Confounding impacts of iron reduction on arsenic retention. *Environ. Sci. Technol.* **42**, 4777-4783.

Vaishya, R.C., S.K. Gupta, 2002. Modeling arsenic(V) removal from water by sulfate modified iron-oxide coated sand (SMIOCS). *J. Chem. Technol. Biotechhol.* **78**, 645-666.

Wolthers, M., Charlet, L., C.H. van der Meijden, P.R. van der Linde, D. Rickard, 2005. Arsenic mobility in the ambient sulfidic environment: sorption of arsenic (V) and arsenic (III) onto dissordered mackinawite. *Geochim. Cosmochim. Acta* **69**, 3483-3492.

Subtask 1.3. Uptake Mechanism of As and Cd by FeS and As by FeS-Coated Sand

Substask 1.3.a. Uptake mechanism of As by nanoscale FeS

Objective

The overarching goal of this subtask was to assess the uptake mechanisms of As by FeS by characterizing the solid phase reaction products.

Background

Recent studies have confirmed that iron monosulfides are potential sinks for arsenic in anoxic environments. These studies indicate that the mechanism of As uptake is highly dependent not only on the type of iron monosulfide, but also on solution conditions. More specifically, studies regarding the uptake of As (As(V) and As(III)) from solution by mackinawite have suggested that the major uptake removal mechanism is via orpiment or realgar (Farquhar et al., 2002) or arsenopyrite precipitation at pH 4 and a arsenite surface complex at pH 9 (Bostick and Fendorf, 2003) In natural systems, realgar is often thought to be the dominant arsenic sulfide present (O'Day et al., 2004). The purpose of this study was to investigate the removal mechanisms of As(III) by mackinawite by identification and characterization of reaction solid products via spectroscopic x-ray absorption, x-ray diffraction (XRD) and transmission electron microscopy (TEM) analyses including high-angle annular dark field (HAADF), scanning transmission electron microscopy (STEM), STEM elemental mapping, and high resolution TEM. This information is also needed for the reactive transport models that were developed as part of this project.

Material and Methods

All work was conducted in a N_2/H_2 glovebox. De-oxygenated water was prepared by bubbling deionized water (18 Mohm) obtained from a Millipore Milli-Q system with 99.99% Nitrogen gas for 2 hours. The de-oxygengated water was used to prepare solutions. Ferrous and sulfide stock solutions were freshly prepared using $FeCl_2 \bullet 4H_2O$ and $Na_2S \bullet 9H_2O$ (Sigma-Aldrich), respectively.

TEM and XRD analysis. Samples for TEM and XRD were prepared by lowering the pH of three 500 mL samples of a 5 g/L suspension of FeS at pH 5, 7 and 9 by adding 1M HCl and equilibrating for 1 week at a constant ionic strength of 0.1 M as NaCl. After the initial solid equilibration time, the samples were spiked with a 0.15 M $NaAsO_2$ stock solution to achieve initial As concentrations of $1x10^{-2}$ M, $1.25x10^{-3}$ M and $2.5x10^{-4}$ M at pH 5, 7 and 9, respectively, to represent a relatively high (0.18) to low (0.004) As:FeS molar ratio. At the end of the reaction period, 15 mL of each of the 6 samples were preserved for TEM analysis. The remainder of the samples was prepared for XRD analysis by centrifugation at 10000 rpm for 20 minutes. The solids were vacuum freeze dried for 48-72 hours to remove all moisture. Samples for XRD analysis were prepared by grinding the solid with a mortar in pestle to produce a fine powder and packing into an aluminum sample holder. XRD samples data were collected on BL 4-2 at 6700 keV in reflection mode on bulk solid samples. Samples were rocked 3 seconds for 2θ range of 10 to 90 degrees with a Co goniometer with $\lambda = 1.76989$.

TEM samples were prepared by diluting the solid suspensions with DI water (at pH 5, 7 and 9) to achieve final solid concentrations of 0.5 g/L. Samples were prepared one day in advance of TEM analysis. Carbon coated copper mesh grids (~3cm dia.) were placed atop a paper filter to wick off excess moisture. A 6 uL aliquot of each sample was placed on a carbon coated copper grid and rinsed with 4 uL of deoxygenated, deionized water. Samples were dried inside N_2/H_2 glove box for 24 hours before transferring into protective plastic bags and stored in the anaerobic chamber until TEM analysis. HAADF-STEM was utilized to evaluate the distribution of arsenic phases in the samples. High-resolution TEM (HRTEM) and HAADF-STEM were conducted using a JEOL-JEM 2010F field emission gun microscope with an energy-dispersive X-ray spectrometer. The microscope was operated at 200 keV. Nanoscale elemental mapping of arsenic, iron, and sulfur was completed with HAADF-STEM coupled with Emispec ES Vision version 4.0 for samples reacted at pH 5 and EDAX Genesis for pH 9 samples (instrument software was converted during the timeframe of the study). Image processing, including the generation of diffraction patterns from the fast Fourier transformation (FFT), was completed using Gatan Digital Micrograph 3.6.4.

X-Ray Absorption Spectroscopy. Samples were prepared 3 days in advance of X-ray Absorption Spectroscopy (XAS) analysis. For XAS data collected were collected at two different times. During the first collection period, two 10 g/L mackinawite suspensions were equilibrated on a rotating mixer for 3 days with HCl to achieve final pH of 5 and 9 in a 0.1M NaCl background to achieve constant ionic strength. After initial equilibration time, the samples were spiked with $NaAsO_2$ stock solution to achieve an initial arsenite concentration of $1x10^{-3}$ M to represent a moderate As:FeS molar ratio (e.g., 0.009). For the second collection period, four samples were prepared in 5g/L mackinawite suspensions at pH 5 and 9, with each pH having an initial As(III) concentrations of either $5.0x10^{-5}$ or $5.0x10^{-4}$ M to represent a moderate (0.009) or low As: FeS (0.0009) molar ratio. At the end of the reaction period, samples were centrifuged at 7000 rpm for 15 minutes. Residual solids were collected and stored under nitrogen until analysis. Solutions were filtered and analyzed via optical emission spectroscopy for final total arsenic concentrations.

XAS data were collected on beamline 11-2 (3 GeV, 100 mA) at the Stanford Synchrotron Laboratory in Menlo Park, CA. Arsenic K-edge x-ray absorption near-edge structure (XANES) and extended x-ray absorption fine structure (EXAFS) fluorescence spectra were collected by using Si(220) double-crystal monochrometer with a 13-element solid state Ge-array fluorescence detector with an unfocused beam. Arsenic spectra were calibrated with As-foil at 11,867 eV. Solid references compounds were collected via Lytle detector in transmission mode. Additionally, a 6 ux Ge filter was used. A minimum of 5 spectra were collected and averaged during data analysis. Spectra were fit by non-linear least squares methods using SixPACK (Webb, 2002) which is a windows interface based on IFFEFFIT (Newville, 2001). Data were fit in k-space for atomic shells up to about 4Å from the central As atom, using the entire k-range in the fit. Theoretical phase-shift and amplitude reference functions were calculated with the program FEFF8 (Ankudinov et al., 1998) for adsorber backscatterer pairs. Atomic structures for input into the ab initio XAFS program FEFF8 were obtained from WEBATOMS or ATOMS (Ravel, 2001) software. ATOMS is a program for generating atomic coordinates from crystallographic data. For analysis of the arsenic spectra, theoretical functions were least-squares fit to solid reference model compounds that were either measured (arsenic metal: As(0), arsenopyrite: FeAsS, and realgar: AsS) or obtained from a model compound library arsenious oxide, As_2O_3, arsenic(V) oxide: As_2O_5, orpiment: As_2S_3; Newville, 2005).

Results and Discussion

Figure 1.6 shows a HAADF-STEM image of FeS reacted with 5×10^{-5} M As(III) at pH 5. Elongated arsenic sulfide particles (showing up brighter in the image due to their higher average atomic mass relative to the FeS) were found up to several μm in length. The inset in lower right corner of the image is a HR-TEM image of a section of one of the elongated particles in the HAADF-STEM image. The lack of lattice fringes indicates that the arsenic sulfide precipitates forming at pH 5 are primarily amorphous. Figure 1.7 shows a HAADF-STEM with EDXS mapping of FeS reacted with 5×10^{-5} M As(III) at pH 5. The EDXS maps specific to As, S, and Fe are shown to the right of the image and confirm the presence of discrete arsenic sulfide phases.

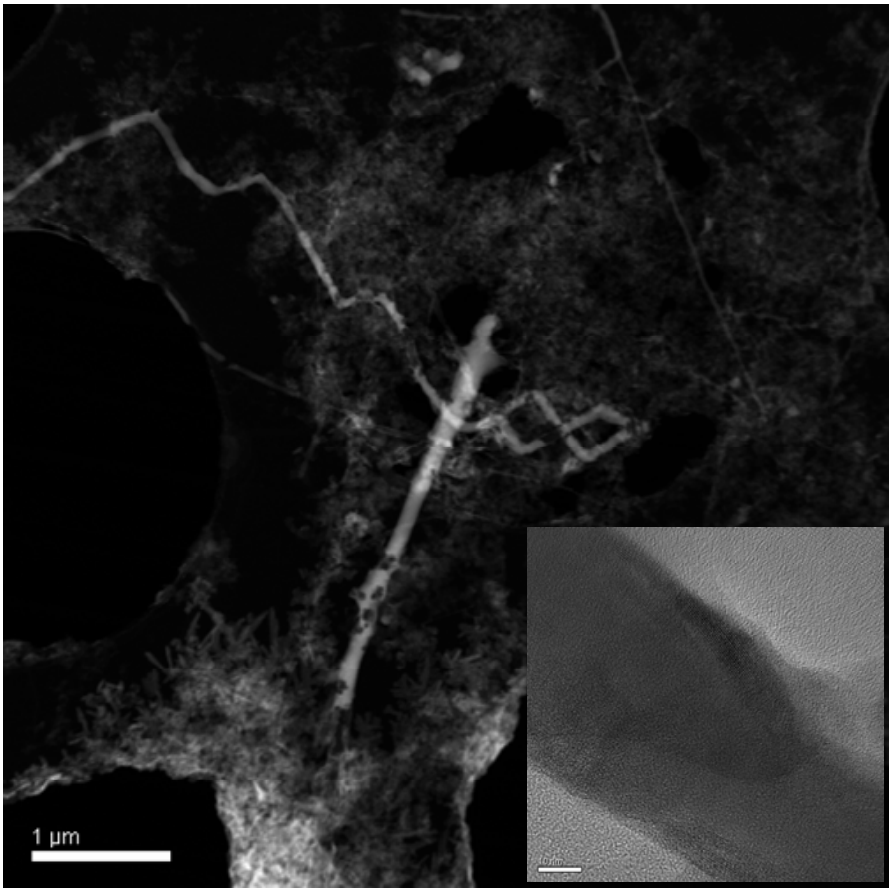

Figure 1.6. HAADF-STEM image of FeS reacted with As(III) at pH 5 (Renock et al., 2009).

Figure 1.8 shows HAAD-STEM images of FeS nanoparticles reacted with 5×10^{-5} M As(III) at pH 9 along with the elemental mapping of As, Fe, and S. As can be seen at this higher pH, sorbed As is well dispersed among the FeS nanoparticles, suggesting surface-limited sorption is responsible for As removal rather than the precipitation of a discrete AsS(s) phase that is observed at pH 5.

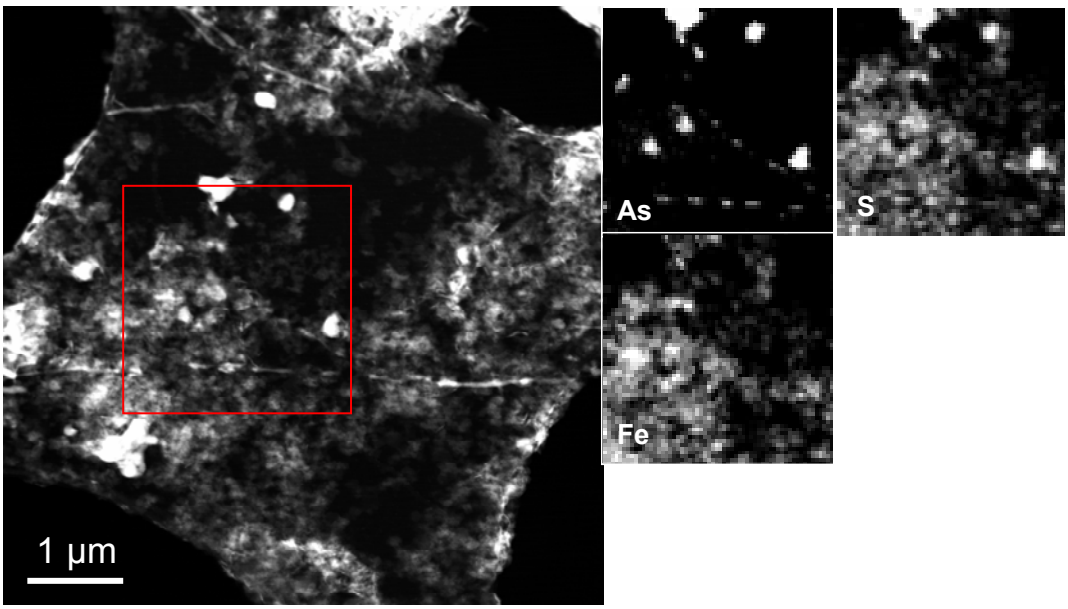

Figure 1.7. HAADF-STEM with EDX mapping of FeS reacted with As(III) at pH 5. The box in the image shows the region of EDS elemental mapping. EDXS maps specific to As, S, and Fe are shown to the right of the image and confirm the presence of discrete arsenic sulfide phases (Renock et al., 2009).

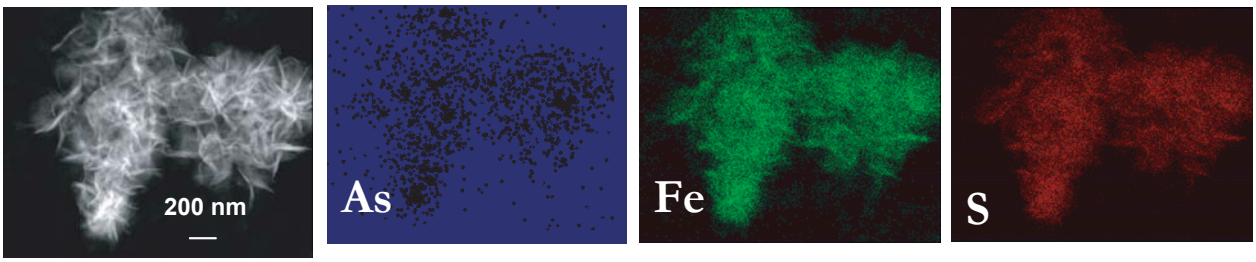

Figure 1.8. HAADF-STEM with EDXS mapping of FeS reacted with As(III) at pH 9. EDXS maps specific to As, S, and Fe are shown to the right of the image and show a homogeneous distribution of As among the FeS aggregates (Renock et al., 2009).

XANES spectra collected for As sorption by FeS along with model As compounds are shown in Figure 1.9. The location of the main peak in the XANES can be taken as an indication of the oxidation state of As in the particular coordination environment. Comparison the location of the XANES features with model compounds of known arsenic oxidation state allows a qualitative assignment of the As oxidation state. From such a comparison it is evident that none of the sorption samples have an As(V) oxidation state (e.g., compare As_2O_5 with the sorption samples). Also, it appears that all pH 5 sorption samples have an oxidation state lower than As(III) since the peak locations for these samples are all below that of orpiment and arsenic oxide (As_2S_3 or As_2O_3). The similarity of the pH 5 sorption major XANES peak to realgar and arsenopyrite suggest that As uptake at pH 5 results in As reduction. The exception is the

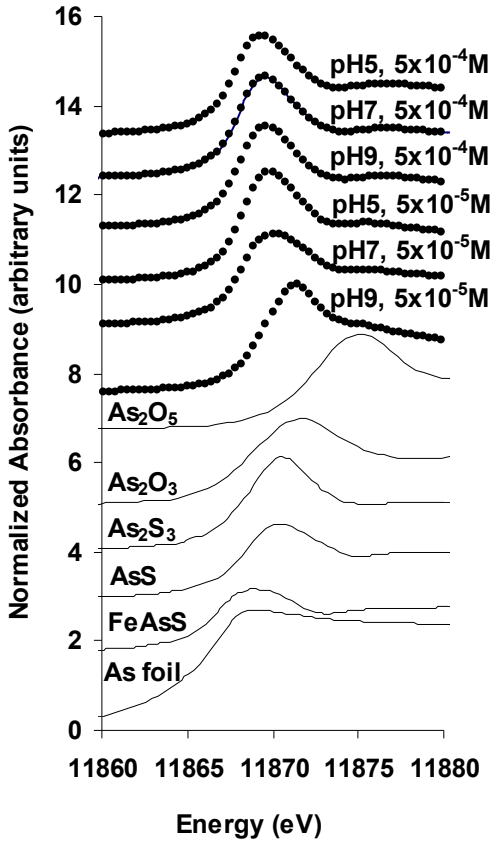

Figure 1.9. XANES spectra of As reacted with FeS (Gallegos et al., 2007).

sorption sample at pH 9, in which As appears to retain its As(III) oxidation state when compared with the XANES of the As(III) models As_2S_3 or As_2O_3. From this qualitative XANES analysis, it appears that precipitation of As, most likely in the form of realgar or arsenopyrite, takes place at pH 5, while at pH 9, arsenic appears to be retained with As(III) oxyacid (AsO_3) structure largely in tack, suggesting that a surface limited adsorption processes is responsible for As uptake at the higher pH.

To provide support for these assignments of uptake mechanisms at pH 5 and 9, an EXAFS analyses was performed on the same samples. EXAFS analysis allows bond distances and coordination numbers to be determined for coordination shells within 6 Å of the central atom of interest, in this case arsenic. The model fits to the EXAFS data for the samples are summarized in Table 1.4, while the model fits for the model compounds are shown in Table 1.5. Figure 1.10 shows the EXAFS spectra and the corresponding radial distribution functions (RDFs) plotted as a function of distance from the central arsenic atom (uncorrected for phase shift). For the mackinawite samples equilibrated at pH 5, 7 and 9 with an initial As(III) concentration of 5.0×10^{-4} M, the EXAFS spectra are fit well by a first coordination shell containing As-S and As-As at average interatomic distances around ~2.26 Å and ~2.54 Å,

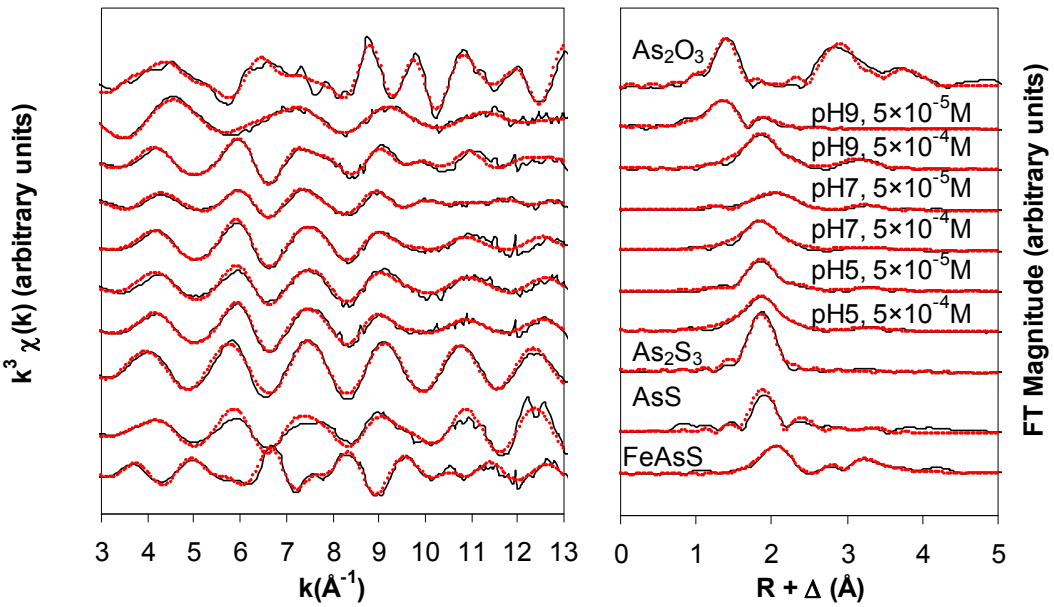

Figure 1.10. EXAFS spectra and radial distribution functions for As sorption and models (Gallegos et al., 2007).

respectively. The As-S and As-As first shell distances are within the range of bond lengths observed in several arsenic sulfides, namely realgar (Mullen et al., 1972), synthetic β-realgar (Porter and Sheldrick 1972), pararealgar (Bonazzi et al. 1995), alacranite (Bonazzi et al., 2003), and uzonite (Bindi et al. 2003). The second shell for the pH 5, 7 and 9 samples may be fit with an As-As bond around 3.57 Å which compares favorably to the realgar crystal structure derived from X-ray diffraction (Mullen et al., 1972). Slight deviations from the more crystalline phase are attributed to the disorder expected for a freshly synthesized amorphous precipitate (Benning et al. 2002) where short-range ordering is expected (Savage et al. 2000). The pH 9 sample requires the inclusion of either a second As-As bond or an As-Fe bond at 3.52 Å to account for the increase in peak size as compared to the pH 5 and 7 samples. An As-As bond of 3.52 Å provides evidence of long- range ordering, whereas, an As-Fe bond of 3.52 Å could be an indication of a realgar-like surface precipitate.

Consistent with XANES, the EXAFS data support the hypothesis that initial concentrations of 5×10^{-4} M As(III) reacts with mackinawite to form a discrete realgar-like phase. Metal sulfide phases have also been reported for reactions of mackinawite with divalent metal cations such as Cd(II) and Cu(II) (Parkman et al. 1999) and Hg(II) (Jeong et al. 2007). Although As(III) is added to the mackinawite suspensions as an As(III) oxyanion, arsenite, As(III) is reduced upon reaction with FeS to form arsenic sulfide precipitates.

At pH 9, the differences between high and low As(III) concentrations are more profound than for samples collected under neutral and acidic conditions. The RDFs of the EXAFS data for the pH 9 mackinawite sample reacted with 5.0×10^{-5} M initial As(III) consist of three peaks up to about 4 Å. The fitting of the first and most prominent peak in this sample consists of 2.7 As-O bonds at a distance of 1.75 Å. The As-O bond is similar to that found in the As_2O_3 model compound and in the $As(OH)_3$ molecule of 1.75 Å (Tossel 1997) and is apparent in all the

Table 1.4. Arsenic local structure for mackinawite samples reacted at pH 5, 7 and 9 with initial concentrations of 5.0×10^{-5} M and 5.0×10^{-4} M As(III) (Gallegos et al., 2007).

	5×10^{-4} M As(III)			5×10^{-5} M As(III)		
	CN	R(Å)	σ^2 (Å ^{2})	CN	R(Å)	σ^2 (Å ^{2})
pH 5	2 S	2.26	0.0035	0.3 O	1.75	0.0010
	1 As	2.54	0.0062	2 S	2.26	0.0053
	1.25 As	3.57	0.0093	1 As	2.53	0.0091
				1.25 As	3.57	0.0107
	R_f=0.053;ΔE_0 =10.33 eV			R_f=0.113; ΔE_0 =10.04 eV		
pH 7	2 S	2.25	0.0034	0.3 O	1.73	0.0020
	1 As	2.52	0.0058	1 S	2.28	0.0065
	1.25 As	3.54	0.0101	2 As	2.51	0.0109
				1.25 As/Fe	3.59	0.0078
	R_f=0.069; ΔE_0=8.25 eV			R_f=0.068' ΔE_0 =15.05 eV		
pH 9	2 S	2.26	0.0047	2.7 O	1.75	0.0056
	1 As	2.55	0.0076	0.4 S	2.28	0.0016
	1.25 Fe/As	3.52	0.0045	0.2 Fe	2.86	0.0010
	1.25As	3.57	0.0111	0.12 As	2.60	0.0031
	R_f= 0.079; ΔE_0 =9.57 eV			R_f=0.065; ΔE_0 =18.0 eV		

samples reacted with 5.0×10^{-5} M initial As(III), but is most dominant in the pH 9 sample. This distance of 1.75 Å is also similar to that reported for As(III) adsorption onto pyrite and troilite (Bostick and Fendorf 2003) and for As(III) adsorption onto lepidocrocite, goethite, and mackinawite, albeit for a four-oxygen-coordinated shell (Farquhar et al. 2003). The second peak is fitted with an As-S bond at 2.28 Å and an As-As bond at 2.60 Å, similar to realgar. The third

Table 1.5. EXAFS data fits and model compound crystallographic information.

Model	EXAFS fit (this work)			XRD Crystallographic Information		
	CN	**R(Å)**	**σ^2 (Å ^{2})**	**CN**	**R(Å)**	**Reference**
As_2O_3	3 O	1.78	0.0018	3 O	1.72-1.81	(Frueh, 1951)
	-	-	-	1 O	2.84	
	3 As	3.23	0.0012	3 As	3.12-3.27	
	2 O	3.46	0.0010	2 O	3.40-3.54	
	6 As	3.89	0.0060	6 As	3.71-4.16	
	R_f= 0.090	**ΔE_0 = 12.47**				
AsS	2 S	2.25	0.0010	2 S	2.228-2.248	(Mullen et al, 1972)
	1 As	2.52	0.0067	1 As	2.566-2.571	
	2.5 As	3.51	0.0077	2.5 As	3.440-3.505	
	1 S	3.50	0.0121	1 S	3.411-3.519	
	1.25 As	3.65	0.0063	1.25 As	3.564-3.628	
	R_f = 0.013	**ΔE_0 = 5.35 eV**				

Note: CN=Coordination Number (fixed), R=Bonding Distance (floated), σ^2= Absolute Value of Debye-Waller Factor (floated), R-factor (R_f)=goodness of fit parameter, ΔE_0 (floated)=photoelectron threshold energy shift for each sample, S_0^2 (fixed at 0.86) is the amplitude reduction factor.

peak is modeled with an As-Fe bond at 2.86 Å, which is consistent with a value of 2.81-2.85 Å reported for arsenite adsorption by pyrite as a mononuclear, bidentate surface complex (Bostick and Fendorf 2003). The adsorbed phase may be either arsenite or a thioarsenite species. Structural properties of thioarsenite species present at high pH under low S:As ratios reported by Bostick et al. display similarities to the structure observed in our study with an As-O bond at 1.78 Å and an As-S bond at 2.28 Å (Bostick et al. 2005). These similarities suggest that the conversion of arsenite to thioarsenite on the mackinawite surface is possible and could explain the arsenic oxidation state similar to $As(OH)_3$ solution species at high pH and the increased As-S coordination seen at pH 5. Alternatively, since EXAFS provides a weight-averaged coordination environment for arsenic, fractional coordination numbers could be indicative of a mixture of an adsorbed arsenite phase with a small amount of the realgar-like precipitate, as seen at higher As(III) loadings.

X-ray diffraction data collected on mackinawite for samples reacted with arsenite at pH 5 under maximum loading conditions of $1x10^{-2}$ M as well a reference library spectra for As-S solids is shown in Figure 1.11. These results suggest that the arsenic sulfide solid realgar likely

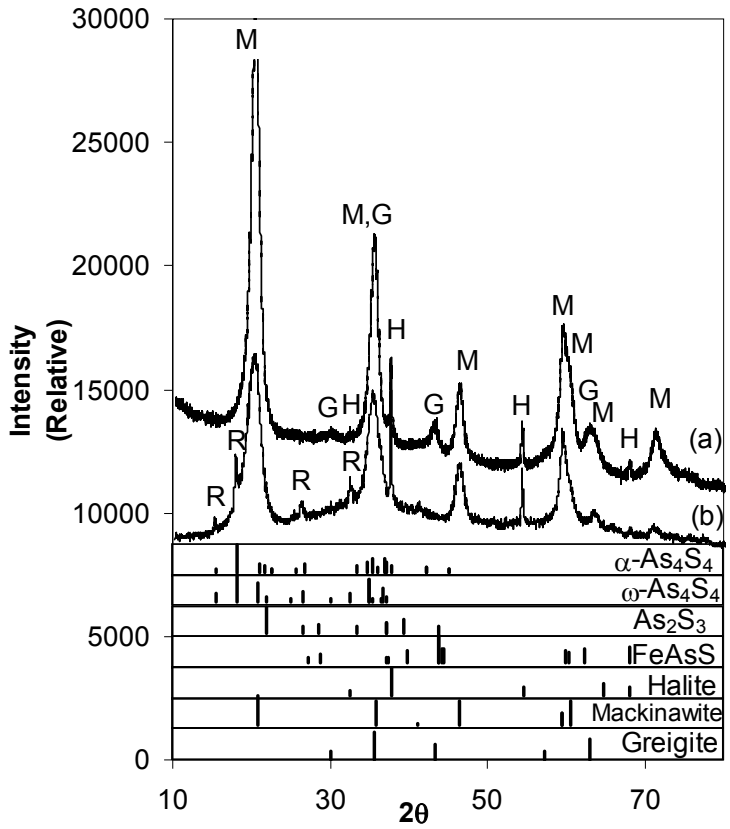

Figure 1.11. XRD spectra for mackinawite samples reacted (a) without As(III) and (b) with 1×10^{-2} M As(III) at pH 5. Reference spectra for mackinawite, halite, realgar polymorphs (α- and ω-As_4S_4), orpiment (As_2S_3) and arsenopyrite (FeAsS) are shown as solid lines at the bottom of the figure. Spectra labels are defined as follows: M=mackinawite, G=greigite, H=halite, R=realgar (Gallegos et al., 2007).

forms under these conditions as indicated by the presence of small new peaks, in addition to those associated with halite and mackinawite. The strongest of these relatively weak intensity peaks are coincident with the location of peaks of the library data for AsS or As_4S_4. Taken together with the other characterization data presented above, these results support the conclusion that realgar forms at low pH when As reacts with FeS.

<u>Summary and Conclusions and Implications for Future Research/Implementation</u>

This study indicates at pH of 5 in the concentration range of $5x10^{-5}$ to $5x10^{-4}$ M and at pH 9 at concentrations of As of $5x10^{-4}$ M, AsS (realgar) precipitation is predominant removal mechanism**.** TEM analyses identified elongated and relatively large AsS(s) precipitates at pH 5. HAAD-STEM with EDXS mapping confirmed the bulk precipitation of AsS(s) at pH 5 and the homogenous distribution of As among FeS nanoparticles at pH 9. XANES analysis indicated the formation of a reduced As(II) oxidation structure (e.g., AsS or FeAsS) at pH 5 upon sorption and the formation of a surface complex on FeS that retained the As(III) oxidation state at pH 9**.** EXAFS analysis provided bond distances and coordination numbers consistent with the uptake mechanism conclusions of the TEM and XANES analysis, viz., at low pH under all loading

conditions investigated, AsS(s) precipitation was predominant, while at pH 9, precipitation was predominant at the higher loading but adsorption and formation of surface complexes or surface precipitation were the main removal mechanisms at the lower loading. XRD analysis confirmed that realgar precipitation occurred at pH 5 under high loading conditions. These results indicate that the high capacity of FeS for As(III), especially at lower pH of 5, results from the precipitation of an arsenic sulfide solid (e.g., AsS(s)). Further, these results indicate that the drop-off in of FeS capacity at higher pH is likely the result of a surface-limited sorption that becomes more prevalent with increasing pH. Based on these results, for PRB implementation of nanoscale FeS, operating at pH values below 7 appears to afford the best removal of As(III), where precipitation is favored over surface-limited sorption.

Literature Cited

Ankudinov, A.L., B. Ravel, J.J. Rehr, and S.D. Conradson, 1998. FEFF8. *Phys. Rev. B*, 7565-7576.

Benning, L. G., 2002. Arsenic sulphides: nucleation and growth from aqueous solution. Geochemistry of the Earth's Surface, pp294–298.

Bindi, L., V. Popova, P. Bonazzi, 2003. Uzonite, As_4S_5, from the type locality: Single-crystal X-ray study and effects of exposure to light. *Canadian Mineralogist* **41**, 1463-1468.

Bonazzi, P., S. Menchetti, G. Pratesi, 1995. The Crystal-Structure of Pararealgar, As_4S_4. *American Mineralogist*. **80**, 400-403.

Bonazzi, P., L. Bindi, F. Olmi, S. Menchetti, 2003. How many alacranites do exist? A structural study of non-stoichiometric $AS_8S_{(9-x)}$ crystals. *Eur. J. Mineral.* **15**, 283-288.

Bostick, B. C., S. Fendorf, 2003. Arsenite sorption on troilite (FeS) and pyrite (FeS2). *Geochim. Cosmochim. Acta* **67**, 909-921.

Bostick, B. C., S. Fendorf, Manning, B.A., 2003. Arsenite adsorption on galena (PbS) and sphalerite (ZnS). *Geochim. Cosmochim. Acta* **67**, 895-907.

Bostick, B. C., S. Fendorf, G.E. Brown, 2005. In situ analysis of thioarsenite complexes in neutral to alkaline arsenic sulphide solutions. *Mineralogical Magazine* **69**, 781-795.

Farquhar, M. L., Charnock, J. M., Livens, F. R., Vaughan, D. J., 2002. Mechanisms of arsenic uptake from aqueous solution by interaction with goethite, lepidocrocite, mackinawite, and pyrite: An X-ray absorption spectroscopy study. *Environ. Sci. Technol.* **36**, 1757-1762.

Frueh, A. J., 1951. The Crystal Structure of Claudetite (Monoclinic As_2O_3). *American Mineralogist* **36**, 833-850.

Gallegos, T. J., S.P. Hyun, K.F. Hayes, 2007. Spectroscopic investigation of the uptake of arsenite from solution by synthetic mackinawite. *Environ. Sci. Technol.* **41**, 7781-7786.

Jeong, H.Y., B. Klaue, J.D. Blum, K.F. Hayes, 2007. Sorption of Mercuric Ion Hg(II) by Iron Sulfide. *Environ. Sci. Technol.* **41**, 7699-7705.

Mullen, D. J. E.; Nowacki, W., 1972. Refinement of Crystal-Structures of Realgar, AsS and Orpiment, As_2S_3. *Zeitschrift Fur Kristallographie* **136**, 48-65.

Newville, M., 2001. IFEFFIT: interactive XAFS analysis and FEFF fitting. J *J. Synchrotron Rad.* **8**, 322-324.

Newville, M., Carroll, S. O'Day, P., Waychunas, G. 2005. XAFS Model Compound Library 2005, http://cars9.uchicago.edu/~newville/ModelLib/search.html.

O'Day, P. A., D. Vlassopoulos, R. Root, N. Rivera, 2004. The influence of sulfur and iron on dissolved arsenic concentrations in the shallow subsurface under changing redox conditions. Proceedings of the National Academy of Sciences, **101**, 13703-13708.

Parkman, R. H., J.M. Charnock, N.D. Bryan, F.R. Livens, D.J. Vaughan, 1999. Reactions of copper and cadmium ions in aqueous solution with goethite, lepidocrocite, mackinawite, and pyrite. *American Mineralogist* **84**, 407-419.

Porter, E. J., G.M. Sheldrick, 1972. Crystal-Structure of a New Crystalline Modification of Tetra-Arsenic Tetrasulfide (2,4,6,8-Tetrathia-1,3,5,7-Tetra-Arsatricyclo 3,3,0,03,7 -Octane). *J. Chem. Soc.-Dalt. Trans.* Issue 13, 1347 &.

Ravel, B., 2001. ATOMS: crystallography for the X-ray absorption spectroscopist. *J. Synchrotron Rad.* **8**, 314-316.

Renock, D., T. J. Gallegos, S. Utsunomiya, K.F. Hayes, R.C. Ewing, and U. Becker, 2009. Chemical and structural characterization of As immobilization by nanoparticles of mackinawite (FeSm), *Chemical Geology*, accepted.

Savage, K. S., T.N. Tingle, P.A. O'Day, G.A. Waychunas, D.K. Bird, 2000. Arsenic speciation in pyrite and secondary weathering phases, Mother Lode Gold District, Tuolumne County, California. *Applied Geochemistry* **15**, 1219-1244.

Tossell, J. A., 1997. Theoretical studies on arsenic oxide and hydroxide species in minerals and in aqueous solution. *Geochim. Cosmochim. Acta* **61**, 1613-1623.

Webb, S. M., 2002. Sam's Interface for XAS Package (SixPACK). Stanford Synchrotron Radiation Laboratory.

Substask 1.3.b. Uptake mechanism of Cd by nanoscale FeS

Objective

The overarching goal of this subtask was to assess the uptake mechanisms of Cd by FeS by characterizing the solid phase reaction products.

Background

Aqueous Cd(II) species, due to its strong affinity for sulfide, is strongly sorbed by Fe sulfide minerals. In general, the mechanisms responsible for Cd(II) sorption by Fe sulfides are thought to include adsorption (Jean and Bancroft, 1986; Kornicker and Morse, 1991), surface Fe(II) exchange (Coles et al., 2000), and precipitation as CdS(s) (Bostick et al., 2000; Erdem and Özverdi, 2006). These previous studies indicate that the principle sorption mechanisms for Cd(II) vary significantly with type of Fe sulfides and experimental conditions (e.g., the ratio of Cd(II) loading to sorbent mass, pH, and background salts). Considering that the mobility and bioavailability of toxic metals are strongly affected by the processes controlling sorption behavior, it is critical to identify reaction products and controlling sorption mechanisms. In this task, XAS and XRD were used to obtain molecular-level and bulk-mineralogy information, respectively, of the solid phase products of Cd(II) reacted with FeS over a range of solution conditions.

Materials and Methods

XAS analysis. XAS data were collected at Stanford Synchrotron Radiation Laboratory (SSRL) at the beam line 11-2. The Cd-loaded mackinawite samples were prepared under conditions consistent with the Cd sorption isotherm experiments, at three different pH values, including 5, 7, and 10, right before the XAS data collection. Mackinawite was added to a 0.2 M NaCl (Fisher) solution to make a 10g/L suspension. Then Cd stock solution prepared using $CdCl_2(s)$ (Aldrich) was added to the suspension to make 0.025 M initial Cd concentration. Solution pH was adjusted to a desired value by adding 0.1 M or 1 M HCl or NaOH (Fisher). After the Cd loading for 2 days, the suspensions were centrifuged and the wet pastes with loaded Cd were stored in tightly sealed septa vials to prevent exposure to atmospheric oxygen and were sent to SSRL. To study the sorption mechanism at lower Cd concentration, mackinawite samples were also prepared at lower Cd loading condition, i.e., 10^{-4} M Cd on 1 g/L mackinawite, at two different pH conditions with 0.01 M NaCl as a background electrolyte. Cd *K* edge (26711 eV) X-ray absorption spectra were collected in a fluorescence mode using a Lytle detector filled with Kr gas, with Ag filter and Al foils in front of the detector to reject noise. EXAFS samples were loaded and sealed in plastic sample cells with Kapton tape windows in a N_2/H_2 glove box at SSRL and were placed in a sample holder with a He atmosphere with He continuously purged through the sample holder during the XAS data collection. The ion chamber detectors were filled with Ar gas. The beam current ranged 80-100 mA. Cd EXAFS patterns of reference compounds of possible Cd phases were also obtained. Solid model compounds were diluted with boron nitride to minimize self absorption.

Pre-edge background removal of the experimental EXAFS data was performed using EXAFSPAK (George and Pickering, 2000). Spline fitting was performed for the data reduction

of the EXAFS spectra using IFEFFIT code (Newville, 2001). The background-subtracted experimental EXAFS was fitted using OPT, the sub-program of EXAFSPAK with a non-linear least squares fitting algorithm. The amplitude and phase function for each path used for the fitting were obtained from theoretical calculations using Feff code (Ankudinov et al., 2002).

XRD analysis. Cd(II) sorption experiments were performed using 15 mL polypropylene centrifuge tubes. To each tube, FeS suspensions were added to obtain the final FeS concentration of 2 g/L. Then, $CdCl_2$ stock solutions were added into the centrifuge tubes containing FeS suspensions to obtain the final Cd(II) concentration of 0.015 M. The pH was adjusted to a range between 4 to 11, using HCl and NaOH solutions. Total chloride concentration (Cl_T) was maintained at 0.2 M. Finally, deoxygenated water was added into the centrifuge tubes to adjust the total solution volume to 10 mL. Thus, the resultant molar ratio of $Cd_0/[FeS]_0$ investigated was about 0.66. The reaction batches were equilibrated for 48 h on a LabQuake shaker (LabIndustries, Berkeley, CA) at 25°C.

At the end of reaction time, a portion of the supernatants was syringe-filtered using 0.2 μm polypropylene filter (Whatman). The filtrates were acidified with 10% (wt./wt.) nitric acid. Dissolved Cd in the acidified solutions were measured by inductively coupled plasma coupled with mass spectrometry (ICP-MS, Perkin-Elmer). Portions of the reacted mixtures were freeze-dried and analyzed for X-ray diffraction (XRD) to identify crystalline reaction products. The diffraction patterns were obtained from a Rigaku 12 kW rotating anode generator at 40 kV and 100 mV with Cu-K_α radiation. Diffraction data were collected in the range of $10^o < 2\theta < 70^o$ at a rate of 0.02^o 2θ per sec.

Results and Discussion

The EXAFS analysis results for model compounds and samples are presented in Tables 1.6 and 1.7 and Figures 1.12 - 1.14. Cd stock solution prepared by dissolving $CdCl_2(s)$ had strong backscattering from Cl, indicating that the cadmium chloride soluble complexes are dominant form of Cd in the stock solution. Cd EXAFS data as well as corresponding Fourier transforms of CdS(*s*) and $Cd(OH)_2(s)$ had features distinct from those of Cd stock solution (Figure 1.12). The structural parameters extracted from EXAFS data analysis show distinct first shell coordination environments (Table 1.6). The EXAFS results from Cd loaded mackinawite samples suggest that the Cd forms a sulfide species upon reaction with mackinawite over the whole range of pH and Cd loading conditions (Table 1.7). Unlike the redox-sensitive As(III), XANES show no sign

Table 1.6. Structural parameters of model compounds extracted from Cd EXAFS data (*CN*: coordination number, *R*: inter-atomic distance, σ^2: Debye-Waller factor).

Samples	Description	Path	*CN*	*R*(Å)	σ^2
Cd stock solution	0.024 mol/L Cd aqueous solution prepared using $CdCl_2(s)$	Cd–Cl	6.7	2.407	0.0131
$Cd(OH)_2(s)$	Cadmium hydroxide solid phase	Cd–O	5.3	2.278	0.0066
		Cd-Cd	5.3	3.488	0.0087
CdS(*s*)	Cadmium sulfide solid phase	Cd–S	4	2.517	0.0045

Table 1.7. Structural parameters of Cd sorbed by synthetic mackinawite extracted from Cd EXAFS data (*CN*: coordination number, *R*: inter-atomic distance, σ^2: Debye-Waller factor).

Samples	Conditions	Path	*CN*	*R*(Å)	σ^2
pH 5-H	ΣCd = 0.025 M, pH = 5.0 *I* = 0.2 M NaCl, 10 g/L mackinawite	Cd–S	3.4	2.507	0.0043
pH 7-H	ΣCd = 0.025 M, pH = 6.9 *I* = 0.2 M NaCl, 10 g/L mackinawite	Cd–S	3.0	2.509	0.0055
pH 10-H	ΣCd = 0.025 M, pH = 10.2 *I* = 0.2M NaCl, 10 g/L mackinawite	Cd–S	3.1	2.508	0.0057
pH 5-L	ΣCd = 10^{-4} M, pH = 5.7 *I* = 0.01 M NaCl, 1 g/L mackinawite	Cd–S	4.4	2.511	0.0052
pH 10-L	ΣCd = 10^{-4} M, pH = 9.9 *I* = 0.2 M NaCl, 1 g/L mackinawite	Cd–S	4.3	2.511	0.0054

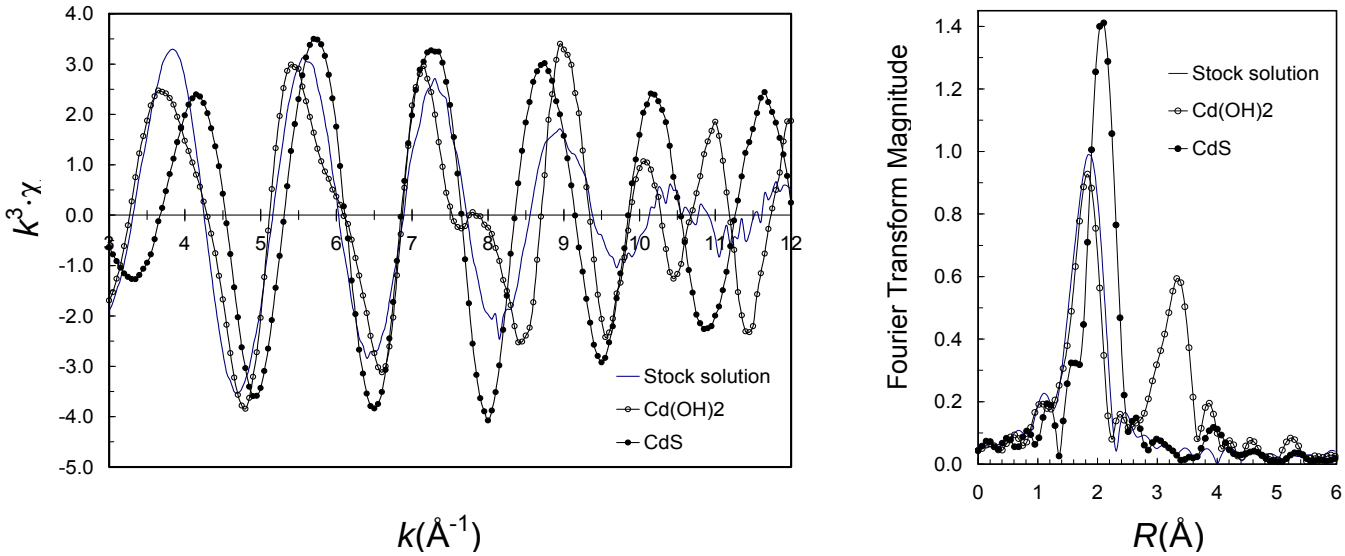

Figure 1.12. EXAFS data and corresponding Fourier transforms of Cd model compounds.

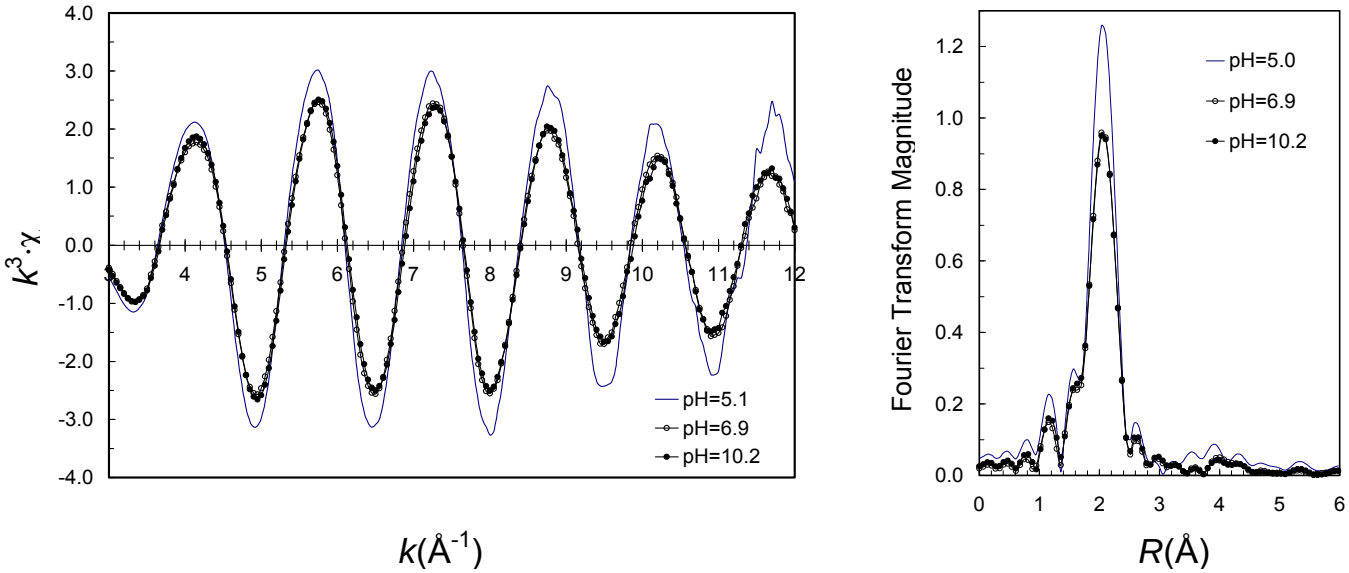

Figure 1.13. EXAFS data and corresponding Fourier transforms of Cd loaded on mackinawite under different pH conditions: ΣCd = 0.025M, I = 0.2M NaCl, 10 g/L mackinawite.

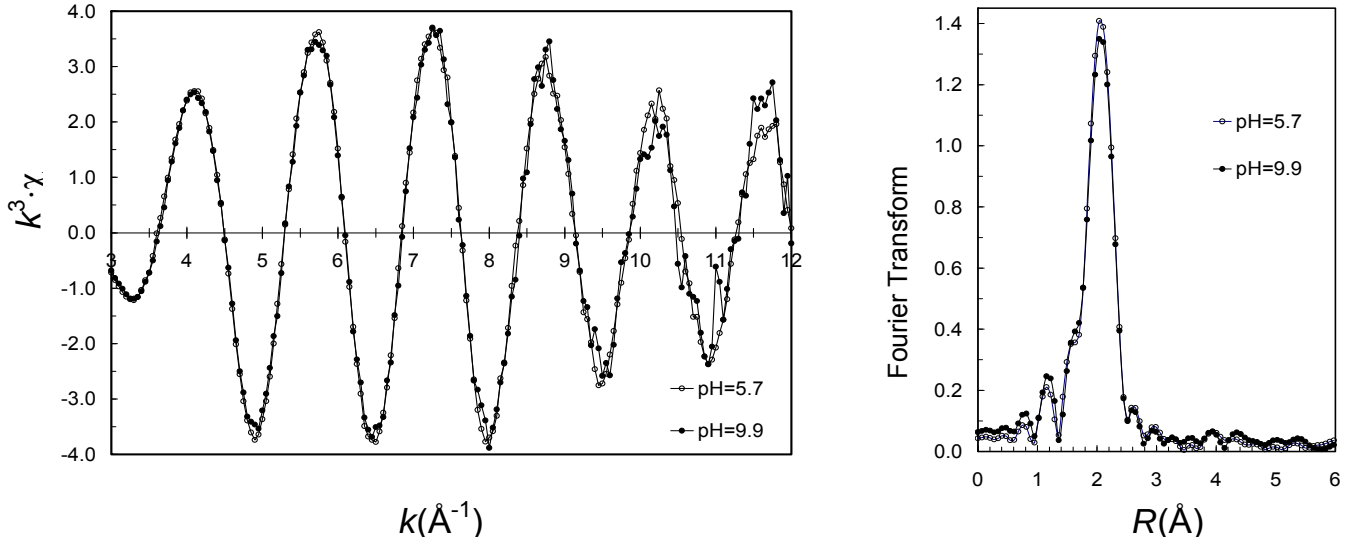

Figure 1.14. EXAFS data and corresponding Fourier transforms of Cd loaded on mackinawite under different pH conditions: ΣCd = 10^{-4} M, I = 0.01M NaCl, 1 g/L mackinawite, dry powder sample.

of reduction of Cd(II) upon reaction with mackinawite suspension. No second shell features are distinct in the EXAFS patterns or their Fourier transforms. The first shell inter-atomic distance values (2.507 – 2.511 Å) matches well with the value from the CdS(s) model compound (2.517 Å). The coordination number ranges from 3.0 to 3.4 for 0.025 M Cd loaded on 10 g/L mackinawite and 4.3 – 4.4 for 10^{-4} M Cd on 1 g/L mackinawite. The first shell of the Fourier transform of Cd EXAFS from pH 5.0 sample is notably stronger than those from pH 6.9 or 10.2

(Figure 1.13), implying the presence of a different cadmium sulfide phase. However, more detailed study using supplementary analytical tools such as XRD will be needed to confirm this hypothesis. Nevertheless, the EXAFS analysis indicates that over a wide range of pH and Cd concentration, cadmium sulfide formation is the dominant Cd removal mechanism by the iron sulfide mineral (Figures 1.13 and 1.14).

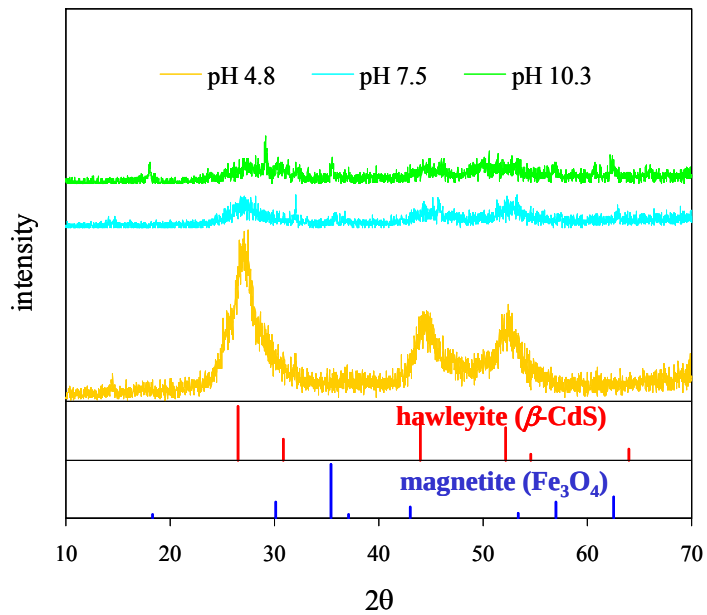

Figure 1.15. XRD characterization of Cd reacted with FeS vs. pH.

XRD results for Cd(II) 0.015 M reacted at pH 4.8, 7.5, and 10.3 with 2 g/L FeS are shown in Figure 1.15. As shown, at the lowest pH, the formation of β-CdS is evident. As pH increases, the signal for β-CdS become less sharp, suggesting that less amounts of crystalline CdS phase are being formed. Interestingly, at the highest pH, there also appears to be evidence of the formation of magnetite as an oxidation product of the exchange of Cd for Fe in FeS. This is consistent with what has been postulated for As(III)/FeS systems at higher pH. Taken together with the XAS results, in which Cd-S coordination predominates at all pH values and at high and low Cd/FeS loadings, indicates that the primary removal mechanism is likely the formation of CdS bulk precipitates at low pH and less crystalline surface precipitates at the higher pH values. In contrast with As(III), it appears that the surface precipitation of CdS does not limit Cd(II) removal in that even at high loading, Cd(II) is quantitatively removed from solution. This suggests that the CdS precipitates or surface phases that form at high pH do not inhibit Cd(II) from effectively accessing sulfide from the FeS particles. Additional work is need (e.g., TEM with elemental mapping) to determine whether CdS particles are homogenously distributed with FeS or form bulk precipitates unassociated with FeS across the pH range of 5 - 10.

<u>Summary and Conclusions and Implications for Future Research/Implementation</u>

Based on XAS analysis of Cd(II) solid phase reaction products upon reaction with FeS, Cd(II) uptake appears result from the precipitation of a Cd-S solid phases or surface associations over a wide range in pH (5-10) and Cd(II) loading (10^{-4} – 2.5×10^{-2} M). XRD results at the higher

loadings indicate that crystalline CdS(s) forms near pH 5, but that less crystalline forms result as pH increases to 10. Given that the quantitatively removal of Cd(II) to below its MCL of 5 ppb occurs over the entire pH range (5-10), suggests that Cd(II) can effectively exchange for Fe(II) in FeS even under the higher pH conditions in which Fe(II) is relatively insoluble. These results indicate the potential favorability of removing Cd(II) by nanoscale FeS in PRB applications by the formation of CdS over a wide range of pH.

Literature Cited

Ankudinov, A.L., B. Ravel, J.J. Rehr, and S.D. Conradson, 1998. FEFF8. *Phys. Rev. B*, 7565-7576.

Bostick, B.C., S. Fendorf, and M. Fendorf, 2000. Disulfide disproportionation and CdS formation upon cadmium sorption on FeS_2, *Geochim. Cosmochim. Acta* **64**, 247-255.

Erdem, M., A. Özverdi, 2006. Kinetics and thermodynamics of Cd(II) adsorption onto pyrite and synthetic iron sulphide. *Separation and Purification Technology* **51**, 240-246.

George, G.N., I.J. Pickering, EXAFSPAK, Stanford Synchrotron Radiation Laboratory, Stanford Linear Accelerator Center, Menlo Park, 2000.

Jean, G.E., G.M. Bancroft, 1986. Heavy-metal adsorption by sulfide mineral surfaces. *Geochim. Cosmochim. Acta* **50**, 1455-1463.

Kornicker, W.A., J.W. Morse, 1991. Interactions of divalent-cations with the surface of pyrite. *Geochim. Cosmochim. Acta* **55**, 2159-2171.

Newville, M., 2001. IFEFFIT: interactive XAFS analysis and FEFF fitting. J *J. Synchrotron Rad.* **8**, 322-324.

Substask 1.3.c. Uptake mechanism of As(III) by FeS-coated sand

Objective

The overarching goal of this subtask was to assess the uptake mechanisms of As(III) by FeS-coated sand by characterization of the solid phase reaction products.

Background

As previously noted (Subtask 1.2), nanoscale FeS has excellent capacity for removal of As(III) and Cd(II) and can be utilized for groundwater treatment via colloidal injection, however, it was desired in this project to also develop an *FeS* material for emplacement in a trench-and-fill constructed PRB (e.g., see Task 4). For this purpose, FeS-coated sand was produced. To determine if FeS-coated sand retained similar reactivity and removal mechanisms to nanoscale FeS particles, this task was devoted to characterizing the reaction products of As(III) reacted with FeS-coated sand. Previous work summarized in Subtask 1.3.a on the mechanism on As(III) uptake by nanoscale FeS as a function of pH showed that at pH 5 As(III) uptake was primarily controlled by precipitation of realgar, AsS(s), while at higher pH (e.g., pH 7 and 9) adsorption and/or surface precipitation of thioarsenite species was the primary removal mechanism. In this subtask, the solid phase products of the reaction of As(III) by FeS-coated sand at as a function of pH were identified using XAS and XPS analyses.

Materials and Methods

For this study 416 g/L of FeS-coated sand (equivalent to 0.5 g/L FeS) were reacted with a 1.33×10^{-3} M As(III) solution in 50 mL polypropylene tubes and mixed by an end-over-end rotating mixer for 2 days. Since the pH measurement of this system could not monitored continuously due to the small reactor volume, multiple samples were prepared and titrated with various amounts of acid (HCl) or base (NaOH) previously found to give pH values bracketing pH 5 or 9. After 2 days-equilibrium time, the samples that gave pH 5 or 9 within 0.1 pH unit were selected for the XAS or XPS analysis. The samples for XAS analyses were filtered using 0.22 µm nylon filters. For XAS analysis, the filtered particle paste was then transferred into an airtight, crimp-sealed serum bottle without drying and shipped to Stanford Synchrotron Radiation Laboratory (SSRL). For XPS analysis, the filtered sample was freeze-dried, crimp-sealed and stored in an anaerobic chamber until analyzed.

XAS analysis. Samples for XAS were prepared inside an anaerobic chamver by applying wet sample pastes into a sample cell sealed on both sides with a double layer of Kapton tape. Arsenic K-edge XAS spectra were collected at SSRL on beamline 10-2 (3 GeV, ~100 mA of maximum current) with an unfocused beam using a Si(220) double-crystal monochromator with a 13-element solid-state Ge fluorescence detector or Lytle detector. Initially samples all samples were collected at room temperature. Since the initial scans for As(III) reacted at pH 9 with FeS-coated sand samples showed evidence of beam induced oxidation based on the continuous shifting of the absorption edge to higher EV with each successive scan, this sample was re-collected using a liquid N_2 cryostat, which eliminated the beam induced oxidation. To avoid exposure of the samples to oxygen when changing samples, a special anoxic sample holder filled with inert N_2 gas was used to transfer the sample cells from the anaerobic chamber to the

beamline detector. While in the detector, the sample cell holder allowed the samples to be contiuously purged with He gas. Based on comparison of multiple scans, no evidence of oxidation from exposure to air was observed during data collection. XAS spectra were also collected for the model compounds grey metallic arsenic As(0), amorphous AsS, amorphous As_2S_3, dissolved As(III) (from $NaAsO_2$), and dissolved As(V) (from $Na_2HAsO_4{\cdot}7H_2O$).

The XAS spectra were analyzed using SixPACK (Webb, 2002). Mulitple spectral scans were first averaged, and then the background absorbance was removed by subtracting a linear fit of the pre-edge region. X-ray absorption near-edge structure (XANES) (e.g., from 11,860−11,890 eV) were obtained by normalizing the fluorescence signal to the edge jump height. The inflection points of the XANES spectra were determined by taking the first derivative of the absorption edge and used to assess the oxidation state of arsenic in the samples by comparison to the inflection point edge energies of reference model compounds. Extended x-ray absorption fine structure (EXAFS) of the XAS spectra were obtained by fitting a quadratic spline function above the edge. EXAFS spectra were normalized using a Victoreen polynomial function and then transformed from energy (eV) to k space ($Å^{-1}$) using E_0 = 11,885 eV. The resultant EXAFS functions ($\chi(k)$) were weighted by k^3 to amplify the higher k region, and then Fourier-transformed to produce radial structural functions (RSF) in R space over k=3.5−11.5 $Å^{-1}$.

Structural parameters were obtained by fitting k^3-weighted EXAFS functions with the phase and amplitude functions derived from FEFF 8 (Ankudinov et al., 1998). The amplitude-reduction factor (S_o^2 = 0.92) was optimized from the fitting of the model compound spectra and kept constant for all EXAFS analysis. The Debye-Waller factors (σ^2) were also fixed based on the similarity between the sample spectra and the model compound spectra or the optimization among the sample spectra to reduce the degree of freedom during the fitting. Coordination number (N), interatomic distance (R), and energy shift (ΔE_0) were allowed to vary. The optimal fitting was obtained by minimizing the goodness of fit parameter (R_f).

XPS Analysis. For XPS scanning, the reference model compounds and As(III) reacted samples were mounted on a sample bar in an anaerobic glove box and transferred using an air-tight container filled with N_2/H_2 gas to minimize exposure of the sample surfaces to atmospheric oxygen. The Al-K_α line (1486.6 eV) was used as radiation source. Survey spectra were obtained with an analyzer pass energy of 160 eV. Narrow XPS scan peaks were obtained for the model compounds with a pass energy 20 eV, however, for the As(III)-reacted FeS-coated sand samples, a higher pass energy of 160 eV was needed due as a result of the limited signal due to the low As quantities of As on FeS-coated sand. While the higher pass energy are often used for qualitative comparison of peak positions to model compounds, quantitative peak analyses is less accurate and should be viewed with caution due to the peak broadening that occurs. Energies were corrected for charging effects using the reference peaks of adventitious carbon C l*s* with a binding energy of 284.6 eV. Raw spectra were smoothed before being fitted using a Shirley base line and a Gaussian-Lorentzian peak shape. To estimate the standard deviation of each of the component's contribution to the overall XPS spectrum in the fitting procedure, Monte-Carlo analysis (CasaXPS software) was applied. The program applied artificial noise to a spectrum and calculated an error matrix to give the variance of each fit based on the fitting constraints used.

Results and Discussion

For the solid phase product characterization, a 1.33×10^{-3} M As(III) solution was reacted with FeS-coated sand 416 g/L (equivalent to 0.5 g/L FeS) at pH 5 and 9. The FeS coated sand

removed 63% of the initial As(III) from solution at pH 5 while at pH 9 the amount was only about 23% of the initial arsenic. These systems were prepared at an inital molar ratio of As:Fe of approximately 0.23 which is approximately 20 times the molar ratio of samples prepared for spectroscopic characterization of reaction products for nanoscale FeS at pH 5 and 9. This was necessary given the limitations on the amount of iron sulfide that could be loaded into the reaction vessel as a coating on sand (e.g., 416 g/L of sand containing 0.5 g/L of FeS and significantly higher concentrations of sand in a batch reactor become impractical for uniform mixing) and the need to maximize the amount of As per gram of solid (FeS + sand) to get above the detection limits of the spectroscopic.

XAS spectra were collected from the reacted solid phase of the As(III)-FeS-coated sand samples prepared at pH 5 and 9. XANES and EXAFS analyses of the spectra were used to identify the solid phase reaction products. While the oxidation state of arsenic can be obtained from XANES analysis, EXAFS analysis is required to determine the structural parameters such as interatomic distance (*R*) and coordination number (*N*). The XANES spectra of the samples are compared with those of model compounds in Figure 1.16. Higher edge energy is indicative

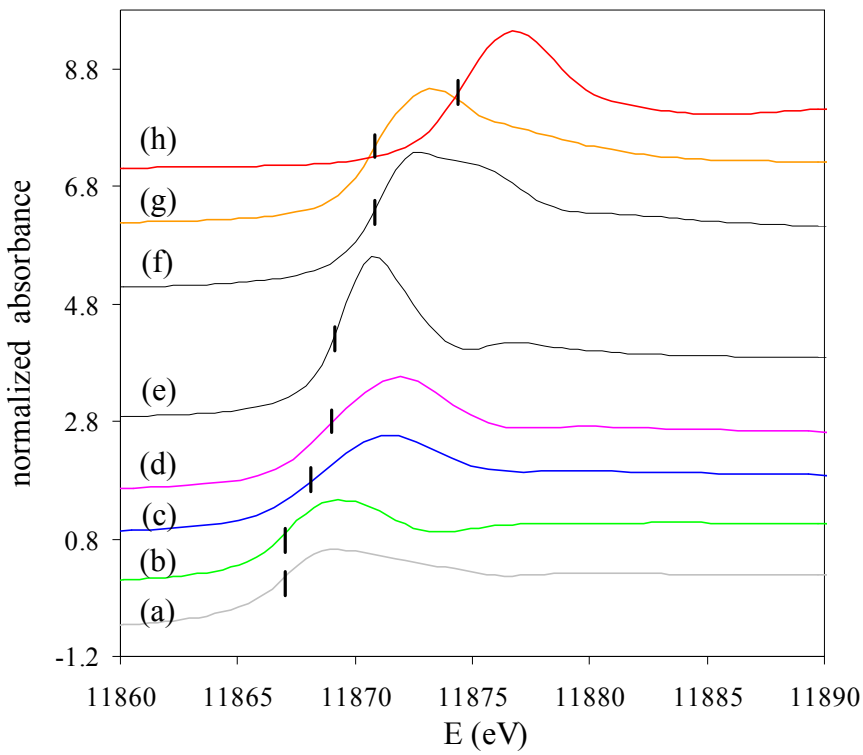

Figure 1.16. Arsenic K-edge XANES spectra for FeS-coated sand reacted with at pH 5 (e) and pH 9 (f), which are enveloped by reference compounds: aqueous As(V) (h), aqueous As(III) (g), disordered As_2S_3 (d), disordered AsS (c), arsenopyrite (b), and As(0) (a). The mark on the absorption edges corresponds to the first derivative maxima of XANES spectra.

The EXAFS spectra and corresponding Fourier transforms for samples and model compounds are compared in Figure 1.17 with the fitted results presented in Table 1.8. For the FeS-coated sand system, the first coordination shell around As at pH 5 is characterized by the As-S

interaction with the coordination number ($N_{As\text{-}S}$) of 2.9 at a distance of 2.26 Å, in good agreement with that of the As_2S_3 model compound ($N_{As\text{-}S}$ = 3.0 at 2.28 Å). Also, both FeS-coated sand sample and the As_2S_3 model compound show very weak second coordination shells ($N_{As\text{-}As}$ = 0.31 at 3.66 Å for the FeS-coated sand system and $N_{As\text{-}As}$ = 0.37 at 3.54 Å for the As_2S_3 model compound) indicating a disordered structure. Consistent with the XANES, the EXAFS analysis of the pH 5 sample indicates the formation of As_2S_3. In the case of pH 9, EXAFS analysis of the reacted FeS-coated sand indicates an As-O coordination with a coordination number ($N_{As\text{-}O}$) of 2.9 at a distance of 1.78 Å. This agrees well with the structure of aqueous As(III) reference solution ($N_{As\text{-}O}$ = 3.0 at 1.76 Å). This agrees well with the XANES, and indicates the adsorption of arsenite species to the FeS-coated sand surface at pH 9. As mentioned above, this differs from the nanoscale FeS reacted with As(III), which showed thioarsenite surface species formation at pH 9. It is possible that at pH 9, the iron oxides such as magnetite that form on the sand surface during the coating process, preferentially sorbed As(III). Given that coated sand had a greater amount of iron oxide surface functional groups exposed at the surface compared to nanoscale FeS as noted from the XPS analyses reported in Subtask 1.2 and the higher As:Fe molar ratio of this system, this could account for the difference in sorption mechanism at pH 9 between the coated sand and nanoscale FeS. Adsorption of As(III) to an iron

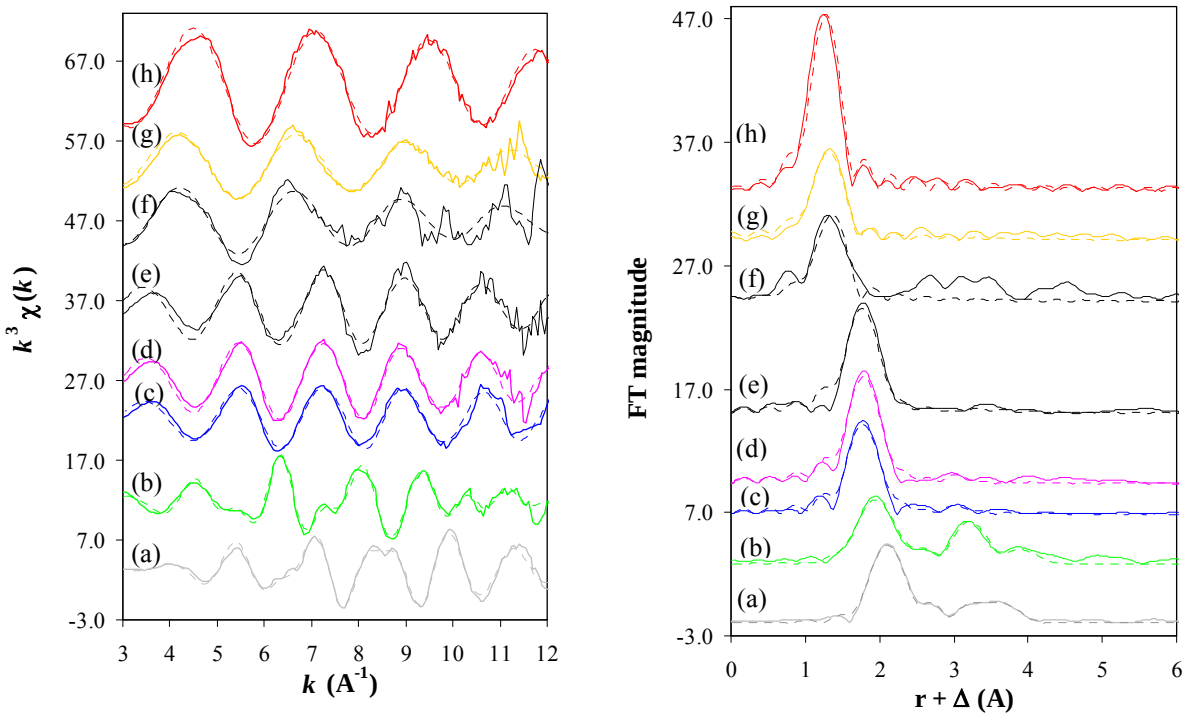

Figure 1.17. k^3-weighted arsenic K-edge EXAFS spectra ($k^3\chi(k)$) (**Left**) and corresponding Fourier transforms (**right**) for FeS-coated samples and reference compounds. Solid lines are the experimental data; dashed lines are the numerical fits. The 416 g/L FeS-coated sand reacted with 1.33×10^{-3} M As(III) at pH 5 (e) and pH 9 (f), which are enveloped by reference compounds: aqueous As(V) (h), aqueous As(III) (g), disordered As_2S_3 (d), disordered AsS (c), arsenopyrite (b), and As(0) (a).

Table 1.8. EXAFS fit results for pH 5 and 9 FeS-coated sand As reacted samples and As reference model compounds.

		EXAFS fit*			Crystallographic data		
	Pair	*N*	*R*(Å)	σ^2(Å^2)	*N*	*R*(Å)	Reference
As(0)	As-As	1.1	2.50	0.0058†	3	2.50	O`Day et al. (2004)
	As-As				3	3.13	
		ΔE_0 = -6.95 eV, R_f = 0.065					
AsS	As-S	2.0	2.26	0.003†	2	2.24	Farquhar et al. (2002)
	As-As				1	2.57	
	As-As	0.41	3.50	0.006†	2.5	3.44-3.51	
	As-S				1	3.41-3.52	
		ΔE_0 = -9.80 eV, R_f = 0.061					
As_2S_3	As-S	3.0	2.28	0.0045†	3	2.24-2.31	Farquhar et al. (2002)
	As-As	0.37	3.54	0.006†	1	3.19	
	As-S				3	3.22-3.57	
	As-As				2.5	3.52-3.64	
		ΔE_0 = -7.75 eV, R_f = 0.047					
pH 5	As-S	2.9	2.26	0.0045†			
	As-As	0.31	3.66	0.006†			
		ΔE_0 = -10.09 eV, R_f = 0.0974					
pH 9	As(III)-O	2.88	1.78	0.0045†			
		ΔE_0 =-2.78 eV, R_f = 0.2119					
$As(III)_{aq}$	As(III)-O	3.0	1.76	0.0045†	3‡	1.78‡	Wolthers et al. (2005)
		ΔE_0 = -7.90 eV, R_f = 0.069					
$As(V)_{aq}$	As(V)-O	4.0	1.69	0.0025†	4‡	1.69‡	Yamauchi and Fowler (1994)
		ΔE_0 = -5.01 eV, R_f = 0.024					

*The amplitude-reduction factor (S_o^2) was set at 0.92.
†The Debye-Waller factors (σ^2) were fixed during the numerical fit.
‡Structural data was obtained from EXAFS analysis.

oxide coating on the surface is also favored near pH 9, as mentioned below in Subtask 1.4.c.

XPS spectra for As(III) reacted with FeS-coated sand at pH 5 and 9 are shown in Figures 1.18 and Table 1.9. Table 1.10 shows the model fitting parameters used to fit the sample data.

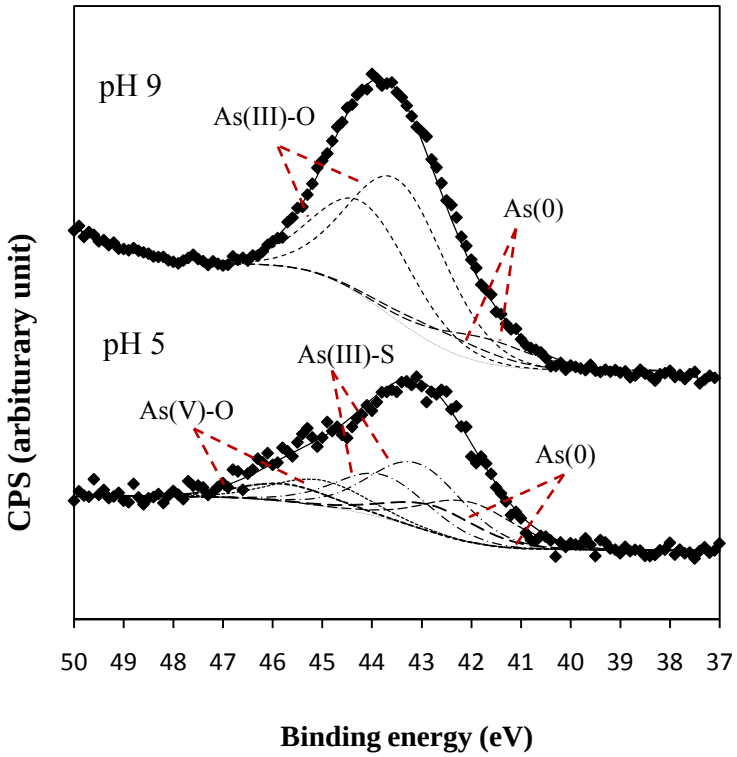

Figure 1.18. XPS As 3d peak spectra for As(III) reacted with FeS coated sand at pH 5 and 9 using a high pass energy of 160 eV.

Table 1.9. Fitting parameters for XPS As 3d for arsenic reference compounds.

	As 3d $_{3/2}$ (eV)	FWHM (pass energy 20 eV)	FWHM (pass energy 160 eV)	Component
As(0)	41.6	1	2.2	As-As
AsS	42.8	1	2.2	As(II)-S
As_2S_3	43.2	1	2.2	As(III)-S
$NaAsO_2$	43.6	1	2.2	As(III)-O
$Na_2HAsO_47H_2O$	44.5	1	2.2	As(V)-O

For quantitative analysis of XPS data the low pass enery 20 eV is most widely used, but due to the low arsenic loading on the FeS-coated sand samples, a pass enery 160 eV was applied. This was done to acquire a higher As 3d peak intensity, but with the trade-off of lower resolution spectra. At pH 5, the XPS analysis indicates that the solid phase reaction product is primarily As(III)-S which is consistent with the formation of orpiment. The presence of As(V)-O suggests some oxidation of the sample may have occurred during the drying for XPS analysis. At pH 9,

the results indicate the presence of primarily As(III)-O on the FeS-coated sand surface suggesting arsenite adsorption. These results support those obtained from the XAS analysis.

Table 1.10. XPS fits showing relative contributions of As species in spectra.

Sample	BE	FWHM	Species	% area with error
pH 5 FeS-coated sand	42.0	2.2	As(0)	30.72 ± 25.2
	43.1	2.2	As(III)-S	49.5 ± 22.5
	45.1	2.2	As(V)-O	19.8 ± 4.7
pH 9 FeS-coated sand	41.8	2.2	As(0)	15.01 ± 18.9
	43.5	2.2	As(III)-O	84.99 ± 18.5

Summary and Conclusions and Implications for Future Research/Implementation

The results of XAS and XPS confirm the mechanism of As(III) removal by FeS coated sand, with removal at pH 5 primarily a result of the precipitation of orpiment, and by the adsorption of arsenite at pH 9. Differences between these results and those for nanoscale FeS are thought to be due to either: (1) the higher As:Fe required in the FeS-coated sand to obtain enough signal to perform the As XAS or XPS analysis, and/or (2) due to the coating process which may leave the surface partially coated with a magnetite-like iron oxide that controls As removal at pH 9 and leaves the system less reducing at pH 5 so that orpiment instead of the more reduced realgar prevails. The implication of these results is, however, that FeS-coated sand still maintains the same primary removal processes (arsenic sulfide preciptation at lower pH and adsorption at higher pH). Future work is needed to better assess the impact of As:Fe loading ratios on the removal mechanism. Nonetheless, the results of this work, allow for a more accurate depiction of the main reaction processes that remove arsenic by FeS-coated sand. This mechanistic information was needed and has been used to develop a reactive transport model for PRB design as discussed in Task 5 later on in this report.

Literature Cited

Ankudinov, A.L., B. Ravel, J.J. Rehr, and S.D. Conradson, 1998. FEFF8. *Phys. Rev. B*, 7565-7576.

Farquhar, M.L., J.M. Charnock, R.R. Livens, and D.J. Vaughan, 2002. Mechanisms of arsenic uptake from aqueous solution by interaction with goethite, lepidocrocite, mackinawite, and pyrite: an x-ray absorption spectroscopy study. *Environ. Sci. Tech*nol. ***36***, 1757-1762.

Gallegos, T. J., S.P. Hyun, K.F. Hayes, 2007. Spectroscopic investigation of the uptake of arsenite from solution by synthetic mackinawite. *Environ. Sci. Technol.* **41**, 7781-7786.

Gu, ZM, J. Fang, and B. L. Deng,. 2005. Preparation and evaluation of GAC-based iron-containing adsorbents for arsenic removal. *Environ. Sci. Technol*. **39**, 3833-3843.

O'Day, P.A., D. Vlassopoulos, R. Root, and N. Rivera, 2004. The influence of sulfur and iron on dissolved arsenic concentrations in the shallow subsurface under changing redox conditions. *Proc. Natl. Acad. Sci. USA* ***101***, 13703-13708.

Roberts, L.C., S.J. Hug, and T. Ruettimann, et al. 2004. Arsenic removal with iron(II) and iron(III) waters with high silicate and phosphate concentrations," *Environ. Sci. Technol*. **38**, 307-315.

Webb, S. M., 2002. Sam's Interface for XAS Package (SixPACK). Stanford Synchrotron Radiation Laboratory.

Wolthers, M., L. Charlet, C.H. van der Weijden, C.H. P.R. van der Linde, and D. Rickard, 2005. Arsenic mobility in the ambient sulfidic environment: sorption of arsenic(V) and arsenic(III) onto disordered mackinawite. *Geochim. Cosmochim. Acta* ***69***, 3483-3492.

Yamauchi, H., B.A. Fowler, 1994. In *Arsenic in the Environment*. Nriagu, J.O., Ed., Wiley: New York, pp. 35-53.

Subtask 1.4. Sorption Behavior of As and Cd by Nanoscale FeS and FeS-Coated Sand

Substask 1.4.a. Impact of solution conditions on As(III) uptake by nanoscale FeS

Objective

The overarching goal of this subtask was to assess the impact of changing solution conditions (pH and FeS concentration) on As(III) uptake by nanoscale FeS.

Background

Iron sulfides such as pyrite (Zouboulis et al., 1993; Farquhar et al., 1993; Bostick and Fendorf, 2003), troilite (Bostick and Fendorf, 2003) and freshly precipitated mackinawite (Farquhar et al., 1993; Wolthers et al., 2002) have shown promise in sequestering dissolved As(III) under reducing conditions (Jong and Parry, 2004; Morse and Arakaki, 1993; Kornicker, and Morse, 1991). Discrepancies exist, however, regarding optimum removal conditions and uptake mechanisms. The solution pH for optimum removal of As(III) by disordered mackinawite has been reported at neutral pH (Wolthers et al., 2005). However, the uptake of arsenite by stable iron sulfides, such as troilite and pyrite, appears most favorable under alkaline conditions and results in the formation of arsenopyrite, iron disulfide and ferric hydroxide (Bostick and Fendorf, 2003. Farquhar et al. found that arsenic uptake by freshly-precipitated mackinawite varied considerably as a function of arsenic concentration with the formation of both a four-oxygen coordinated sorbed species as well as co-precipitated orpiment (As_2S_3) (Farquhar et al., 1993). However, in natural shallow aquifer sediments, in which aged mineral phases typically exist, realgar was identified as the primary arsenic-bearing phase (O'Day et al., 2004). Our mechanistic work in this project has shown that the reaction products formed by interaction of synthetic mackinawite with As(III) produce a discrete realgar precipitate upon reaction of mackinawite, whereby As(III) was reduced (Gallegos et al., 2007). At high pH and low As(III) concentrations, reductive precipitation is thought to be minimal in comparison to As-O bonding thought to be either due to an arsenite or a thioarsenite surface complex (Gallegos et al., 2007). In aqueous solutions, the speciation of arsenite in the presence of sulfur may result in thioarsenite (Bostick et al., 2005; Wilkin et al., 2003; Eary, 1992) or thioarsenate (Stauder et al., 2005) species (Helz andTossell, 2008; Beak et al., 2008) although the identity and thermodynamic formation reaction constants of these species are not fully resolved. Given the many factors that can influence arsenite uptake in iron sulfide systems, in this study, a comprehensive set of macroscopic data were collected to determine the effects of pH and mackinawite solid/solution ratio on uptake of arsenic.

Materials and Methods

Arsenite uptake studies were conducted under strict anoxic conditions inside an anaerobic chamber with an atmosphere of 95% N_2 and 5% H_2. De-oxygenated water was prepared by bubbling deionized (DI) water (18 MΩ·cm) obtained from a Millipore Milli-Q system with 99.99% N_2 gas for two hours and was used to prepare all solutions. Reagent grade chemicals including: $FeCl_2{\cdot}4H_2O$, $Na_2S{\cdot}9H_2O$, HCl, NaOH, HNO_3, NaCl, and $NaAsO_2$, were obtained from

Sigma-Aldrich, St. Louis, MO. Mackinawite synthesis was performed as described previously (Gallegos et al., 2007).

The pH edge experiments, in which As(III) uptake was measured as a function of pH, were conducted in a 0.015 M NaCl background electrolyte in 15 mL polyethylene reactor tubes at an ambient temperature of 27.5° C. Each reactor tube was spiked with varying amounts of 0.01 M NaOH or 0.1 M HCl to achieve a final pH value ranging from 5 to 10. A mackinawite stock suspension was then added to achieve a solid/solution ratio ranging from 0.1 to 40 g FeS/L. Some mackinawite dissolution was evident; however, a solid was present in all batch reactors. Subsequently, a $NaAsO_2$ stock solution (1.3×10^{-3} M) was added to each reactor tube to achieve an initial As(III) concentration of 1.3×10^{-5} M in all samples. The reactor tubes were equilibrated on an end-over-end rotating mixer until the pH oscillated within 0.1 unit (around 96 hours). At the end of the reaction period, the equilibrium pH of the samples was measured using an Accumet calomel reference polypropylene combination electrode (Cole Parmer Instrument Company, Vernon Hills, Illinois). All samples were filtered through a 0.1 μm nylon syringe filter to remove solids. The clear filtrates were then acidified to pH 2 with HNO_3 for analysis. Filtrates were analyzed for total dissolved arsenic using Optical Emission Spectroscopy (Optima 3300 DV ICP-OES; Perkin Elmer; USA). The ICP-OES analysis provided reproducible results above 2×10^{-7}M As. Batch experiments were conducted in duplicate or triplicate.

Total dissolved Fe concentration were measured after equilibrating 1.0 g FeS/L of mackinawite as a function of pH by varying the amounts of 1 or 0.1 N HCl or 0.01 M NaOH. Studies were conducted at background ionic strength values of 0.15 M NaCl. Measurements were conducted in the pH range of 4 to 11. The concentration of total soluble Fe was measured as total iron by Optical Emission Spectroscopy (Optima 3300 DV ICP-OES; Perkin Elmer; USA).

Results and Discussion

Figure 1.19 shows the measured pH edges for varying mackinawite solid/solution ratios for an initial As(III) concentration of 1.3×10^{-5} M (~1 mg/L). Arsenic pH edges are plotted as the percent of the total dissolved arsenic removed from a filtered solution as a function of pH. The pH edge data demonstrate a distinct change in pH edge shape as the As(III)-mackinawite system transitions from acidic to alkaline solution conditions. Complete removal of As(III) from solution by mackinawite is achieved below pH 6.5 for all mackinawite solid/solution ratios ranging from 0.1 to 40 g/L. A earlier section of this report has indicated that the dominant removal mechanism in this region is bulk precipitation of a realgar-like solid (see also Gallegos et al., 2008). Above pH 6.5, removal of As(III) depends on both mackinawite solid/solution ratio and pH. Under alkaline conditions, only at the higher mackinawite solid/solution ratio is all of the As(III) removed from solution. Bebié et al. (1998) consider that, under alkaline conditions, the dissolved metal (i.e., in this case iron) essentially coats the metal sulfide as an oxyhydroxide or hydroxide. Above pH 8.3, the removal resembled that of As(III) sorption onto iron oxides, which exhibits maximum sorption at the pK_{a1} for arsenite (pH = 9.2) (Raven et al., 1998; Goldberg and Johnston, 1998; Manning et al., 2002). Since both >SOH and >FeOH surface reactive functional groups have been hypothesized for iron sulfide surfaces (Bebié et al., 1998), it is not unreasonable to consider that arsenite removal from solution may be due, in part, to a ligand exchange sorption reaction with surface hydroxyl groups in this region. From the results

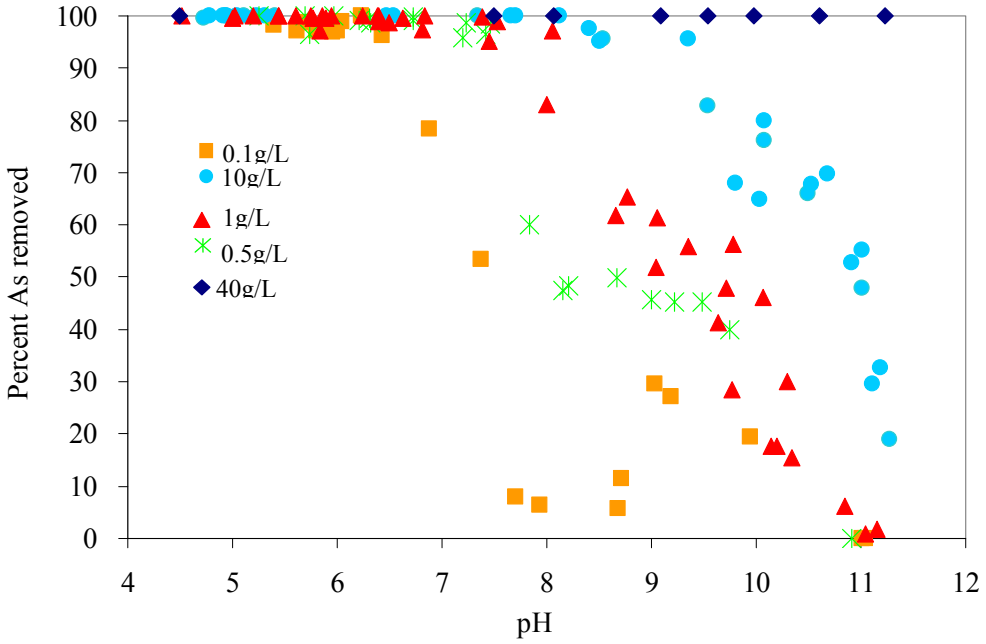

Figure 1.19. pH edges measured at varying solid FeS:solution ratios for initial As(III) concentration of 1.3×10^{-5} M (1 mg/L) and ionic strength of 0.015M.

of this project, when mackinawite was reacted with 5×10^{-5} M As(III), either a thioarsenite surface complex or an arsenite surface phase was postulated to form at pH 9 (Gallegos et al., 2007). However, when mackinawite is reacted with 5×10^{-4} M As(III) at pH 9, mackinawite dissolves in favor of iron oxides at higher pH and more dissolved sulfide became available to complex with arsenic to form realgar, either as a discrete bulk precipitate or on the surface of mackinawite (Gallegos et al., 2007). This suggests that removal at high pH may result from realgar precipitation and/or adsorption, depending on the ratio of arsenic to mackinawite. The removal trend as a function of pH is contrary to As(III) uptake behavior by other iron sulfides, viz., troilite and pyrite, in which little removal occurred below pH 5 and optimum removal occurred between pH 5 and 10 Bostick and Fendorf, 2003). Figure 1.20 shows the dissolved Fe concentration in the presence and absence of 1.3×10^{-5} M As as a function of pH. Because mackinawite is more soluble at low pH than these other iron sulfides, dissolved sulfide is available for precipitation of realgar. The slight increase in dissolved iron at low pH resulting from the addition of 1.3×10^{-5} M As(III) supports the consumption of sulfide by this mechanism.

<u>Summary and Conclusions and Implications for Future Research/Implementation</u>

As(III) uptake by FeS increases with decreasing pH. When nanoscale FeS is in sufficient excess (e.g., molar ratios of As(III)/FeS(s) approaching 10^{-5} for 40g/L FeS concentrations and 1.3×10^{-5} M total As(III)), 100% removal of As(III) is possible at all pH values. Nearly all of the sulfide in FeS is available for precipitation of AsS at lower pH (e.g., pH 6) where FeS solubility is higher and dissolution of FeS is favorable compared with surface limited adsorption and co-precipitation at higher pH. These results are consistent with the previous capacity measurement results that indicate the optimum removal of As(III) by nanoscale FeS occurs at pH values below

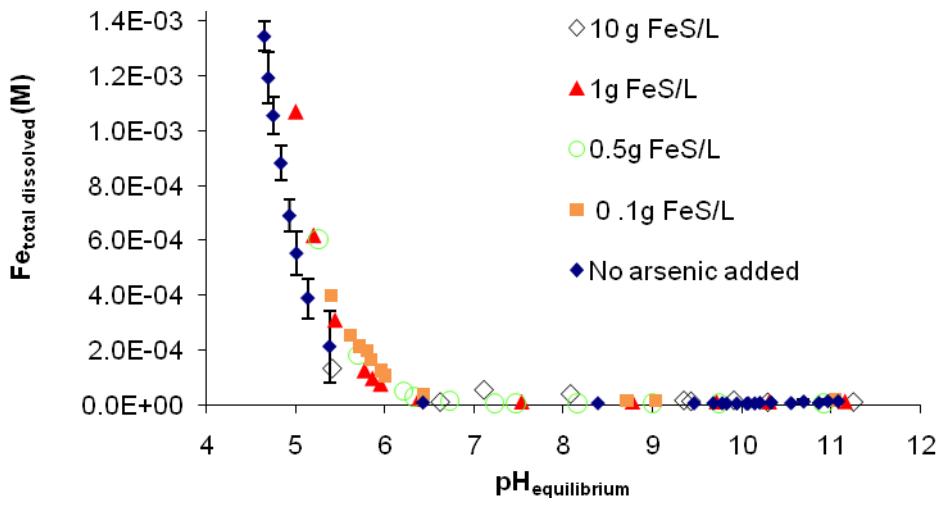

Figure 1.20. Total iron concentrations measured in 0.1, 0.5, 1, and 10 g/L FeS after equilibration with 1.3×10^{-5} M As(III) and in the absence of arsenite (1g/L system only).

7. Hence, in PRB applications, operating at below pH 7 will provide for better overall removal of arsenic by nanoscale FeS.

Literature Cited

Beak, D. G.; R. T. Wilkin, R. G. Ford, S. D. Kelly, 2008. Examination of arsenic speciation in sulfidic solutions using X-ray absorption spectroscopy. *Environ. Sci. Technol.* **42**, 1643-1650.

Bebie, J., M. A. A.Schoonen, M. Fuhrmann, D.R. Strongin, 1998. Surface charge development on transition metal sulfides: An electrokinetic study. *Geochim. Cosmochim. Acta* **62**, 633-642.

Bostick, B. C., S. Fendorf, 2003. Arsenite sorption on troilite (FeS) and pyrite (FeS2). *Geochim. Cosmochim. Acta* **67**, 909-921.

Bostick, B. C., S. Fendorf, G.E. Brown, 2005. In situ analysis of thioarsenite complexes in neutral to alkaline arsenic sulphide solutions. *Mineralogical Magazine* **69**, 781-795.

Eary, L. E., 1992. The Solubility of Amorphous As2S3 from 25 to 90-Degrees-C. *Geochim. Cosmochim. Acta* **56**, 2267-2280.

Farquhar, M. L., Charnock, J. M., Livens, F. R., Vaughan, D. J., 2002. Mechanisms of arsenic uptake from aqueous solution by interaction with goethite, lepidocrocite, mackinawite, and pyrite: An X-ray absorption spectroscopy study. *Environ. Sci. Technol.* **36**, 1757-1762.

Gallegos, T. J., S.P. Hyun, K.F. Hayes, 2007. Spectroscopic investigation of the uptake of arsenite from solution by synthetic mackinawite. *Environ. Sci. Technol.* **41**, 7781-7786.

Goldberg, S., C. T. Johnston, 2001. Mechanisms of arsenic adsorption on amorphous oxides evaluated using macroscopic measurements, vibrational spectroscopy, and surface complexation modeling. *J. of Coll. Interf. Sci.* **234**, 204-216.

Helz, G. R.; J. A. Tossell, 2008. Unique redox behaviors induced by polysulfide and sulfide; Arsenic the latest example. *Geochim. Cosmochim. Acta* **72**, A365-A365.

Jong, T., D. L. Parry, 2004. Adsorption of Pb(II), Cu(II), Cd(II), Zn(II), Ni(II), Fe(II), and As(V) on bacterially produced metal sulfides. *J. of Coll. Interf. Sci.* **275**, 61-71.

Kornicker, W.A., J.W. Morse, 1991. Interactions of divalent-cations with the surface of pyrite. *Geochim. Cosmochim. Acta* **55**, 2159-2171.

Manning, B. A., M. L. Hunt, C. Amrhein, J.A. Yarmoff, 2002. Arsenic(III) and Arsenic(V) reactions with zerovalent iron corrosion products. *Environ. Sci. Technol* **236**, 5455-5461.

Morse, J. W. Arakaki, T., 1993. Adsorption and Coprecipitation of Divalent Metals with Mackinawite (Fes). *Geochim. Cosmochim. Acta* **57**, 3635-3640.

O'Day, P. A., D. Vlassopoulos, R. Root, N. Rivera, 2004. The influence of sulfur and iron on dissolved arsenic concentrations in the shallow subsurface under changing redox conditions. Proceedings of the National Academy of Sciences, **101**, 13703-13708.

Raven, K. P., A. Jain, R.H. Loeppert, 1998. Arsenite and arsenate adsorption on ferrihydrite: Kinetics, equilibrium, and adsorption envelopes. *Environ. Sci. Technol* **32**, 344-349.

Stauder, S.; B. Raue, F. Sacher, 2005. Thioarsenates in sulfidic waters. *Environ. Sci. Technol.* **39**, 5933-5939.

Wilkin, R. T.; D. Wallschlager, R. G. Ford, 2003. Speciation of arsenic in sulfidic waters. *Geochemical Transactions* **4**, 1-7.

Wolthers, M., Charlet, L., van der Meijden, C.H., van der Linde, P.R., Rickard, D. 2005. Arsenic mobility in the ambient sulfidic environment: sorption of arsenic (V) and arsenic (III) onto dissordered mackinawite. *Geochim. Cosmochim. Acta* **69**, 3483-3492.

Wolthers, M., C. H. van der Weijden, D. Rickard, P. Van Cappellen, L. Charlet, 2002. Arsenic association with iron sulphides, adsorption and incorporation. *Geochim. Cosmochim. Acta* **66**, A843-A843.

Zouboulis, A. I., K. A. Kydros, K. A. Matis, 1993. Arsenic(III) and Arsenic(V) Removal from Solutions by Pyrite Fines. *Separation Science and Technology* **28**, 2449-2463.

Substask 1.4.b. Impact of solution conditions on Cd(II) uptake by nanoscale FeS

Objective

The overarching goal of this subtask was to assess the impact of changing solution conditions (pH, Cd(II) loading, and FeS concentration) on Cd(II) uptake by nanoscale FeS.

Background

Aqueous Cd(II) species, due to its strong affinity for sulfide, is strongly sorbed by Fe sulfide minerals. In general, the mechanisms responsible for Cd(II) sorption by Fe sulfides are thought to include adsorption (Jean and Bancroft 1986; Kornicker and Morse 1991), surface Fe(II) exchange (Coles et al. 2000), and precipitation as CdS(s) (Bostick et al. 2000; Erdem and Özverdi 2006). As stated earlier in this report, these previous studies indicate that the principle sorption mechanisms for Cd(II) vary significantly with type of Fe sulfides and experimental conditions (e.g., the ratio of Cd(II) loading to sorbent mass, pH, and background salts). In this task, Cd(II) uptake by nanoscale FeS have been examined as a function of initial Cd(II) concentration, FeS mass loading, and pH.

Materials and Methods.

Sorption experiments were conducted using 12 mL centrifuge tubes by reacting aqueous $CdCl_2$ solutions with FeS suspensions. The initial Cd(II) concentrations (Cd_0) used were 2×10^{-2}, 1.5×10^{-2}, 1×10^{-2}, 7.5×10^{-3}, 5×10^{-3}, 1×10^{-3}, 5×10^{-4}, and 5×10^{-5} M, and the initial FeS concentrations ($[FeS]_0$) were 10, 5, and 2 g/L, resulting in the molar ratio of $Cd_0/[FeS]_0$ less than 1 (i.e., sulfide in excess to Cd(II)). The equilibrium pH ranged over 4 to 11, and the total chloride concentration (Cl_T) was fixed at 0.2 M. The sorption batches were allowed to equilibrate for 48 hours on a LabQuake shaker (Lab Industries, Berkeley, CA) at 25 ^{o}C. This was sufficient for completion of sorption reaction (Di Toro et al. 1992; Erdem and Özverdi 2006). At the end of reaction time, a portion of the supernatants was syringe-filtered using 0.2 µm polypropylene filter (Whatman). The filtrates were acidified with 10% (wt./wt.) nitric acid. Dissolved Cd and Fe concentrations in the acidified solutions were measured by inductively coupled plasma coupled with optical emission spectrometry (ICP-OES, Perkin-Elmer). Some of the reacted mixtures were vacuum-filtered, freeze-dried, and analyzed by XRD to identify crystalline reaction products.

Results and Discussion

Figure 1.21A shows the removal of Cd(II) as a function of pH at two initial Cd concentration, a high loading of 0.015 M and a lower loading of $5.0\text{x}10^{-4}$ M Cd. Due to the extremely high removal capacity of FeS for Cd as noted earlier in this report, Cd(II) is removed below its MCL value over the entire pH range of 4 to 11. Figure 1.18B shows Fe_{Diss} as a function of pH and the initial Cd(II) concentrations (Cd_0) for 10 g/L FeS. As seen in Figure 1.21B, Fe_{Diss} increases with increasing Cd_0 below pH ~7. This finding suggests that precipitation of CdS(s) is responsible for Cd(II) uptake by FeS as confirmed by the XRD results reported

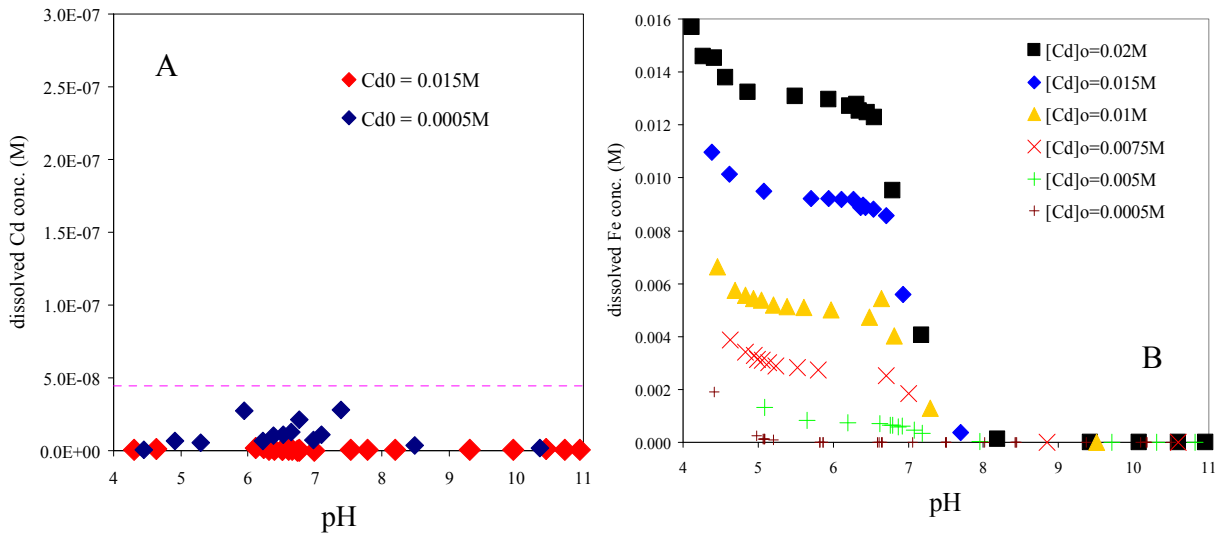

Figure 1.21. Cd(II) uptake in 10 g/L FeS as function of (A) pH at two different initial Cd(II) concentrations (Cd_0), and (B) Dissolved Fe concentration (Fe_{Diss}) as a function of pH at various initial Cd(II) concentrations (Cd_0).

earlier in this report for Cd(II) uptake by FeS. Similarly, others have reported that precipitation of CdS(s) is the main mechanism for Cd(II) removal by FeS (Framson and Leckie 1978; Erdem and Özverdi 2006). Above pH > ~7, however, no significant amount of Fe was detected. This is likely due to precipitation of exchanged Fe(II) as a Fe (hydr)oxide phase as also supported by the XRD results presented earlier.

When the surface reactive sites on FeS(s) are in excess to the initially added Cd(II), it is also possible that the aqueous Cd(II) species are removed via surface complexation with the surface sites on the FeS solid. In a previous study, we found that aqueous Hg(II) species were removed by adsorption when FeS(s) was in large molar excess to Hg(II) (Jeong et al., 2007). If Cd(II) exchange for Fe(II) precipitation of CdS(s) were the sole sorption mechanism, sorbed Cd(II) concentrations (Cd_{sorb}) should be equal to the exchanged Fe(II) concentrations (Fe_{exch}). Figure 1.22 is a plot of Cd_{sorb} vs. Fe_{exch} with the line drawn to show the location of the 1:1 exchange between Cd(II) and Fe(II). Since Fe_{exch} in all cases is below the dashed line, non-Fe(II)-exchange reaction(s) may be responsible for the uptake of Cd(II) by FeS. The most logical additional removal process is adsorption of Cd to the FeS surface. No conclusive evidence for this was found from the XAS studies reported earlier in this report. While the EXAFS analysis of the XAS data for Cd(II)/FeS systems showed some slight differences in coordination number and bonding distances for Cd-S nearest pairs, the data was most suggestive of CdS precipitation over the entire pH range of 5-10. It should be noted, however, that the lowest Cd(II) loading investigated by XAS was for Cd(II)/FeS molar ratio near 0.01. At such high surface coverage, the surface precipitation is likely predominant. At lower loadings, however, in addition to CdS(s) precipitation (a Fe(II) exchange reaction), non-Fe(II)-exchange reactions such as adsorption and surface precipitation are possible. Previously, Coles et al. (2000) have suggested multiple mechanisms for Cd(II) sorption by FeS. In their study, precipitation of [Cd,Fe]S(s) on the FeS surface and adsorption of Cd(II) on this surface precipitate were proposed for Cd(II) sorption.

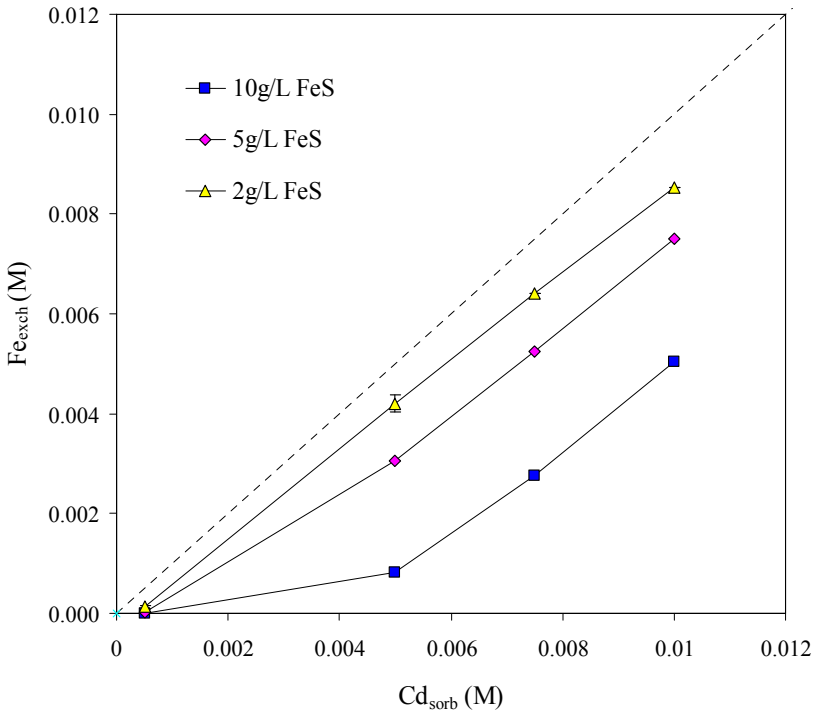

Figure 1.22. Exchanged Fe(II) concentration (Fe_{exch}) versus sorbed Cd(II) concentration (Cd_{sorb}) at pH 5.5 ~ 6.0 where precipitation of Fe (hydr)oxides is avoided.

Summary and Conclusions and Implications for Future Research/Implementation

Cd(II) species are effectively removed by mackinawite (FeS) over a wide range of pH and Cd(II) and FeS concentrations. For $Cd_0/[FeS]_0$ ratios less than 1, nearly quantitative removal is possible. The removal processes responsible for Cd(II) uptake as a function of pH, Cd and FeS concentration are adsorption, surface precipitation, and precipitation as CdS(s), with the relative contribution dependent on the Cd to FeS loading. The first two sorption reactions do not involve the Fe(II) exchange, but the latter reaction requires sulfides to form CdS(s), thus leading to FeS dissolution and subsequent release of Fe and sulfide into the solution phase. The relative importance of non-Fe(II)-change sorption over CdS(s) precipitation decreases at higher $Cd_0/[FeS]_0$ due to its surface-bound nature. To date, we have no spectroscopic confirmation of the adsorption or surface precipitation processes occurring at lower Cd loadings. This is a topic which will require future investigation. The results of this study indicate that nanoscale FeS should be very effective in removal of Cd(II) from contaminated water over a pH of 5-10 in PRB applications.

Literature Cited

Bostick, B.C., S. Fendorf, and M. Fendorf, 2000. Disulfide disproportionation and CdS formation upon cadmium sorption on FeS_2, *Geochim. Cosmochim. Acta* **64**, 247-255.

Coles, C.A., S.R. Rao, and R.N. Yong, "Lead and Cadmium interactions with mackinawite: Retention mechanisms and the role of pH," *Environ. Sci. Technol*. **34**, 996-1000, 2000.

Erdem, M., A. Özverdi, 2006. Kinetics and thermodynamics of Cd(II) adsorption onto pyrite and synthetic iron sulphide. *Separation and Purification Technology* **51**, 240-246.

Jean, G.E., G.M. Bancroft, 1986. Heavy-metal adsorption by sulfide mineral surfaces. *Geochim. Cosmochim. Acta* **50**, 1455-1463.

Jeong, H.Y., B. Klaue, J.D. Blum, K.F. Hayes, 2007. Sorption of Mercuric Ion Hg(II) by Iron Sulfide. *Environ. Sci. Technol.*, 41, 7699-7705.

Kornicker, W.A., J.W. Morse, 1991. Interactions of divalent-cations with the surface of pyrite. *Geochim. Cosmochim. Acta* **55**, 2159-2171.

Substask 1.4.c. Impact of solution conditions on As(III) uptake by FeS-coated sand

Objective

The overarching goal of this subtask was to assess the impact of changing solution conditions (in this case, pH) on As(II) uptake by FeS-coated sand.

Background

As discussed previously in this report, the removal of As(III) by FeS is highly pH dependent. For example in section Subtask 1.2, isotherm data showed the sorption capacity of nanoscale FeS depended strongly on pH in the order of pH 5 > pH 7 > pH 9 (Figure 1.4A). Similarly, FeS-coated sand's sorption capacity depended on pH (Figure 1.4B), however in this case, the trend was pH 5 > pH 7 ≅ pH 9. The higher capacity at pH 9 for the coated sand was attributed to the formation of magnetite (or some other iron oxyhydroxide oxidation product) during the preparation procedure that enhanced As(III) sorption near pH 9 where such iron oxides typically have maximal sorption for As(III) (see subtask 1.4.b). Adsorption edge data collected for nanoscale FeS reported earlier in this subtask (Figure 1.19), showed that nanoscale FeS effectively removed 100% of an initial concentration of As(III) of 1.33 $x10^{-5}$ M up to pH 9 when the FeS solids concentration was greater than 10 g/L. When the concentration of FeS was increased to 40g/L, effective As(III) removal was found across the entire pH range investigated from pH 4.5 to 11.5 (Figure 1.19). In this subtask, the pH edge data was collected in a 100 g FeS-coated sand/L of solution. The concentration of 100 g FeS-coated sand /L (for a total of 0.124 mg FeS /L) was selected for comparison with the 0.1 mg/L nanoscale FeS, since the pH edge was most distinctive for this condition. It was hypothesized that if FeS-coated sand behaved similarly to nanoscale FeS at this condition, then it was likely that the coated material retained the primary pH-dependent sorption characteristics of nanoscale FeS.

Materials and Methods

The FeS-coated sand used for these As(III) uptake experiments was prepared as discussed previously in subtask 1.1. The pH-dependent As(III)-sorption test was performed over the range pH of 2 to 12. One gram of FeS-coated sand was collected in 15 mL polypropylene tube and 9.9 mL 0.1N NaCl solution and 0.1 mL of 1.33×10^{-3} M $NaAsO_2$ solution was added in each tube to achieve an As(III) concentration of 1.33×10^{-5} M As/L (1 mg/L), a total concentration of 100 g coated sand/L, and a total FeS concentration of 0.124 g FeS/L (based on 1.24 mg FeS/g coated sand formulation). Various amounts of 0.08N HCl and 0.1N NaOH solultion were added to each reactor tube and mixed with an end-over-end rotator. The change of ionic strength that occured when adjusting the pH was negligible (maximum addition of ionic strength was less than 0.01 M). After 2 days of mixing, half of supernatant was filtered with 0.1 µm nylon filter and acidified for the analysis of dissolved As and Fe using the inductively coupled plasma mass spectrometry (ICP-MS, Perkin Elmer SCIEX, ELAN DRC-e). The other half of supernatant was used to measure the 2-day equilibrium pH. The same tests were performed using FeS-uncoated natural sand (Wedron sand) to compare As(III)-uptake amount and pH-dependent character of FeS-coated sand.

Results and Discussion

The influence of pH on 1.33×10^{-5} M As(III) removal efficiencies were studied over pH range from 2 to 12. As shown in Figure 1.23, the FeS-coated sand removal behavior resembles that of nanoscale FeS on an equivalent amount of FeS basis (e.g., compare the 0.1 g/L edge in Figure 1.19 to Figure 1.23). In pH-dependent As(III) sorption test of 0.1 g FeS/L system shown in Figure 1.19, 1.33×10^{-5} M of initially loaded As(III) exhibited 100% removal at pH values less than 6, 30% removal at pH 9.2, the lowest removal near pH 8, and maximum removal near pH 9.2. These trends match those from FeS-coated sand system shown in Figure 1.23.

The pH-dependent As(III) removal behavior can be described in terms of the primary uptake mechanism operating in given pH range. At pH below 7 (Zone I in Figure 1.23, As(III) uptake of As(III) is greatest. Removal in this pH range is primarily attributed to the bulk precipitation of an arsenic sulfide solid either AsS(s) or As_2S_3(s) (e.g., see Gallegos et al. 2007 and 2008; and Subtasks 1.3.a. and 1.3.c). The enhanced precipitation in this region is thought to result from the presence of high concentrations of dissolved sulfide at lower pH. As shown in Figure 1.24, the solubility of Fe from FeS-coated sand increases significantly below pH 7, Assuming congruent dissolution (i.e., sulfide dissolved in equivalent concentration to Fe), this can be taken as an indication of the significantly increased concentration of aqueous H_2S, the principal dissolved sulfide species, in this region. The trend of increasing FeS solubility is similar to that shown earlier in this report for nanoscale FeS (Figure 1.20). Interestingly, the

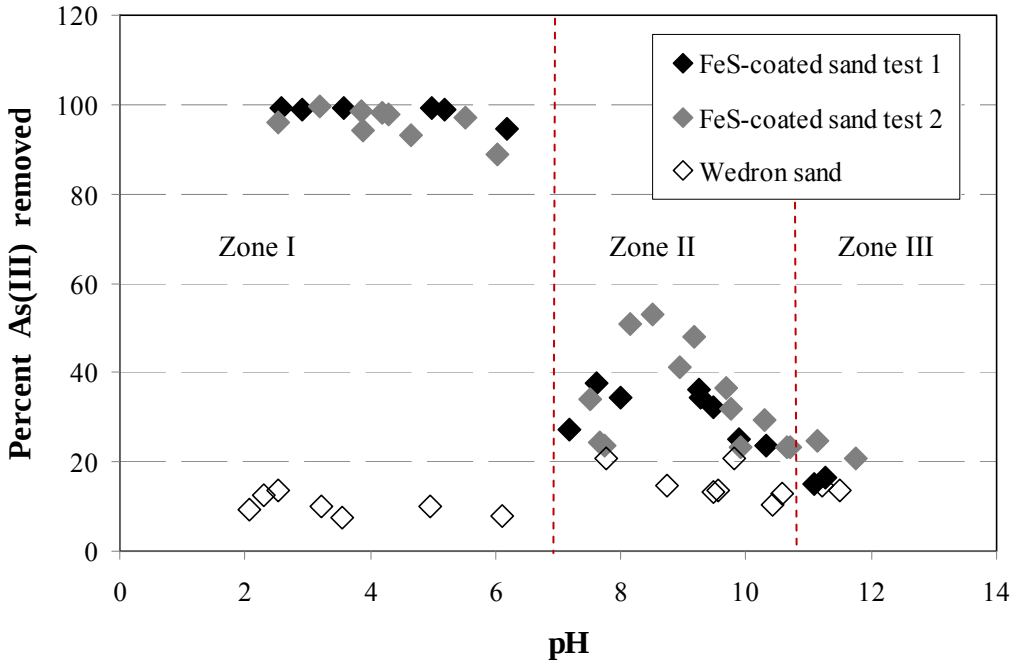

Figure 1.23. Percent removed of 1.33 x 10^{-5} M (1 mg/L) As(III) (left) as a function of pH for 100 g FeS-coated sand (0.124 g FeS) and uncoated 100g Wedron sand/L in 0.1M NaCl aqueous solutions.

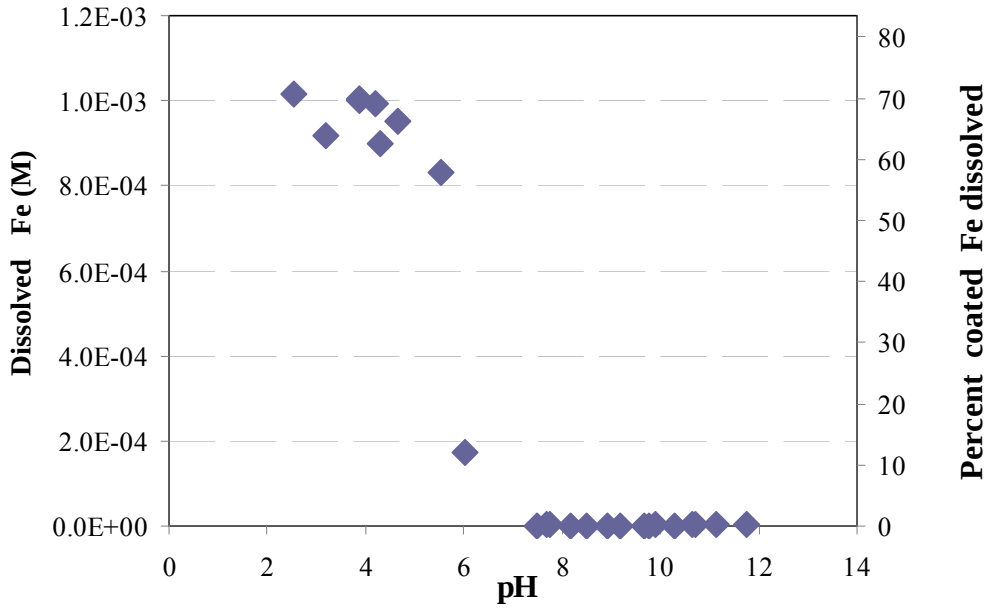

Figure 1.24. Dissolved Fe concentration as a function of pH for 100 g FeS-coated sand/L in 0.01 M NaCl. Also shown is the percentage of total iron removed from the sand.

value of dissolved Fe levels off below pH 4 at a total dissolved Fe concentration that is only approximately 70% of the total iron coated on the sand ($1.0x10^{-3}$ M vs $1.4x10^{-3}$M). This suggests that a fraction of the FeS-coated material (~ 30%) is in a non acid extractable form. While acid volatile sulfides like freshly prepared nanoscale FeS (as mackinawite) typically dissolve with less stringent acid extraction conditions, iron sulfide oxidation products are not so easily removed and typically require more extensive acid treatments (Huerta-Diaz and Morse, 1990; Rueda et al., 1992; Cooper and Morse, 1998; van Oorschot and Dekkers, 2001). We surmise from this that a portion of the original nanoscale FeS was oxidized during the coating procedure.

In Zone II from pH 7-11 in Figure 1.23, As(III) removal shows a local maximum near pH 9, which is the near pK_{A1} of 9.2 for arsenite. This suggests a ligand exchange sorption reaction with: (1) the FeS surface, which consistents of both >SOH and >FeOH or (2) the surface sites of the solid phase oxidation products of FeS such as magnetite (Gallegos et al. 2008). In both Zone I and II, the FeS-coated surface appears to regulate As(III) removal according to the shape of pH-dependent sorption envelopes of FeS-coated sand and Wedron sand. In contrast, in Zone III, the removal of As(III) corresponds to that of the uncoated Wedron sand, indicating that the original Fe coating may be controlling the low amount of As(III) removed at pH greater than 11. Practically speaking the pH dependent As(III) removal behavior in Zones I and II of are interest in the application of FeS-coated sand in PRBs.

As also shown in Figure 1.23, in the case of sand without the FeS coating, the percent As(III) removal is relatively low and does not seem to be strongly affected by pH. This suggests that the primary removal of As(III) by FeS-coated sand is controlled primarily by the FeS coating and its surface oxidation products, rather than the original Fe(III) oxide coating of the natural sand. Similar to nanoscale FeS (see e.g., Figure 1.19), the precent removal of As(III) by

FeS-coated sand is expected to substantially improve as more sorbent is contacted with the solution phase. This is illustrated in the column studies using FeS-coated sand discussed below in Subtask 1.6, in which As(III) is completely removed from solution at pH 5, 7, and 9, but with decreasing capacity as pH increases and after fewer pore volumes before As(III) breakthrough.

Summary and Conclusions and Implications for Future Research/Implementation

For a similar amount of FeS (~1 mg FeS/L), FeS-coated sand exhibits similar pH-dependent to nanoscale FeS for removal of As(III) at an initial As(III) concentration of 1.33 $x10^{-5}$ M (1 ppm). This suggests that the primary removal mechanisms over the range of pH values investigated are similar for both types of materials. From an application perspective, FeS performance of FeS-coated sand can be determined by the amount of FeS per unit volume that can be delievered regardless of whether FeS is delivered in nanoscale form or coated on sand grains using the procedures developed in this work. Given this, for improved performance of FeS in PRB systems that are maintained under anoxic conditions, future work should be focused on increasing the amount of FeS that can be emplaced in the PRBs without clogging the porous media. This could either be done by either using smaller sand particles or developing forms of granular FeS.

Literature Cited

Cooper, D. C. Morse, J. W., 1998. Extractability of metal sulfide minerals in acidic solutions: Application to environmental studies of trace metal contamination within anoxic sediments. *Environ. Sci. Technol.* **32**, 1076-1078.

Gallegos, T. J., Hyun, S. P., Hayes, K. F., 2007. Spectroscopic investigation of the uptake of arsenite from solution by synthetic mackinawite. *Environ. Sci. Technol.* **41**, 7781-7786.

Gallegos, T. J., Han, Y.-S., Hayes, K. F., 2008. Model precipitation by reaction of As(III) with synthetic mackinawite under anoxic conditions. *Environ. Sci. Technol.*. **42**, 9338-9343.

Huerta-Diaz, M. A. Morse, J. W., 1990. A Quantitative Method for Determination of Trace-Metal Concentrations in Sedimentary Pyrite. *Mar. Chem.* **29**, 119-144.

Rueda, E.H., Ballesteros, M.C., Grassi, R.L., Blesa, M.A. 1992. Dithionite as a dissolving reagent for goethite in the presence of EDTA and citrate. Application for soil analysis. *Clays and Clay Minerals* **40**, 575-585.

van Oorschot, I.H.M., Dekker, M.J. 2001. Selective dissolution methods of magnetite iron oxides in acid-ammonium oxalate/ferrous iron extraction method-1. Synthetic samples. *Geophys. J. Int.* **145**, 740-748.

Substask 1.4.d. Impact of dissolved silicate on As(III) uptake by FeS and FeS-coated sand

Objective

Silicate, a commonly existing oxyanion in natural groundwater, is often reported to inhibit the sorption of other anions (e.g., arsenate and arsenite) onto mineral surfaces. Since FeS-coated sand is a silica-based material, its dissolution results in dissolved silicate in aqueous phase so the FeS-coated sand system will always have some dissolved silicate under typical geochemical conditions. In this section, therefore, the effect of dissolved silicate on As(III) sorption of FeS-coated sand was assessed.

Background

Silicate (hereafter refers to all monomeric silicate ions such as $H_4SiO_4^0$, $H_3SiO_4^{-1}$ etc.) concentration in natural groundwater ranges from 0.054 - 0.380 mM (1.5 - 10.65 ppm as Si) with levels as high as 0.814 mM (22.82 ppm) (Elgawhar.Sm and Lindsay, 1972). In natural waters at pH less than 9.5, silicate is present primarily as silicic acid, $H_4SiO_4^0$ and remains in monomeric form unless the dissolved Si concentration and pH are considerably higher (Hiemstra et al., 2007). The silicate ion is known to form inner-sphere complexes with Fe(III) solids by exchanging ligands with surface hydroxyl groups with adsorption strongly pH-dependent (Pokrovski et al., 2003). As such, when silicate adsorbs to ferric iron solids, it may affect its surface properties. For example, when goethite was equilibrated solutions containing silicate, the pH of the point of zero charge (i.e., pH_{pzc}) surface shifted to higher pH with increasing silicate concentration (Hiemstra et al., 2007, Garman et al., 2004). This surface charging effects may impact adsorption of other anions and cations (Anderson and Benjamin, 1985).

The effect of silicate on arsenic adsorption/desorption has been studied mostly in relation to iron oxyhydroxides sorbents. Silicic acid has pK_1 value of 9.5 and a maximum sorption to the goethite surface near pH 9 (Hiemstra et al., 2007). Arsenite has a similar pK_1 of 9.2 with its maximum sorption also near its pK_1 so the competition of silicate with arsenite on iron oxide surfaces is generally expected to be much stronger than the competition between any other anion such as sulfate, chloride and fluoride (Gu et al., 2005). Previous studies of the competitive interaction between silicate and arsenite sorption on Fe(III)-oxide indicate that silicate reduces both the adsorption rate and the total arsenic adsorbed (Swedlund and Webster, 1999, Waltham and Eick, 2002, Roberts et al., 2004). Luxton and co-workers, who investigated the effect of silicate on the uptake of arsenite by goethite, speculated that silicate blocked potential adsorption sites and/or displacing adsorbed arsenite, thereby reducing the total adsorbed arsenite (Luxton et al., 2008).

In this section, the role of silicate on arsenite uptake of FeS-coated sand was investigated. Although the impact of silicate on arsenite uptake by Fe-oxyhydroxides has been previously investigated, few studies have been conducted detailing the impact of silicate on arsenite sorption in iron sulfide systems under controlled anoxic geochemical conditions. Therefore, in the section, the effects of silicate on arsenite sorption of FeS and FeS-coated sand were investigated in laboratory batch systems.

Materials and Methods

FeS-coated sand, a silica-based material, when placed in water will dissolve according to its aqueous solubility properties and rates of dissolution. Therefore, dissolved silicate concentration was measured with and without the presence of arsenic under various pH conditions from in systems comprised of 100g FeS-coated sand/L solution. The pH of the solution was maintained by continuously monitoring and adding either HCl or NaOH as needed. To prepare the solutions, one gram of FeS-coated sand was collected in 15 mL polypropylene tube and 9.9 mL of a 0.1M NaCl solution. For the As(III) containing system, 0.1 mL of a 1.33×10^{-3} M $NaAsO_2$ solution was added to each tube to achieve an As(III) concentration of 1.33×10^{-5} M (1 ppm as As(III)). Various amounts of HCl and NaOH solution were then added in each tube and mixed with an end-over-end rotator. The change of ionic strength that occurs in adjusting pH was assumed negligible (maximum addition of ionic strength was less than 0.01 M). After 2 days of mixing, the half of supernatant was filtered with 0.1 μm nylon filter and acidified for the analysis of Si using the inductively coupled plasma mass spectrometry (ICP-MS, Perkin Elmer) and the another half of supernatant was used for measuring 2-day equilibrium pH.

After finding out the FeS-coated sand system releases appreciable amounts of silicate in the aqueous system under all applied pH conditions (pH 2-12), the pure FeS was tested as a control experiments for simulating silicate-free condition. The 2g/L FeS stock suspension was prepared from mackinawite solid synthesized in the laboratory and was added in the each tube to achieve a 0.5g/L FeS. Arsenic and silicate stock solutions were prepared using $NaAsO_2$ and Na_2SiO_3, respectively. FeS suspension samples with and without silicate were spiked with arsenic stock solution. The 10ml final solutions thus contain 0.5g/L FeS, 0.1N buffer, and desired amount of arsenite (0.133 mM or 0.0133 mM) with and without silicate (0.35 mM). Prepared sample tubes were mixed with an end-over-end rotator for 2 days and equilibrated samples were filtered through a 0.1 μm nylon syringe filter and acidified with HNO_3 for ICP-MS analyses.

For investigating the effect of silicate on FeS-coated sand, test tubes with 5 g of FeS-coated sand and 10 ml of buffer solutions with and without 0.35mM dissolved silicate were mixed using an end-over-end rotator for 1 day to condition its surface with buffer solution in the absence and presence of silicate. An aliquot of As(III) stock solution was then added to achieve desired ranges from 1 ppm to 50 ppm initial As(III) concentrations for pH 5, and from 1 ppm to 20 ppm for pH 7 and 9. The prepared reaction tubes were then mixed with an end-over-end rotator for another 2 days. After 2 days, the supernatant in tubes was filtered through a 0.1 μm nylon filter, diluted, and then acidified with HNO_3 and analyzed for arsenic with ICP-MS. All the experimental steps except acidifying were performed in the anaerobic chamber (N_2/H_2 = 5%/95%).

Results and Discussion

In FeS-coated sand samples, the amount of silicate dissolved at pH 5, 7 and 9 in 0.1M NaCl solution for 2 days equilibration period was measured and is displayed in Figure 1.25. The results show that dissolved silicate is minimal from pH 7 to 9, but progressively increases below and above pH 9 regardless of the presence of 1 ppm As(III). The presence of As(III)

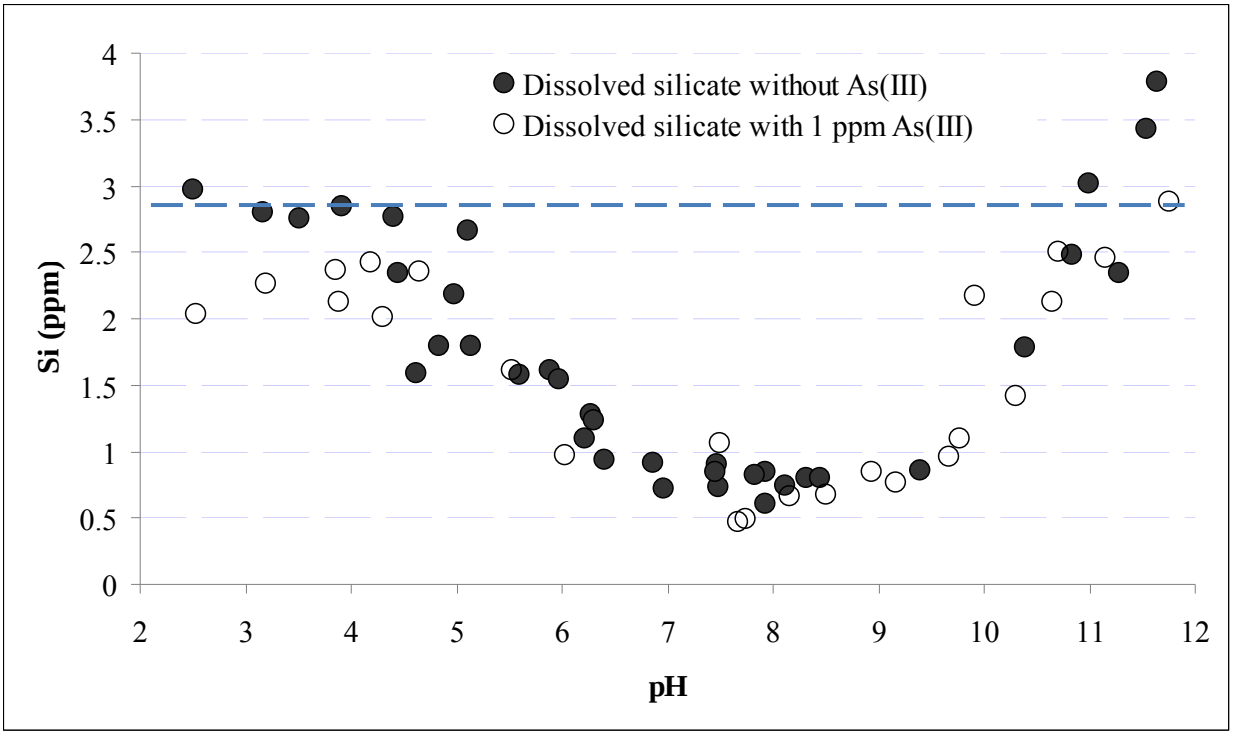

Figure 1.25. Dissolved silica concentration as a function of pH in 100 g FeS-coated sand/L of water.

seems to have little effect on the concentration of dissolved silicate throughout the pH range investigated, presumably because the added As(III) concentration is relatively low compared to dissolved silicate. The pH dependence of dissolved silicate in equilibrium with $SiO_2(s)$ is well known and expected to be relatively constant below 9 but progressively increases above 9.5 as the predominant speciation in solution changes from $H_4SiO_4^0$ to $H_3SiO_4^{-1}$ (Stumm and Moargan, 1981). The solubility of crystalline forms of silica is around 3 ppm while that of amorphous silica can an order of magnitude higher. As shown in Figure 1.25, dissolved silicate concentrations are below 3 ppm over most of the pH range except at very low and very high pH conditions. Under these more extreme pH values, the dissolution of silica sand may reach to its equilibrium value faster than under the moderate pH conditions. In Elgawhary and Lindsay (1972), amorphous silica dissolution in 0.02 M $CaCl_2$ required around 10 days to reach a constant concentration condition at pH 5 and 7. The higher pH above 9 is also expected based on the solubility increase above this value.

Similar results have been previously reported in the literature. For example, Beckwith and Reeve (1964) found the least amount of aqueous in precipitated silicic acid experiments in which silicate concentration was lowest at pH about 7 to 9, while considerable higher below pH 4 (Beckwith and Reeve, 1964). Hiemstra et al (2007) also found that dissolved silicate was lowest near pH 9 but increases at lower pH in systems in which silica was mixed with goethite. These results of these studies may also be related to the slower dissolution kinetics of silica at moderate pH conditions.

The effect of the dissolved silicate on As(III) uptake of nanoscale FeS was tested over a range of pH conditions at two different initial As(III) concentrations but, in general, found to have little impact over the range of conditions tested (Figure 1.26). For example, at pH 7, in the

absence of dissolved silicate, a 0.5 g FeS suspension removed 0.112 mM and 0.012 mM of As(III) out of initially As(III) concentration of 0.133 mM and 0.0133 mM, respectively. When 0.35 mM silicate was present in the system, As(III) uptake was measured to be 0.110 mM and 0.012 mM As(III) in 0.133 mM and 0.0133 mM As(III), respectively, indicating no impact. At pH 9, As(III) removal also was also not affected by the presence of dissolved silicate, even though the As(III) removal efficiency was less than at pH 7. At pH 5, where the highest As(III) uptake was observed, again no significant impact of dissolved silicate was observed. Since precipitation of arsenic sulfide has been shown to be the main mechanism of As uptake at pH 5 (as previously summarized in Subtask 1.3.a. above), this was not surprising. However, the fact that no impact was also observed at pH 5 and 7, where As(III) adsorption and/or precipiation may occur, indicates that As(III) adsorption by nanoscale FeS is not inhibited by dissolved silicate, regardless of the uptake mechanism. This suggest a potential advantage of FeS based PRB materials over ferric oxydroxide sorbents emplaced in groundwater environments where silica sand and dissolves silicate is expected to typically be present.

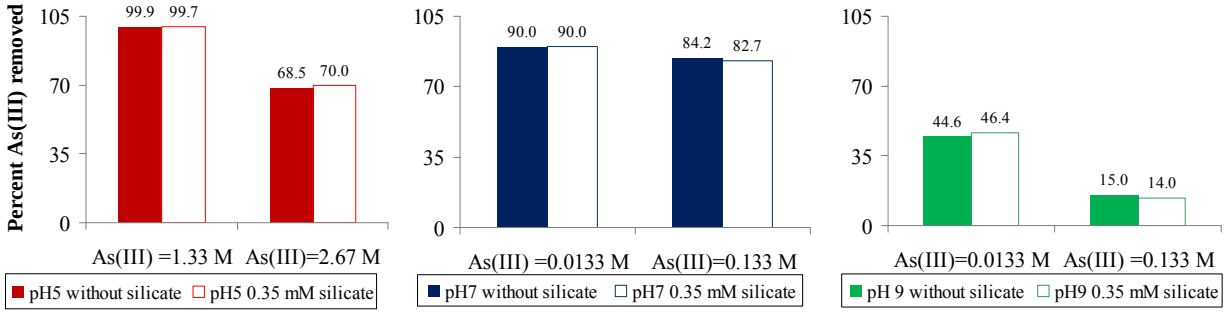

Figure 1.26. Effect of dissolved silicate on As(III) uptake by nanoscale FeS at pH 5, 7 and 9.

Similar to the the FeS system, the dissolved silicate did not have much effect on As(III)-uptake at pH 5 and pH 7 in the FeS-coated sand system (Figure 1.27). However, at pH 9, the addition of 0.35 mM dissolved silicate indicated less arsenic uptake compared to the silicate free system. Under basic pH conditions, As(III) uptake of FeS-coated sand is attributed to both FeS surface coated on sand and the natural sand surface containing iron-oxide as mentioned previously in this report. Hence, the decrease in As(III) uptake compared to the FeS system at pH 9 is thought to result from the competition between arsenite and the silicate ion to the iron oxide fraction exposured on the natural Wedron sand at pH 9. This finding is consistent with results reported by Robert et al. (2004) who showed that the sorption of arsenic on iron hydroxides is hindered by dissolved silicate. At pH 5 and 7, the dissolved silicate had little impact in these FeS-coated sand systems, presumably because the primary removal mechanism of As(III) is precipitation at of AsS(s) at pH 5 and either precipitation or adsorption by FeS at pH 7 rather than sorption to iron oxyhydroxide surface phases that are present on the Wedron sand.

The inhibitory effect of dissolved silicate on anion adsorption to Fe(III)-oxide surfaces has been previously attributed to competition for surfaces sites for anions such as phosphate, chromate, arsenate and arsenite (Garman et al., 2004, Swedlund and Webster, 1999, Waltham and Eick, 2002, Luxton et al., 2008, Mayer and Jarrell, 2000, Su and Puls, 2001). Since the adsorption of silicate on Fe-oxide surface is expected to be greatest near the pH of the pK_1 of silicic acid (e.g., pH of 9.5) the competitive effect on anion sorption is typically greatest near this

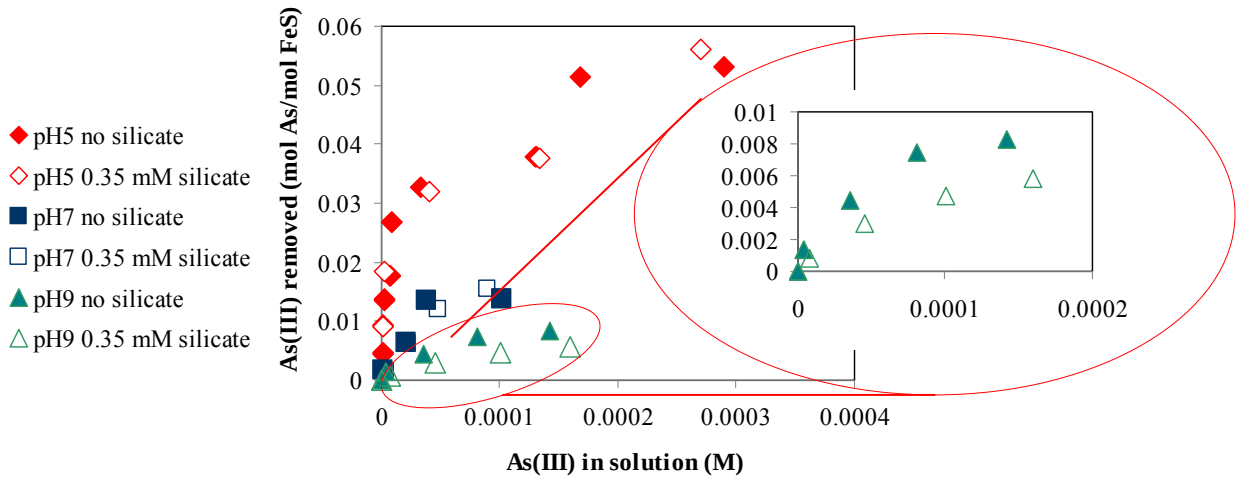

Figure 1.27. Effect of dissolved silicate on As(III) uptake by FeS-coated sand at pH 5, 7 and 9. The circled area is enlarged for better viewing.

pH. Because arsenite sorbs more weakly than arsenate to Fe-oxide surfaces (Garman et al., 2004), desorption by competition with silicate will be more significant when the primary removal mechanism of arsenite is adsorption to such surfaces (Waltham and Eick, 2002, Luxton et al., 2008). Fortunately, when a system is comprised primarily by sorption to FeS, this impact will be minimized, regardless of the pH.

Summary and Conclusions and Implications for Future Research/Implementation

In this study of the potential of dissolved silicate to reduce As(III) sorption by FeS, no impact on As(III) removal was observed at pH 5, 7 and 9 for nanoscale FeS and at pH 5 and 7 for FeS-coated sand. However, a slight lowering of As(III) uptake was noted at pH 9 for in the FeS-coated sand system. This reduction is attributed to the inhibition by silicate of As(III) adsorption to the iron oxyhydroxide phases originally present on the natural sand or the iron oxyhydroxide phases that may have formed from the oxidation of FeS during the coating procedure or in subsequently. Although the impact at pH 9 is relatively small it suggests that operating an FeS-based PRB at higher pH may not be advisable, given that a continous supply of dissolved silicate in groundwater flowing through the PRB could eventually cause the release of As(III) back into solution.

Literature Cited

Anderson, P.R., and Benjamin, M.M. 1985. Effects of silicon on the crystallization and adsorption properties of ferric oxide. *Environmental Science & Technology* **19**, 1048-1053.

Beckwith, R.S. and Reeve, R., 1964. Studies on soluble silica in soils. II. The release of onosilicic acid from soils. *Australian J Soil Res* **2**(1), 33-45.

Elgawhar, S.M., and Lindsay, W.L., 1972. Solubility of silica in soils. *Soil Science Society of America Proceedings* **36**(3), 439-442.

Garman, S.M., Luxton, T.P. and Eick, M.J., 2004. Kinetics of chromate adsorption on goethite in the presence of sorbed silicic acid. Journal of Environmental Quality 33(5), 1703-1708.

Gu, Z.M., Fang, J. and Deng, B.L., 2005. Preparation and evaluation of GAC-based iron-containing adsorbents for arsenic removal. *Environmental Science & Technology* **39**(10), 3833-3843.

Hiemstra, T., Barnett, M.O. and van Riemsdijk, W.H., 2007. Interaction of silicic acid with goethite. *Journal of Colloid and Interface Science* **310**(1), 8-17.

Luxton, T.P., Eick, M.J. and Rimstidt, D.J., 2008. The role of silicate in the adsorption/desorption of arsenite on goethite. *Chemical Geology* **252**(3-4), 125-135.

Mayer, T.D. and Jarrell, W.M., 2000. Phosphorus sorption during iron(II) oxidation in the presence of dissolved silica. *Water Research* **34**(16), 3949-3956.

Manning B.A., S. Goldberg, 1996. Modeling competitive adsorption of arsenate with phosphate and molybdate on oxide minerals. *Soil Sci Soc Am J* **60**, 121-131.

Morse J.W., 1991. Oxidation kinetics of sedimentary pyrite in seawater. *Geochim Cosmochim Acta* **55**, 3665-3667.

Moses C.O., and J.S. Herman, 1991. Pyrite oxidation at circumneutral pH. *Geochim Cosmochim Acta* **55**, 471-482.

Nordstrom D.K., and D.G. Archer, 2003. In *Arsenic in Ground Water*, eds Welch AH, Stollenwerk KG (Kluwer Academic Publishers, Boston), pp 1-25.

O'Day P.A., D. Vlassopoulos, R. Root, and N. Rivera, 2004. The influence of sulfur and iron on dissolved arsenic concentrations in the shallow subsurface under changing redox conditions. *Proc Natl Acad Sci USA* **101**, 13703-13708.

Pokrovski, G.S., Schott, J., Garges, F. and Hazemann, J.L., 2003. Iron (III)-silica interactions in aqueous solution: Insights from X-ray absorption fine structure spectroscopy. *Geochimica Et Cosmochimica Acta* **67**(19), 3559-3573.

Refait P.H., O. Benali, M. Abdelmoula, and J.-M.R. Génin, 2003. Formation of 'ferric green rust' and/or ferrihydrite by fast oxidation of iron(II-III) hydroxychloride green rust. *Corros Sci* **45**, 2435-2449.

Roberts, L.C., Hug, S.J., Ruettimann, T., Billah, M., Khan, A.W. and Rahman, M.T., 2004. Arsenic removal with iron(II) and iron(III) waters with high silicate and phosphate concentrations. *Environmental Science & Technology* **38**(1), 307-315.

Saulnier I., and A. Mucci, 2000. Trace metal remobilization following the resuspension of estuarine sediments: Saguenay Fjord, Canada. *Appl Geochem* **15**, 191-210.

Stauder S., B. Raue, and F. Sacher, 2005. Thioarsenates in sulfidic waters. *Environ Sci Tech* **39**, 5933-5939.

Stumm, W. and Morgan, J.J., 1981. Aquatic chemistry, Chemical equilibria and rates in natural waters, A Wiley Interscience Series of Texts and Monographs, New York.

Stumm W., and J.J Morgan, 1996. *Aquatic Chemistry, 3rd ed* (Wiley-Interscience, New York).

Su, C.M. and Puls, R.W., 2001. Arsenate and arsenite removal by zerovalent iron: Effects of phosphate, silicate, carbonate, borate, sulfate, chromate, molybdate, and nitrate, relative to chloride. *Environmental Science & Technology* **35**(22), 4562-4568.

Swedlund, P.J. and Webster, J.G., 1999. Adsorption and polymerisation of silicic acid on ferrihydrite, and its effect on arsenic adsorption. *Water Research* **33**(16), 3413-3422.

Waltham, C.A. and Eick, M.J., 2002. Kinetics of arsenic adsorption on goethite in the presence of sorbed silicic acid. *Soil Science Society of America Journal* **66**(3), 818-825.

Waychunas G.A., B.A. Rea, C.C. Fuller, J.A. Davis, 1993. Surface chemistry of ferrihydrite: part 1. EXAFS studies of the geometry of coprecipitated and adsorbed arsenate. *Geochim Cosmochim Acta* **57**, 2251-2269.

Wilkin R.T., and R.G. Ford, 2006. Arsenic solid-phase partitioning in reducing sediments of a contaminated wetland. *Chem Geol* **228**, 156-174.

Wilkin R.T., and R.G. Ford, 2002. Use of Hydrochloric acid for determining solid-phase arsenic partitioning in sulfidic sediments. *Environ Sci Tech* **36**, 4921-4927.

Williamson M.A., and J.D. Rimstidt, 1994. The kinetics and electrochemical rate-determining step of aqueous pyrite oxidation. *Geochim Cosmochim Acta* **58**, 5443-5454.

Wolthers M., L. Charlet, C.H. van der Weijden, P.R. van der Linde, and D. Rickard, 2005. Arsenic mobility in the ambient sulfidic environment: sorption of arsenic(V) and arsenic(III) onto disordered mackinawite. *Geochim Cosmochim Acta* **69**, 3483-3492.

Yamauchi H., Fowler B.A., 1994. In *Arsenic in the Environment*, ed. J.O Nriagu (Wiley, New York), pp 35-53.

Substask 1.5. Impact of Oxygen on the Mobilization of As Sorbed by FeS

Objective

Although FeS materials in this project have been developed specifically for application in anoxic PRBs, it is possible that oxygen intrusion into such PRBs may occur due aerobic ground water entering the PRB at the inlet side or as a result of seasonal or episodic fluctuations of the water table allowing oxygenated water intrusion. When oxygenated water is present, it is expected that reduced forms of arsenic species will be oxidized (e.g., dissolved As(III) to As(V)) and that reduce iron solid phases will be oxidized (e.g., FeS to Fe(III) oxides). As such, the overall objective of this task was test the efficacy of aresnic previously sequestered by FeS against oxidative mobilization to the water phase as a result of exposure to oxygenated water.

Background

Groundwater recharge, water table fluctuations, and oxygenated water groundwater entering a PRB operating under anoxic conditions can expose the reduced solid phases present to oxic conditions. In such situations, Fe sulfides are oxidatively dissolved, causing the release of the associated metals and arsenic to waters (Holmes, 1999, Saulnier and Mucci, 2000, Caetano et al., 2003). Under persistent oxidizing conditions, the released Fe forms insoluble Fe (oxyhydr)oxides, which may subsequently adsorb and/or coprecipitate with the mobilized trace metals and arsenic (Holmes, 1999, Saulnier and Mucci, 2000, Caetano et al., 2003). Fe (oxyhydr)oxides, produced as a result of oxidation, are known to be strong adsorbents for arsenic (Farquhar et al., 2002, Waychunas et al., 1993, Fendorf et al., 1997, Manning and Goldberg, 1996). Yet, the sequence of events during FeS oxidation and their impact on arsenic mobilization has not been clarified. For example, the rate of arsenic release to the water phase when oxygen is introduced may depend on the rates of FeS oxidation and Fe (oxyhydr)oxide formation. Slower precipitation of Fe (oxyhydr)oxide relative to arsenic release from Fe sulfides has been shown to cause elevated arsenic contamination at intermediate oxidation stages (Saulnier and Mucci, 2000). The speciation of the arsenic sorbed by FeS may also impact dissolved arsenic concentrations. The release of the surface-complexed arsenic is strongly affected by the rate and mechanism of FeS oxidation, whereas the mobilization of discrete arsenic sulfide phases is largely determined by their resistance to oxidation. A change in the oxidation state of arsenic may significantly alter its sorption behavior. For example, As(III) species, only weakly associated with Fe sulfides, are oxidized to As(V) species, which are strongly adsorbed by Fe (oxyhydr)oxides (Farquhar et al., 2002, Saulnier and Mucci, 2000).

In this task, we report on the oxidative mobilization of the arsenic previously reacted with mackinawite (FeS) under ambient atmospheric conditions at three pH values (4.9, 7.1, and 9.1). Changes in the concentration of dissolved species (e.g., Fe, sulfate, As(III), and As(V)) were monitored as a function of oxidation time to assess the oxidation rate of FeS and the mobilization of arsenic. Bulk mineralogical composition, the oxidation state of arsenic, and the local coordination structure around arsenic were examined before and after oxygen exposure using x-ray diffraction (XRD) and x-ray absorption spectroscopy (XAS) techniques. The results of this study point to the complex sequence of the reaction steps that control the release and subsequent uptake of dissolved arsenic under oxidizing conditions and from oxidation of arsenic-containing solids previously maintained under anoxic conditions.

Materials and Methods

Mackinawite (FeS) was prepared by mixing a ferrous solution with a sulfidic solution inside an anaerobic chamber as described in Jeong et al., (2008). The synthesized FeS is nanoparticulate with the specific surface area of 276–345 m^2/g (Jeong et al., 2008). One gram of FeS powder was weighed into reactor bottles containing one liter of the deoxygenated, deionized water inside the anaerobic chamber. The solution pH was buffered at pH 4.9 with 0.1 M acetate buffer, pH 7.1 with 0.1 M MOPS buffer, and pH 9.1 with 0.1 M CHES buffer. NaCl was added to adjust the ionic strength to 0.1 M. A stock solution containing $NaAsO_2$ was spiked to the reaction batches. The initial FeS and As(III) concentrations were 1.0 g/L and 2×10^{-4} M, respectively.

Before the oxidation experiments, the batches were equilibrated on a magnetic stirrer inside the anaerobic chamber for 3 d. The batches were then removed from the chamber and oxidized under the atmosphere while vigorously stirring at 25°C in the dark. At specified intervals, 8 mL aliquots of slurries were withdrawn from the batches and immediately brought into the anaerobic chamber to prevent further oxidation. A portion of the aliquots were syringe-filtered using 0.02 μm filter (Whatman). Four mL of the filtrate was acidified with 4 mL of 10% HNO_3 for measurement of Fe_{diss} and As_{diss} by an inductively coupled plasma coupled with mass spectroscopy (ICP-MS). Although the acidification of samples from anoxic sediments may underestimate the dissolved arsenic due to arsenic sulfide precipitation (Stauder et al., 2005), comparison of untreated and acidified filtrates showed no difference beyond the analytical errors. The acidified filtrates were also measured for $As(III)_{diss}$ using ICP-MS following selective hydride generation of As(III) at pH 4.9 with 1.0 M acetate buffer (Anderson et al., 1986). One mL of the filtrate was acidified with 1 mL of 0.1 M HCl for measurement of dissolved sulfate using an ion chromatography (IC). The remaining slurries were centrifuged at 2,000 rpm for 5 min, and the supernatant was carefully decanted. A portion of wet paste was dried inside the chamber for XRD data collection. The other wet paste was stored in air-tight serum vials and kept frozen until XAS data collection.

Diffraction patterns were obtained on a Rigaku 12 kW rotating anode generator at 40 kV and 100 mV with Cu-K_α radiation. Diffraction data were collected for dried samples in the range of $7^o < 2\theta < 65^o$ at a rate of 2° 2θ per min.

XAS samples were prepared by mounting wet paste into Teflon sample holders and sealing them with a double layer of Kapton tape inside the anaerobic chamber. XAS spectra were collected at Stanford Synchrotron Radiation Laboratory on beamline 10-2 (3 GeV, ≈ 100 mA of maximum current) using a unfocused beam. Arsenic K-edge XANES and EXAFS spectra were collected using a Si(220) double-crystal monochromator with a 13-element solid-state Ge-array fluorescence detector or Lytle detector. Several reference compounds were also collected for XAS spectra to compare with the sample spectra. A minimum of four spectra were collected and calibrated with an arsenic foil at 11,867 eV while the sample chamber was continuously purged with He(g) to prevent the potential oxidation. Comparison of spectra indicated that no oxidation occurred during XAS data collection.

Results and Discussions

Solution-phase Chemistry. During FeS oxidation, both pH and redox potential were continuously monitored, with the pH change less than 0.2 units (Figure 1.28). Dissolved Fe

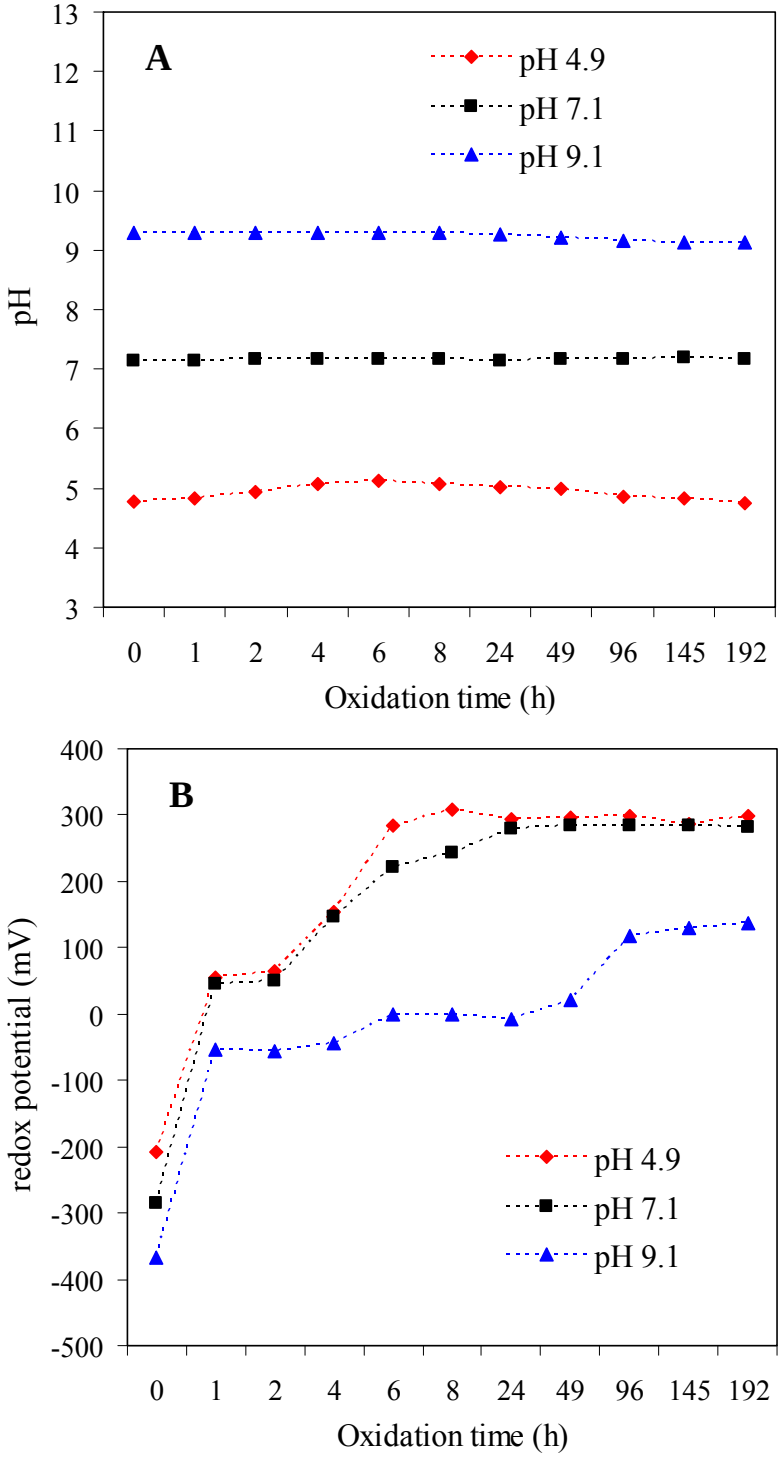

Figure 1.28. Profiles of pH (A) and redox potential (B) during mackinawite (FeS) oxidation. The redox potentials measured using a Ag/AgCl ORP combination electrode were corrected for the stand hydrogen electrode (SHE).

concentrations (Fe_{diss}) were found to be distinct among the pH conditions (Figure 1.29A). The Fe_{diss} at pH 4.9 rapidly increased and reached the maximum in ≈4 h, where most Fe was present in the dissolved form. This indicates that aerobic oxidation of FeS at acidic pH results in FeS dissolution, causing the release of Fe into the solution. Following the initial increase, the Fe_{diss} gradually decreased with the oxidation time. This decrease was due to a slow oxidation of the dissolved Fe(II) to Fe(III)-containing (oxyhydr)oxides). Similar patterns were observed in the oxidation of sulfidic sediments by dissolved oxygen (Saulnier and Mucci, 2000). Although the initial increase in Fe_{diss} at pH 7.1 was also followed by a subsequent decrease, the maximum Fe_{diss} at ≈1 h accounted for only < 1% of the total Fe. The Fe_{diss} at pH 9.1 were near the detection

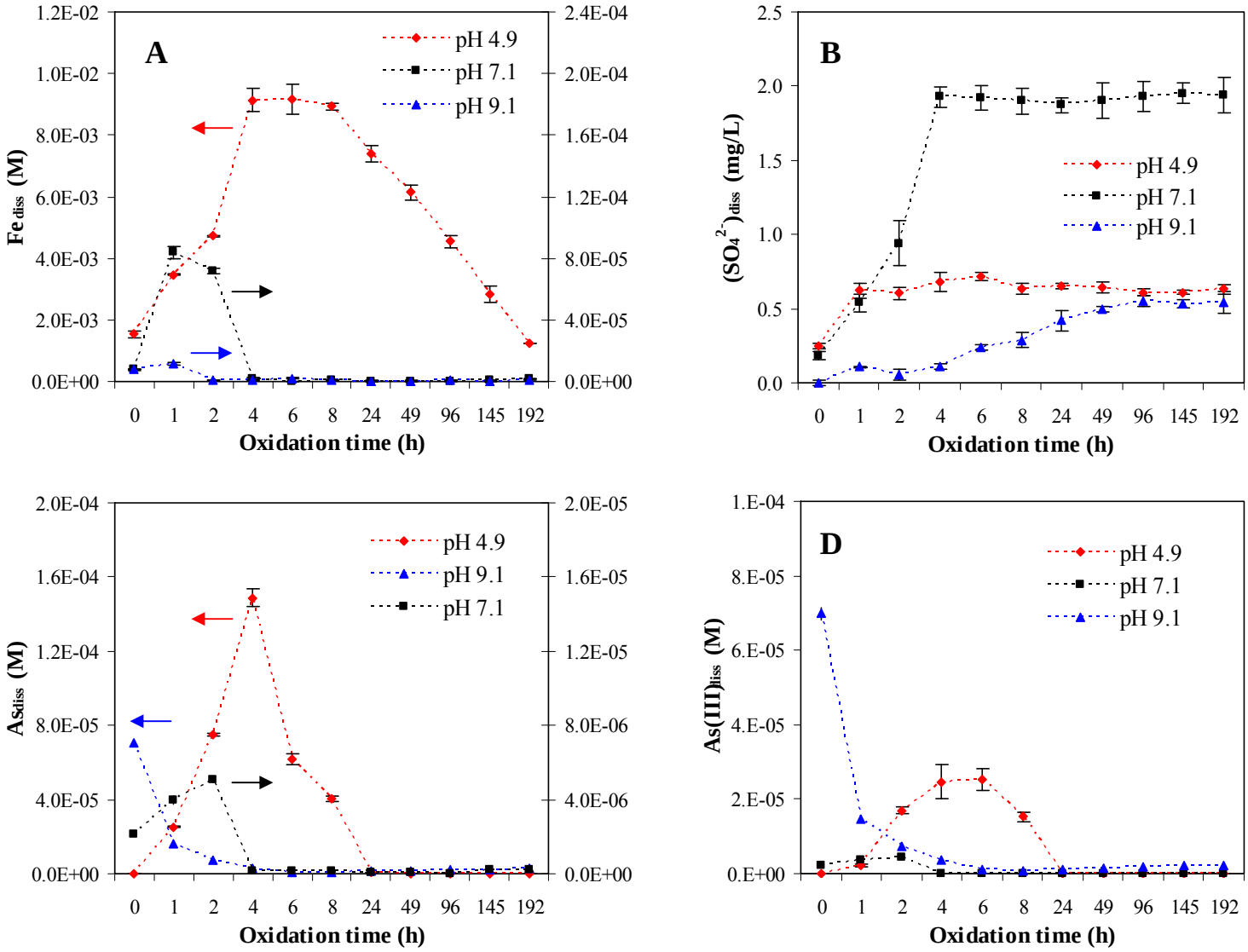

Figure 1.29. Dissolved Fe concentrations Fe_{diss} (A), dissolved sulfate concentrations $(SO_4^{2-})_{diss}$ (B), dissolved arsenic concentrations As_{diss} (C), and dissolved As(III) concentrations $As(III)_{diss}$ (D) during mackinawite (FeS) oxidation. Error bars correspond to one standard deviation. Arrows inserted in parts (A) and (C) guide which y-axis the data can be read from.

limit (≈4×10^{-7} M) with no significant release of Fe into the solution phase. Such pH-dependent Fe_{diss} profiles imply that the mechanism of FeS oxidation varies with pH.

Sulfate, a product of sulfide oxidation, increased with the oxidation time (Figure 1.29B). Sulfate production was used as a measure of pyrite oxidation rates (Moses and Herman, 1991). The initial sulfate production rates in this study were 4.7 $\mu M\cdot h^{-1}$ at pH 4.9, 3.7 $\mu M\cdot h^{-1}$ at pH 7.1, and 1.3 $\mu M\cdot h^{-1}$ at pH 9.1. The decreasing sulfate production rates at higher pH indicate slower oxidation of FeS at higher pH, which is different from the faster oxidation of pyrite with increasing pH (Williamson and Rimstidt, 1994). Despite the fastest oxidation of FeS at pH 4.9, the steady-state sulfate concentration at pH 4.9 was much lower than at pH 7.1. This was likely due to rapid volatilization of the dissolved hydrogen sulfide (evidenced by a strong rotten egg odor) at acidic pH where H_2S(aq) predominates (e.g., pK_{a1} of H_2S(aq) = 6.97; Stumm and Morgan, 1996).

Similar to the Fe_{diss} profiles, dissolved As concentrations (As_{diss}) were strongly affected by pH (Figure 1.29C). Arsenic was rapidly mobilized at pH 4.9 with the maximum As_{diss} accounting for ≈75% of the initially added As(III) ($As(III)_0 = 2\times10^{-4}$ M). After reaching the maximum, the dissolved arsenic gradually decreased as a result of its resorption by Fe (oxyhydr)oxides (Saulnier and Mucci, 2000). Similarly, the As_{diss} at pH 7.1 initially increased, with the maximum (e.g., ≈2.5% of $As(III)_0$) much less than that at pH 4.9. In contrast, the As_{diss} at pH 9.1 continuously decreased as the oxidation proceeded. Dissolved As(III) concentrations ($As(III)_{diss}$) are shown in Fig. 1*d*. Despite the slow oxidation of dissolved As(III) even in the presence of Fe (oxyhydr)oxides (Cherry et al., 1979), the $As(III)_{diss}$ at pH 4.9 accounts for only ≈40% of the total dissolved arsenic in the oxidized samples. The maximum value of $As(III)_{diss}$ at pH 4.9 is reached at a longer time compared with that of As_{diss} in Figure 1.29C, indicating less favorable resorption of As(III) than As(V) at acidic pH.

FeS Oxidation Products and Mechanisms. Mineralogical composition during FeS oxidation was identified by XRD (see Figure 1.30 for individual diffractograms and Figure 1.31 for summary). The initially present mackinawite (FeS) phase quickly disappeared, consistent with its high susceptibility to aerobic oxidation (Holmes, 1999). While mackinawite was not detected at 4 h oxidation at pH 4.9 and 7.1, this phase was persistent at pH 9.1 even after 8 h oxidation. The pH also had a pronounced impact on the intermediate and final oxidation products of FeS. At pH 4.9, the diffraction peaks at 2θ = 9.1° and 9.7º appeared at 4−11 h oxidation, with their corresponding *d*-spacings of 0.98 and 0.91 nm, respectively. Although these spacings do not match exactly with known green rusts, such larger spacings are characteristic of layered mineral structures. The difference between our diffraction patterns and those of known green rusts is attributable to a variation of chemical compositions as observed for hydroxyl-incorporating green rusts (Génin et al., 1998) or formation of ferric-type green rusts by rapid oxidation (Refait et al., 2003). Furthermore, the other transient peaks at 2θ =18.0, 19.6, 36.3, and 38.2º at 4−11 h oxidation are crystallographically consistent with those at 2θ = 9.1º and 9.7º, indicating that green rust-like precipitates form as intermediate oxidation products at acidic pH. Similarly, a green rust-like phase was observed at 1−4 h oxidation at pH 7.1, with its diffraction peaks at 2θ = 10.3, 20.4, and 30.7º. In contrast, no intermediate oxidation product was detected from the oxidized samples at pH 9.1. The final oxidation products of FeS were goethite (α-FeOOH) at acidic pH and lepidocrocite (γ-FeOOH) at neutral to basic pH. At pH 4.9, goethite started to form after 11 h oxidation. In contrast, lepidocrocite was copresent with FeS as early as 2 h oxidation at

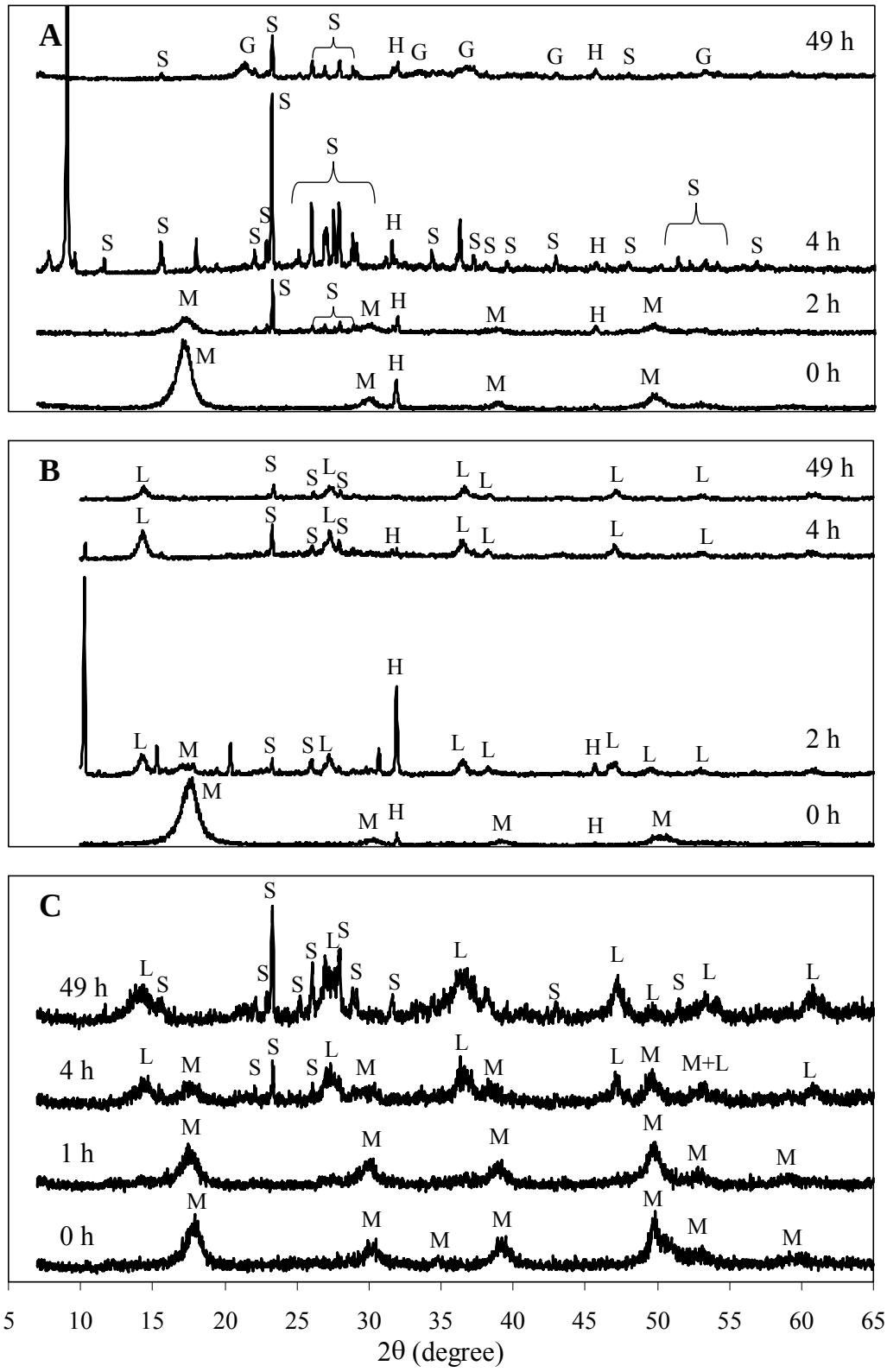

Figure 1.30. Diffraction patterns of the samples oxidized at pH 4.9 (A), 7.1 (B), and 9.1 (C). Oxidation times are indicated in the diffractograms. Reflection peaks are labeled for mackinawite (M), goethite (G), lepidocrocite (L), sulfur (S), and halite (H).

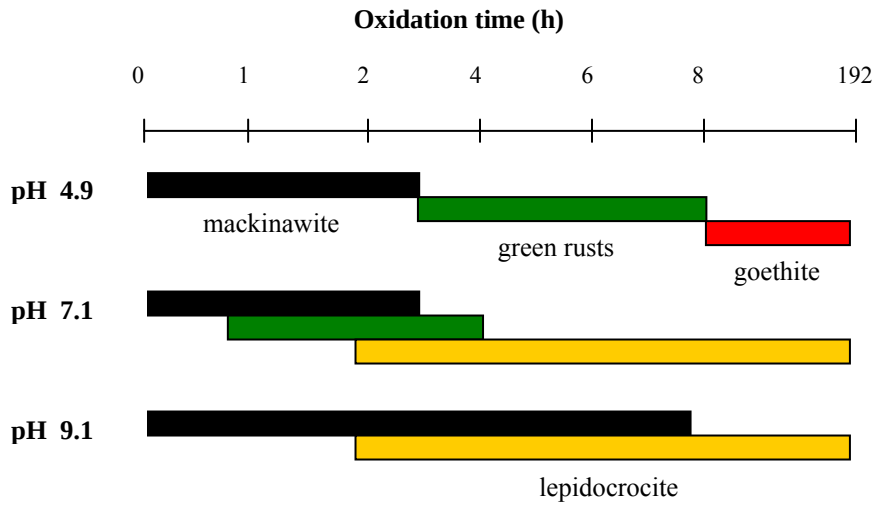

Figure 1.31. Change of Fe crystalline minerals during mackinawite (FeS) oxidation.

neutral to basic pH. Elemental sulfur was observed as an oxidation product of sulfides at all pH conditions.

As indicated by the initial rapid increase of Fe_{diss} and the evolution of $H_2S(g)$, FeS oxidation at pH 4.9 began with oxidative dissolution (i.e., $FeS(s) + 2H^+ \rightarrow Fe^{2+} + H_2S(aq)$). Following this decomposition reaction, the released Fe and S species were oxidized in the solution phase. This oxidation mechanism is completely different from the surface-mediated mechanisms proposed for pyrite oxidation (Moses and Herman, 1991, Williamson and Rimstidt, 1994). Such a difference is likely due to the high solubility of mackinawite and the low solubility of pyrite at acidic pH. Considering the lack of the initial increase of Fe_{diss} at pH 9.1, the surface-mediated oxidation (Burton et al., 2006) is proposed for FeS oxidation at basic pH. Given that gGreen rust-type precipitates were observed at pH 4.9, but not at pH 9.1, due to their structural dissimilarity with FeS, green rusts are unlikely to form via a surface-mediated oxidation. The gradual decrease of mackinawite with a concomitant appearance of Fe (oxyhydr)oxides at pH 9.1 in this study is similar to that observed during its dry oxidation (Boursiquot et al., 2001), supporting the surface mediated oxidation at basic pH. Furthermore, the bulk precipitation of Fe (oxyhydr)oxides from the solution phase is not thermodynamically feasible in the presence of FeS.

The slowest sulfate production as well as the persistence of FeS against oxidation at pH 9.1 can be attributed to formation of a Fe (oxyhydr)oxide coating on the FeS surface. Such a coating was found to retard pyrite oxidation (Morse, 1991). To verify this, additional oxidation experiments were performed using 0.1 M TAPS buffer. As evidenced by higher Fe_{diss} in TAPS buffer than in CHES buffer Figure 1.32A), TAPS buffer appeared to form stronger soluble complexes with Fe(III). As a result, TAPS buffer reduced the Fe (oxyhydr)oxide coating on the FeS surface compared with CHES buffer and increased the sulfate production rate (1.32B). FeS oxidation at neutral pH was consistent with the combined effects of both the solution-phase oxidation following FeS oxidative dissolution and the surface-mediated oxidation. A similarity between Fe_{diss} and As_{diss} as a function of pH suggests that the resorption of arsenic during FeS

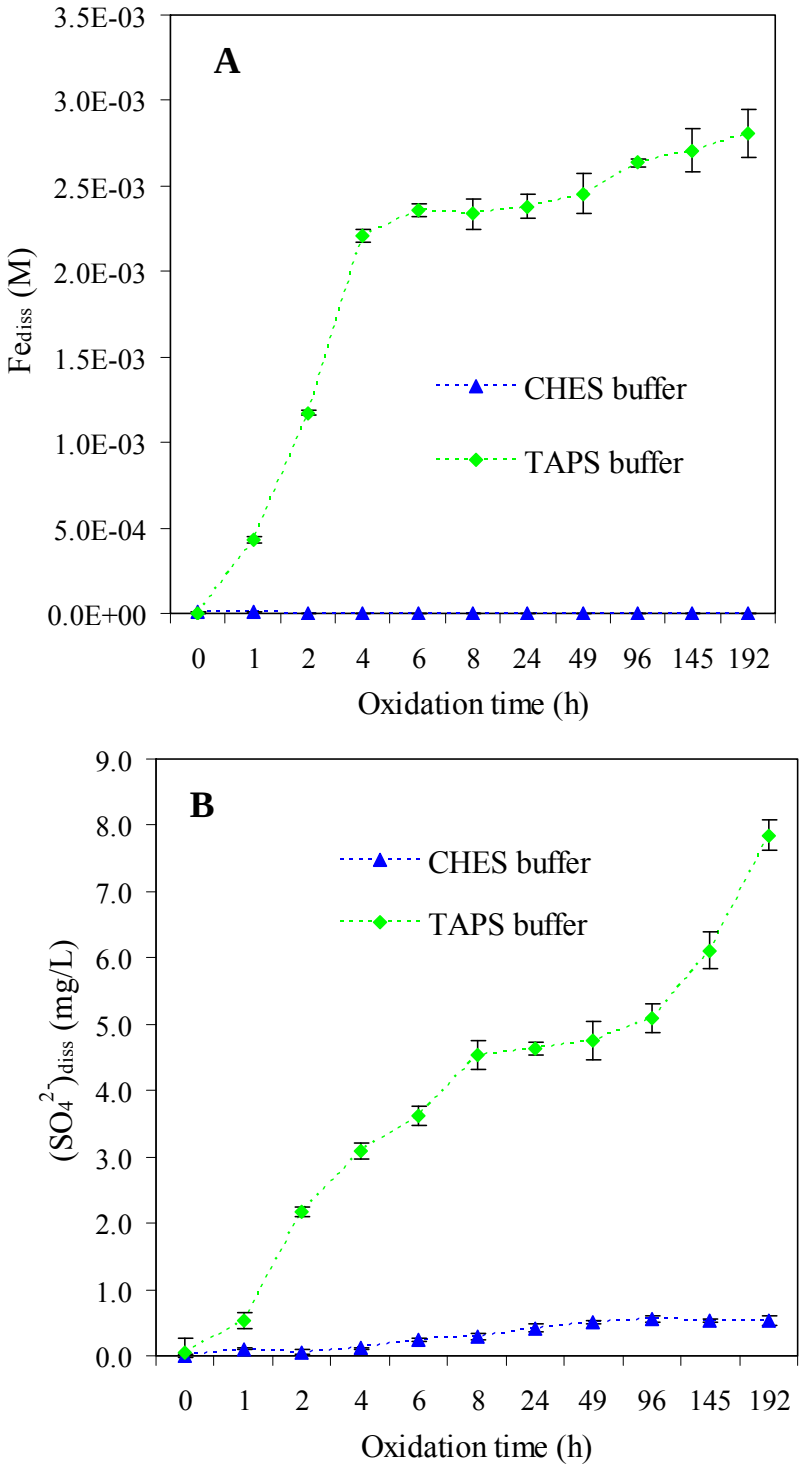

Figure 1.32. Comparison of dissolved Fe concentrations Fe_{diss} (A) and dissolved sulfate concentrations $(SO_4^{2-})_{diss}$ (B) between 0.1 M CHES buffer and 0.1 M TAPS buffer. The solution pH in both buffer systems was 9.1 ± 0.2.

oxidation is likely controlled by the FeS oxidation mechanisms. The oxidative dissolution of FeS at acidic pH resulted in elevated arsenic levels in the solution, whereas the surface-mediated oxidation at basic pH maintained sufficient amounts of solid-associated Fe for resorption of the released arsenic to keep dissolved arsenic below the toxic level.

Arsenic Speciation by XAS. The arsenic speciation in the solid phase was examined by XAS using x-ray absorption near-edge structure (XANES) and extended x-ray absorption fine structure (EXAFS) analyses. In XANES spectra (Figure 1.33), the absorption edges (i.e., inflection energies) of the samples are compared with those of reference compounds with different oxidation states of arsenic. Note that disordered AsS and As_2S_3 were used as reference compounds. No crystalline phase of arsenic was observed in the diffractograms (Figure 1.30). Furthermore, a disordered realgar phase was observed in reaction of FeS with As(III) (Gallegos et al., 2007). Thus, disordered AsS and As_2S_3 are more likely to control the precipitation of arsenic sulfides in our experiments than their crystalline counterparts. Absorption edge position is sensitive to oxidation state, with higher absorption edge energy indicative of a higher oxidation state of arsenic. The absorption edges of all unoxidized samples (11, 867.7 eV at pH 4.9 and 7.1; 11,868.8 eV at pH 9.1) are much lower than that of the soluble As(III) (11,870.9 eV) and even below that of disordered As_2S_3 (11,869.0 eV), indicating that the initially added As(III) was extensively reduced to lower valent-state compounds. The absorption edges were expected to shift to higher energies with the oxidation time. At pH 4.9, the edges shifted to a higher energy (11,868.8 eV) from 0 to 1 h oxidation, but upon further oxidation from 1 to 2 h oxidation shifted back to that of disordered AsS (11,868.1 eV). Such a pattern suggests formation of arsenic phases at multiple oxidation states in the unoxidized sample at acidic pH. Highly oxidized samples (≥ 4 h oxidation) at pH 4.9 resulted in their edge positions close to that of the soluble As(V) (11,874.4 eV). At pH 7.1 and 9.1, the samples oxidized for 1 h have two adsorption edges with the lower edge close to that of the dissolved As(III) and the higher one close to that of the dissolved As(V). Although two edges could not be located for further oxidized samples at pH 7.1 and 9.1, a gradual shift of the edge positions to higher energies indicated successive oxidation of As(III) to As(V). Due to thermodynamic unfavorability of arsenic (hydr)oxide formation under our experimental conditions, the arsenic resorption in oxidized samples was due to its surface complexation with Fe (oxyhydr)oxides.

Arsenic K-edge EXAFS analysis provides structural information on the near coordination environment around arsenic (e.g., interatomic distances (R) and coordination number (N)). The EXAFS spectra and corresponding Fourier transforms of samples are compared with those of reference compounds in Figure 1.34. Structural parameters obtained from the numerical fitting analyses are summarized in Tables 1.11 - 1.14. Unlike orpiment, crystalline realgar shows characteristic doublets over k = 6−10 $Å^{-1}$ in the EXAFS spectrum due to significant As-As interaction at ≈3.5 Å (O`day et al., 2004, Helz et al., 1995). Surprisingly, no such pattern is observed for disordered AsS (Figure 1.34), making its EXAFS spectrum similar to that of disordered As_2S_3. The lack of the second coordination shell in R-space as well as doublet patterns in k-space for disordered AsS is likely due to structural disorder. Similarly, disordered As_2S_3 was found to exhibit fewer interatomic interactions at long distances compared with crystalline orpiment (Helz et al., 1995). The EXAFS spectra of all unoxidized samples are similar to those of disordered AsS and As_2S_3, suggesting a common coordination structure

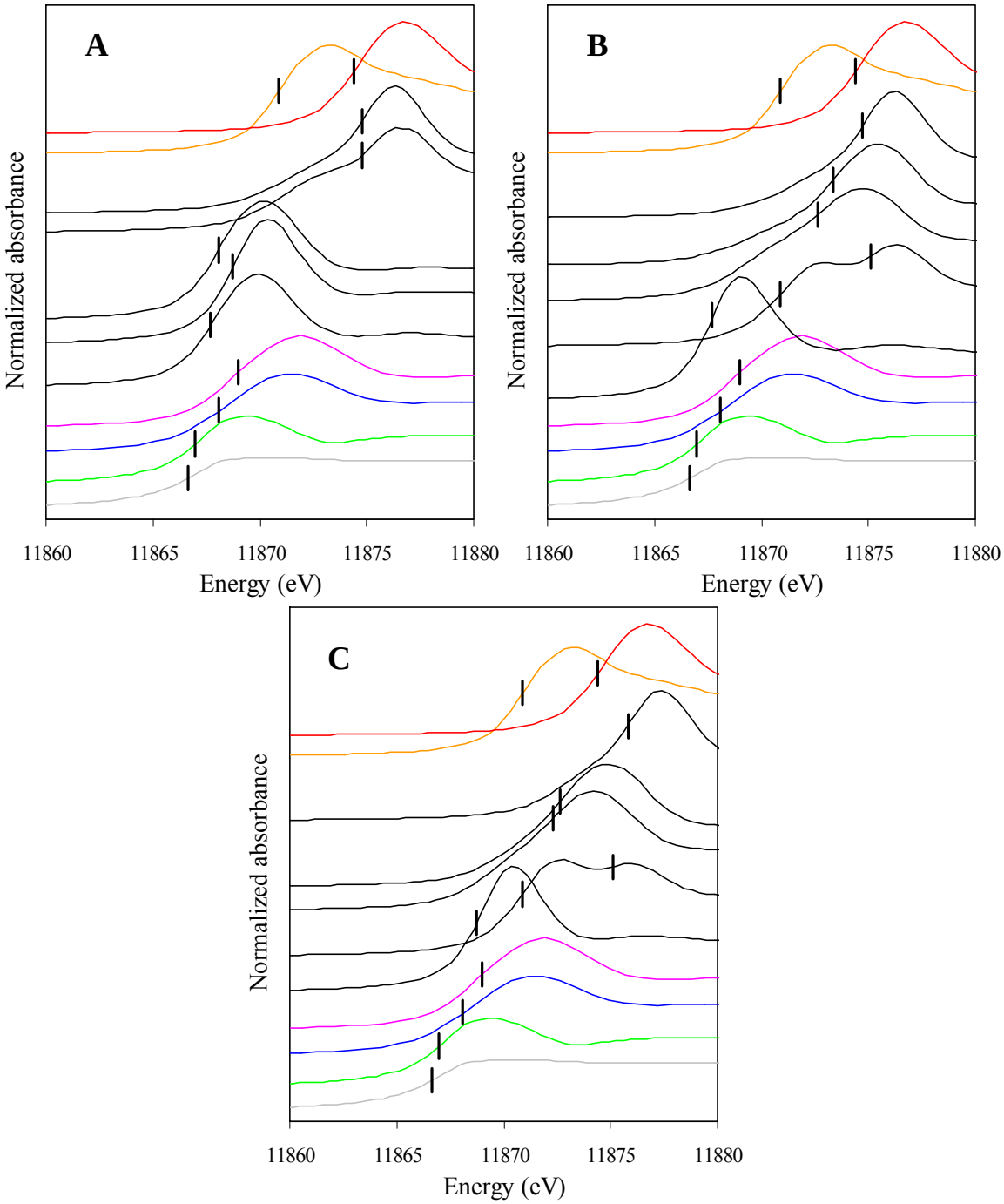

Figure 1.33. Arsenic K-edge XANES spectra for the samples oxidized at pH 4.9 (A), 7.1 (B), and 9.1 (C) as well as reference compounds. The samples oxidized for 0, 1, 2, 4, and 192 h (all black) are arranged from the bottom to the top, which are enveloped by reference compounds: aqueous As(V) (red), aqueous As(III) (orange), disordered As_2S_3 (pink), disordered AsS (blue), arsenopyrite (green), and As(0) (grey). The absorption edges correspond to the first derivative maxima of XANES spectra.

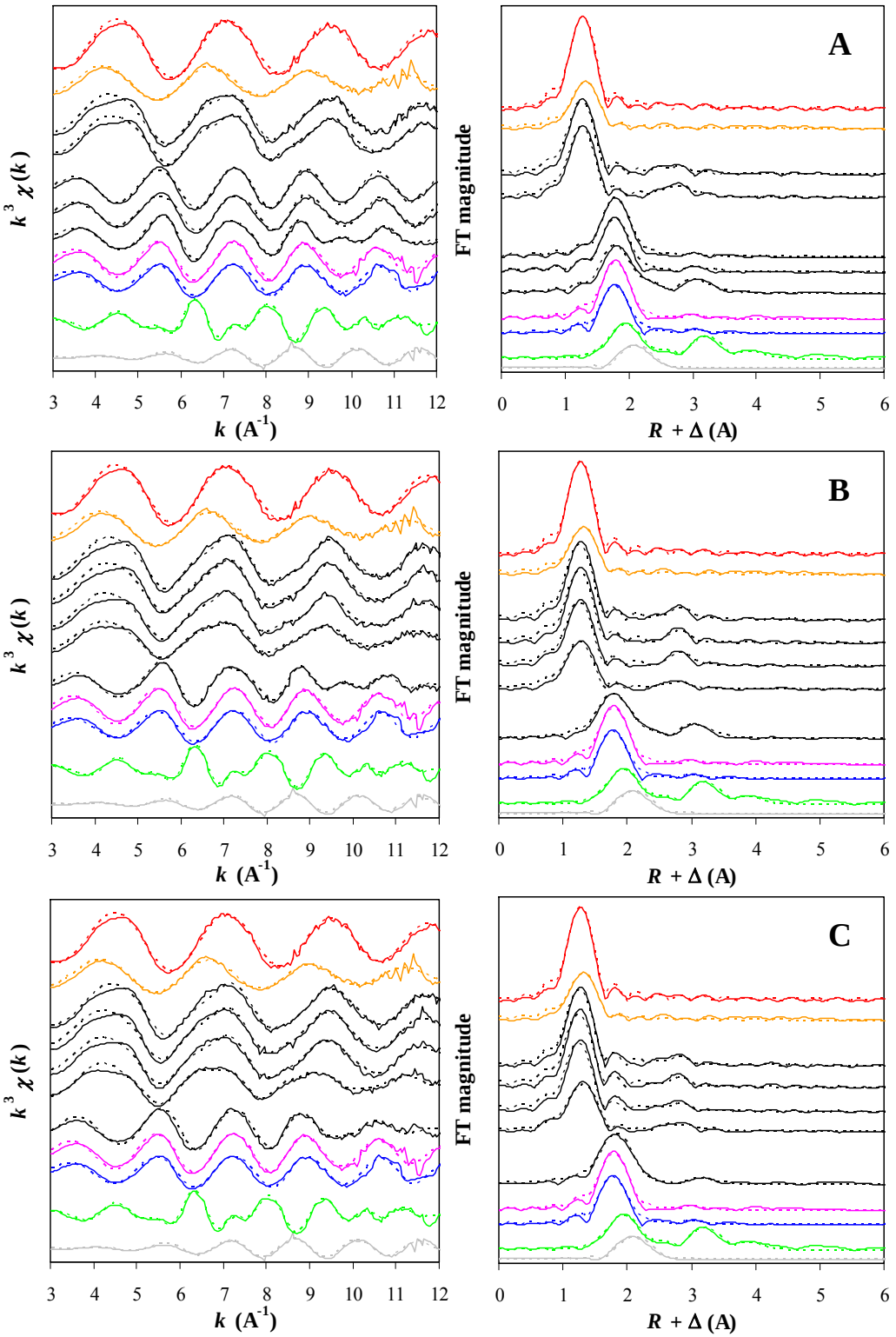

Figure 1.34. k^3-weighted arsenic K-edge EXAFS spectra ($k^3\chi(k)$) and corresponding Fourier transforms for the samples oxidized at pH 4.9 (A), 7.1 (B), and 9.1 (C) as well as reference compounds. Solid lines are the experimental data; dashed lines are the numerical fits. The samples oxidized for 0, 1, 2, 4, and 192 h (all black) are arranged from the bottom to the top, which are enveloped by reference compounds: aqueous As(V) (red), aqueous As(III) (orange), disordered As_2S_3 (pink), disordered AsS (blue), arsenopyrite (green), and As(0) (grey).

Table 1.11. EXAFS fit results and crystallographic data for reference compounds.

		EXAFS fit*			Crystallographic data		
	Pair	*N*	*R*(Å)	σ^2(Å^2)	*N*	*R*(Å)	Reference
As(0)	As-As	1.1	2.50	0.0058†	3	2.50	Wolthers et al. 2005
	As-As				3	3.13	
		ΔE_0 = -6.95 eV, R_f = 0.065					
FeAsS	As-S	1.3	2.34	0.035†	1	2.34	Gallegos et al. 2007
	As-Fe	3.1	2.37	0.011†	3	2.36	
	As-As	3.0	3.06	0.013†	3	3.06-3.18	
	As-S				3	3.30	
	As-As	2.0	3.31	0.0092†	2	3.32	
	As-Fe	4.0	3.78	0.0091†	4	3.75	
	As-As	2.0	4.29	0.0065†	2	4.12	
		ΔE_0 = -8.88 eV, R_f = 0.038					
AsS	As-S	2.0	2.26	0.003†	2	2.23-2.25	LaForce et al. 2000
	As-As				1	2.57	
	As-As	0.41	3.50	0.006†	2.5	3.44-3.51	
	As-S				1	3.41-3.52	
		ΔE_0 = -9.80 eV, R_f = 0.061					
As_2S_3	As-S	3.0	2.28	0.0045†	3	2.24-2.31	LaForce et al. 2000
	As-As	0.37	3.54	0.006†	1	3.19	
	As-S				3	3.22-3.57	
	As-As				2.5	3.52-3.64	
		ΔE_0 = -7.75 eV, R_f = 0.047					
$As(III)_{aq}$	As-O	3.0	1.76	0.0045†	3‡	1.78‡	Wilkin and Ford 2006
		ΔE_0 = -7.90 eV, R_f = 0.069					
$As(V)_{aq}$	As-O	4.0	1.69	0.0025†	4‡	1.69‡	Yamachi and Fowler 1994
		ΔE_0 = -5.01 eV, R_f = 0.024					

*The amplitude-reduction factor (S_o^2) was set at 0.92.
†The Debye-Waller factors (σ^2) were fixed during the numerical fit.
‡Structural data was obtained from EXAFS analysis.

Table 1.12. EXAFS fit results for samples oxidized at pH 4.9*.

Samples	Shell No.	Pair	N	R(Å)	σ^2(Å^2)	$\log_{10}\Gamma^{\ddagger}$
0 h oxidation	1	As-S	2.0	2.25	0.003†	-1.69
		As-As	1.2	2.53	0.0058†	
	2	As-As	1.8	3.51	0.006†	
		ΔE_0 = -7.81 eV, R_f = 0.011				
1 h oxidation	1	As-S	2.3	2.26	0.003†	-1.66
	2	As-As	0.60	3.48	0.006†	
		ΔE_0 = -7.97 eV, R_f = 0.028				
2 h oxidation	1	As-S	2.6	2.27	0.003†	-1.73
	2	As-As	0.19	3.50	0.006†	
		ΔE_0 = -7.43 eV, R_f = 0.020				
4 h oxidation	1	As(V)-O	3.6	1.69	0.0033†	-1.65
	2	As-Fe	0.40	2.90	0.0044†	
		As-Fe	0.87	3.33	0.0048†	
		ΔE_0 = -9.67 eV, R_f = 0.035				
192 h oxidation	1	As(V)-O	3.8	1.69	0.0033†	-1.71
	2	As-Fe	0.37	2.88	0.0044†	
		As-Fe	0.57	3.32	0.0048†	
		ΔE_0 = -11.45 eV, R_f = 0.049				

*The amplitude-reduction factor (S_o^2) was set at 0.92.
†The Debye-Waller factors (σ^2) were fixed during the numerical fit.
$^{\ddagger}\Gamma$ is defined as the surface loading, which is given by the molar ratio of sorbed As to solid-phase Fe.

Table 1.13. EXAFS fit results for samples oxidized at pH 7.1*.

Samples	Shell No.	Pair	N	R(Å)	σ^2(Å^2)	$\log_{10}\Gamma^{\ddagger}$
0 h oxidation	1	As-S	2.6	2.26	0.0055†	-1.76
		As-As	0.93	2.53	0.0058†	
	2	As-As	1.8	3.51	0.006†	
		ΔE_0 = -8.07 eV, R_f = 0.029				
1 h oxidation	1	As(V)-O	2.4	1.69	0.0033†	-1.76
		As(III)-O	0.84	1.79	0.0037†	
	2	As-Fe	0.27	2.92	0.0044†	
		As-Fe	0.52	3.37	0.0048†	
		ΔE_0 = -11.24 eV, R_f = 0.051				
2 h oxidation	1	As(V)-O	3.3	1.69	0.0033†	-1.76
		As(III)-O	0.54	1.79	0.0037†	
	2	As-Fe	0.30	2.95	0.0044†	
		As-Fe	1.0	3.37	0.0048†	
		ΔE_0 = -12.00 eV, R_f = 0.044				
4 h oxidation	1	As(V)-O	3.8	1.69	0.0033†	-1.76
	2	As-Fe	0.36	2.94	0.0044†	
		As-Fe	0.78	3.36	0.0048†	
		ΔE_0 = -12.60 eV, R_f = 0.044				
192 h oxidation	1	As(V)-O	3.9	1.69	0.0033†	-1.76
	2	As-Fe	0.32	2.92	0.0044†	
		As-Fe	0.90	3.36	0.0048†	
		ΔE_0 = -10.86 eV, R_f = 0.041				

*The amplitude-reduction factor (S_o^2) was set at 0.92.
†The Debye-Waller factors (σ^2) were fixed during the numerical fit.
$^{\ddagger}\Gamma$ is defined as the surface loading, which is given by the molar ratio of sorbed As to solid-phase Fe.

Table 1.14. EXAFS fit results for samples oxidized at pH 9.1*.

Samples	Shell No.	Pair	N	R(Å)	σ^2(Å^2)	$\log_{10}\Gamma^{\ddagger}$
0 h oxidation	1	As-S	2.8	2.28	0.0055†	-1.94
		As-As	0.66	2.52	0.0058†	
	2	As-As	0.79	3.56	0.006†	
		ΔE_0 = -3.69 eV, R_f = 0.034				
1 h oxidation	1	As(V)-O	1.4	1.69	0.0033†	-1.79
		As(III)-O	2.2	1.79	0.0037†	
	2	As-Fe	0.33	2.95	0.0044†	
		As-Fe	0.64	3.42	0.0048†	
		ΔE_0 = -5.31 eV, R_f = 0.054				
2 h oxidation	1	As(V)-O	3.7	1.69	0.0033†	-1.77
		As(III)-O	0.28	1.79	0.0037†	
	2	As-Fe	0.41	2.90	0.0044†	
		As-Fe	0.69	3.37	0.0048†	
		ΔE_0 = -14.50 eV, R_f = 0.045				
4 h oxidation	1	As(V)-O	4.0	1.69	0.0033†	-1.76
	2	As-Fe	0.35	2.90	0.0044†	
		As-Fe	0.72	3.35	0.0048†	
		ΔE_0 = -14.74 eV, R_f = 0.043				
192 h oxidation	1	As(V)-O	3.8	1.69	0.0033†	-1.76
	2	As-Fe	0.36	2.91	0.0044†	
		As-Fe	0.61	3.38	0.0048†	
		ΔE_0 = -8.96 eV, R_f = 0.042				

*The amplitude-reduction factor (S_o^2) was set at 0.92.
†The Debye-Waller factors (σ^2) were fixed during the numerical fit.
$^{\ddagger}\Gamma$ is defined as the surface loading, which is given by the molar ratio of sorbed As to solid-phase Fe.

interatomic distance of ≈2.26 Å. By XRD, Gallegos et al. (2007) found a disordered realgar phase at pH 5 in As(III)-reacted FeS. In their study, a much higher As(III) was used (e.g., 2×10^{-3} mol As(III) per g FeS). Similarly, Wilkin and Ford (2006) observed formation of orpiment and alacranite (a polymorph of realgar) when acidifying As(III)-reacted FeS. At pH 7.1 and 9.1, As-S interactions result from surface complexation or precipitation of thioarsenites on FeS rather than discrete arsenic sulfide phases. Even after 1−2 h oxidation, the samples at pH 4.9 maintain a first shell featured by As-S interaction, supporting the persistent nature of a realgar-like precipitate against oxidation. This indicates that under mildly oxidizing, acidic conditions, the solubility of arsenic may be controlled by discrete arsenic sulfides including realgar and orpiment, both of which are known to be oxidized more slowly than pyrite, which is far more resistant to oxidation than mackinawite (Lengke and Tempel, 2005).

The first coordination shell peaks of the unoxidized samples, compared with those of disordered AsS and As_2S_3, are noticeably broader on the higher *R* side. Such a feature is likely due to additional path in the first coordination shells. As shown in the Fourier transforms, either arsenopyrite or As(0) may contribute to the broader shoulders on the higher *R* side of the first coordination shell peaks. Although the strong oscillations at low *k* in the EXAFS spectrum of arsenopyrite are incompatible with the EXAFS spectra of the unoxidized samples, the relatively weak oscillations in the As(0) spectrum at $k < \approx 7$ Å^{-1} are compatible. Inclusion of As-As subshell at ≈2.52 Å, close to As-As bonding distance in As(0) (Foster est al., 1998), significantly improves the numerical fits. X-ray photoelectron spectroscopy (XPS) analysis (unpublished data) also supports the formation of As(0). Considering a strong affinity of As(III) with sulfides, the observation of As(0) was unexpected. Nonetheless, thermodynamic calculations (Ferguson and Gavis, 1972, Nordstrom and Archer, 2003) support As(0) formation in highly reduced aquatic environments. Indeed, Stauder et al. (2005) reported As(0) formation in sulfidic solutions. The As-As component in the first shells quickly disappeared in 1 h oxidation at all pH conditions (see Tables 1.12-1.14), indicating the high instability of As(0) under oxic conditions.

Unlike disordered AsS and As_2S_3, the unoxidized samples have apparent second coordination shells at ≈3.5 Å, causing their EXAFS spectra to significantly deviate from those of these arsenic sulfides at $k > \approx 9$ Å^{-1}. These second shells can be assigned to either As-Fe or As-As bondings. Although As-Fe bonding may result from the surface complexes of thioarsenites with FeS, such a possibility can be ruled out by geometric consideration. Bostick et al. (2003) have proposed a surface cluster or precipitate in the form of trimeric arsenic sulfide ($As_3S_3(SH)_3$) in As(III) uptake by PbS and ZnS. The As-As bonding distance of ≈3.6 Å in their study is close to that observed here. Also, in agreement with the structure of trimeric thioarsenites (Helz et al., 1995), the As-As coordination number in the second shells ($N_{As\text{-}As}$) at pH 4.9 and 7.1 is close to 2, indicating the dominance of trimeric thioarsenite cluster. However, the much smaller $N_{As\text{-}As}$ at pH 9.1 indicates a mixture of monomeric and trimeric thioarsenites on the FeS surface. The As-As second shells at pH 7.1 and 9.1 disappear more quickly than at pH 4.9, consistent with the faster oxidation of arsenic sulfides observed at higher pH (Lengke and Tempel, 2005). In previous XAS studies (Farquhar et al., 2002, Wolthers et al., 2005, Gallegos et al., 2007), As(III) was found to be sequestered by FeS via surface complexation at low surface loadings (e.g., moles of arsenic sorbed per g FeS) and formation of discrete arsenic sulfides at high loadings. The relatively higher surface loading used here favors formation of thioarsenite surface clusters and bulk arsenic phases (e.g., As(0) and a realgar-like precipitate).

Except for the sample oxidized for 1−2 h at pH 4.9, the EXAFS spectra of the oxidized samples are similar to one another (Table 1.12). Their first coordination shells are characterized

by As(III)-O interaction at 1.79 Å and As(V)-O interaction at 1.69 Å, suggesting that arsenic oxyanions form surface complexes with Fe (oxyhydr)oxides. The longer interatomic distance of As(III)-O compared to As(V)-O in the surface complexes is consistent with that observed in their aqueous counterparts (Table 1.11). In agreement with the gradual shift of the XAS absorption edges to higher energies at pH 7.1 and 9.1, $N_{\mathrm{As(III)-O}}$ decreases as $N_{\mathrm{As(V)-O}}$ increases with the oxidation time (see Tables 1.13 and 1.14). The second coordination shells of the oxidized samples consist of two subshells: As-Fe pair interactions at ≈2.9 and ≈3.4 Å. These As-Fe distances are much shorter than the value reported for a monodentate surface complex (≈3.6 Å) (Waychunas et al., 1994, Fendorf et al., 1997), but close to the distances reported for a bidentate-mononuclear (edge-sharing) complex (2.80−2.83 Å) and a bidentate-binuclear (double corner-sharing) complex (3.25−3.29 Å) (Manceau and Charlet, 1994). The slightly longer As-Fe distances here reflect the distorted, elongated surface groups on Fe (oxyhydr)oxides. Fendorf et al. (1997) observed the dominance of bidentate-type complexes at higher surface loadings, which were even lower than those investigated here. Such innersphere complexes provide strong sequestration paths for the dissolved arsenic in oxic environments. In this study, lower dissolved arsenic concentrations were observed in highly oxidized samples than their corresponding unoxidized samples. Despite the difference of FeS oxidation mechanisms with pH, the long-term fate of arsenic can be effectively controlled by reaction with Fe (oxyhydr)oxides if these Fe phases are generated and maintained in the vicinity of arsenic contamination. Also, a rapid conversion of As(III) to As(V) during FeS oxidation results in the decreased arsenic toxicity.

Summary and Conclusions and Implications for Future Research/Implementation

Arsenic contamination of water is closely associated with changing redox conditions. Although the reductive dissolution of Fe (oxyhydr)oxides is generally considered the main path for arsenic mobilization, the oxidative dissolution of Fe sulfides may also lead to its mobilization. The results presented in this task show that arsenic mobilization and resorption occurs during aerobic oxidation of mackinawite (FeS), a major acid-volatile sulfide (AVS). When reacted with FeS, arsenic is sequestered by forming zerovalent arsenic (As(0)), surface clusters, and a realgar (AsS)-like precipitate. When oxygen is introduced, both As(0) and arsenic surface clusters are quickly destabilized whereas a realgar-like precipitate is more resistant. Arsenic mobility during FeS oxidation is controlled by its oxidation mechanisms, which are sensitive to pH. At acidic pH (and to some extent at neutral pH), the oxidative dissolution of FeS results in arsenic accumulation in water. The subsequent slow precipitation of Fe (oxyhydr)oxides retards the resorption of the released arsenic. Similar to oxidation of pyrite (a common non-AVS), FeS oxidation at basic pH proceeds via a surface-mediated reaction, leading to direct formation of Fe (oxyhydr)oxides and resorption of the arsenic species with no increase in the dissolved concentrations. This study reveals that although oxidation of FeS can lead to mobilization of arsenic for short periods of time, the Fe (oxyhydr)oxides oxidation products that form provide some level of protection against mobilization by resorbing arsenic regardless of pH. This suggests that in PRB applications of FeS, if oxidants such as oxygen enter the PRB for short periods of time, this should not lead to significant mobilization of arsenic, particular as released arsenic moves into regions in which oxidized Fe (oxyhydr)oxides have been formed.

Literature Cited

Anderson R.K., M. Thompson, and E. Culbard, 1986. Selective reduction of arsenic species by continuous hydride generation: part 1. Reaction media. *Analyst* **111**, 1143-1152.

Bostick B.C., and S. Fendorf, 2003. Arsenite sorption on troilite (FeS) and pyrite (FeS_2). *Geochim Cosmochim Acta* **67**, 909-921.

Bostick B.C., S. Fendorf, and B.A. Manning, 2003. Arsenite adsorption on galena (PbS) and sphalerite (ZnS). *Geochim Cosmochim Acta* **67**, 895-907.

Boursiquot S., M. Mullet, M. Abdelmoula, J.-M. Génin, and J.-J. Ehrhardt, 2001. The dry oxidation of tetragonal FeS_{1-x} mackinawite. *Phys Chem Mineral* **28**, 600-611.

Burton E.D., R.T. Bush, and L.A. Sullivan, 2006. Acid-volatile sulfide oxidation in coastal flood plain drains: iron-sulfur cycling and effects on water quality. *Environ Sci Tech* **40**, 1217-1222.

Caetano M., M.-J. Madureira, and C. Vale, 2003. Metal remobilisation during resuspension of anoxic contaminated sediment: short-term laboratory study. *Water Air Soil Poll* **143**, 23-40.

Cherry J.A., A.U. Shaikh, D.E. Tallman, and R.V. Nicholson, 1979. Arsenic species as an indicator of redox conditions in groundwater. *J Hydrol* **43**, 373-392.

Farquhar M.L., J.M. Charnock, F.R. Livens, and D.J. Vaughan, 2002. Mechanisms of arsenic uptake from aqueous solution by interaction with goethite, lepidocrocite, mackinawite, and pyrite: an x-ray absorption spectroscopy study. *Environ Sci Tech* **36**, 1757-1762.

Fendorf S., M.J. Eick, P. Grossl, and D.L. Sparks, 1997. Arsenate and chromate retention mechanisms on goethite. 1. Surface structure. *Environ Sci Tech* **31**, 315-320.

Ferguson J.F., J. Gavis J., 1972. A review of the arsenic cycle in natural waters. *Water Res* **6**, 1259-1274.

Foster A.L., G.E. Brown Jr., T.N. Tingle, and G.A. Parks, 1998. Quantitative arsenic speciation in mine tailings using x-ray absorption spectroscopy. *Am Mineral* **83**, 553-568.

Gallegos T.J., S.P. Hyun, and K.F. Hayes, 2007. Spectroscopic investigation of the uptake of arsenite from solution by synthetic mackinawite. *Environ Sci Tech* **41**, 7781-7786.

Génin J.-M.R., *et al*., 1998. Thermodynamic Equilibria in aqueous suspensions of synthetic and natural Fe(II)-Fe(III) green rusts: occurrences of the mineral in hydromorphic soils. *Environ Sci Tech* **32**, 1058-1068.

Helz G.R., *et al*., 1995. Oligomerization in As(III) sulfide solutions: theoretical constraints and spectroscopic evidence. *Geochim Cosmochim Acta* **59**, 4591-4604.

Holmes J., 1999. Fate of incorporated metals during mackinawite oxidation in sea water. *Appl Geochem* **14**, 277-281.

Jeong H.Y., J.H. Lee, K.F. Hayes, 2008. Characterization of synthetic nanocrystalline mackinawite: crystal structure, particle size, and specific surface area. *Geochim Cosmochim Acta* **72**, 493-505.

LaForce M.J., C.M. Hansel, and S. Fendorf, 2000. Arsenic speciation, seasonal transformations, and co-distribution with iron in a mine waste-influenced palustrine emergent wetland. *Environ Sci Tech* **34**, 3937-3943.

Lengke M.F., and R.N. Tempel, 2005. Geochemical modeling of arsenic sulfide oxidation kinetics in a mining environment. *Geochim Cosmochim Acta* **69**, 341-356.

Manceau A., and L. Charlet, 1994. The mechanism of selenate adsorption on goethite and hydrous ferric oxide. *J Colloid Interface Sci* **168**, 87-93.

Manning B.A., S. Goldberg, 1996. Modeling competitive adsorption of arsenate with phosphate and molybdate on oxide minerals. *Soil Sci Soc Am J* **60**, 121-131.

Morse J.W., 1991. Oxidation kinetics of sedimentary pyrite in seawater. *Geochim Cosmochim Acta* **55**, 3665-3667.

Moses C.O., and J.S. Herman, 1991. Pyrite oxidation at circumneutral pH. *Geochim Cosmochim Acta* **55**, 471-482.

Nordstrom D.K., and D.G. Archer, 2003. In *Arsenic in Ground Water*, eds Welch AH, Stollenwerk KG (Kluwer Academic Publishers, Boston), pp 1-25.

O'Day P.A., D. Vlassopoulos, R. Root, and N. Rivera, 2004. The influence of sulfur and iron on dissolved arsenic concentrations in the shallow subsurface under changing redox conditions. *Proc Natl Acad Sci USA* **101**, 13703-13708.

Refait P.H., O. Benali, M. Abdelmoula, and J.-M.R. Génin, 2003. Formation of 'ferric green rust' and/or ferrihydrite by fast oxidation of iron(II-III) hydroxychloride green rust. *Corros Sci* **45**, 2435-2449.

Stauder S., B. Raue, and F. Sacher, 2005. Thioarsenates in sulfidic waters. *Environ Sci Tech* **39**, 5933-5939.

Saulnier I., and A. Mucci, 2000. Trace metal remobilization following the resuspension of estuarine sediments: Saguenay Fjord, Canada. *Appl Geochem* **15**, 191-210.

Stumm W., and J.J Morgan, 1996. *Aquatic Chemistry, 3rd ed* (Wiley-Interscience, New York).

Waychunas G.A., B.A. Rea, C.C. Fuller, J.A. Davis, 1993. Surface chemistry of ferrihydrite: part 1. EXAFS studies of the geometry of coprecipitated and adsorbed arsenate. *Geochim Cosmochim Acta* **57**, 2251-2269.

Wilkin R.T., and R.G. Ford, 2006. Arsenic solid-phase partitioning in reducing sediments of a contaminated wetland. *Chem Geol* **228**, 156-174.

Wilkin R.T., and R.G. Ford, 2002. Use of Hydrochloric acid for determining solid-phase arsenic partitioning in sulfidic sediments. *Environ Sci Tech* **36**, 4921-4927.

Williamson M.A., and J.D. Rimstidt, 1994. The kinetics and electrochemical rate-determining step of aqueous pyrite oxidation. *Geochim Cosmochim Acta* **58**, 5443-5454.

Wolthers M., L. Charlet, C.H. van der Weijden, P.R. van der Linde, and D. Rickard, 2005. Arsenic mobility in the ambient sulfidic environment: sorption of arsenic(V) and arsenic(III) onto disordered mackinawite. *Geochim Cosmochim Acta* **69**, 3483-3492.

Yamauchi H., Fowler B.A., 1994. In *Arsenic in the Environment*, ed. J.O Nriagu (Wiley, New York), pp 35-53.

Subtask 1.6. Column Studies of As(III) Uptake by FeS-Coated Sand

Objective

The goal of this subtask was to assess the As(III) transport behavior in FeS-coated sand columns and to compare the column results with batch results. In this subtask, laboratory column studies were conducted to evaluate the use of FeS-coated sand to immobilize As(III) under in a column reactor under anoxic conditions. The column experiments were performed to evaluate the uptake of As(III) under hydrodynamic flow conditions more representative of PRBs. Experiments were performed over a range of pH values (5, 7, and 9). Capacities of the FeS-coated sand column reactor breakthrough data were compared to batch reactor data (Subtask 1.2) through the use of the retardation factor analysis and differences discussed.

Background

As one of the first acid volatile sulfides (AVS) to form, mackinawite is often found in the reactive zones of natural sediments and permeable reactive barriers (Herbert et al., 2000, Smyth et al., 2001, Burton et al., 2008). For example, in a natural sediment, more than 300 μmol S/g of AVS was measured and determined to be nanoparticulate mackinawite (Burton et al., 2008). The accumulation of disordered mackinawite was also observed in permeable reactive barriers composed of organic material to stimulate sulfate reducing conditions (Herbert et al., 2000). When present, mackinawite provides an effective sink for trace metals, resulting in an improvement of down-gradient groundwater quality (Ohfuji and Rickard, 2006). These examples illustrate the potential benefits of mackinawite-containing porous media for sequestering toxic metal ions and metalloids like Cd(II) and As(III).

Although mackinawite is often found in natural sediments or in the reactive zones of permeable reactive barriers, specific emplacement of FeS as a PRB material has not yet been attempted. When formed under low temperature aqueous conditions, freshly precipitated mackinawite is typically nanoparticulate and, as such, has extensive reactive surface area for a permeable reactive barrier (see e.g, Subtask 1.1). Although nanosized mackinawite is highly reactive, it may not be suitable for trench and fill PRB applications due to its potential to create low permeability zones and short circuiting within a PRB. To eliminate the possibility of permeability reduction by nanoscale particles, FeS-coated sand was developed in this project (Subtask 1.1; Han et al., 2009). While reducing the possibility of pore plugging, the FeS-coated sand also carries appreciable sorptive capacity for As(III) at pH 5, 7 and 9 under anoxic conditions as summarized in Subtasks 1.2.

Comparison of Batch and Column Results. Batch and column results may be compared in a variety of ways. For example, Wibulswas compared the Langmuir isotherm type adsorption capacity and column capacity in the adsorption system of methylene blue and its derivatives by montmorillonite and its modified forms (Wibulswas, 2004). The column capacity was determined as the adsorbed amount up to the BTC point at C/C_0=0.1 and was 78%, 19% and 18% of the batch results in three different clay columns. In contrast, a higher maximum removal capacity was obtained in column experiments using a variety of heavy metals (As, Cd, Cr, Cu, Hg, Pb and Zn) and natural sediment column. Thus, discrepancy was attributed to extra retention

of heavy metals by metal sulfide precipitation, a mechanism which was hypothesized not to occur in the batch system (Seo et al., 2008).

Estimating R from Batch Reactor Results. Alternatively, batch and column results may be compared using retardation factors. In column systems, the degree of sorption is often manifested in terms of retardation factor, R, whereas in batch systems, the degree of sorption may be described by a distribution coefficient K_d, defined as the ratio of adsorbate concentrations between the aqueous phase and solid phase. The two parameters may be related through the expression $R = 1 + \frac{\rho K_d}{\theta}$, where ρ and θ are the bulk density (g/cm^3) and porosity (unitless), respectively, of a porous medium. Yet this expression presumes a linear adsorption isotherm. If Langmuir sorption behavior is observed, the following equation can be utilized to describe the isotherm (Appelo and Postma 2005):

$$S = \frac{S_{\max} C_{eq}}{K_L + C_{eq}} \tag{1.5}$$

where S (μg/g) is the equilibrium concentration of solute in solid, K_L (μg/L) is the Langmuir constant related to the binding energy of the sorption system and $S_{\max}$ (μg/g solid) is the adsorption capacity. If the equilibrium concentration of the solute is low enough, the curve is essentially linear and the distribution coefficient, K_d can be estimated simply as

$$K_d = S / C_{eq} = S_{\max} / K_L \tag{1.6}$$

When the surface approaches saturation, the distribution coefficient becomes a function of equilibrium solute concentration, C_{eq}, and can be expressed by the following equation:

$$K_d = \frac{S_{\max} K_L}{(1 + K_L C_{eq})^2} \tag{1.7}$$

Using the fitted Langmuir isotherm, the determined S_{max} and K_L predicts K_d for the varying equilibrium concentrations of As(III) in solution. Therefore, in Langmuir type sorption, a retardation factor $R = 1 + \frac{\rho}{\theta} K_d$ can be expressed using equation (1.7):

$$R = 1 + \frac{\rho}{\theta} \frac{S_{\max} K_L}{(1 + K_L C_{eq})^2} \tag{1.8}$$

Estimating R from Column Reactor Results. The one-dimensional equilibrium transport model of a sorbing solute through a homogeneous, saturated soil column is described by the advection-dispersion equation (ADE):

$$\theta \frac{\partial C}{\partial t} + \rho \frac{\partial S}{\partial t} = \theta D \frac{\partial^2 C}{\partial x^2} - \theta v \frac{\partial C}{\partial x} \tag{1.9}$$

where x is distance (cm), t is time (h), ρ is bulk density (g/cm^3), θ is the water content, in this case, it is equal to the porosity (dimensionless), D is the hydrodynamic dispersion coefficient (cm^2/h), v is average pore-water velocity (cm/h), C is solution concentration (mol/cm^3) and S is sorbed concentration (mol/g).

The solute breakthrough curve (BTC) may be viewed as a probability distribution function. The nth absolute moments and normalized absolute moments for a pulse input may be defined as

$$\mu_n = \int_0^\infty t^n C(L,t)dt \tag{1.9}$$

$$\mu_n^* = \frac{\mu_n}{\mu_0} \tag{1.10}$$

where C(L,t) is the flux-averaged concentration at the exit boundary (x=L) at time t. For a pulse input of solute of duration t_0, the analytical expressions for the moments of the BTC are (Leij and Dane, 1991):

$$\mu_1^* = \frac{\mu_1}{\mu_0} = \frac{RL}{v} + \frac{t_0^2}{2} \tag{1.11}$$

Here, R can be back-calculated using the used experimental conditions L, ν and t_0. The method of moments (MOM) implicitly assumes reversible sorption so 100% mass recovery should be obtained, but in many cases, MOM is used where there is irreversible sorption (Limousin et al., 2007).

Interpretation of the Non-Ideal BTCs. Shapes of breakthrough curves are extensively used to characterize the physical and/or chemical processes of solute transport in porous media. Ideally, a non-sorbing conservative tracer will generate a symmetric breakthrough curve (BTC) with effluent concentration equaling 0.5 of the influent when one pore volume has passed through the column and eventually reaching a point when the effluent and influent concentrations are equal. In sorbing-solute transport associated with linear, reversible, adsorption, the BTC lags that of a conservative tracer, but has a similar shape. However, in real and complex systems, asymmetric BTCs with effluent concentrations that do not reach influent concentrations are observed.

Processes that can create an asymmetric BTC have been reviewed by Limousin et al. (2007) and include: 1) non-linear sorption behavior, 2) the presence of immobile water zones, 3) slow adsorption or desorption kinetics, 4) preferential flowpaths, 5) colloidal transport, or 6) low Peclet numbers. If the solute transport is coupled with biodegradation, a plateau of $C/C_0 <1$ would be observed due to a loss of contaminant mass (Angley et al. 1992; Brusseau et al. 1999). However, a plateau of $C/C_0 <1$ has also been reported even when abiotic processes govern solute transport and retention reactions. Incomplete BTC have been attributed to colloid deposition (Kretzschmar et al. 1997), non-equilibrium sorption, or due to contaminant transformation

reactions (Pang and Close 1999; Prima et al. 2002), irreversible sorption (Kim et al., 2006) or rate-limited sorption/desorption of contaminants (Jia et al. 2007; Pang and Close 1999).

In most cases, the apparent reduction of the total mass of a solute can be accounted for by an additional term in an advection-diffusion equation (ADE), which may be given as

$$\theta \frac{\partial C}{\partial t} + \rho \frac{\partial S}{\partial t} = \theta D \frac{\partial^2 C}{\partial x^2} - \theta v \frac{\partial C}{\partial x} - \theta \lambda C \qquad (1.12)$$

$$\lambda = \rho_b k \qquad (1.13)$$

where k is the rate constant (L/μg/hr) and λ is the first order reaction coefficient (1/h) that may be due to biodegradation, or in the case of abiotic causes, to irreversible contaminant sorption, chemical contaminant transformation, or colloid deposition of contaminant.

General Reasons of Discrepancies between Batch and Column Results. Although some consistency between distribution factors from column and batch experimental data have been observed when sorption is rapid and linear (Macintyre et al. 1991), more often discrepancies exist between them in reactive chemical transport systems. For example, in a study of strontium removal by crushed basalt, the researchers found that the distribution coefficient determined from batch tests did not accurately reflect the K_d value determined from a basalt packed column (Porro et al. 2000). In many cases, the K_d value from a flowing column system is lower than that from a well-mixed batch system (Dufresne and Hendershot 1986; Rainwater et al. 1987), but the reverse trend has also been reported (Miller et al. 1989; Seo et al. 2008). For example, in a study of the uptake of heavy metal ions by a natural sediment, Seo et al. (2008) reported the higher sorption capacity in the column experiments. They speculated the reason for the higher capacity was that metal sulfides co-precipitating in the column enhanced the metal retention compared to the batch system where only adsorption uptake was occurring. Other reasons for apparent discrepancies between uptake capacity data obtained from batches and column experiments include: (1) solid/solution ratio (SSR) where column reactors, which have a higher SSR have a lower uptake on a mass basis (Porro et al., 2000); (2) mixing effects which can result in greater particle disaggregation and therefore higher reactivity in well-mixed batch systems; (3) and adsorption/desorption or precipitation/dissolution reactions differences that can occur from a build up of reaction products in batch reactors compared to column flow systems where reaction products do not accumulate; and (4) differences in equilibration time in which batch reactor are typically given sufficient time to reach equilibrium compared to flowing column reactors in which rate limiting processes may become important.

Materials and Methods

Column Experiments. FeS-coated sand was packed in a glass column (internal diameter = 4.8 cm; length = 15 cm or 4.8 cm) by successively depositing approximately 1.5 cm of sand layers and compacting evenly with a ceramic pestle. Acid extraction of the FeS-coated sand used in the column tests yielded 1.42×10^{-5} mol FeS/g sand. Thus the total amount of FeS contained in a column was calculated to be 6.75 mmol (539 mg) FeS for a column packed with approximately 475.4 g sand for the 15 cm column. The experimental conditions and physical parameters of the column experiments are presented in Table 1.15. An influent solution of 1 ppm As(III) was prepared with deionized and de-aerated Milli-Q water to simulate groundwater under reducing

conditions and buffered at pH 5, 7 and 9. The buffer was 0.1M acetate buffer for pH 5, 0.1M 3-(N-morpholino)-propanesulfonic acid (MOPS) for pH 7 and 0.1M 2-(cyclohexylamino) ethanesulfonic acid (CHES) for pH 9. The columns were conditioned with

Table 1.15. Column experimental conditions.

	pH	Column Length	Pore water velocity*	Dispersivity*	Porosity	Retention time	Bulk density
Col #		cm	cm/hr	cm	-	hr	g/cm^3
1	pH 5	15	4.42	0.09	0.35	3.37	1.70
2	pH 7	15	4.55	0.06	0.34	3.27	1.73
3	pH 9	15	4.55	0.08	0.34	3.31	1.72
4	pH 5	4.8	4.11	0.08	0.35	1.16	1.67
5	pH 9	4.8	4.55	0.08	0.35	1.16	1.67
6	pH 9	4.8	1.39	0.14	0.35	3.44	1.67

*The parameters were obtained using CXTFIT fitting results of bromide breakthrough curves. Retention time is defined as the time it takes for 1 pore volume of the influent solution to pass through the column.

buffer solution in the absence of As(III) first until the iron concentration of the effluent became constant. At that point, an aqueous solution containing 1 ppm As(III) was then injected at the same pore water velocity of the conditioning fluid. The solution was pumped in an up-flow mode through the vertically oriented column at a constant flow rate with an HPLC pump (Varian Dynamax SD-200). Then, effluent from the column was collected with an automated fraction collector (ISCO ISIS autosampler), with about 1/10 of pore volume collected in each sampling tube. The injection of As(III) was terminated when the effluent As(III) concentration reached a plateau. Upon reaching the plateau, As(III)-free buffer solution was pumped into the column until the effluent As(III) concentration approached 0 ppm. All of the steps described above were performed in an anaerobic glove box with 95% nitrogen and 5% hydrogen atmosphere. The collected effluent samples were taken out of the glove box after acidification with nitric acid and then analyzed for their As(III) and Fe(II) concentration as total concentrations of As and Fe using an inductively coupled plasma mass spectrometry (ICP-MS, Perkin Elmer SCIEX, ELAN DRC-e).

Results and Discussion

As(III) Transport in FeS-Coated Sand. Figures 1.35 – 1.37 show the breakthrough curves of FeS-coated sand columns at pH 5, 7 and 9 in the 15-cm columns (Columns #1-#3, Table 1.15). The column shows the highest As(III) removal at pH = 5, with the observed breakthrough occurring at 213 pore volumes. The As(III) removal occurring up to the breakthrough point was 100%, so that the effluent concentration was zero up to this point. The total removed As(III) up to breakthrough is 3.46×10^{-2} g As(III) uptake/g FeS, about 82% of As(III) uptake determined

from batch experiments. After breakthrough, the As(III) concentration increased gradually until it reached 0.3 ppm (i.e., 30% of initial As(III) injected) and remained at this value for the next 85 pore volumes. This continuous high removal of As(III) at pH 5 is hypothesized to be due to the continuous dissolution of FeS, providing sulfide ion for the formation of arsenic sulfide (AsS).

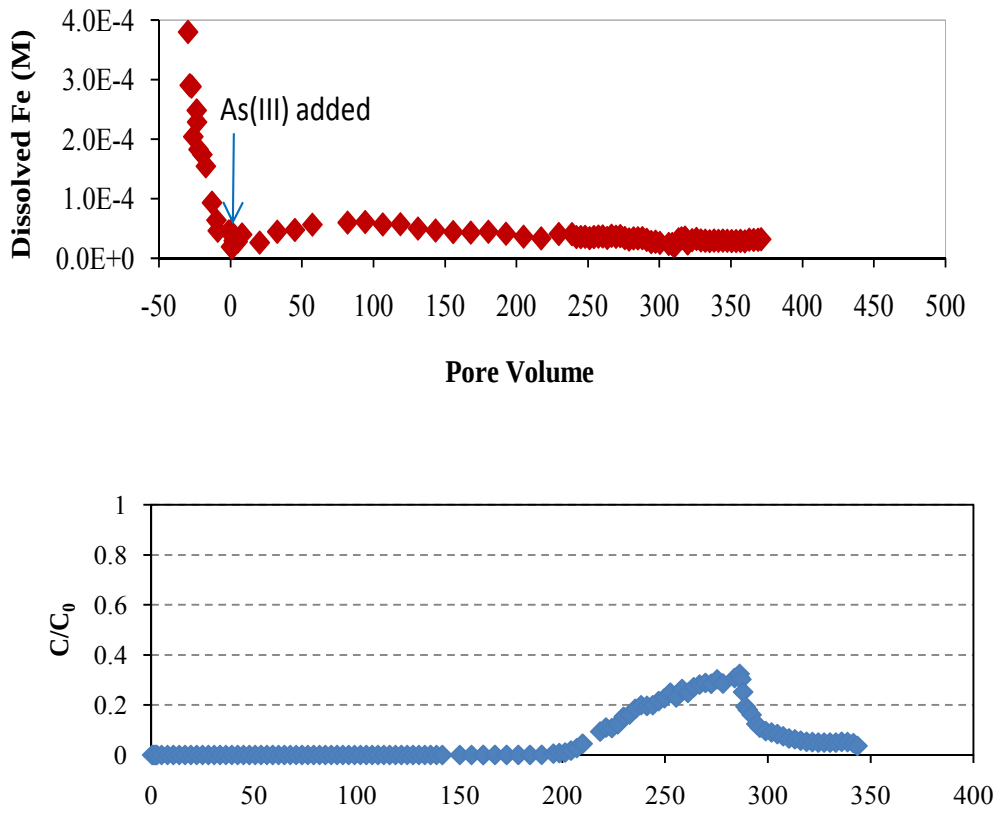

Figure 1.35. Column breakthrough curve at pH 5 (**bottom**) of FeS-coated sand column and concentration of dissolved Fe measured in effluent (**top**). (Influent: 0.1 M buffered solution with 0.013 mM (1 ppm) As(III) and 10 mM bromide with an average pore water velocity of 4.59 cm/hr).

The column experiment performed at pH 7 (Figure 1.36) resulted in the complete removal of As(III) over 10 pore volumes (effluent concentration was < 0.01 ppm). This behavior resulted in an estimated removal capacity of 1.5 $\times 10^{-3}$ g As(III)/g FeS. This value is about 13.7% of the removal capacity observed in batch experiments. In the pH 9 column (Figure 1.37), the effluent concentration of As(III) was below the detection level of 1 ppb until 2 pore volumes. Over the subsequent 4 pore volumes, more than 98% of the initially injected As(III) (under 0.02 ppm As(III)) was removed until the breakthrough point, which occurred at 6.4 pore volumes. The removal capacity at 6.4 pore volumes was 0.6 mg of As(III), which was 8.8% of the estimated batch-obtained removal capacity at pH 9.

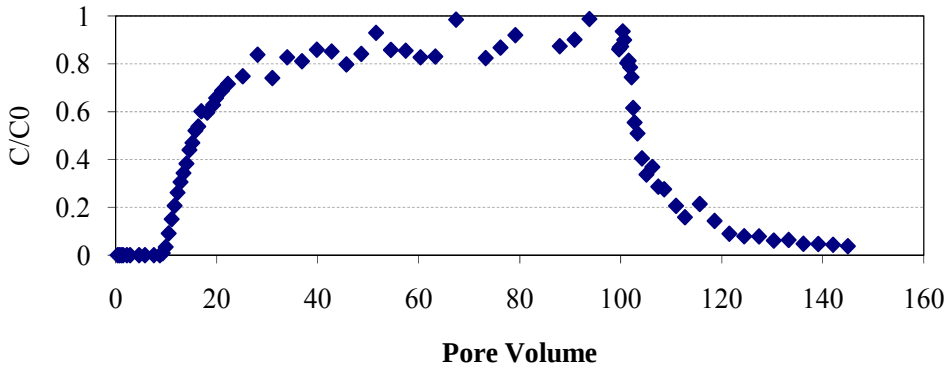

Figure 1.36. Column breakthrough curve at pH 7 of FeS-coated sand column. (Influent: 0.1 M buffered solution with 0.013 mM (1 ppm) As(III) and 10 mM bromide with an average pore water velocity of 4.59 cm/hr).

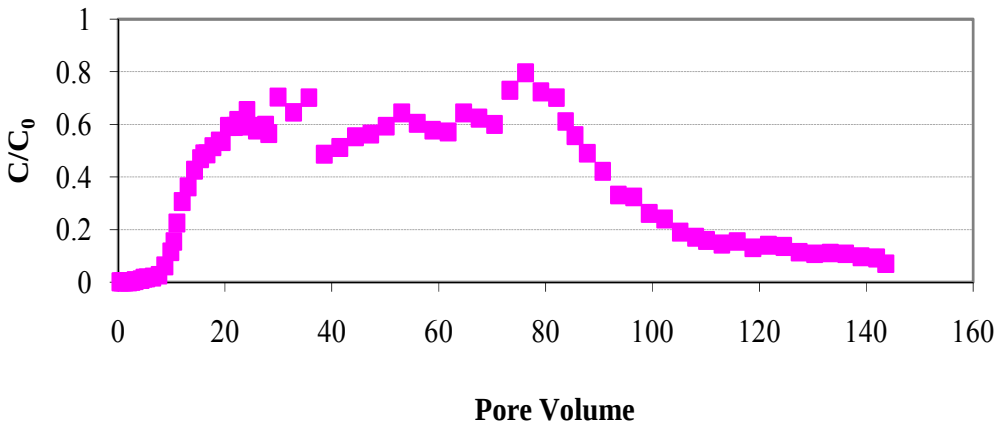

Figure 1.37. Column breakthrough curve at pH 9 of FeS-coated sand column. (Influent: 0.1 M buffered solution with 0.013 mM (1 ppm) As(III) and 10 mM bromide with an average pore water velocity of 4.59 cm/hr).

From the desorption part of each breakthrough curve, the relative potential for the remobilization of removed As(III) from FeS-coated sand columns may be evaluated. At pH 5, only 1.8 % of the removed As(III) was eluted indicating very effective retention of As(III) at this pH. In contrast, at pH 7 and pH 9 much higher amounts of As(III) were eluted during the desorption step, 34.6 % and 61.3 %, respectively. At pH 9, the desorption curve was much less steep than that at pH 7, which showed a sharper decrease. The pH 9 column curve also showed a longer tailing feature. The differences in the desorption behavior at the various values of pH suggests differences in the removal mechanisms. The formation of realgar is thought to be the primary removal mechanism at pH 5 and to a lesser extent at pH 7, resulting in more irreversible removal. The higher extent of desorption at pH 9 is thought to be caused by the slow reversibility of the adsorption that occurs during most of the column uptake (except for the initial phase of nearly complete removal prior to breakthrough which is thought to be through precipitation).

Comparison of the Column vs. Batch Results using Capacity Calculations. Differences in the capacity estimations of FeS-coated sand for As(III) uptake were observed between the experimental results from batch and column reactors. Table 1.16 summarizes the total immobilized As(III) per unit mass of FeS-coated sand in the batch reactor (column e, in Table 1.16) and in column reactor at the starting point of breakthrough (a) and total amount of As(III) uptake (b) and retained amount (c) after subtracting desorption (d).

If the total amount of As(III) retained at pH 5 in the long column (Table 1.16, Column #1) after breakthrough is considered, the As(III) removal capacity of the column is greater than that obtained in the batch. In fact, the maximum capacity would be expected to be greater than 105.6% since further arsenic removal would be expected as the concentration of iron (Figure 1.34), indicative of the presence of sulfide, does not show signs of declining even at 350 pore volumes. However, the maximum computed capacities of the columns at the higher values of pH, pH 7 and pH 9 are considerably less than their respective batch capacities. Yet this comparison may not be valid as the As concentrations in the batch systems were considerably greater than those in the column systems, as the influent concentration in the column systems was only 1 ppm.

Table 1.16. Comparison As(III) removal capacity between column and batch reactor results for long column experiments (Columns #1-#3).

	Calculated result of As(III) removal (unit: µg As(III)/g FeS-coated sand)				**Estimated parameters using Langmuir isotherm model**				**Using MOM**
Index	**a**	**b**	**c**	**d**	**e**	**f**	**g**	**h**	**i**
	BT capacity (BT point, % batch result)	**Total removed (Injected PV)**	**Maximum capacity (% batch)**	**Percent desorption**	**S_{max} (g As/g sand)**	**K_L (L/g As)**	**R^2**	**R_B at Ceq=1ppm**	**R_C with MOM Ceq=1ppm**
pH 5	43.3 (215 PV, 82.2 %)	56.6 (298 PV)	55.6 (105.6%)	1.8	5.20×10^{-5}	1388.15	0.99	61.3	>300
pH 7	1.9 (10 PV, 13.9 %)	5.62 (100 PV)	3.8 (27.7 %)	34.6	1.34×10^{-5}	781.74	0.95	16.7	14.1
pH 9	1.3 (6.4 PV, 8.9 %)	7.36 (80PV)	2.84 (20.1%)	61.3	1.58×10^{-5}	1076.13	0.96	19.7	24.9

BT capacity = As(III) removal capacity of packed column until the effluent As(III) concentration meets the regulated As(III) concentration for drinking water (10 ppb)
% batch result = mass of As(III) removed in column as percent of that removed in batch.
PV = pore volume.
Total removed = Total adsorption – Total desorption.
Maximum capacity = mass removed in batch system at the given pH.
Percent desorption = mass of total As(III) removed that elutes upon injection with As(III)-free solution expressed as percent of total mass removed.
R_B = retardation factor defined by batch experiments (Eqn. 1.8).
R_C = retardation factor obtained from column experiments (Eqns. 1.9-1.11).

Comparison of the Long Column vs. Batch Results Based on Retardation Factors. Table 1.16 gives the batch-obtained retardation coefficients, R_B, and the column-obtained retardation

coefficients, R_C. The values of R_B and R_C are more similar at pH 7 and pH 9, when adsorption dominantly controls the As(III) removal process. Since the sorption behavior of As(III) on FeS-coated sand shows a high degree of non-linearity with a shape typical of Langmuir-type sorption, the retardation factors should vary with different equilibrium As(III) concentrations. In the same manner, the column retardation factors should vary with different concentrations of injected As(III). Thus, the retardation factors were recalculated using Eqn. 1.8, for various equilibrium As(III) concentrations and are shown in Figure 1.38. The retardation factor approaches R=1 as the As(III) concentration becomes larger, while the retardation factor increases abruptly when the equilibrium As(III) concentration becomes smaller.

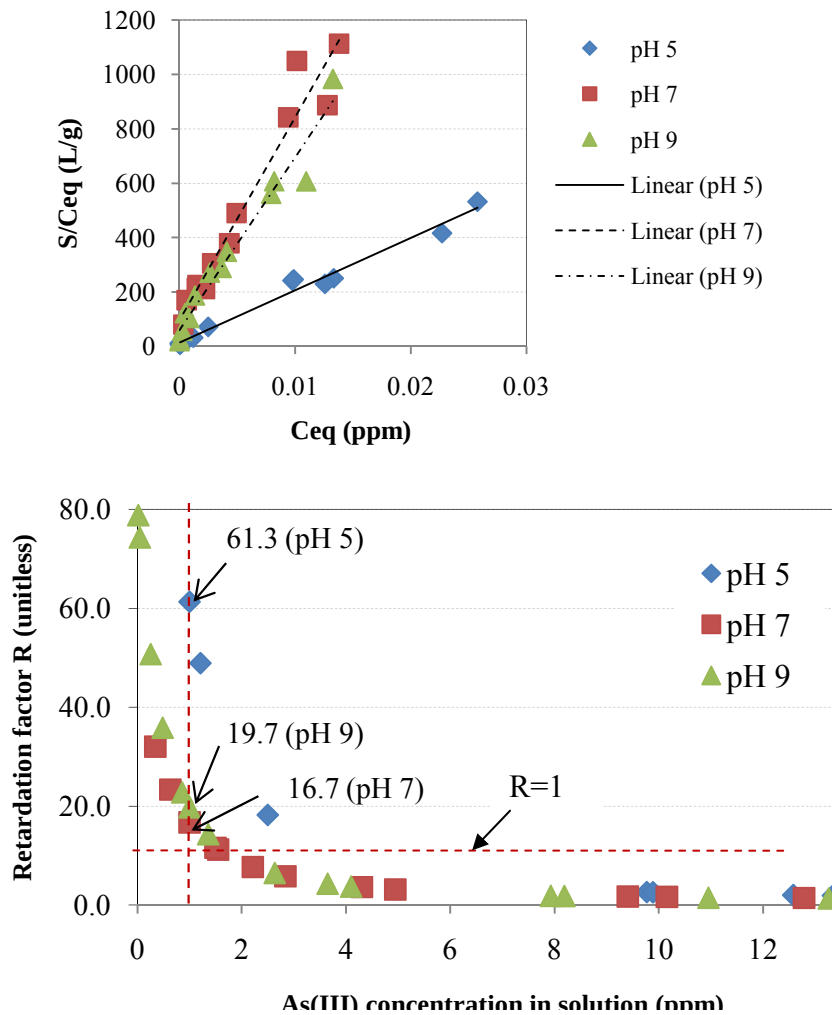

Figure 1.38. Linearized Langmuir sorption isotherms at pH 5, 7 and 9 (**top**) and estimated retardation factors (**bottom**) at varying equilibrium aqueous arsenic concentrations at pH 5, 7 and 9. The vertical dotted line denotes As(III) concentration = 1 ppm, the influent column concentration, and the horizontal dotted line shows that R approaches the value of 1 as the As(III) concentration increases.

Based on Eqn. 1.8, the values of R_B at aqueous As(III) concentrations equal to 1 ppm were estimated as 61.3, 16.7 and 19.7 at pH 5, 7, and 9, respectively. On the other hand, the

values of R_C calculated using the method of moments (MOM) are 14.9 (88% of R_B) and 24.9 (126% of R_B) at pH 7 and pH 9, respectively. At pH 5, the MOM cannot truly be applied since the effluent concentration never reaches a value greater than $0.5C_0$, due to the continuous removal by precipitation. However, the data presented suggests that the value of R_C at pH 5 would be greater than 300, or greater than 400% of the value of R_B.

Speculations about the Discrepancies between Batch and Column Results. Two different approaches were applied to compare As(III) removal results obtained in the batch and column reactors. The first approach used a capacity calculation based on total removed amount of As(III). This approach suggested greater removals in the column reactor at pH = 5 where the precipitation of arsenic sulfide predominates as the As(III) removal mechanism, and lesser removals at pH 7 and pH 9, where adsorption dominates. On the other hand, the results from MOM suggested far greater removals in the column at pH 5, slightly more at pH 9, and comparable removals at pH 7.

These differences may be attributable to two factors: (1) the difference in the mechanism of uptake and (2) the difference in the solid solution ratio (SSR) effect at pH 5 versus pH 9. At pH 5, As(III) removal occurs through the precipitation of arsenic sulfide solids (e.g., orpiment, As_2S_3 or realgar, AsS). Since the flowing column system leads to a greater mass of sulfide being available for the formation of precipitates, the removals are greater in the column. At pH 7 and 9, uptake occurs mostly via a surface-limited sorption reaction (Gallegos et al., 2007). Therefore, the distribution of As(III) between solid and solution phases is more important; if the uptake in the batch and columns systems is evaluated at similar concentrations (e.g., As(III) = 1 ppm), the uptake is comparable.

Solid-Solution Ratio (SSR) Effect and Redox Change. The data presented in Figure 1.39 shows the impact of the solid-solution ratio (SSR) defined as mass solid (g): volume solution (L). At pH 5 (Figure 1.39a), a lower SSR results in less uptake, perhaps due to a reduction in the concentration of dissolved sulfide and an enhancement in the oxidation of FeS, resulting in the inhibition of precipitation. Figure 1.40 shows the concentration of Fe in solution as a function of SSR. The concentration of dissolved Fe, indicative of the concentration of dissolved sulfide ion, increases with SSR and may be the main cause of greater removal of As(III) at higher SSRs. Additionally, at pH 5, the oxidation state of the FeS-coated sand suspension varies with SSR. FeS has a reductive potential so more FeS induces a more reduced condition; this was verified from measured Eh values in FeS suspensions at various concentrations (Gallegos et al., 2008). The right part of Figure 1.40 displays measured pe values with varying SSR in FeS-coated sand suspensions. The trend of decreasing pe with increasing SSR is consistent with what was observed in the pure FeS system (Gallegos, 2007). The relationship between pe and As(III) uptake is unclear, but it can be speculated that a reduced condition may be more conducive to the removal of As(III) from systems where iron sulfide actively plays a role. Under highly oxidizing conditions, the FeS may be oxidized to a less soluble form of iron sulfide or iron oxide and consequently, the free sulfide ion would be less. Therefore, a lower arsenic removal with a lower SSR could result partly from a more oxidized condition.

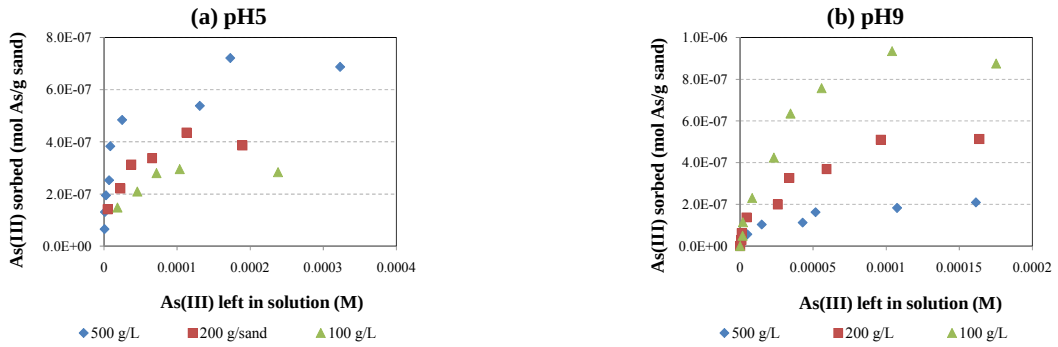

Figure 1.39. Sorption isotherm of As(III) as a function of solid (g)-solution (L) ratio of FeS-coated sand suspensions at (a) pH 5 and (b) pH 9.

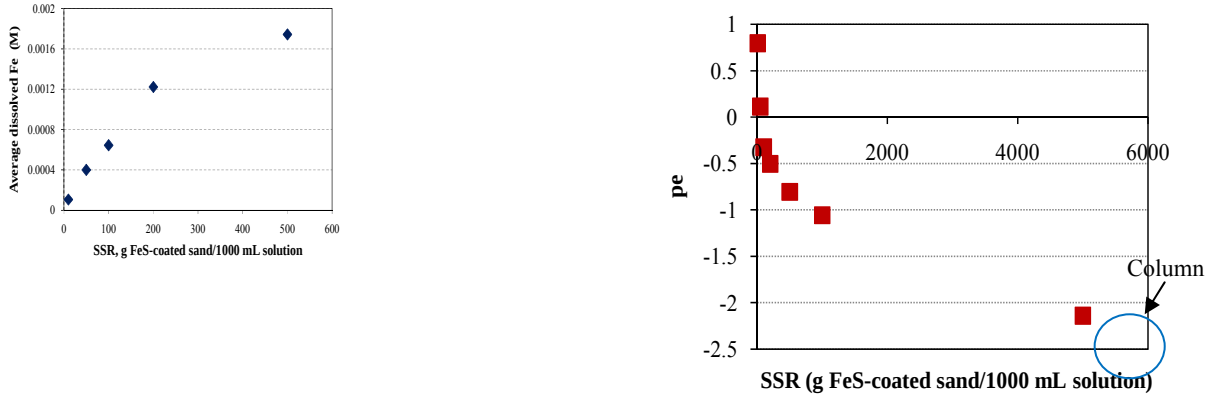

Figure 1.40. SSR-dependent Fe dissolution concentration (**left**) and the measured pe (**right**) in FeS-coated sand batch suspensions at pH 5. The x-axis number means the g mass of sand per 1000 mL solution. The marked point in the right plot shows the equilibrium pe value measured in a closed effluent chamber attached at the column end.

The opposite trend of SSR effect was observed at pH 9 compared to that observed at pH 5; however the trend observed at pH 9 is the more commonly reported effect. The literature suggests that solute sorption generally decreases with SSR (Bajracharya et al., 1996; Porro et al., 2000; Phillippi et al., 2007). The reason why a higher SSR results in the inhibition of the adsorption process is not clear, but several possible explanations have been posited. At low SSRs, the amount of solute is abundant compared to the limited number of surface sites so the most sorption sites would be utilized, regardless of favorability (due to perhaps, energetics or accessibility), while at high SSRs, the degree of sorption is far below full saturation so only the most favorable sites only would be utilized (Hemming et al., 1997). The degree of favorability

may also be due to competitive adsorption. For example, in the study presented by Grolimund et al. (1995), prewashing the solids eliminated the SSR effect suggesting that pre-adsorbed ions may have caused the SSR effect. In the pH 9 system here, aqueous arsenite or thioarsenite species may be present along with silicate dissolved from the natural silica sand. Moreover, the solid surface of FeS-coated sand may present a variety of sorption sites, due to the existence of FeS, oxidized magnetite or greigite of the coating and the iron oxide uncoated surface of the natural sand (Figure 1.23).

Kinetic Effect (Retention Time Dependent BTC Behavior). Often kinetic-limitations play a role in the determination of the shape of column breakthrough curves (Darland and Inskeep, 1997; Limousin et al., 2007). To examine the role of kinetics in these complex systems with different mechanisms of removal and opposite impacts of SSR, additional column experiments were carried with different retention times, obtained by varying the column length (Col. #1 and Col. #4 for pH 5, and Col. #3 and Col. #5 for pH 9) and by varying the flow rate (Col. #5 and Col. #6 for pH 9) (Table 1.15).

The results are presented in Figure 1.41. At pH 5, the relative effluent concentration eventually reaches 1 in the shorter column at about 150 pore volumes, whereas when the retention time is three times as long, the effluent concentration does not reach even 0.4 after over 250 pore volumes. At pH 5, the removal of As(III) is dominated by precipitation of arsenic sulfide (Gallegos et al., 2007). Thus, the comparative lack of removal at a smaller retention time may be due to the kinetics of the formation and deposition of the precipitate. A similar phenomenon was reported in a study investigating the deposition of goethite colloids in a column in that eventual breakthrough occurred at longer time scales as the flow velocity decreased (Satmark et al., 1996). Furthermore, in a study of zerovalent iron nano-particle deposition, He et al. (2009) found that particle deposition efficiency was proportionally related to the travel distance or travel time of the particles through the porous media, resulting in the achievement of different concentration plateaus (C/C_0) at different flow rates.

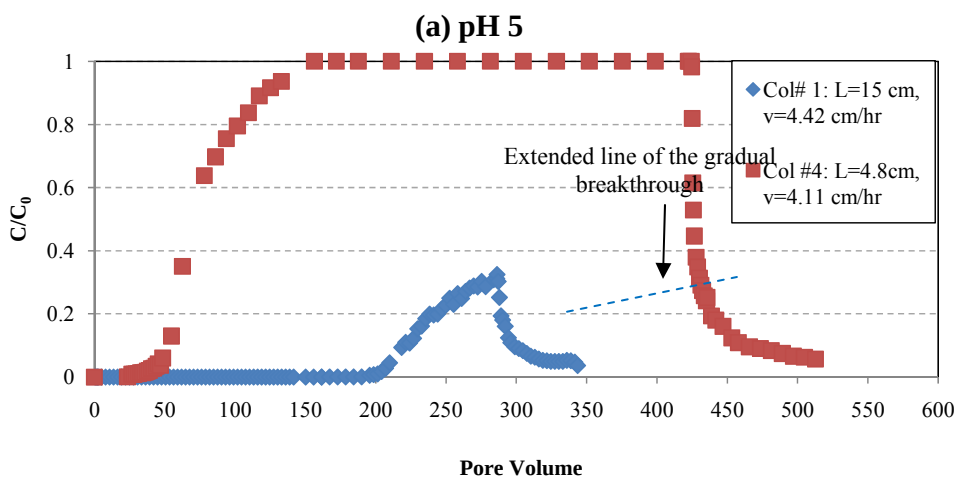

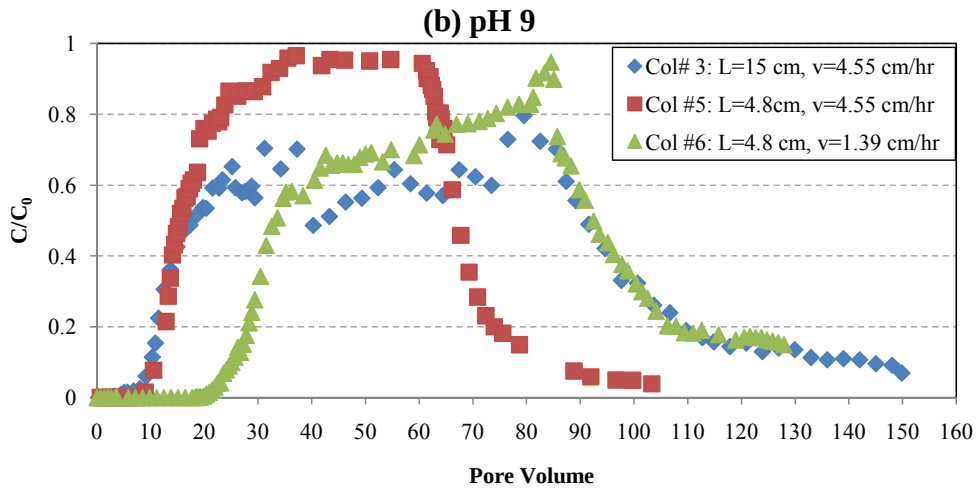

Figure 1.41. As(III) breakthrough curve with different column experimental conditions for (a) pH 5 and (b) pH 9 column influent with 1.3×10^{-5} M (1 ppm) As(III). The solute retention (travel) times for the columns are 3.37 hr (Col. #1), 1.16 hr (Col. #4), 3.31 hr (Col. #3), 1.16 hr (Col. #5) and 3.44 hr (Col. #6).

At pH 9, the short column with the higher velocity (retention time = 1.16 hr) (Col. #5) broke through with the fewest pore volumes of throughput and plateaued at a relative concentration of 1.0. The longer column at the same velocity (Col. #3), but with a longer retention time (retention time = 3.31 hr) showed initial breakthrough occurring at the same number of pore volumes as in the shorter column with the same flowrate (Col. #5); however the effluent concentration plateaued at a relative concentration of about 0.7 in the longer column, followed by a subsequent increase approaching 1.0. The difference in behavior based on residence time suggests a rate-limited process in the shorter column. The short column with the slower velocity (Col. #6), with a similar retention time (retention time = 3.44 hr) to the longer column (Col. #3) showed a later breakthrough, but similar behavior in that the relative concentration reached an initial plateau of about 0.6, followed by an increase over another 50 pore volumes or so. The columns with the longer retention times seem to show evidence for irreversible sorption, as well as for multiple types of adsorption sites. Kim et al. (2006) showed, by incorporating irreversible sorption into the advection-dispersion equation, that plateaus at relative concentrations of less than 1.0 could be simulated. In addition, simulations with two-site models showed rising relative concentrations, following breakthrough. Certainly, the spectroscopic assessment of the FeS-coated sand surface suggests the existence of a variety of sorption sites, including FeS, the oxidized magnetite or greigite of the coating and the iron oxide uncoated surface of the natural sand (Figure 1.23).

Summary and Conclusions and Implications for Future Research/Implementation

FeS-coated sand packed columns were tested to evaluate the As(III) uptake capacity under anaerobic conditions at pH 5, 7 and 9. A mechanistic understanding of the different removal processes at different pH conditions is important to the interpretation of the column experiment results. At pH 5, wherein precipitation of arsenic sulfide plays the major role in the uptake of

arsenic, the column shows a greater removal efficiency than the batch system for the removal of As(III) due to the continuous dissolution of sulfide and precipitation of arsenic sulfide. This greater removal is evident whether the comparison calculations are performed using capacity calculations or the method of moments (MOM). At pH 9, where adsorption mainly governs the arsenic removal, with a minor contribution of arsenic sulfide precipitation, capacity calculations suggest that greater removals are achieved in the batch systems than in the column systems. However, this comparison does not account for the observed nonlinearity in the sorption behavior. If the nonlinearity is accounted for, as in the MOM, removals are comparable in the column system. Column experiments with lower retention times, achieved either by increasing the flowrate or decreasing the column length, show that retention time is an important factor in controlling the efficiency of As(III) removal in the FeS-coated sand columns, both at pH 5 where the removal is primarily through precipitation and at pH where the removal is primarily through adsorption. Overall, the results of the column study suggest that FeS-coated sand removes As(III) as efficiently in a column system as in a batch system, provided that an adequate retention time is provided. These results suggest that FeS-coated sand is a viable alternative for removing As(III), and is especially effective if the pH is maintained below 7. The results reported here do not consider the field complexities of, for example, spatially and temporally variable pH and pe regimes or background solutes. Further investigation should focus on developing optimum geochemical site criteria in order to maximize the efficiency of the FeS-coated sand reactive medium presented here.

Literature Cited

Angley, J.T., Brusseau, M.L., Miller, W.L. and Delfino, J.J., 1992. Nonequilibrium sorption and aerobic biodegradation of dissolved alkylbenzenes during transport in aquifer material - Column experiments and evaluation of a coupled-process model. *Environmental Science & Technology* **26**(7), 1404-1410.

Appelo, C.A.J. and Postma, D., 2005. *Geochemistry, Groundwater and Pollution*, A.A. Balkema Publishers

Bajracharya, K., Tran, Y.T. and Barry, D.A., 1996. Cadmium adsorption at different pore water velocities. *Geoderma* **73**(3-4), 197-216.

Brusseau, M.L., Hu, M.Q., Wang, J.M. and Maier, R.M., 1999. Biodegradation during contaminant transport in porous media. 2. The influence of physicochemical factors. *Environmental Science & Technology* **33**(1), 96-103.

Burton, E.D., Bush, R.T., Sullivan, L.A., Johnston, S.G. and Hocking, R.K., 2008. Mobility of arsenic and selected metals during re-flooding of iron- and organic-rich acid-sulfate soil. *Chemical Geology* **253**(1-2), 64-73.

Darland, J.E. and Inskeep, W.P., 1997. Effects of pore water velocity on the transport of arsenate. *Environmental Science & Technology* **31**(3), 704-709.

Dufresne, A. and Hendershot, W.H., 1986. Comparison of aluminum speciation in soil solutions extracted by batch and column methods. *Canadian Journal of Soil Science* **66**(2), 367-371.

Gallegos, T.J., 2007. Sequestration of As(III) by synthetic mackinawite under anoxic conditions, Ph.D. diss., The University of Michigan, Ann Arbor.

Gallegos, T.J., Han, Y.S. and Hayes, K.F., 2008. Model Predictions of Realgar Precipitation by Reaction of As(III) with Synthetic Mackinawite Under Anoxic Conditions. *Environmental Science & Technology* **42**(24), 9338-9343.

Gallegos, T.J., Hyun, S.P. and Hayes, K.F., 2007. Spectroscopic investigation of the uptake of arsenite from solution by synthetic mackinawite. *Environmental Science & Technology* **41**, 7781-7786.

Grolimund, D., Borkovec, M., Federer, P. and Sticher, H., 1995. Measurement of sorption isotherms with flow-through reactors. *Environmental Science & Technology* **29**(9), 2317-2321.

Han, Y.S., Gallegos, T.J., Demond, A.H. and Hayes, K.F., 2009. FeS-coated sand for removal of arsenic(III) under anaerobic conditions: Coating method and characterization. *Water Research* **x**(x), xxx-xxx.(article submitted)

He, F., Zhang, M., Qian, T.W. and Zhao, D.Y., 2009. Transport of carboxymethyl cellulose stabilized iron nanoparticles in porous media: Column experiments and modeling. *Journal of Colloid and Interface Science* **334**(1), 96-102.

Hemming, C.H., Bunde, R.L., Liszewski, M.J., Rosentreter, J.J. and Welhan, J., 1997. Effect of experimental technique on the determination of strontium distribution coefficients of a surficial sediment from the Idaho National Engineering Laboratory, Idaho. *Water Research* **31**(7), 1629-1636.

Herbert, R.B., Benner, S.G. and Blowes, D.W., 2000. Solid phase iron-sulfur geochemistry of a reactive barrier for treatment of mine drainage. *Applied Geochemistry* **15**(9), 1331-1343.

Jia, Y., Breedveld, G.D. and Aagaard, P., 2007. Column studies on transport of deicing additive benzotriazole in a sandy aquifer and a zerovalent iron barrier. *Chemosphere* **69**, 1409-1418.

Kim, S.B., Ha, H.C., Choi, N.C. and Kim, D.J., 2006. Influence of flow rate and organic carbon content on benzene transport in a sandy soil. *Hydrological Processes* **20**(20), 4307-4316.

Kretzschmar, R., Barmettler, K., Grolimund, D., Yan, Y.D., Borkovec, M. and Sticher, H., 1997. Experimental determination of colloid deposition rates and collision efficiencies in natural porous media. *Water Resources Research* **33**(5), 1129-1137.

Leij, F.J. and Dane, J.H., 1991. Solute transport in a 2-layer medium investigated with time moments. *Soil Science Society of America Journal* **55**(6), 1529-1535.

Limousin, G., Gaudet, J.P., Charlet, L., Szenknect, S., Barthes, V. and Krimissa, M., 2007. Sorption isotherms: A review on physical bases, modeling and measurement. *Applied Geochemistry* **22**(2), 249-275.

Macintyre, W.G., Stauffer, T.B. and Antworth, C.P., 1991. A comparison of sorption coefficients determined by batch, column, and box methods on a low organic-carbon aquifer material. *Ground Water* **29**(6), 908-913.

Miller, D.M., Sumner, M.E. and Miller, W.P., 1989. A comparison of batch-generated and flow-generated anion adsorption-isotherms. *Soil Science Society of America Journal* **53**(2), 373-380.

Ohfuji, H. and Rickard, D., 2006. High resolution transmission electron microscopic study of synthetic nanocrystalline mackinawite. *Earth and Planetary Science Letters* **241**(1-2), 227-233.

Pang, L.P. and Close, M.E., 1999. Non-equilibrium transport of Cd in alluvial gravels. *Journal of Contaminant Hydrology* **36**(1-2), 185-206.

Phillippi, J.M., Loganathan, V.A., McIndoe, M.J., Barnett, M.O., Clement, T.P. and Roden, E.E., 2007. Theoretical solid/solution ratio effects on adsorption and transport: Uranium(VI) and carbonate. *Soil Science Society of America Journal* **71**(2), 329-335.

Porro, I., Newman, M.E. and Dunnivant, F.M., 2000. Comparison of batch and column methods for determining strontium distribution coefficients for unsaturated transport in basalt. *Environmental Science & Technology* **34**(9), 1679-1686.

Prima, S., Evangelou, V.P. and McDonald, L.M., 2002. Surface exchange phase composition and nonionic surfactant effects on the nonequilibrium transport of atrazine. *Soil Science* **167**(4), 260-268.

Rainwater, K.A., Wise, W.R. and Charbeneau, R.J., 1987. Parameter-estimation through groundwater tracer tests. *Water Resources Research* **23**(10), 1901-1910.

Satmark, B., Albinsson, Y. and Liang, L., 1996. Chemical effects of goethite colloid on the transport of radionuclides through a quartz-packed column. *Journal of Contaminant Hydrology* **21**(1-4), 231-241.

Seo, D.C., Yu, K. and DeLaune, R.D., 2008. Comparison of monometal and multimetal adsorption in Mississippi River alluvial wetland sediment: Batch and column experiments. *Chemosphere* **73**(11), 1757-1764.

Smyth, D.J.A., Blowes, D.W., Benner, S.G. and Ptacek, C.J., 2001. In situ treatment of metals-contaminated groundwater using permeable reactive barriers. *Bioremediation of Inorganic Compounds* **6**(9), 71-78.

Wibulswas, R., 2004. Batch and fixed bed sorption of methylene blue on precursor and QACs modified montmorillonite. *Separation and Purification Technology* **39**(1-2), 3-12.

Task 2. EVALUATE MICROBIAL METHODS FOR REGENERATION OF FeS PRBS (ADRIAENS)

Objective

The two major objectives of this task were to evaluate the potential of sulfate reducing bacteria for regeneration of FeS from its oxidized iron products and to assess the reactivity of biogenically produced FeS for As(III) and Cd(II) removal from groundwater.

Background

Biotic sulfate reduction is a naturally occurring process resulting from activities of Gram-negative sulfate reducing bacteria (SRB, belonging to the δ–subclass of the Proteobacteria), and Gram-positive SRB and *Archaea,* that together are referred to as sulfate reducing prokaryotes. Gram-negative SRB are often present at low levels in environments (Lovley and Phillips, 1992) with high sulfate-reducing activity, suggesting either Gram-positive SRB or *Archaea* significantly contribute to SRB activity in sulfate rich environments (Hristova *et al*., 2000). Consistent with this, *Desulfotomaculum* sp., a Gram positive mesophilic bacterium, was recently isolated from an enrichment culture from a high sulfate containing sediment layer of the Pacific Ocean (Barnes *et al*., 1998). However, Sass et al. (1997) have also isolated SRB of the genus *Desulfotomaculum* from deeper sediment layers of a low sulfate bearing, oligotrophic lake. Likewise, *Desulfovibrio* spp. (Gram-negative) have been detected in high sulfate marine sediments (Barnes *et al*., 1998; Sahm *et al*., 1999) while *Desulfotomaculum* spp. (Gram-positive) have been encountered in low sulfate groundwater aquifers (Boivin-Jahns *et al*., 1996). These SRB have been found to generate a variety of mono and di-sulfide iron minerals, however, the form and SRB species-specific impact on the type of iron sulfide minerals generated are not well understood. These observations clearly indicate the need to assess the ability of SRB species on type and abundance of iron sulfides that they can produce.

SRB have been directly implicated in the formation of a variety of iron sulfides including mackinawite and/or gregite (Rickard, 1969; Herbert *et al*., 1998; Benning *et al*., 1999), pyrrhotite (Neal *et al*., 2001), and pyrrhotite or mackinawite (Matsuo *et al*., 2000). Schoonen and Barnes (1991) have shown SRB produce sulfur species with various oxidation states that may react with iron to form an array of different mono-, di- and poly-sulfides. Although these investigations have revealed the types of metal or iron sulfides that may form in the presence of SRB (Hebert *et al*., 1998; Matsuo *et al*., 2000; Neal *et al*., 2001; Posfai *et al.,* 1998) or the impact of different iron sources/acceptors on the formation of iron hydroxide solid phases (Zachara *et al*., 1998; Tebo and Obraztsova, 1998; Karnachuk *et al*., 2002), the importance of SRB phylogeny or iron source on the type of iron sulfide phase generated has not been systematically explored.

The reactive capacity of iron sulfide-based permeable reactive barriers (PRB) to complex and co-precipitate heavy metal ions from groundwater will depend on the potential for regeneration of reactive FeS during the expected lifetime of the PRB. FeS reactivity may decrease in a PRB in time as the result of the following processes: (i) oxidation of FeS and the formation of ferric iron (Fe(III)) oxide solids in the presence of oxygenated groundwater at the entrance of the PRB, (ii) oxidation of FeS in the presence of redox active metals like As(V) with the formation of ferric solids, (iii) co-precipitation of heavy metals within the PRB with the reactive FeS leading to the formation of insoluble metal sulfide co-precipitates with the concomitant release of ferrous iron and formation of ferrous (Fe(II) oxide, hydroxide, or

carbonate solids, (iv) and clogging of the PRB pore structure due to formation of precipitate products from processes (i) – (iii).

This work sought to develop the conditions for the biogenic production of FeS from iron sources likely to be present in PRBs, with the sulfides and FeS so formed to be subsequently used for enhanced treatment of metals (e.g., Cd(II)) and metalloids (e.g., As(III)) through bulk and surface precipitation of metal sulfides and the adsorption of metals and metalloids onto FeS. SRB play a primary role in the development of appropriate reducing conditions for the generation of biogenic iron sulfide solids, and in the maintenance of sulfide mineral activation during redox fluctuations. The predominance of SRB communities in anaerobic and reducing ground waters, and their prevalence in zero-valent iron reactive barriers, render them ideal candidates for the development of long term FeS-based reactive barrier technology. The long-term reactivity of PRBs is expected to be influenced by a set of complex biogeochemical reactions, based on evidence from zero-valent iron barriers. Hence, an operational framework is required to evaluate the roles of SRB in FeS barriers and the potential to stimulate them for FeS regeneration. Therefore, in this task an evaluation of microbial control methods for the optimal biogenic production of FeS from various iron sources and subsequent sequestration of As(III) and Cd(II) by biogenically produced FeS was investigated.

Materials and Methods

Bacteria and chemicals. Five strains of sulfate-reducing bacteria were obtained from American Type Culture Collection (ATCC), viz., *Desulfovibrio vulgaris* (ATCC culture# 29579), *Desulfovibrio desulfuricans* (#13541), *Desulfobacterium autotrophicum* (#43914), *Desulfotomaculum acetoxidans* (#49208), *and Desulfotomaculum nigrificans* (#7946). These bacteria were grown chemolithtrophically in ATCC recommended media. Each differ considerably in their cell wall structure, acetate vs. lactate metabolism, and the type of cytochromes they contain (Bruschi *et al.,* 2007). All chemicals used for media preparation or analytical purposes were of ACS grade. High purity stock gases of nitrogen (N_2), and hydrogen (H_2) were purchased from Cryogenic gases (Detroit, MI, U.S.A.). The N_2 used in establishing anaerobic conditions for media was pre-treated to remove trace oxygen by running the gas stream through a heated bed (450 ^{0}C) of copper metal (Cu(0)) turnings. When needed, the copper scavenger was reactivated (reduced) by passing pulses of hydrogen through a bed of heated Cu coils.

Cell culturing and growth conditions. Pure strains of *D.vulgaris*, *D.desulfuricans, D.autotrophicum, D.acetoxidans, and D.nigrificans* were grown in ATCC-1249, -1250 (with 2.5 % NaCl), -1627 (with 10 mM lactate) and -1964 media, respectively. These media, with slight variations, were used for both the culture maintenance and generation of biogenic minerals. To establish anoxic conditions, fresh media were purged for 30 min with N_2 gas and then boiled under vaccum at room temperature for 15 min. Subsequent operations requiring strictly anaerobic conditions were performed in an anaerobic glove bag filled with 98 % N_2 and 2 % H_2 (Coy Laboratory, Ann Arbor, MI). All experiments were conducted in batch tube reactors at a temperature of 30±1 ^{0}C (for *D.vulgaris*, *D.desulfuricans*, *D.autotrophicum*, and *D.acetoxidans*) or 55±1 ^{0}C (for *D.nigrificans*).

The bacterial strains were grown in 75-ml flat serum bottles having 40 ml of the specified media flushed with 90% (v/v) N_2 and 10% H_2 (v/v). All media were sterilized by autoclave at 121 $^\circ$C for 20 min prior to the inoculation. The media had lactate as the electron donor and

sulfate as the electron acceptor. The bottles were capped with soft butyl rubber stoppers, allowing repeated sampling. The strictly anoxic conditions were established by flushing the fresh media for 30 min with N_2 after sterilization and then boiling under vacuum at room temperature for 15 min. All subsequent operations were performed in an anaerobic glove bag filled with 98% N_2 and 2% H_2. All cultures were maintained in fresh media as a slurry in anaerobic culture tubes after purging the headspace with nitrogen. Culture transfers took place using a metal cannula system. Cell densities were measured with UV spectrophotometer set at a wavelength 600 nm (OD_{600}). An OD_{600} of 1 was determined to correspond to a cell dry-weight concentration of 0.21 g/l to 0.41 g/l depending on the type of strain as described below. Stock solutions of sulfate, sulfite, and lactate were sterilized by filtration (0.2 µm pore size). For determination of maximum specific growth rates, growth curve data were examined by standard polynomial curve fitting in Microsoft Excel applied to calculate the derivative (dx/dt), which was then used to calculate the specific growth rates. Calculated curve fits had an R^2 of > 0.95-0.97 in all cases examined.

Biogenesis of FeS and its purification. The experiments used to quantify the biogenic production of FeS were conducted by transferring exponential phase cells (by cell volume or concentration) into fresh media with varying concentrations of electron donor (lactate) and electron acceptor (sulfate). The *D. vulgaris, D.desulfuricans, D.autotrophcum, D.acetoxidans,* or *D.nigrificans* were grown anaerobically in ATCC specified medium as described above. The exponential phase cells (0.90 - 1.00 of OD_{600}) harvested by centrifugation (8000 *x g*, 10 min, 4 ^{0}C), were washed to remove residual medium and purged with O_2-free N_2. Cells were then added to fresh media to obtain a final concentration of 2.8×10^8 cells/ml. The approximate initial OD_{600} of the culture prepared in this fashion was 0.05-0.08. Sources of iron were added either as a dissolved salt or a solid form. Hydrous ferric oxide (HFO) was prepared by following the procedure described by Fredrickson *et al.*(2003) and the green rusts were prepared as per the procedure mentioned in Aaron *et al.* (2001). Laboratory grade goethite and ferric citrate salts were procured from commercial sources. HFO was maintained in an aqueous suspension under anaerobic suspension and added to the media to obtain a final iron concentration in the range of 13.6 mM to 110 mM as specified. The other iron sources (green rust or goethite) and an Fe(III) salt (ferric citrate) were added as powders under anaerobic condition to obtain a total iron concentrations within the same range. In the case of 13.6 mM total iron systems, lactate (15mM, 16.5 mM, or 30 mM) was added as the electron donor and sulfate (15 mM) as the electron acceptor. Although in a few cases as noted, the total concentrations of iron, sulfate, and electron donor differed from these conditions, the molar concentration ratio of lactate to sulfate was always set at 1:1, 1.1:1, or 1:2 and sulfate was used in excess of iron (1.1:1 molar basis) in solution to allow for complete conversion of Fe(II) to a monosulfide (e.g., FeS) solid. The formation of a black precipitate was typically observed within 1-2 days for *D. vulgaris, D.desulfuricans,* and *D.autotrophcum*, and 3-4 days for *D.acetoxidans* and *D.nigrificans* after inoculation. After 10 days of incubation, the cultures were resuspended by manually mixing for 20s. The precipitated solids were collected by decanting the spent media supernatant, resuspending the solids, and then washing them in fresh anoxic buffer followed by a 30-sec immersion in a low energy sonication bath (Fisher Scientific-FS6) to dislodge cells and cell debris. After sonication, the solids were separated from the liquid (and from any debris) using syringe filter (0.11µ) and washed 4 times with Milli Q water. Three sonication/washes were found to be sufficient to reduce the protein content (of the biomass on solids) to below detection

by the Bradford protein assay. Samples of cells (0.1 mg/ml dryweight) were collected by decanting the supernatant solution, washing the cells twice with DI water, and disrupting them by an alkaline lysis method, whereby the pH was adjusted to 10.5 – 11.5 with 1N NaOH and held 10 min at 70 $^{\circ}$C followed by a 30 sec immersion in a low energy sonication bath. After centrifugation (8000 *g*, 12 min), the supernatant was recovered and analyzed for total protein using the Bradford assay and Bovine Syrum Albumin (BSA) as a standard. Sulfate was measured by ion chromatography (Dionex DX-100) and sulfide was quantified by a dimethyl-phenylene diamine assay (Cline, 1969). The Eh was measured using an Oxidation-Reduction Potential platinum electrode with Ag/AgCl reference electrode. Control experiments (in the mineral media without bacteria) did not yield any FeS solids indicating that abiotic mineralization was not occurring in these systems.

Reactivity studies. The reactivity and capacity for As(III) sequestration of biogenically-produced FeS (from *D.acetoxidans*) in comparison with synthetically-made mackinawite was evaluated using batch isotherm experiments. These experiments were conducted with 0.15 M NaCl electrolyte concentration. The experiments were conducted at pH 5.0, 7.0 and 9.0. The pH of the solution was adjusted with an addition of an appropriate amount of 0.01M HCl or 0.01 M NaOH and equilibrated for 48 hrs before the addition of analyte. The solids concentration was maintained at 1 g l^{-1} in all reaction tubes. Each tube was then introduced to varying amounts of an As(III) stock solution to reach the desired total concentration of As(III) added (1.34×10^{-4} – 6.7×10^{-7} M). After the required incubation period (ca. 48 hrs), samples were filtered through 0.01 μm nylon syringe filter. The final pH of filtrates was measured and used them in ICP-MS analysis.

The reactivity and capacity for Cd(II) sequestration of biogenically-produced mackinawite was also evaluated using batch isotherm experiments as mentioned above. Each isotherms at a given pH was produced by with varying the amount of a Cd(II) stock solution to reach the desired total concentrations (1.3×10^{-4} – 6.9×10^{-7} M for the first set of isotherms and 2.0×10^{-4} – 2.0×10^{-3} M for a second set). After the required incubation period (ca. 48 hrs), samples were filtered through 0.01 μm nylon syringe filter. The final pH of filtrates was measured and the used for determining the Cd concentration in ICP-MS analysis.

In some experiments pH edge data were generated. For these, the experiments were conducted at various concentrations of biogenic FeS (0.1 g/L to 10 g/L). The pH of the solution was adjusted with an addition of an appropriate amount of 0.01M HCl or 0.01 M NaOH and then plotted as a percent of the total Cd(II) or As(III) removed as a function of pH. For these experiments the total Cd(II) or As(III) was keep constant at 13.4 μM and 0.015 M NaCl.

X-ray diffractometry analysis. X-ray diffraction (XRD) analyses were conducted using a Rigaku Rotaflex rotating anode XRD apparatus (Cu Kα radiation, 40 kV, 100 mA). Dry XRD samples were prepared by freeze-drying the solid collected after the sonication washing and filling the freeze drying chamber with N_2 gas prior to starting the vacuum to prevent potential oxidation. The dried solids appeared to be stable (no visible color change) for the period of time required for XRD measurements and were therefore analyzed without protective tape.

Scanning electron microscopy (SEM). Samples of precipitated FeS minerals were directly imaged using a field emission scanning electron microscope (LEO, Model 981) to obtain crystal morphology. This analysis was performed at 5 keV and 90 μA.

Subtask 2.1. Biogenic formation of FeS by SRBs

Results and Discussion

To evaluate and assess the potential of sulfate-reducing bacteria for biogenic production of FeS, two strains of complete acetate oxidizers (*D.autotrophicum* and *D.acetoxidans*) and three strains of incomplete acetate oxidizers (*D.desulfuricans, D. vulgaris* and *D.nigrificans*) were examined on various iron sources using exponentially grown cells. A summary of the experimental conditions, bacterial characteristics, and growth rate constants are given in Table 2.1.

Table. 2.1. General metabolic characteristics of SRB used in this study

Sulfate reducing bacteria	**Gram +/-**	**Growth temperature (°C)**	**Specific growth rate* (μ) (h^{-1})**	**Electron donor used#**	**Oxidation of organic substrates**
Desulfovibrio desulfuricans	-	30 ± 1	0.25 ± 0.02	Lactate	Incomplete
Desulfovibrio vulgaris	-	30 ± 1	0.21 ± 0.01	Lactate	Incomplete
Desulfobacterium autotrophicum	-	30 ± 1	0.19 ± 0.01	Lactate Acetate	Complete
Desulfotomaculum acetoxidans	+	30 ± 1	0.08 ± 0.01	Lactate	Complete
Desulfotmaculum nigrificans	+	55 ± 1	0.05 ± 0.01	Lactate	Incomplete

** Specific growth rate (μ) = dx/(xdt), see Materials and Methods. In all cases, iron solid phase used was HFO (13.6 mM).*

Batch microcosm experiments were conducted to evaluate the production of biogenic FeS by exponentially grown cells of bacteria. The exponential phase cells (0.95 of OD_{600}) were harvested by centrifugation (8000 g , 10 min, 4 ^{0}C) and added to fresh medium modified with iron (HFO) , lactate, sulfate in different concentrations (15 mM – 45 mM) and buffered to 7.5 using 50 mM HEPES. These experiments were conducted in 450 ml bottles and the cell number found to be 1 x 10^{11} in 200 ml solution. The approximate OD_{600} was found to be 0.5.

The formation of black precipitation (indication of the FeS biogenesis) was found in nearly all of the microcosms regardless of ferric iron source, with the formation requiring 48-50 hrs (for *D. vulgaris*, *D. autotrophicum,* and *D. desulfuricans*) and 72-80 hrs (for *D. acetoxidans* and *D. nigrificans)* of incubation (after inoculation). Initially, the FeS formation was seen only when the lactate to sufate molar ratio was ca. 2:1. In contrast, *D.autotrophicum* showed biogenesis of FeS in presence of acetate (with 1:1 sulfate to acetate moalr ratio) as well. In later experiments, lactate to sulfate was always maintained in excess.The control experiments (either without lactate or without bacteria) did not yield FeS solids. After 8-day (for *D. vulgaris* and *D.autotrophcum*) and 10-day (for *D.desulfuricans*) of incubation with biogenically produced FeS, cells seem to be dropping out of medium - possibly due to the FeS toxicity. These results are explained in terms of FeS formation, sulfate reduction and sulfide formation.

Effect of biomass concentration. In an effort to evaluate the effect of increasing biomass concentration on biogenic production of FeS, experiments were conducted with increasing amount of biomass density (0.1, 0.2, 0.4, 0.6, 0.8 and 1.0 g dry biomass/L). These results show that the increase in biomass concentration of *D. vulgaris* (thereby increasing the bacterial protein amount) from 0.1 g/L to 0.8 g/L (23 μg/mL – 131 μg/mL bacterial protein) indeed resulted in higher sulfate depletion rates (see Figure 2.1; with HFO) and biogenic production of FeS (total FeS separated from reaction mixture) from 45% to 64 % based on % Fe conversion. However, FeS production was drastically decreased when protein concentration increased from 131 μg/mL to 172 μg/mL (Table 2.2). After 26 hrs of incubation, the black coloration (indication of biogenic production of FeS) started from a whitish-red solution in highest biomass density flasks (1.0 g/L) and continued up to ca. 70 hrs. These observations may indicate that SRB activity is highly sensitive to biomass density.

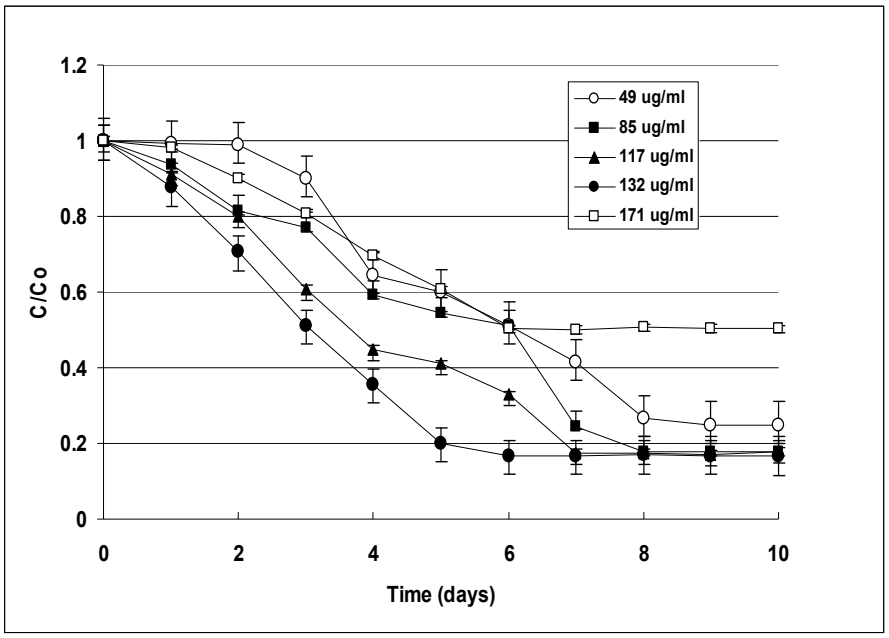

Figure 2.1. Loss of sulfate in biogenic production of FeS by *D. vulgaris* in terms of protein concentration. The lactate:sulfate ratio 2:1. The reaction solution was buffered to pH 7.2 by 50 mM HEPES.

pH and redox potential. A drastic drop in Eh from -188 mV to approximately -270 mV occurred within the first 48 hrs for *D.vulgaris*. This decrease continued for 72 hrs, stabilizing at -360 mV but after the 10-day incubation period, the Eh remained essentially constant. All other bacterial strains followed similar trends of decreasing redox potential with time. The pH values, in general, decreased with the biogenesis of FeS solids in all bacterial strains studied. This change in pH correlated with the production of FeS solids in the solution. The maximum decrease in pH was found to be 0.5-1.2 pH units from initial pH of 7.0-7.2, depending on the type of sulfate reducing bacteria (Figure 2.2). Based on balanced overall redox reactions, both

Table 2.2. Biogenic FeS production by *D. vulgaris* in terms of protein concentration.

Bacterial biomass dry concentration (g/L)	*Protein concentration* (μg/L)*	*Biogenic production of FeS (mg)*
0.1	26 ± 3.1	13 ± 2.0
0.2	50.0 ± 3.5	58 ± 4.2
0.4	84 ± 4.2	88 ± 5.7
0.6	117 ± 2.5	104 ± 9.7
0.8	133 ± 1.7	142 ± 4.3
1.0	171 ± 3.5	42 ± 4.2

** The protein measurements were taken for 0.5 mL of samples and measured by Bradford assay (Bio-Rad Inc.).*

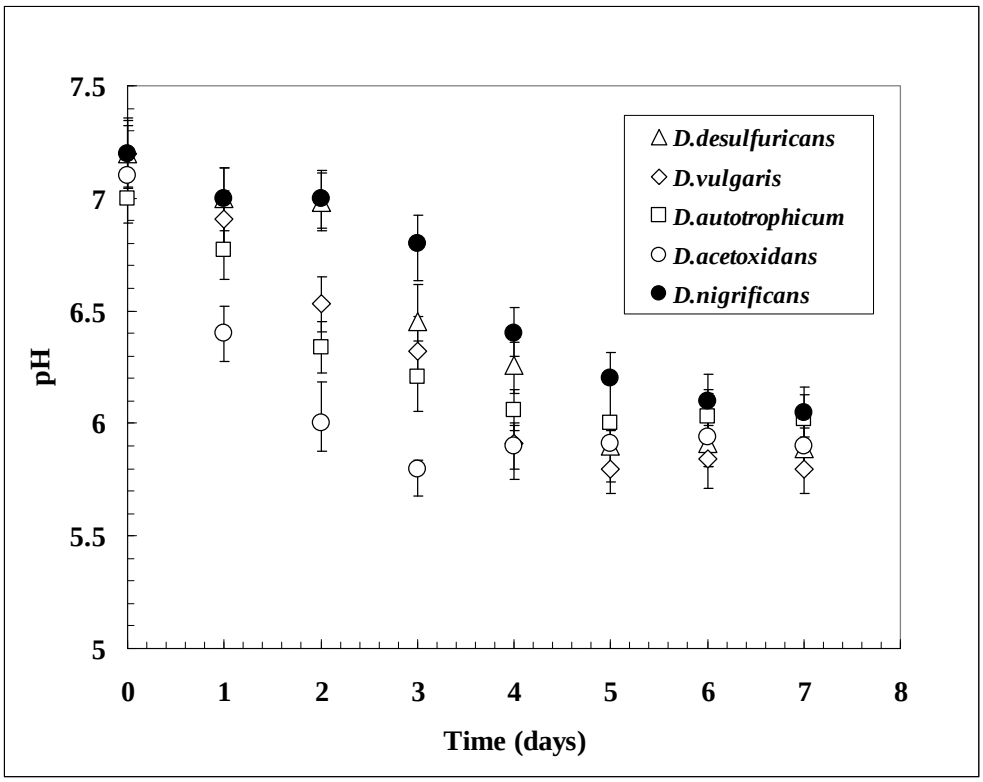

Figure 2.2. pH changes during the biogenesis of ferrous sulfide minerals in presence of sulfate reducing bacteria.

the reduction of lactate and the formation of FeS are expected to lead to a net production of protons and to lower the pH. The lower Eh is also expected and consistent with increased sulfate conversion to sulfide according to pe estimates based on the sulfate to sulfide half reaction and concentration ratios.

Impact of SRB metabolism on sulfate/sulfide activity. The extent of sulfate conversion was estimated by comparing the extent of conversion after a 10-day incubation period to the complete conversion based on total sulfate added. For *D.desulfuricans*, the sulfate measurements showed that sulfate reduction started after 20 hrs of incubation with hydrous ferric oxide (HFO) then decreased slowly, finally stopping after 7-days (Figure 2.3)**.** Similar patterns were observed for *D.acetoxidans* and *D.nigrificans*. However, the sulfate depletion was somewhat different for *D.autotrophicum* and *D .vulgaris*, with lower amounts of sulfate reduced on daily basis for the first several days.

Sulfide generation, in general, was found to increase after the second day. *D.nigrificans* showed highest overall sulfide generation at the end of 9 days (7.9 mmol) followed by *D. vulgaris* (7.6 mmol), *D.acetoxidans* (7.5 mmol), *D.desulfuricans* (7.11 mmol), and *D.autotrophicum* (5.5 mmol) per gram of cell weight (dry wt.) after a 10-day incubation period (Figure 2.4). In an effort to get higher total yields, these set of experiments were carried out with relatively higher concentrations of iron (50 mM), sulfate (55 mM), and lactate (110 mM). Based on the sulfide generation amounts found with the four different iron sources (i.e., HFO, goethite, green rust, or ferric citrate), the sulfide conversion efficiencies ranged from 42-81% for *D. vulgaris*, 64-72% for *D.desulfuricans*, 35-66% for *D.nigrificans*, 51-61% for *D.acetoxidans*, or

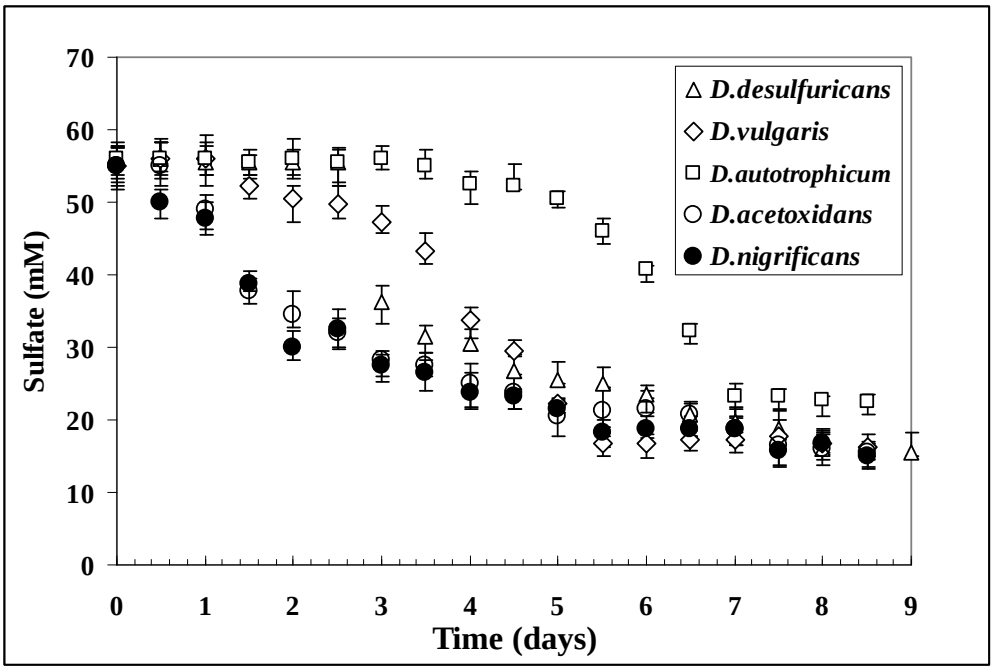

Figure 2.3. Measurement of sulfate during the biogenesis of ferrous sulfide minerals in presence of sulfate reducing bacteria.

43-55% for *D. autotrophicum* when the lactate to sulfate molar ratio was 2:1.

The sulfate depletion rates (average between two consecutive values) were found to vary with different iron sources and were quite low in the presence of green rust (Table 2.3)**.** Sulfate depletion efficiency was found to be the highest for *D. vulgaris* (e.g., 81% of the total initial sulfate converted) followed by *D.desulfuricans* (72%), *D.nigrificans* (66%), *D.acetoxidans* (61%) and *D.autotrophicum* (55%) in presence of HFO. These results indicate that organism

Table 2.3. Sulfate depletion rates (*1/d*) of various incubations in presence of sulfate reducing bacteria.

Strain	Rates of sulfate depletion (*1/d*)			
	HFO	*Fe (III) citrate*	*Green rust*	*Goethite*
D. desulfuricans	-0.19	-0.05	-0.07	No depletion
D. vulgaris	-0.15	No depletion	-0.03	-0.26
D. autotrophicum	-0.47	-0.07	-0.04	-0.52
D. acetoxidans	-0.26	-0.18	-0.14	-0.28
D.nigrificans	-0.20	-0.08	-0.02	-0.22

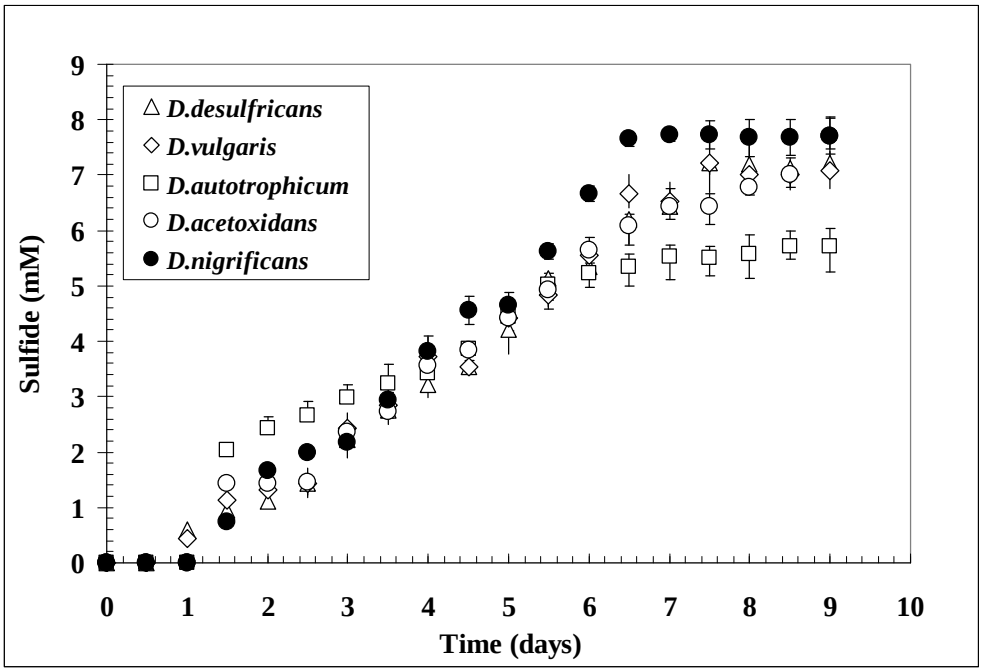

Figure 2.4. Measurement of sulfide concentrations during the biogenesis of ferrous sulfide minerals in presence of sulfate reducing bacteria.

metabolic pathway (e.g., oxidizers vs. non oxidizers) does not apparently correlate with the ability to transform sulfate to sulfide.

In general, FeS was produced regardless of iron source (with two exceptions noted) with the degree of Fe conversion different among the various iron phases. In all cases, the poorly crystalline HFO showed the greatest conversion, with lower conversions for the more crystalline solids, and with the lowest conversion for the completely dissolved iron citrate. Although dissolved ferric citrate was initially expected to show the most complete conversion, its lack of conversion was likely due to the strong ferric citrate complex that forms in solution, which apparently inhibits its redox conversion and iron sulfide formation.

The following order of preference of iron source in terms of amount of FeS generated was found (see Table 2.4 for details):

***Desulfovibrio desulfuricans*:** HFO > Green Rust > Fe(III) citrate

***Desulfovibrio vulgaris*:** HFO > Green Rust > Goethite

***Desulfobacterium autotrophicum*:** HFO > Green Rust > Goethite > Fe(III) citrate

***Desulfotomaculum acetoxidans*:** HFO > Green rust > Goethite > Fe (III) citrate

Desulfotomaculum nigrificans: HFO > Green rust > Goethite > Fe(III) Citrate

Table 2.4. Iron sulfide production and Fe conversion efficiency in the presence of different iron solid phases.

Strain	*HFO*		*Fe (III) citrate*		*Green rust*		*Goethite*	
	FeS produced (mM)	*Fe conversion (%)*	*FeS produced (mM)*	*Fe conversion (%)*	*FeS produced (mM)*	*Fe conversion (%)*	*FeS produced (mM)*	*Fe conversion (%)*
D. desulfuricans	5.6 ± 0.5	41.1	3.9 ± 0.3	28.9	4.9 ± 0.3	36.3	0.0	NA*
D. vulgaris	6.7 ± 0.1	49.3	0.0	NA*	6.0 ± 0.5	44.2	4.5 ± 0.3	33.4
D. autotrophicum	4.2 ± 0.5	30.7	2.1 ± 0.3	15.3	3.0 ± 0.2	22.3	2.6 ± 0.1	19.3
D. acetoxidans	6.0 ± 0.3	44.2	2.9 ± 0.2	21.4	5.1 ± 0.4	37.3	3.8 ± 0.42	28.5
D. nigrificans	3.8 ± 0.2	28.3	1.5 ± 0.1	11.4	2.7 ± 0.3	20.1	1.9 ± 0.3	14.2

** NA – Fe conversion to FeS was not applicable as FeS was not observed under these conditions*

FeS formation (grams of FeS solids per day) in the solution was also measured to establish kinetics involved in the iron sulfide generation. The results of growth yields ($Y_{sulfate}$), dissolved sulfide generated, (with HFO as an iron source) along with cell protein measurements are given in the Table 2.5**.** The maximum growth yield ($Y_{sulfate}$) during lactate oxidation was found to be 10.1 g cells formed per mol sulfate with *D.vulgaris* followed by 9.46 g, 8.64 g, 8.12 g, and 8.01 g for *D.desulfuricans*, *D.autotrophicum*, *D.acetoxidans* and *D.nigrificans* respectively.

In this study, the formation of black precipitation (indication of the FeS biogenesis) was found in nearly all of the microcosms regardless of ferric iron source, with the formation requiring 48-50 hrs (for *D. vulgaris*, *D. autotrophicum,* and *D. desulfuricans*) and 72-80 hrs (for *D. acetoxidans* and *D. nigrificans)* of incubation (after inoculation). Differences in the biogenesis times observed for the Gram positive vs. Gram negative organisms, however, ,may indicate that cell wall characteristics play a role in the type of solid generated. Given that the biogenic formation rates did not appear to depend significantly on the ferric iron source for a given cell wall type, suggests that the iron sulfide production rate was not limited by the availability or Fe by rather by the rate of reduction of Fe(III) to Fe(II) or the subsequent precipitation reaction between sulfide and Fe(II) as discussed below.

Phase characterization of SRB biogenic FeS. Biogenically produced solids were qualitatively observed in all experimental combinations of microorganisms, electron donor, and iron source. The XRD spectra of biogenically produced material of *D.vulgaris* and *D.autotrophicum* indicate the presence of FeS (Figure 2.5). The products resulting from *D. vulgaris* and *D.autotrophicum* in the presence of hydrous ferric oxide and Ferric citrate were identified as pyrrhotite using X-ray diffraction (XRD) analysis.

Table 2.5. Sulfate reducing bacterial protein concentrations, growth yields, and amount of sulfide produced per g of cells (dry weight) during 10-day incubation with HFO.

Bacterial strain	***Cell protein conc. (mg/L)***	***Growth yield ($Y_{sulfate}$)***	***Sulfide* produced (mM)***
D.desulfuricans	25.8	9.5 ± 1.1	7.1 ± 0.3
D. vulgaris	22.0	10.1 ± 0.9	7.6 ± 0.2
D.autotrophicum	21.9	8.6 ± 0.7	5.5 ± 0.3
D.acetoxidans	25.6	8.1 ± 0.9	7.5 ± 0.2
D.nigrificans	24.9	8.0 ± 0.5	7.9 ± 0.4

* Sulfide produced includes the amount that was converted to FeS and the amount remaining in the solution at the end of 10-day period.

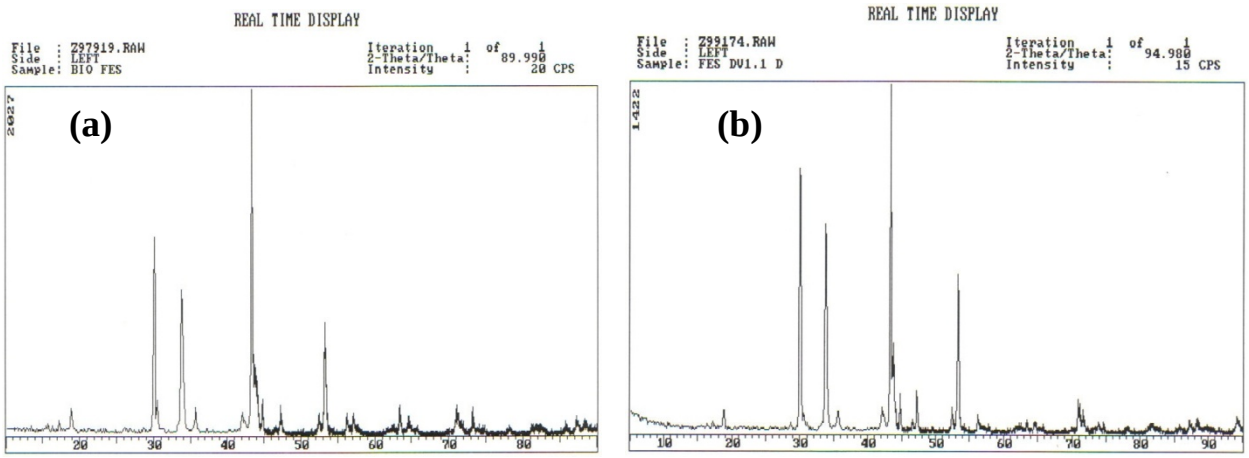

Figure 2.5. XRD spectra of (a) *D.vulgaris* and (b) *D. autotrophicum*; Experiments conducted in presence of HFO; lactate:sulfate ratio 2:1.

Earlier investigations have reported the presence of biogenically produced pyrrhotite when *D.desulfuricans* was grown in the presence of hematite and lactate (Neal *et al*., 2001). Pyrrhotite has also been observed in anoxic marine sediments (Roberts and Turner, 1993; Horng *et al*., 1998), H_2S-rich environments (Berner, 1964; Sweeney and Kaplan, 1973) and in other laboratory incubations in presence of sulfate reducing bacteria and lactate (Matsuo *et al*., 2000). More recently, Matsuo *et al*. (2000) reported both pyrrhotite and mackinawite formation by sulfate reducing bacterial activity in presence of ferrous ions. Pyrrhotite is usually found in more crystalline form in nature and is a thermodynamically more stable iron sulfide compared to mackinawite.

Scanning electron microscopy (SEM). The iron sulfide minerals precipitated under these conditions exhibited a convoluted and unique textured pattern (Figure 2.6). The particles seen in the SEM images appear as square and spherical shaped aggregates showing a porous rosette shape ranging from 40-100 μm in diameter. The biogenically produced minerals shown indicate no evidence of bacterial cells on the mineral surfaces due to the procedure used in this study to wash the mineral solids. In an earlier study conducted by Herbert *et al.* (1998), the presence of

of numerous bacterial cells on iron sulfide minerals were found in samples in which cell debris was not specifically removed.

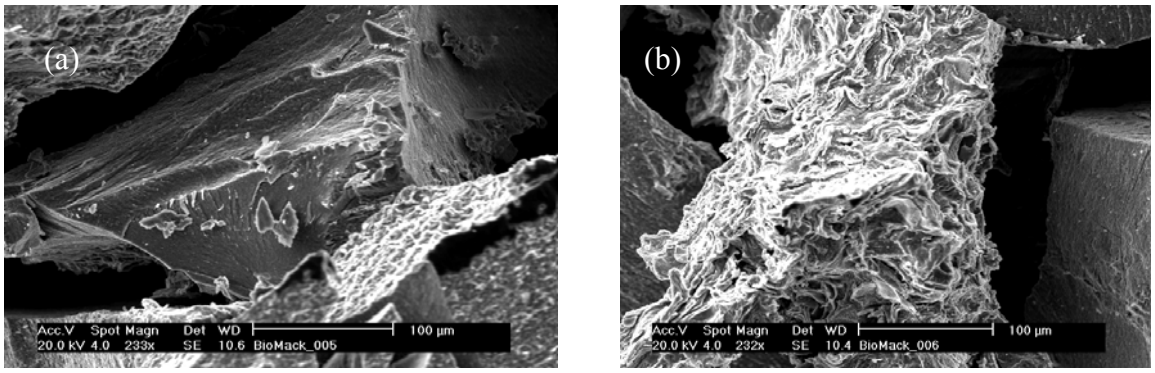

Figure 2.6. Scanning electron micrographs of biogenically produced minerals; Minerals generated by (a) *D. vulgaris* and (b) *D. acetoxidans*.

Summary and Conclusions and Implications for Future Research/Implementation

The specific objective of this subtask was *to examine the ability of a range of SRB to regenerate FeS from oxidized iron products.* The experiments conducted so far demonstrate that biogenic FeS can be generated in the presence of oxidized forms of hydrous ferric oxide (HFO), Fe (III) citrate, green rust, and goethite. These results have also allowed us to demonstrate the feasibility of regenerating FeS from iron solids that may be produced when (i) oxidation of FeS produces ferric iron (Fe(III)) oxide solids in the presence of oxygenated groundwater at the entrance of the PRB and (ii) oxidation of FeS in the presence of redox active metals like As(V) gives rise to ferric solids. We have established that an electron donor (lactate or acetate) to electron acceptor (sulfate) ratio (of either 2:1 or 1:1, respectively) is required to complete the reaction in the presence of different iron sources.

Assessment of sulfate reduction by these strains was carried out in terms of reaction efficiencies by computing reaction rates and stoichiometries and demonstrates that the conversion effeciencies depend on organism type and iron source. Based on the observations in the laboratory to date, the conversion efficiencies ranged from 42-80% for *D. vulgaris* and 62-79% for *D. autotrophicum* when the lactate:sulfate ratio was 2:1. The conversion efficiencies were dependent on the iron source present in the medium and the order of preference was found to be *D. desulfuricans*: HFO < Green rust < Goethite < Fe(III) citrate; *D. acetoxidans*: Green rust < Goethite < Fe (III) citrate < HFO. The X-ray diffraction revealed the pyrrhotite forms of FeS for *D.desulfuricans* and *D.autotrophicum*.

Before biogenic regeneration of FeS by SRB can be optimized for field applications, future work will need to assess the conversion efficiencies in column reactors under flow conditions more representative of PBRs. These experiments should be targeted with multi-species regimes (consortia of SRBs) representative of selected field sites.

Subtask 2.2. Sorption Behavior of As and Cd by Biogenic FeS

pH edges of As sorption. The biogenically generated FeS from *D.acetoxidans* was tested for its reactivity for As(III) as a function of pH. The pH edge experiments were conducted at various concentrations of biogenic FeS. It is apparent from the present study that biogenic FeS is highly efficient (ca. 100%) in removing As(III) from water, especially, in lower pH range from 4.0 to 7.5 under all FeS concentrations examined (Figure 2.7) and also that the uptake behavior is similar to mackinawite samples synthesized as described in Task 1 (see Figure 1.19). As(III) uptake generally decreased with increasing pH above 9 and increased with decreasing pH except when the solid concentration was very low and not enough sulfide was present for AsS precipitation. Based on studies in Task 1, the mechanism of As(III) uptake at low pH was shown to result from dissolution of FeS and AsS precipitation, while at higher pH it is thought to be primarily due to the adsorption of As(III) oxyacid species to surface sites on the FeS solid. The decrease in sorption with increasing pH results from the unfavorable adsorption of the oxyanion as the FeS becomes increasingly more negatively charged with increasing pH.

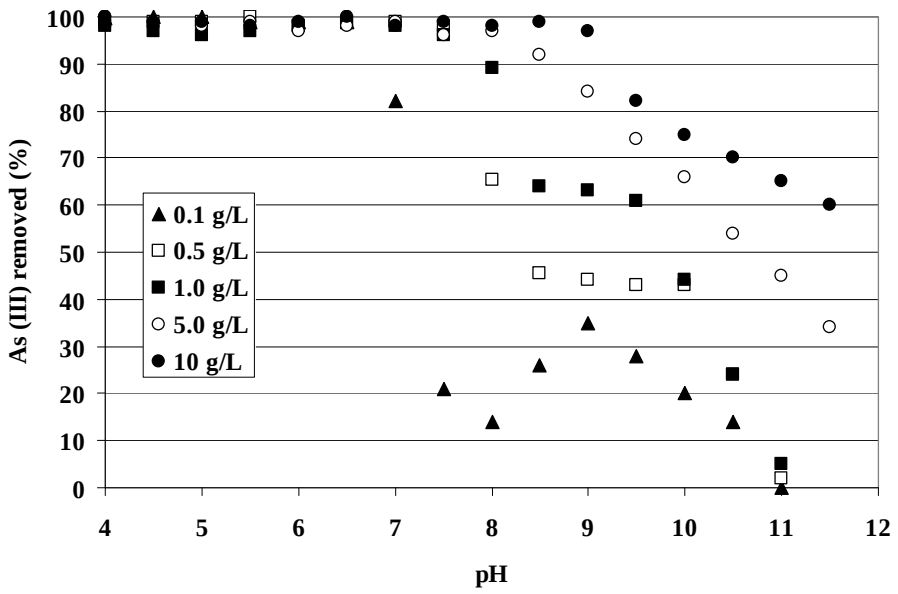

Figure 2.7. pH edges measured at different biogenic FeS concentrations. Initial As(III) concentration was 13.4 μM; ionic strength 0.015M.

As(III) uptake Rates. The concentration of metal ions and the contact period is known to play an important role in metal uptake rates as well as in total metal uptake. Several experiments were conducted to examine the equilibrium incubation time at pH 5.0, 7.0 and 9.0 on biogenic and synthetic mackinawite uptake. These results show that approximately 2 day equilibration period is sufficient to attain maximum and level uptake extent (Figure 2.8) with maximum uptake values of 4.1 mmol/g, 3.3 mmol/g, and 2.8 mmol/g of biogenic FeS at pH values 5.0, 7.0, and 9.0, respectively (Figure 2.8), and had consistently greater capacity compared to synthetically generated FeS. The pH 5.0 produced highest uptake followed by pH 7.0 and 9.0.

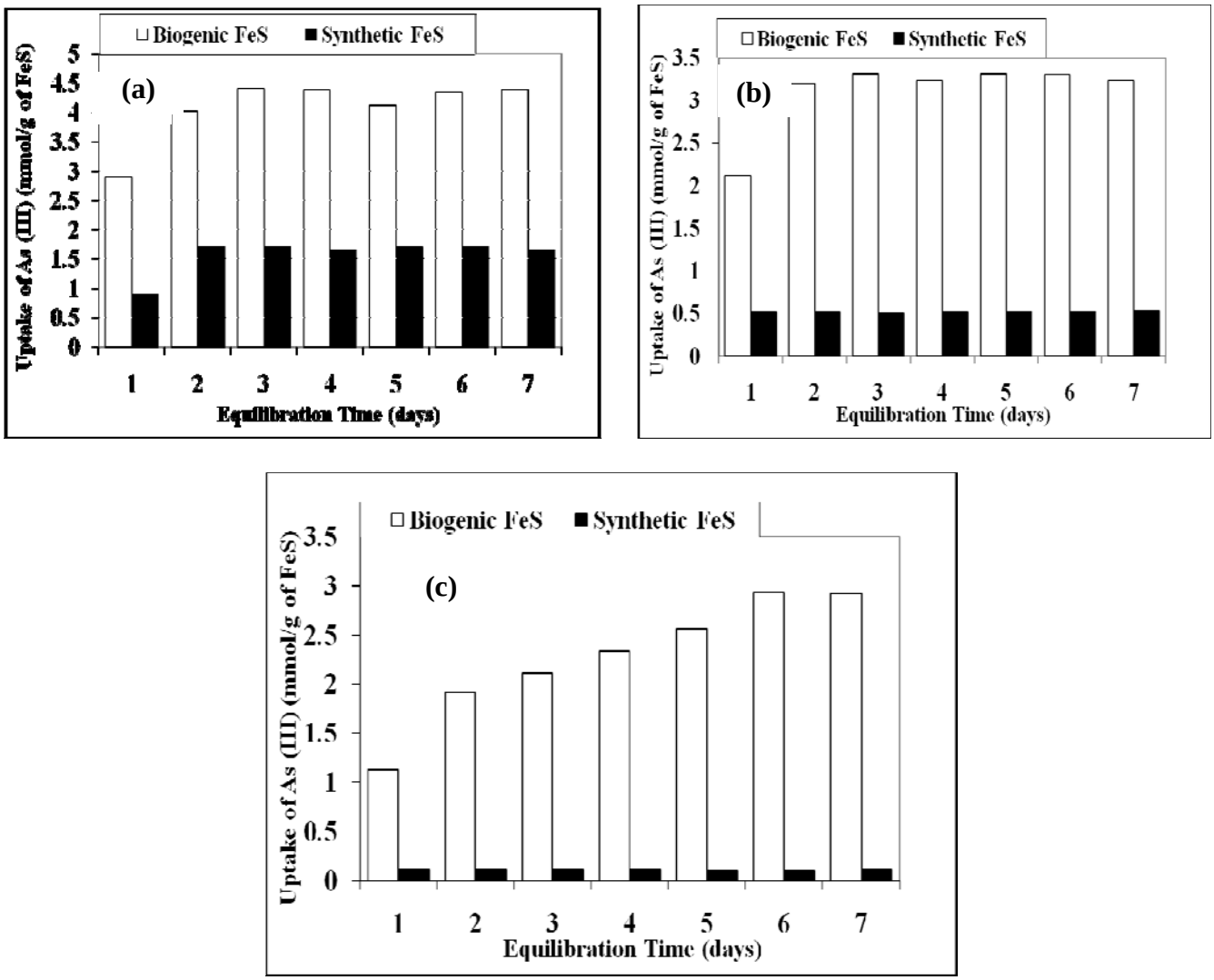

Figure 2.8. Effect of equilibration time on As(III) uptake by biogenic FeS and synthetic mackinawite; (a) pH 5.0; (b) pH 7.0; (c) pH 9.0. FeS concentration 1 g/L; pH adjusted with 0.1 N HCl or 0.1 N NaOH; initial As (III) concentration 6.4 mM.

The increase in As(III) uptake over a time did not show any major difference between biogenic and chemically synthesized FeS at pH 5.0 and 7.0 but did show significant differences at pH 9.0 where the As(III) uptake by biogenic FeS increased until 6th day whereas the uptake by synthetic FeS showed no increase after 2 day period.

As (III) removal Isotherms. Equilibrium isotherm studies can be used to obtain maximum uptake (loading capacity), as well as allowing further characterization of uptake behavior of FeS from low to high As(III) loading concentrations over a range of pH values. The uptake of As(III) by biogenic FeS was evaluated at different initial concentrations of As(III) as a function of pH (pH 5.0, 7.0, and 9.0). The results are plotted in terms of As(III) uptake against equilibrium (final) concentration (Figure 2.9).

The uptake capacity of biogenic FeS in the present study showed increasing As(III) sorption with increasing metal concentrations. Isotherm data plotted at pH 5.0 produced a maximum metal uptake of 4.1 mmol As/g of biogenic FeS followed by pH 7.0 (2.9 mmol As/g) and pH 9.0 (1.8 mmol As/g). This trend of highest uptake at pH 5.0 was also observed when the isotherms were conducted with lower initial metal concentrations (Figure 2.9). The higher

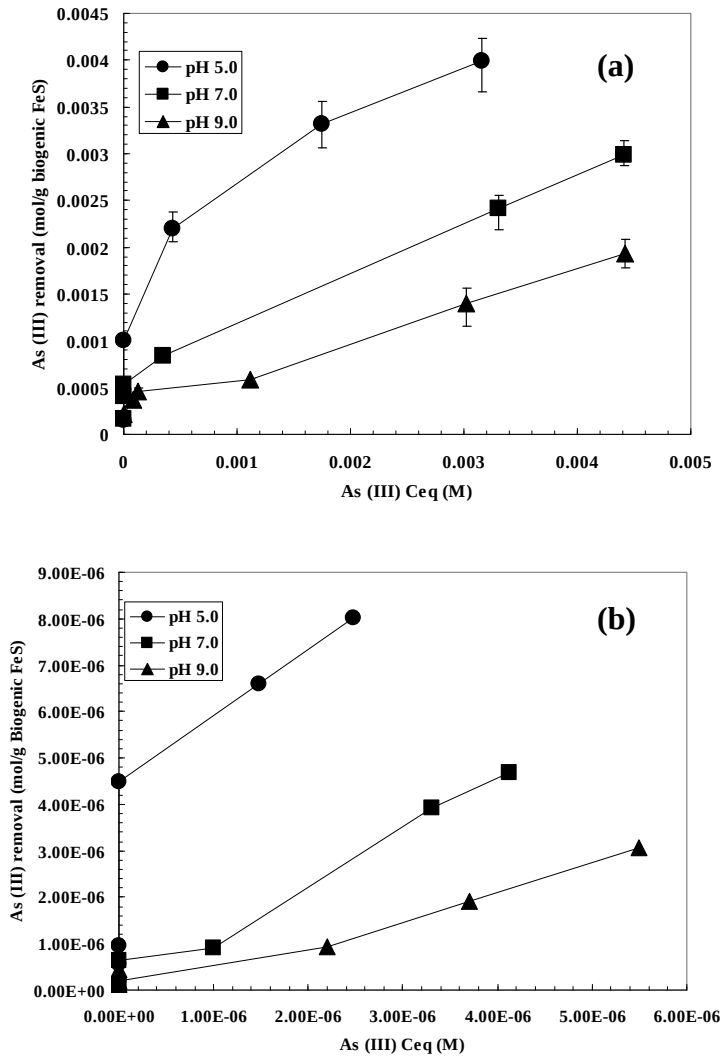

Figure 2.9. Sorption isotherms of As(III) ion by biogenic FeS at constant pH with (a) higher and (b) lower initial concentrations. FeS concentration 1 g/L; pH; adjusted with 0.1 N HCl or 0.1 N NaOH; ionic strength 0.015M.

sorption capacity found at lower pH is in agreement with the isotherm trends as a function of pH for chemically synthesized FeS in Task 1 (Figure 1.4), and is consistent with the predominance of AsS(s) precipitation at lower pH and surface-limited precipitation and adsorption at the higher pH. The steep nature of isotherm at pH 5.0 and higher As(III) loading capacity (2.61 mmol/g) of biogenic mackinawite at low equilibrium concentration (e.g., 0.23 mM) indicates that biogenically produced FeS would be an efficient scavenger of As(III), even at low solution

concentrations. The gradual increase of As(III) uptake at higher As concentrations differs from the synthetically generated FeS and suggests that the biogenic FeS has more accessible sulfide at lower pH and more accessible surface at higher pH as t As(III) concentration increases.

pH edges of Cd (II) removal. The biogenically generated FeS from *D.acetoxidans*, was tested for its reactivity for Cd(II) as a function of pH by monitoring the change of Cd(II) uptake versus pH at constant total Cd(II) concentrations. pH edges were generated for various total concentrations of biogenic FeS (0.1 g/L to 10 g/L) at 13.4×10^{-6} M total Cd. It is clear from the results shown in Figure 2.1 that biogenic FeS is highly efficient (ca. 100%) in removing Cd(II) at the lower pH range tested (from 3.0 to 4.5) for all FeS concentrations. Surprisingly, Cd(II) uptake dropped dramatically at approximately pH 4.5 for all FeS solid concentrations examined. This decrease in Cd(II) uptake at pH 4.5 may be a result of the biogenic FeS being completely dissolved at lower pH causing the formation of CdS(s) from the released sulfide, but not so at pH greater than 4.5 where surface limited sorption process are operating. Cd (II) removal slowly increased with increasing pH from 5.0 until approximately pH 10.0 and thereafter slightly decreased or leveled off up to pH 12.0, the highest pH monitored. At the pH of 12, ca. 66% of the Cd(II) uptake was observed with 10 g/L solid concentration where as it was ca. 21% when the solid concentration was 0.1 g/L (Figure 2.10). Based on studies in Task 1, the mechanism of Cd(II) uptake is thought to be primarily due to the bulk precipitation of CdS(s) at low pH where FeS dissolves but may be limited to surface precipitation or adsorption of CdS species upon reaction with FeS throughout the rest of the pH range under the Cd(II)/FeS < 1 molar solution ratio conditions investigated.

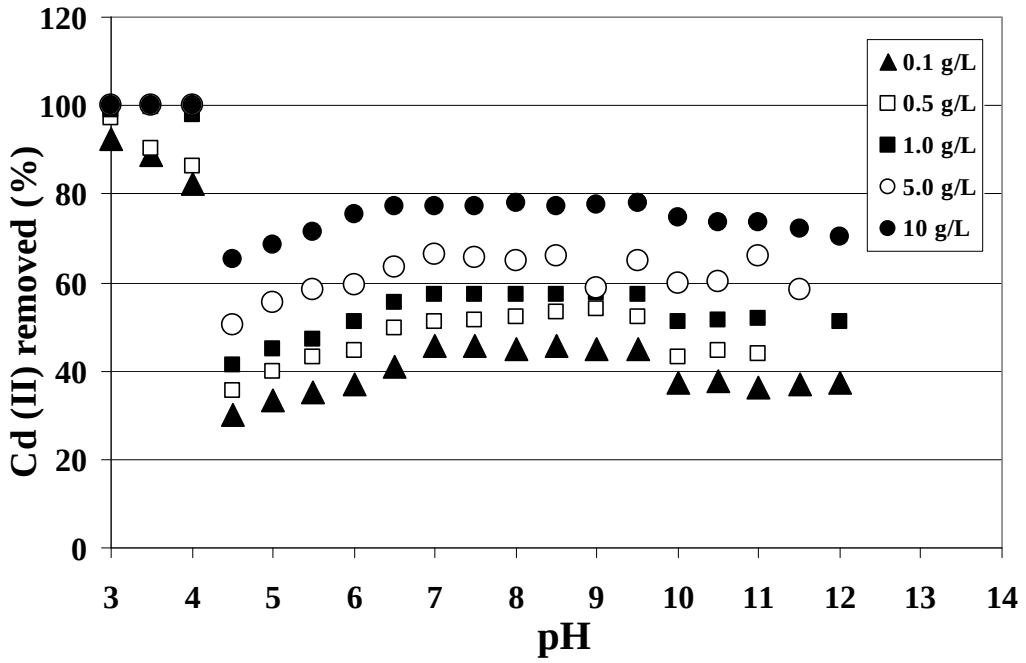

Figure 2.10. pH edge experiments at different biogenic FeS concentrations; Cd (II) initial concentration 13.4 μM; Ionic strength 0.015 M NaCl.

Cd(II) isotherm experiments. Equilibrium isotherm studies provide maximum uptake (loading capacity), as well as allowing further characterization of uptake behavior of FeS from low to high Cd(II) loading concentrations over a range of pH values. The reactivity and capacity for Cd(II) sequestration of biogenically-produced FeS was evaluated using batch isotherm experiments similar to the earlier experiments on As(III). The experiments were conducted at pH 5.0, 7.0 and 9.0. The solids concentration was maintained at 1 g l^{-1} in all reaction tubes. The uptake capacity of biogenic FeS in the present study showed increasing Cd(II) sorption with increasing metal concentrations. The Cd(II) initial concentrations were in the range of 0.02 mM to 0.2 mM. The results showed that pH 5.0 produced a maximum metal uptake of 0.84 mmol Cd/g of biogenic FeS followed by pH 7.0 (0.52 mmol Cd/g) and pH 9.0 (0.29 mmol Cd/g). The pH 5.0 uptake resulted in the removal of 0.073 mmol/g at initial concentrations of 0.02 mM Cd(II) concentration (Figure 2.11). Doubling the initial concentration to 0.04 mM resulted in 0.213 mmol/g, and at 0.08 mM the uptake was 0.291 mmol/g. The uptake capacity of biogenic FeS at pH 5.0 was found to saturate at 0.91 mM, leading to 0.84 mmol/g (Figure 2.11). At pH 7.0, the same material was shown to sequester 0.028 mmol/g at 0.02 mM, and 0.48 mmol/g at 0.2 mM (Cd(II)). This trend of decreasing uptake capacity of biogenic FeS with pH continued at pH 9.0, resulting in 0.29 mmol/g of uptake at the highest initial concentration studied (0.2 mM).

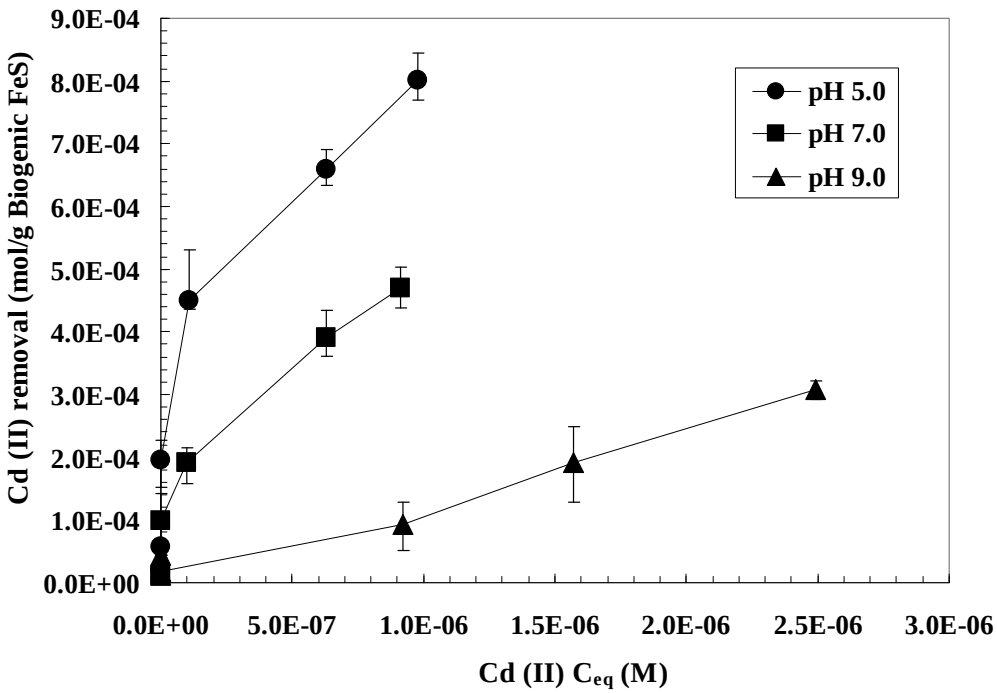

Figure 2.11. Sorption isotherms of Cd(II) by biogenic FeS at different pH; Cd initial conc. 0.02 mM to 0.2 mM; FeS concentration 1 g/L; pH adjusted with 0.1 N HCl or 0.1 N NaOH; ionic strength 0.015M.

Isotherm experiments were also run at higher total Cd(II) concentrations of 0.2 mM to 2.0 mM. The data again show that pH 5.0 produced the maximum metal uptake with 8.1 mmol Cd/g of biogenic FeS followed by pH 7.0 (6.3 mmol Cd/g) and pH 9.0 (3.8 mmol Cd/g). The pH 5.0 uptake resulted in to 0.83 mmol/g at initial concentrations of 0.2 mM Cd(II) concentration

(Figure 2.12). Doubling the initial concentration to 0.4 mM resulted in 2.4 mmol/g, and at 0.8 mM the uptake was 4.0 mmol/g (Figure 2.12). The uptake capacity of biogenic FeS at pH 5.0 was found to saturate at 1.8 mM, leading to 8.1 mmol/g. At pH 7.0, the same material was shown to sequester 0.4 mmol/g at 0.2 mM, and 6.3 mmol/g at 2.0 mM (Cd(II)). This trend of decreasing uptake capacity with pH was observed even at pH 9.0, resulting in 3.8 mmol/g of uptake at the highest initial concentration (2.0 mM). The final solution pH was found to vary (approximately 0.1 units) slightly in all reaction tubes.

The high sorption capacity of biogenic FeS for Cd(II) found at all pH values is in agreement with the earlier studies conducted in Task 1, and is consistent with the predominance of CdS(s) precipitation across the pH range. The steep nature of isotherm at pH 5.0 and high Cd(II) loading capacity (5.5 mmol/g) of biogenic FeS at low equilibrium concentration of Cd (0.53 mM) indicates that biogenically produced FeS would be an efficient sorbent for Cd(II).

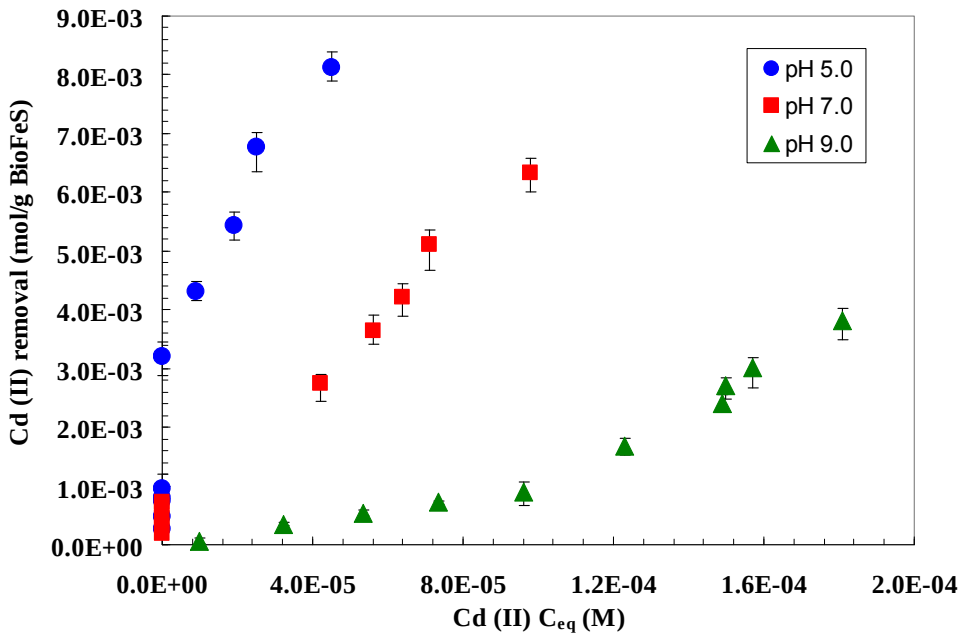

Figure 2.12. Sorption isotherms of Cd(II) by biogenic FeS at different pH; FeS concentration 1 g/L; pH adjusted with 0.1 N HCl or 0.1 N NaOH; ionic strength 0.015M.

Summary and Conclusions and Implications for Future Research/Implementation

The reactivity of the biogenic FeS generated by *D.acetoxidans* was evaluated for As(III) uptake with the highest uptake of 4.1 mmol As(III)/g obtained, which is almost 2.5-fold higher than the synthetic mackinawite under similar equilibrium concentration. This was attributed to the unique textural properties and high porosity of the biogenic FeS.

Isotherm studies of Cd(II) uptake by biogenically produced FeS at pH 5, 7 and 9 illustrates that the removal capacity of FeS for Cd(II) depends on pH with the greatest removal achieved at lower pH. The pH dependence suggests that sulfide availability was more significantly limited with increasing pH at the higher loadings. The high removal across the entire pH range is suggestive of removal by precipitation of CdS(s) as the Cd/FeS molar ratio approaches 1. At the lower Cd/FeS molar ratios (0.0001 – 0.01) used to generate pH edge data,

the Cd(II) removal was also limited by sulfide availability for the removal of Cd by precipitation of CdS(s), but that the sulfide availability was not as sensitive to pH for the lower Cd(II) loadings.

Additional work is needed to illustrate the effective sorption of As(III) and Cd(II) species under site-specific conditions (such as effect of common groundwater co-ions such as Ca and dissolved silicate) before utilizing biogenically produced FeS in the field.

Literature Cited

Aaron, G., Williams, B. and Scherer, M. 2001. Kinetics of Cr (VI) reduction by carbonate green rust. *Environ. Sci. Technol.* **35**, 3488-3494.

Adziong, W. and Thauer, R.K. 1980. Vectorial electron transport in *Desulfovibrio vulgaris* (Marburg) growing on hydrogen plus sulfate as sole energy source. *Arch. Microbiol.* **125,**167-174.

Benning, L.G., R.T.Wilkin, H.L. Barnes. 2000. Reaction pathways in the Fe-S system below 100°C. Chem. Geol. **167**: 25–51.

Berner, R.A. 1964. Iron sulfides formed from aqueous solutions at low temperatures and pressures. *J. Geol.* **72**, 293–306.

Barnes, S., Bradbrook, S.D., Cragg, B.A., Marchesi, J.R., Weightman, A.J. and Parkes, R.J. 1998. Isolation of sulfate-reducing bacteria from deep sediment layers of the Pacific Ocean. *Geomicrobiol. J.* **15,** 67-83.

Bruschi, M., Barton, L.L., Goulhen, F. and Plunkett, R.M. 2007. Enzymatic and genomic studies on the reduction of mercury and selected metallic oxyanions by sulfphate-reducing bacteria. p. 435-457. *In* L.L. Barton, W.A. Amilton (ed.), Sulphate-reducing bacteria, Cambridge.

Cline, J.D. 1969. Spectrophotometric determination of hydrogen sulfide in natural waters. *Limnol. Oceanogr.* **14**, 454-458.

Fredrickson, J.K., Kota, S., Kukkadapu, R.K., Liu, C. and Zachara, J.M. 2003. Influence of electron donor/acceptor concentrations on hydrous ferric oxide (HFO) bioreduction. *Biodegradation.* **14,** 91-103.

Herbert, R.B., Benner, S.G., Pratt, A.R. and D.W.Blowes. 1993. Surface chemistry and morphology of poorly crystalline iron sulfides precipitated in media containing sulfate-reducing bacteria. *Chem. Geol.* **144,** 87-97.

Horng, C.S., Torii, M., Shea, K.S. and Kao, S.J. 1998. Inconsistent magnetic polarities between greigite- and pyrrhotite/magnetite-bearing marine sediments from the Tsailiano-chi section, southwestern Taiwan. *Earth Planet. Sci. Lett.* **164**, 467–481.

Hristova, K.R., Mau, M, Zheng, D, Aminov, R.I., Macie, R.I., Gaskins, H.R. and Raskin, L. 2000. *Desulfotomaculum* genus- and subgenus-specific 16S rRNA hybridization probes for environmental studies. *Environ. Microbiol.* **2,**143-159.

Karnachuk, O.V., S.Y. Kurochkina, O.H. Tuovinen. 2002. Growth of sulfate-reducing bacteria with solid-phase electron acceptors. Appl.Microbiol.Biotechnol. **5:**482-486.

Lovley, D.R. and Phillips, E.J.P. 1992. Bioremediation of uranium contamination with enzymatic uranium reduction. *Environ.Sci.Technol.* **26,** 2228-2234.

Matsuo, M., Kawakami, M. and Sugimori, K. 2000. Mossbauer spectroscopic study on chemical changes of iron compunds with the aid of sulfate-reducing bacteria. *Hyperfine Inter.* **126,** 53-58.

Neal, A.L., Techkarnjanaruk, S., Dohnalkova, S., McCready, D., Peyton, M. and Geesey, G.G. 2001. Iron sulfides and sulfur species produced at hematite surfaces in the presence sulfate-reducing bacteria. *Geochim.Cosmochim. Acta.* **65,** 223-235.

Posfai, M., P.R. Buseck, D.A. Bazylinski, R.B. Frankel. 1998. Iron sulfides from magnetotactic bacteria: Structure, composition, and phase transitions. *American Mineral*. **83,** 1469-1481.

Rickard, D.T. 1969. The microbiological formation of iron sulphides. *Stokholm Contrib. Geol.* **20**, 49–66.

Roberts, A.P. and Turner, J. 1993. Diagenetic formation of ferrimagnetic iron sulfide minerals in rapidly deposited marine sediments, South Island, New Zealand. *Earth Planet. Sci. Lett.* **115**, 257–273.

Saas, H., Cypionka, H. and Babenzien, H.-D. 1997. Vertical distribution of sulfate-reducing bacteria at the oxic-anoxic interface in sediments of the oligotrophic Lake Stechlin. *FEMS Microbiol. Ecol.* **22,** 245-255.

Schoonen, M.A.A., H.L. Barnes. 1991. Reactions forming pyrite and marcasite from solution: II. Via FeS_2 precursors below 100°C. Geochim. Cosmochim. Acta **55**: 1505–1514.

Sweeney, R.E. and Kaplan. I.R. 1973. Pyrite framboid formation: laboratory synthesis and marine sediments. *Econ. Geol.* **68**, 618–634.

Tebo, B.M., A.Y. Obraztsova. 1998. Sulfate-reducing bacterium grows with Cr(VI), U(VI), Mn(IV) and Fe(III) as electron acceptors. *FEMS Microbiol Lett.* **162,** 193-198.

Zachara, J.M., J.K. Fredrickson, S.M. Li, D.W. Kennedy, S.C. Smith, P.L. Gassmann. 1998. Bacterial reduction of crystalline Fe^{3+} oxides in single phase suspensions and subsurface materials. *American Mineral.* **83,** 1426-1443.

Task 3. OPTIMIZATION OF COLLOIDAL INJECTION METHODS FOR THE EFFECTIVE INTRODUCTION AND DISPERSAL OF NANOSCALE FeS INTO POROUS MEDIA (Olson)

Subtask 3.1. Chemical Optimization of Deposition with Colloidal FeS

Objective

The installation of PRBs by trench-and-fill methods can be costly and applications are limited to depths of a few tens of meters. Colloidal injection methods of PRB installation were examined as a means of expanding the possible range of depths over which a FeS-type PRB technology could be employed. Optimal emplacement of the colloidal FeS was hypothesized to require sufficient, yet not excessive, repulsive interaction forces between the depositing particles and the aquifer sediment surfaces. Experiments were designed to establish the optimal chemical conditions for these conditions using a model silica sand porous media system.

Background

Deposition rates of colloidal particles flowing through granular porous media depend on the interaction forces between the particles and granular media surfaces. If deposition rates are not inhibited by electrostatic repulsive forces, or if the particles themselves are aggregating rapidly, plugging of pores in the inlet region will occur. The extent to which the injected particles are stable with respect to either deposition or aggregation depends critically on the particle surface charge characteristics, as well as other factors. At the initiation of this project, a clear understanding of FeS surface charge was not available. Unfortunately conventional methods of characterizing its surface charge or potential, such as potentiometric titrations or electrokinetic methods, were not practical for nano-particulate FeS due to the interference caused by its dissolution at pH < 6. These interferences were thought to explain in part, the wide range of point of zero charge (pH_{pzc}) values reported for the mineral ($pH_{pzc} < 3$, Bebie et al., 1998; $pH_{pzc} < 4$, Mullet et al., 2004; $pH_{pzc} \sim 7.5$, Wolthers et al., 2005; $pH_{pzc} \sim 5$, Gallegos, 2007). In light of these complications, an approach was taken in this study to measure the aggregation rates of FeS suspensions as a function of pH. Since the self-interaction of FeS colloids would largely depend on its surface charge (at constant ionic strength), these experiments were expected to elucidate the nature and sensitivity of its surface charge as a function of pH.

Solution chemistry variables such as pH and ionic strength can modulate the repulsive interaction forces, and thereby the deposition rates, of charged colloids on granular surfaces. Changes in solution pH affect the extent of ionization of weakly acidic or basic surface functional groups on either mineral surface, while increases in solution ionic strength serve to screen the surface charge and reduce the distance over which repulsive interaction forces between a colloid and porous media grain are exerted. Near the pH_{PZC} of the FeS, for example, the colloid has a net zero surface charge and electrostatic repulsive forces between approaching surfaces are minimal. At pH > $pH_{PZC,}$ FeS and silica sand surfaces are both negatively charged and FeS-sand interactions are repulsive. The self stability of FeS suspensions with respect to aggregation is also expected to increase. The optimum solution conditions for FeS emplacement in model granular media, silica sand, were investigated to demonstrate the the sensitivity of the deposition process to changes in these solution variables.

Materials and Methods

FeS Aggregation Kinetics. The aggregation kinetics of FeS particle suspensions was studied as a function of solution pH and ionic strength. Since pH was maintained with two buffer systems, the potential effect of buffer type was also tested. For initially monodisperse suspensions with particle number concentration, N, the rate of singlet aggregation to form doublets is a second-order process,

$$\frac{dN}{dt} = -k_{11}N^2 \qquad (3\text{-}1)$$

where k_{11} is the second order rate constant (von Smoluchowski, 1917). Changes in the initial light scattering intensity of FeS suspensions with time, as a result of changes in aggregate radius, were used to estimate k_{11} as follows:

$$k_{11} = \frac{2}{r_0 \cdot N_0}\left(\frac{I_1(q)}{I_2(q)}\right)\frac{r_{h2}}{r_{h2} - r_{h1}}\left(\frac{dr}{dt}\right)_{t=0} \qquad (3\text{-}2)$$

where r_0 and N_0 are the initial radius and number concentration of particles, respectively, r_{h1} and r_{h2} are the respective hydrodynamic radii of the singlet and doublet, and $I_1(q)/I_2(\mathrm{q})$ is the ratio of the singlet and doublet scattering intensities as a function of scattering vector magnitude, q (Virden and Berg, 1992). Experimental measurements of the initial rate of aggregate radius increase, $(dr/dt)_0$, were obtained by photon correlation spectroscopy (PCS) in an anoxic chamber. Values of the intensity ratio, $I_1(\mathrm{q})/I_2(\mathrm{q})$, were estimated according to the method outlined by Virden and Berg.

Nanoparticulate FeS was synthesized following the method of Butler and Hayes (1999). After rinsing, the FeS was freeze-dried under vacuum and stored in an anoxic chamber until use. Sample FeS suspensions for the aggregation experiments were prepared from twice-filtered (0.1 μm GE syringe filter) stock suspensions (prepared at pH ~ 9.4) at 13 mg/L FeS, with a mean initial diameter of 40 ±10 nm. Sample pH was adjusted with buffers; MOPS for the pH range 6.5 to 8.0 and borate buffer for pH 8.3 to 9.0. Potassium chloride was added to obtain the desired ionic strength. All stock buffer and KCl solutions were pre-filtered (0.01 μm) before use.

FeS Deposition Tests. Rates of FeS particle deposition on sand were examined in packed column tests. The quartz sand (U.S. Silica, Pacific, MO) had a mean grain diameter of approximately 150-210 um. Prior to use, the sand was rinsed sequentially with solutions of sodium dithionite and hydrogen peroxide to remove surface metal oxides and organic matter. Column experiments were conducted in a 2.6 cm diameter, 25 cm long glass column. Sand was dry-packed with a resulting porosity of 0.34 ± 0.01. The packed column was pre-equilibrated with 10 pore volumes of background electrolyte having the same chemical composition as the influent FeS suspensions. An HPLC pump was used to introduce the suspensions in an upflow mode at a superficial velocity of 0.57 cm/min. Influent suspensions contained 1 g/L FeS and were prepared by redispersing the freeze-dried FeS in deoxygenate, deionized water, mixing for 24 hours, and adding pH buffers and salt as needed. Ten pore volumes of the suspension were injected in each run. Column effluent fractions were collected with an automatic fraction

collector (Frac-100, Pharmacia). Particle mass concentrations of the fractions were estimated from their total iron content after acidification in 2% nitric acid and analysis by ICP-MS (Perkin Elmer, Model ELAN DRC-e). Particle coverage of the sand was quantified after each of the deposition experiments by rinsing suspended particles in the pore fluid with two pore volumes of particle-free electrolyte, hydraulically extruding sequential 2.5 cm long sections of the sand, extracting the dried sections with 6 N HCl, and analyzing the extracts for total iron by ICP-MS.

Results and Discussion

Aggregation Kinetics. PCS measurements of the change in FeS aggregate size as a function of pH at fixed ionic strength (0.05 M) are presented in Figure 3.1. Values of the second order rate constant, k_{11}, were determined from the initial slopes of these data sets, $(dr/dt)_0$. The measured initial aggregation rate constant can be modeled as the product of the singlet collision frequency, β_{11} and the aggregation efficiency, α, i.e., $k_{11} = \beta_{11}\alpha$. Suspensions are considered 'stable' when collisions are less than 100% efficient, $\alpha < 1$, in producing an aggregate. Under diffusion-limited colloid aggregation conditions (DLCA), $\alpha = 1$, von Smoluchowski (1917) showed that the rate constant could be calculated as:

$$k_{11,\mathrm{DLCA}} = \frac{8k_B T}{3\mu} \qquad (3\text{-}3)$$

where k_B is the Boltzmann constant, T is absolute temperature, and μ is the absolute visocity of the solution. The relative importance of electrostatic repulsion in stabilizing FeS particle suspensions was assessed by estimating the dimensionless stability ratio, W, at varying solution pH and ionic strengths:

$$W = \frac{k_{11,\mathrm{DLCA}}}{k_{11,\,\mathrm{expt}}} \qquad (3\text{-}4)$$

where $k_{11,\mathrm{expt}}$ is the rate constant estimated from experiments. Under DLCA conditions, the stability ratio approaches unity, and for suspensions that are significantly stabilized by electrostatic repulsive forces, $W >> 1$. The pH dependence of the stability ratio for FeS suspensions is plotted in Figure 3.2 for a constant ionic strength of 0.05 M. Suspensions are observed to monotonically increase as pH increases. Over the range pH > 6.5, the FeS surface is apparently negatively charged. Between pH 6.5 to 8.3, however, W is relatively small and insensitive to changes in pH, suggesting that surface charge densities are small at these pH conditions. Significant deprotonation of FeS surface functional groups is implicated at pH > 8.3, based on the large increase in FeS stability with increasingly alkaline pH. Appreciable dissolution of the FeS at pH < 6.5 prevented determinations of aggregation rates for more acidic pH conditions. These aggregation results demonstrate that under ambient pH conditions in an aquifer, repulsive interactions between the aquifer matrix and FeS particles will be exerted if the subsurface porous media surfaces are also negatively charged.

With the addition of buffers to a suspension, there is a general concern that specific adsorption of the buffer ion could change the surface charge of the colloids being studied. To test the effect of the pH buffers on FeS stability, a comparison of particle stability ratios was

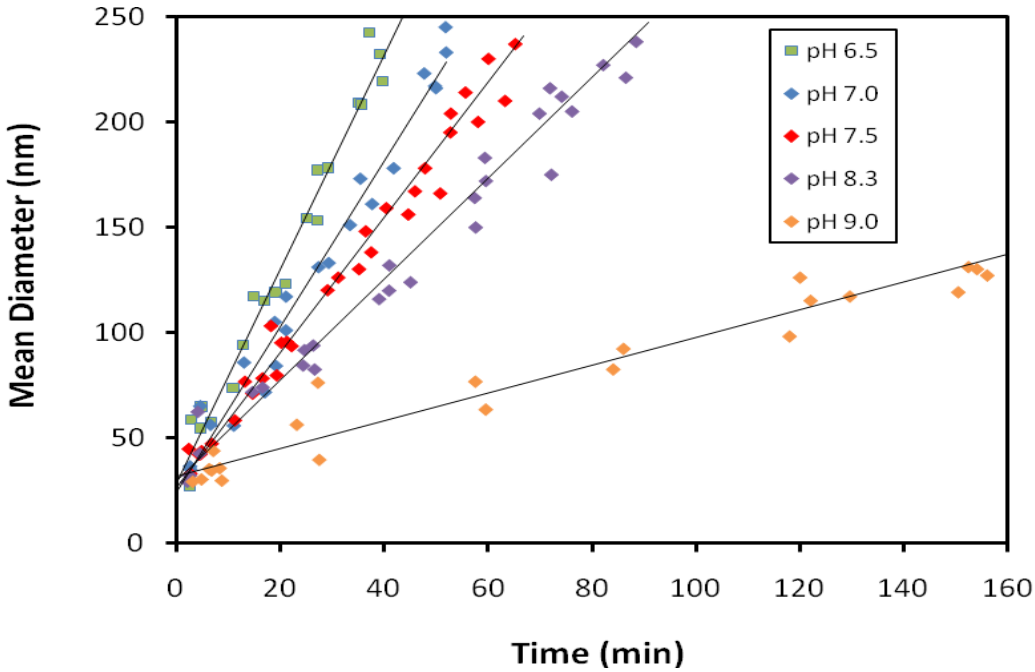

Figure 3.1. Initial aggregation rates of nanoparticulate FeS suspensions at varying pH and constant ionic strength, 0.05 M. Particle diameters were measured by PCS.

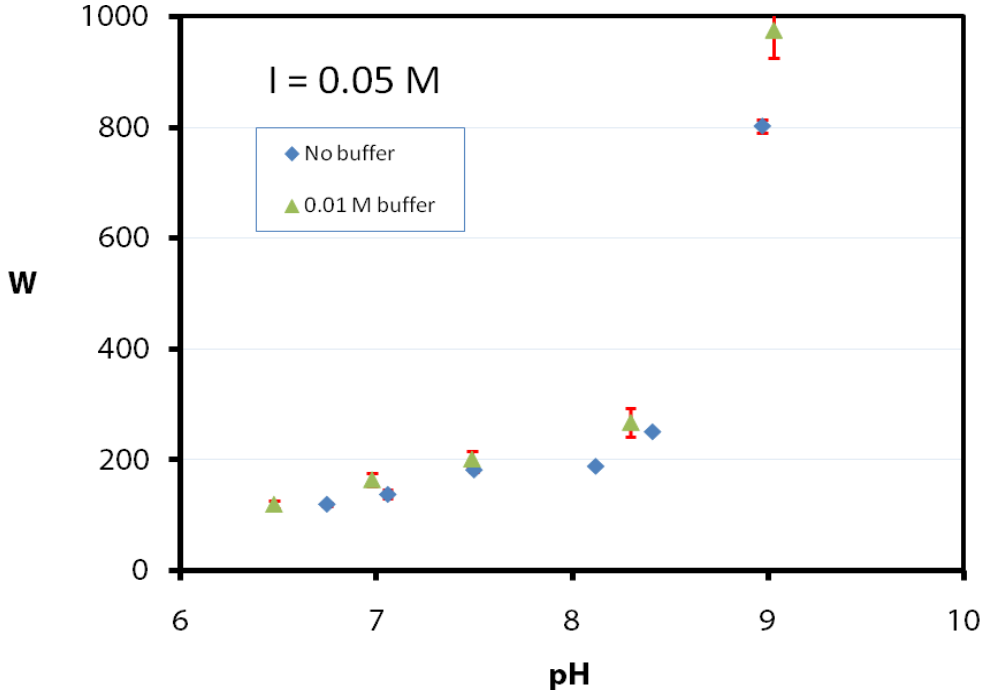

Figure 3.2. Stability ratio dependence on pH with and without pH buffers. Error bars represent one standard deviation, and are obscured by the symbols in some cases.

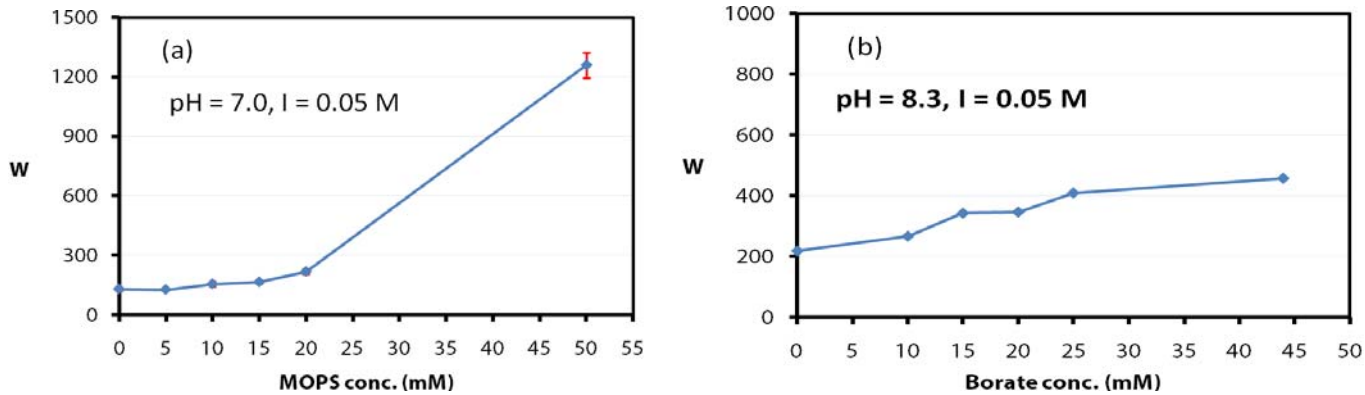

Figure 3.3. FeS stability ratios as a function of buffer concentration at fixed ionic strength. (a) MOPS buffer at pH 7.0, (b) borate at pH 8.3.

conducted using unbuffered suspensions and the stability ratios are compared to the buffered suspensions in Figure 3.2 as well. Further variation of the buffer concentration at a fixed pH 8.3 (see Figures 3.3 a,b) demonstrate that buffer effects are eventually observed, but only at buffer concentrations exceeding 0.02 M. The organic buffer, MOPS (3-(N-Morpholino)-propanesulfonic acid, MW = 209.3), also had a more significant effect than borate. In previously discussed aggregation experiments, buffer concentrations did not exceed 0.01 M.

At pH 8.3, the effect of ionic strength was examined over the range 0.025 to 0.1 M. As shown in Figure 3.4, FeS stability ratios are relatively sensitive to ionic strength; *W* decreased from 33,800 to 5.5 as the ionic strength increased from 0.025 to 0.1 M. Based on classical DLVO theory, estimates of the characteristic Debye lengths ranged from ~ 2 to 1 nm at the lowest and

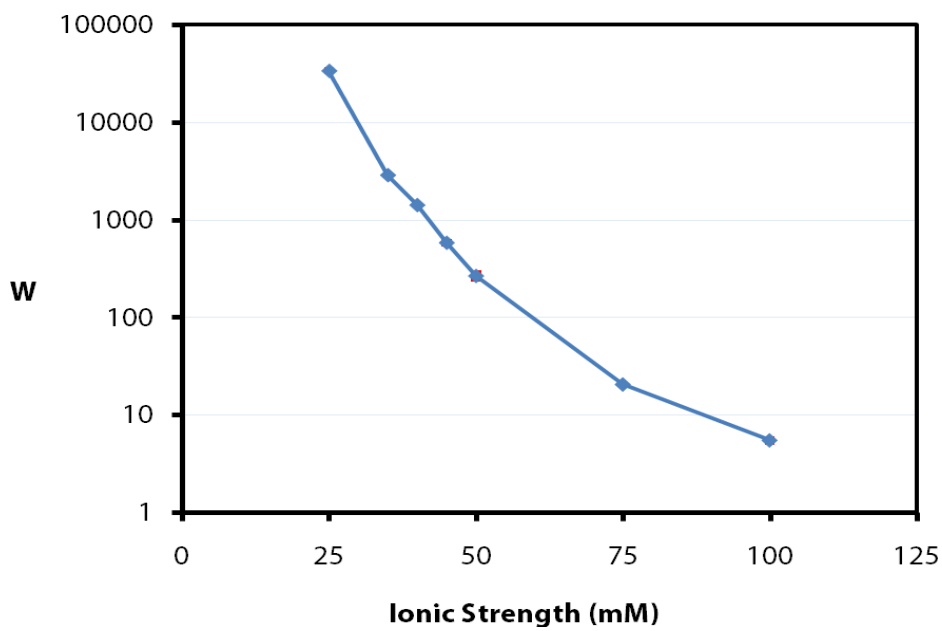

Figure 3.4. Semi-logarithmic plot of FeS stability ratios as a function of ionic strength at pH 8.3 and 0.01 M borate buffer.

highest ionic strengths, respectively (Derjaguin and Landau, 1939; Verwey and Overbeek, 1948). These conditions provided helpful context to interpret the necessary conditions for FeS penetration

FeS Deposition Tests. Deposition rates of FeS particles on clean sand were studied as a function of pH and ionic strength. Influent particle concentrations were maintained at 1 g/L FeS, which was significantly higher than the 13 mg/L concentration used in the previous aggregation experiments. These relatively high particle concentrations were used in order to effectively obtain FeS coatings on the sand over practical time periods, and thereby simulate conditions that might be used in the field. Given that the particle number concentration was quite large, it was not possible to maintain monodisperse influent suspensions and the turbidity prevented an assessment of average particle size. The influent particle suspensions, however, were observed to remain stable with repect to gravitational settling over the course of the injection experiments.

In each experiment the effluent breakthrough concentrations of particles were monitored over a 10-pore volume injection period. Specific deposit concentrations of FeS on the sand were also determined as a function of depth at the end of the injection period. Results obtained at varying pH and fixed ionic strength (0.025 M) are presented in Figures 3.5a,b. Nearly complete breakthrough of the FeS particles was observed after 2 to 3 pore volume, suggesting that the deposition of particles on previously deposited particles was significantly unfavorable (net repulsive interaction force present). The data in both Figure 3.5a and b reveal two 'clusters' of pH conditions: pH 6.5 to 8.3 and pH 9.0 to 10.3 where breakthrough and deposited concentrations are similar. Breakthrough, for example, was slightly more retarded at pH 6.5, 7.5, and 8.3, than at pH 9.0 or 10.3. Specific deposit concentrations over the deepest 20 cm of the profile were similar for the pH range 6.5 to 8.3, and approximately twice the specific deposit concentration in the same zone at pH 9 and 10.3. Specific deposit concentrations in the inlet zone (top 5 cm) were more scattered and less reproducible between replicates (data not shown), than the uniform particle concentrations observed in deeper sections of the column. It was suspected that this was a result of variations in the particle size distribution of the influent between experiments. The pH ranges describing the above mentioned 'clusters' happen to coincide with the same pH ranges over which aggregation is relatively pH independent and pH-sensitive. It is hypothesized that the pH independence of coverage between pH 6.5 and 8.3 is due to a relatively constant FeS surface charge in this pH range. Once the FeS attains saturation coverage of the quartz sand surface, the deposited particles present a similar and repulsively charged surface to new approaching particles.

FeS deposition experiments were also conducted at higher ionic strengths. The results are summarized in Table 3.1. At $I = 0.05$ M, FeS coverage of the sand in the final 2.5 cm section of sand was approximately 50% greater than at $I = 0.025$ M (at pH 8.3), however, the inlet (first 2.5 cm section) concentration was six times greater than inlet concentration in the 0.025 M experiment. When the ionic strength was increased to 0.077 M, particle effluent concentrations were suddenly and completely filtered after 6 pore volumes, and hydraulic flow rates could not be maintained, indicating that plugging of the inlet had occurred. To prevent plugging and maximize coverage of the sand, solution conditions in the pH range of 6.5 to 8.3 at an ionic strength of approximately 0.025 M are apparently optimal.

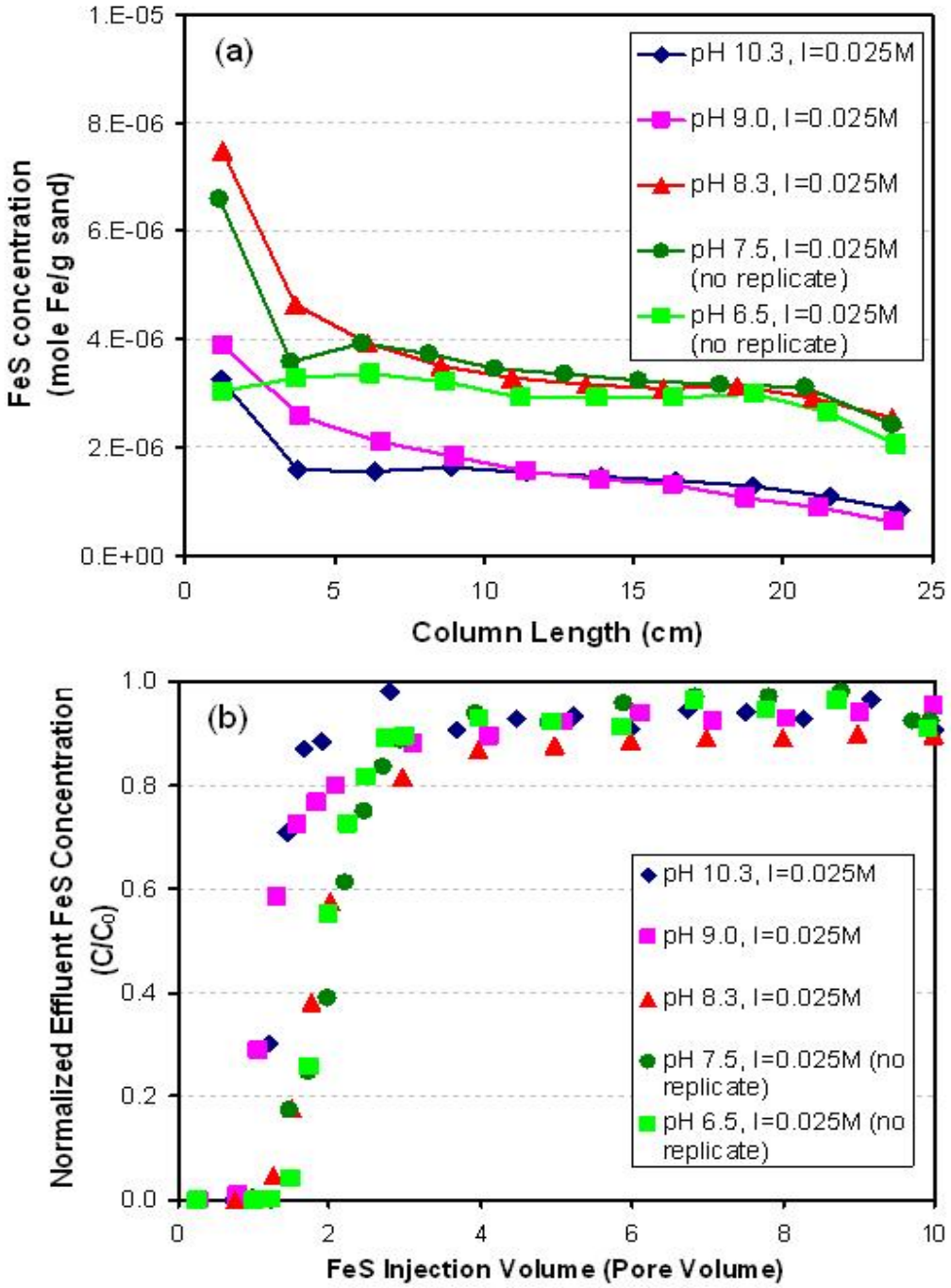

Figure 3.5. Deposition experiments of 1 g/L FeS suspensions in sand columns at varying pH and fixed ionic strength (0.025 M). (a) deposited FeS concentration profiles after 10 pore volumes (b) effluent breakthrough curves.

Table 3.1. Summary of deposited FeS concentrations at varying pH and ionic strength.

1g/L FeS Suspensions		Average FeS Coverage (mol Fe/g sand)	FeS deposition in first 2.5cm (mol Fe/g sand)	FeS deposition in last 2.5cm (mol Fe/g sand)	Normalized standard deviation*
pH	Ionic strength (M)				
10.3	0.025	1.56×10^{-6}	3.25×10^{-6}	1.08×10^{-6}	0.41
9.0	0.025	2.43×10^{-6}	3.87×10^{-6}	8.81×10^{-7}	0.55
8.3	**0.025**	**3.76×10^{-6}**	**7.48×10^{-6}**	**2.91×10^{-6}**	**0.38**
7.5	**0.025**	**3.66×10^{-6}**	**6.50×10^{-6}**	**3.12×10^{-6}**	**0.30**
6.5	**0.025**	**2.93×10^{-6}**	**3.04×10^{-6}**	**2.65×10^{-6}**	**0.13**
10.3	0.050	5.08×10^{-6}	1.52×10^{-5}	3.01×10^{-6}	0.73
9.0	0.050	1.19×10^{-5}	3.98×10^{-5}	5.40×10^{-6}	0.69
8.3	0.050	1.45×10^{-5}	4.55×10^{-5}	4.31×10^{-6}	0.93
8.3	0.077	5.74×10^{-6}	**8.06×10^{-5}****	4.93×10^{-6}	1.42

*** Normalized standard deviation = standard deviation/mean of data from 10 sections in the column**

** 100% retention of FeS particles occurred.

Summary and Conclusions and Implications for Future Research/Implementation

Solution chemistry variables such as pH and ionic strength exert an important influence on the stability and mobility of FeS particles in porous media. Successful emplacement of FeS *in situ* by injection requires sufficiently stable suspensions with respect to self-aggregation in order to avoid plugging of the aquifer matrix. Based on aggregation kinetic studies of nanoparticulate FeS, suspensions are weakly stable over most groundwater pH conditions and FeS stability over the pH range of 6.5 to 8.3 is relatively insensitive to pH. At pH greater than 8.3, particle stability was much more pH-sensitive and hence greater deprotonation of surface sites is indicated. Ionic strength conditions in an aquifer may be more important than pH in assessing the tendency of FeS particles to aggregate, since the particles are weakly charged in the neutral pH range. Column deposition tests were consistent with the aggregation study trends. Deposition rates of FeS on sand surfaces were also relatively pH insensitive over the neutral pH range. Optimal solution conditions for colloidal FeS injection were identified as pH 6.5-8.3 and I ~ 0.025 M, based on the goal of maximizing FeS coverage of the porous media and minimizing plugging. Average coverages of the FeS on the sand under these conditions were similar to the coatings achieved in batch in Subtask 1.1. Additional studies to examine the feasibility of *in situ* emplacement in the field will be necessary.

Literature Cited

Bebie, J., M. A. A.Schoonen, M. Fuhrmann, and D.R. Strongin, 1998. Surface charge development on transition metal sulfides: An electrokinetic study. *Geochim. Cosmochim. Acta* **62**, 633-642.

Butler, E.C. and K.F. Hayes, 1999. Kinetics of the transformation of trichloroethylene and tetrachloroethylene by iron sulfide, *Environ. Sci. Technol.*, **33**, 2021-2027.

Derjaguin, B.V. and L. Landau, 1939. A theory of interaction of particles in presence of electric double layers and the stability of lyophobic colloids and disperse systems, *Acta Physicochimica* URSS, **14**, 333-346.

Gallegos, T.J., "Sequestration of As(III) by Synthetic Mackinawite under Anoxic Conditions," Ph.D. Dissertation, Department of Civil and Engineering, University of Michigan, August 2007.

Mullet, M., S. Boursiquot, and J.J. Ehrhardt, 2004. Removal of hexavalent chromium from solutions by mackinawite, tetragonal FeS. *Colloids and Surf. (A)*, **244**, 77-85.

Verwey, E.J. and T.G. Overbeek, 1948. *Theory of the Stability of Lyophobic Colloids*, Amsterdam: Elsevier.

Virden, J.W. and J.C. Berg, 1992. The use of photon-correlation spectroscopy for estimating the rate constant for doublet formation in an aggregating colloidal dispersion, *J. Colloid Interface Sci.*, **149**, 528-535.

von Smoluchowski, M., 1917. Drei vortrage uber diffusion, brownsche molecular bewegung and koagulation von kolloidteilchen. *Physikalische, Zeitschrift*, **17**, 557-599.

Wolthers, M., L. Charlet, P.R. van der Linde, D. Rickard, and C.H. van der Weuden, 2005. Surface chemistry of disordered mackinawite (FeS), *Geochim. Cosmochim. Acta*, **69**, 3369-3481.

Subtask 3.2 FeS Release Evaluations

Objective

Once deposited by an *in situ* emplacement technique, the physical loss of FeS coatings could limit the longevity of the installed PRB and cause the re-mobilization of contaminants. Two mechanisms of loss, dissolution and particle detachment, are possible. Column experiments were designed to assess the relative importance of these mechanisms and the rates at which they occur as a function of solution conditions.

Background

During the operation phase, as contaminant plumes flow through an installed PRB, the non-equilibrium nature of the system inevitably induces changes in any reactive phase, such as precipitation, passivation/oxidation, or aging. When the reactive phase emplaced as colloidal particles on another supporting surface, mechanisms including dissolution or particle release can occur. The solubility of FeS has previously been characterized in by Gallegos (2007), as well as by other investigators (Richard, 2006). These studies have demonstrated that the solubility of mackinawite increases significantly below pH 6.5. It is also well known that chemical disturbances can result in colloidal detachment in field and laboratory sediments (Liang et al, 2000). Bunn et al. (2002) found that pH pulses were more effective in mobilizing colloids from sediments than changes in ionic strength. In considering both release mechanisms for the case of FeS, it was hypothesized that dissolution might represent the most important release mode at lower pH, while particle detachment could become important when the FeS surface was the most negatively charged (higher pH). Such opposing trends would suggest that optimal pH conditions for FeS longevity might exist.

In order to simulate the coated sand media, some compromise in the experimental design became necessary to establish a well defined starting point for the FeS release experiements. Some limited experiments were conducted with sand media that was coated by depositing FeS particles in a packed bed arrangement. Unfortunately by this approach, the starting concentration of deposited FeS is not uniform throughout the column, but more importantly, it is not possible to characterize FeS content of the starting column prior to studying FeS release. An alternative design was pursued in which the sand was coated in batch and the coated sand was used in subsequent FeS release tests.

Materials and Methods.

Synthesis of FeS Pre-coated Sand. The FeS pre-coated sand was prepared by mixing 50 g of clean quartz sand and 30 mL of 3.7 g/L of well-dispersed FeS suspension in 50 mL polypropylene centrifuge tubes. The mixture of sand and FeS was acidified by adding 3.8 mL of 1 N HCl and rotary-mixed for 48 h. The resulting slurry pH was 5.2. After filtration to remove excess solution, the wet FeS coated sand was dried in a glovebox for 72 h and finally stored until used. Analysis of the coating indicated that it contained 2.0 mg FeS/g sand.

Release Tests. The FeS release tests were conducted in 16 mm-diameter, 100 mm-long columns in an anaerobic glovebox. The FeS-coated sand was dry-packed with resulting porosities of 0.32

±0.01. The packed column was saturated by processing 25 pore volumes of conditioning electrolyte (pH 9, with 3.5 mM borate buffer, I = 0.005 M), prior to the release tests. Iron concentrations in the conditioning stage effluent were less than the detection limit, ~ 50 µg/L Fe. A peristaltic pump was used throughout the conditioning and elution stages. All but one of the elution experiments were conducted with a Darcy velocity of 0.024 cm/s. To test the effect of flow rate and examine possible mass transfer effects, an additional elution experiment was conducted at 1/10 slower velocity, . To examine the effect of electrolyte pH on FeS release, solutions contained 0.01 M borate, MOPS, acetate buffers for pH 9.0 and 10.0, pH 6.5 and 7.5, and pH 5.5 electrolytes, respectively. Effluent fractions were collected in an automatic fraction collector, every 1 to 2 pore volumes. To distinguish between particulate and dissolved Fe, the portions of the effluent fractions were filtered using 0.02 µm syringe filters. Filtered and unfiltered samples were acidified with nitric acid and analyzed for Fe by ICP-MS. Particulate iron concentrations were estimated by the difference between dissolved and total iron.

Results and Discussion

As pH was varied (with fixed I = 0.01 M) iron release was detected only at pH less than 9.0. The individual contributions and patterns of dissolved and particulate iron in the effluent are discussed separately.

Dissolved Fe Release. The pH dependence of dissolved iron elution is shown in Figure 3.6. As expected, effluent dissolved iron concentrations increased as the pH decreased, and especially as

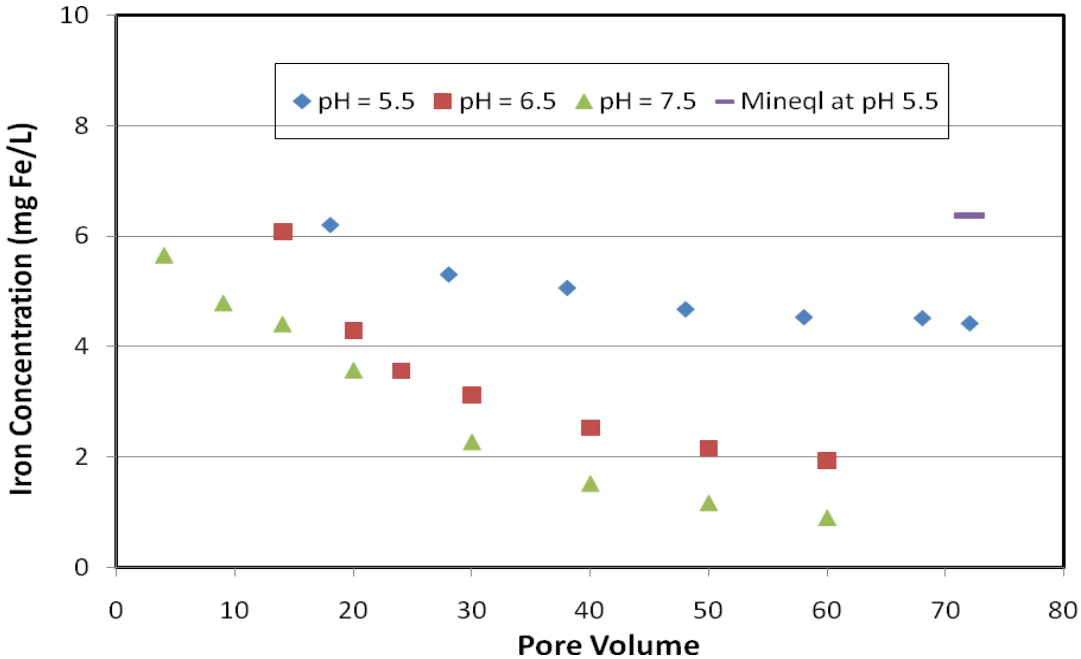

Figure 3.6. Eluted dissolved iron as a function of pH in FeS coated sand column. I = 0.01 M, Darcy velocity = 0.024 cm/s. Purple horizontal line indicates MINEQL+ prediction of saturation iron concentration with respect to FeS at pH 5.5.

the pH decreased below 6.5. While the elution curves appeared to attain steady-state, the final steady state values were only attained after 60 pore volumes were processed. Predictions of the saturation concentration of dissolved iron at pH 5.5 using MINEQL+ (Environmental Research Software, 2001) were also over predictions relative to the steady-state value (see Figure 3.6). It is suspected that slow phase changes of the FeS may account for the slow approach to steady state and apparent under saturation. Total and dissolved effluent Fe concentrations at pH 5.5 are shown in Figure 3.7, and it is clear that Fe loss is primarily as dissolved iron at these pH conditions, but that at lower ionic strength, a slightly greater difference in the total and dissolved iron concentrations was observed. Possible reasons for this are discussed with particulate iron release trends.

Particulate Fe Release. The pH dependence of particulate iron release from the FeS-coated sand is plotted in Figure 3.8 (constant 0.01 M ionic strength). Unexpectedly, the elution profiles indicate that particulate iron release was a maximum at pH 6.5 and that steady state was approached more slowly at this pH. One possible explanation for the maximum could involve a complex dissolution-driven particle release mechanism. For example, particles may be shed from the surface due to the dissolution of weak points in the fine structure of the coating. Although this same process may release even more particles at pH 5.5, the released particles may themselves dissolve before exiting the column.

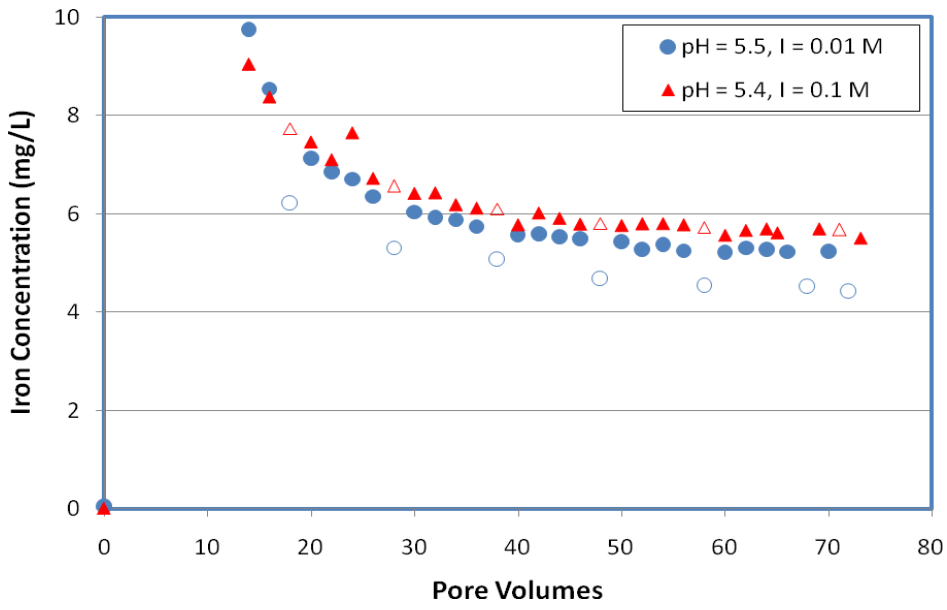

Figure 3.7. Comparison of total and dissolved iron concentrations at pH 5.4-5.5 eluted from FeS-coated sand column. Filled markers are total iron concentrations, unfilled symbols are dissolved iron concentrations. Circles and triangles correspond to ionic strength conditions of 0.01 and 0.1 M, respectively.

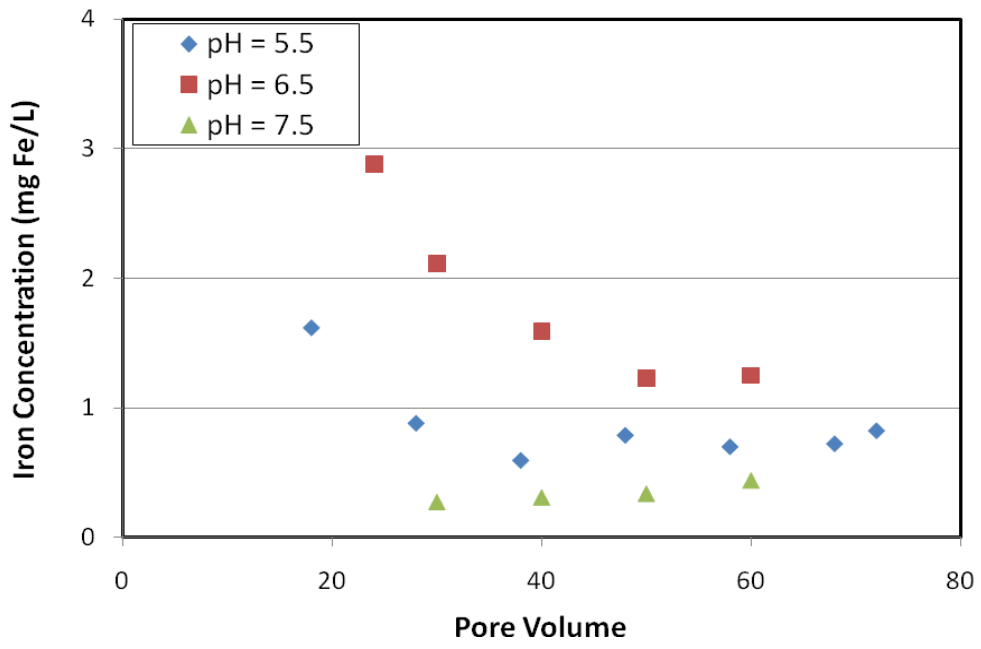

Figure 3.8. pH dependence of particulate Fe release from FeS-coated sand columns. I = 0.01 M, Darcy velocity = 0.024 cm/s.

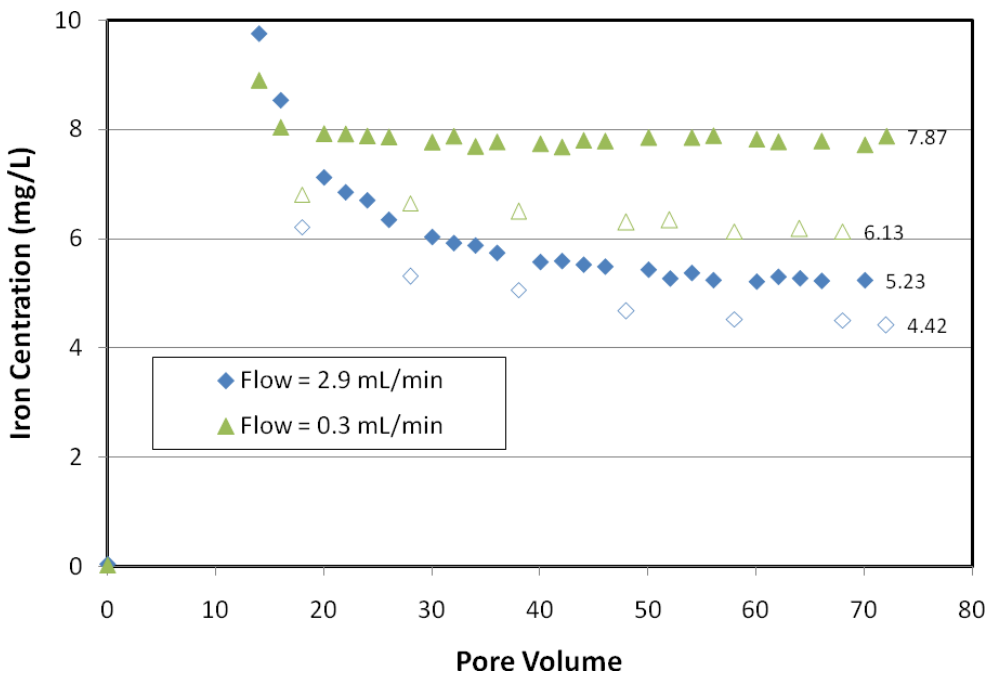

Figure 3.9. Effect of flow rate on total and dissolved iron elution from FeS-coated sand column at pH 5.5, I = 0.01 M. Numeric values next to curves are steady-state iron concentrations. Unfilled markers are particulate iron concentrations, filled markers are total Fe concentrations.

Effect of Flow Rate. The rate of iron release was expected to depend on flow rate. At pH 5.5, upon decreasing the flow velocity by an order of magnitude, the steady state total effluent iron concentration increased, as shown in Figure 3.9, although the approach to steady state was more rapid (20 pore volumes compared to 60). Calculations based on simple mass transfer-limited dissolution models were not able to explain the differences in steady-state iron loss at these two flow rates. An alternative explanation that is consistent with the slow approach to steady-state at high flow rates is one that also involves phase changes or corrosion of the media at higher flow rates. At slower flow rates, the redox potential of the pore solution is likely to be controlled by FeS over a longer distance in the column and is therefore expected to be more reducing on average. As FeS corrodes more slowly, the steady-state concentration of dissolved iron in Figure 3.9 more closely approaches the saturation concentration predicted by MINEQL+ (see Figure 3.6).

Summary and Conclusions and Implications for Future Research/Implementation

Dissolution was the dominant mechanism of FeS loss, but was only significant at pH < 7.5. Simple calculations based on the loss rates of iron in these experiments, assuming a 2 mg FeS coating per gram of sand, a Darcy velocity of 10^{-3} cm/s, and a 5 m thick FeS zone, suggest the loss of iron sulfide per year would be 2.4, 5.2, and 11.9% of the original FeS at pH 7.5, 6.5, and 5.5, respectively. Particle release was relatively unimportant, and where detected appeared to be due to a complex dissolution-driven mechanism. In terms of the site conditions that promote FeS longevity, less acidic aquifers would favor less mobilization of the FeS. Slower Darcy velocities, are also suspected to favor slower corrosion rates of the FeS.

Literature Cited

Bunn, R.A., R.D. Magelky, J.N. Ryan, and M. Elimelech, 2002. Mobilization of natural colloids from an iron oxide-coated sand aquifer: Effect of pH and ionic strength, *Environ. Sci. Technol.*, **36**, 314-322.

Butler, E.C. and K.F. Hayes, 1999. Kinetics of the transformation of trichloroethylene and tetrachloroethylene by iron sulfide, *Environ. Sci. Technol.*, **33**, 2021-2027.

Environmental Research Software. 2001. MINEQL+ version 4.5.

Gallegos, T.J., "Sequestration of As(III) by Synthetic Mackinawite under Anoxic Conditions," Ph.D. Dissertation, Department of Civil and Engineering, University of Michigan, August 2007.

Liang, L., A. Hofmann, and B. Gu, 2000, Ligand-induced dissolution and release of ferrihydrite colloids, *Geochim. Cosmochim. Acta*, **64**, 2027-2037.

Richard, D., 2006. The solubility of FeS, *Geochim. Cosmochim. Acta*, **70**, 5779-5789.

Task 4. INVESTIGATION OF SUITABLE METHODS OF EMPLACEMENT OF *FeS* IN MIXED POROUS MEDIA FOR EFFECTIVE SEQUESTRATION OF METALS AND PLUGGING AVOIDANCE (Demond)

Subtask 4.1. Development of the Optimal Particle-Size Distributions of PRB Media for Limiting the Reduction in Permeability

Objective

A key issue that affects the feasibility and performance of PRBs is their longevity, which can be compromised by permeability reduction. To ensure long-term removal of heavy metals from groundwater, it is crucial to minimize permeability loss due to precipitate accumulation. It was hypothesized that PRBs constructed of FeS, like the more common material, ZVI, would be subject to permeability reduction, and that engineered particle-size distributions could mitigate these undesired hydraulic changes.

Background

Based on geochemical considerations and reported field experience with ZVI, precipitation occurs in most PRBs. For example, precipitation of solids in the 100% ZVI section of the PRB at Monticello, UT, caused failure of that PRB (Mushovic et al., 2006). Because of the parallels between the ZVI and FeS systems, it was expected that FeS-based PRBs may be subject to loss of permeability, as well. This reduction in permeability is not a consequence of the removal of the targeted contaminant, but rather, results from the precipitation of background groundwater constituents. For example, at the UMTRA site (Durango, CO), uranium made up only 0.2% (by weight) of the precipitates (Matheson et al., 2002) and solid-phase uranium was below the detection limit at the Y-12 site (Oak Ridge, TN), although it was being removed in the barrier (Phillips et al., 2000).

Studies with ZVI have shown that corrosion reactions with a variety of oxidants, ranging from oxygen to water itself, convert the surface of ZVI to iron oxides of a higher iron oxidation state, ranging from green rusts with predominantly Fe(II) species, to mixed Fe(II)/Fe(III) solids such as magnetite, to Fe(III) oxyhydroxides such as ferrihydrite (Liang et al., 2003; Jambor et al., 2005). In PRBs, oxygen is consumed quickly, near the upgradient end of the PRB, whereas anaerobic oxidation by other oxidants (e.g., water or targeted redox active contaminants) may happen deeper in the PRB, where the iron minerals discussed above or iron carbonates – if carbonate is present in the groundwater – may form (Furukawa et al., 2002). As with ZVI, the oxidation of FeS may produce mixed and higher-valence iron oxides, such as goethite; in addition, oxidized iron sulfide forms such as the mixed Fe(II)/Fe(III) iron sulfide greigite or pyrite may be formed (Lennie et al., 1997). Even if reduced iron PRB materials are oxidized, the resulting solid phases can still remove metal cations (Furukawa et al., 2002) and oxyacids (Su and Puls, 2001).

Over 120 iron-based PRBs had been installed worldwide as of 2004 (ITRC, 2005), yet they are still considered an experimental technology (Warner and Sorel, 2003), largely because their long-term performance was not well understood. As Wilkin and Puls (2003) point out, "[f]ew case studies are available that evaluate the long-term performance of these in-situ systems, especially with respect to the long-term efficiency of contaminant removal, the buildup of mineral precipitates, and the buildup of microbial biomass."

Attempts to mitigate the hydraulic effects of precipitation in ZVI have largely been through the installation of a pretreatment zone (PTZ) placed immediately upgradient of a PRB. It is constructed of large-grained media, gravel or sand and can serve to distribute the groundwater flow more evenly across the face of the PRB. If reactive media is mixed in, such a zone allows for precipitate formation with minimal permeability reduction, and can therefore reduce potential clogging at the upgradient of a PRB (Dwyer, 2000; Sarr, 2001).

At the outset of this project, the state of knowledge in the field indicated the potential for harmful precipitation in ZVI systems; from this it was inferred that permeability reduction would be an issue in FeS systems as well. Thus, the objective of the research in this task was to investigate solids formation, the resultant permeability reduction, and the mitigation thereof, in FeS systems.

Materials and Methods

Given the uncertainty in the literature about factors that control precipitation in ZVI systems, this subtask focused on understanding conditions under which precipitation would be likely in ZVI and FeS systems. To identify conditions in which precipitation was expected to be a problem, an analysis of existing reports about field PRB performance was conducted and the results of geochemical modeling simulations were evaluated. .

Literature Review and Statistical Analysis of ZVI Field Sites

An extensive literature and statistical analysis of PRB case studies was carried out in order to target those factors which are most likely to control permeability reduction in the field. This analysis was developed into a journal article (Henderson and Demond, 2007) that examines geochemical parameters that have been postulated to control PRB longevity. In the literature, the longevity of a PRB is thought to be linked to either a loss of media reactivity or a loss of permeability, both of which depend on groundwater composition. Because only a handful of PRBs have failed, the analysis focused on changes that put a PRB "at risk" for future failure; these changes were decreases in hydraulic conductivity and decreases in treatment efficacy. Because of the limited comprehensive geochemical data available in the literature, the quantitative analysis was, of necessity, confined to 16 ZVI in situ field PRBs treating organics and/or metals for which extensive information was available (Table 4.1).

Based on the information generally available in the literature and geochemical considerations, 37 parameters were selected for inclusion in the study. Table 4.2 and Table 4.3 present these parameters. In order to distill multiple measurements for the same parameter to a single value (e.g., measurement of pH inside the PRB at several sampling events), an arithmetic mean was used for all parameters except hydraulic conductivity, hydraulic gradient, and flow rate. At a given site, these parameters often vary over several orders of magnitude, so a geometric mean was used. Sites were grouped into those which were performing as expected, and those that had failed or were "at risk", defined as a report of a loss in permeability, a loss in reactivity, or some other indication of compromised performance.

Statistical analyses included univariate logistic regression , and a maximization of odds ratios (Hosmer and Lemeshow 1989). All statistical tests were conducted using the SPSS statistical software package (SPSS Inc., Chicago, IL). Highly collinear variables were discarded.

In logistic regression, the independent predictor variable x is related to the conditional probability, π(x), of a dependent variable outcome of "at risk" as follows:

$$\pi(x) = \frac{\exp(g(x))}{1 + \exp(g(x))}$$

where g(x) is a linear predictor such that $g(x) = \beta_0 + \beta_1 x_1 + \varepsilon$, where ε accounts for variations that are not covered by terms in the model. In estimating each value of β^i, a standard error (S.E.) is estimated, and thus the Wald statistic ($\text{Wald}^i = \beta^i$ / S.E.(β^i)) may be calculated. The Wald statistic tests the null hypothesis that $\beta^i = 0$; if the significance (or p-value) associated with the regression is acceptably small (e.g., ≤ 0.25), it may be assumed with the associated confidence level (for p ≤ 0.25, this confidence level is 75%) that the null hypothesis may be rejected, and thus the estimate of β^i may be taken as the value of β^i.

The odds ratio estimates how much more likely it is for a certain outcome (e.g., "at risk") given an input above a cutoff value (e.g., influent alkalinity concentration above a specified cutoff). To evaluate the importance of the calculated odds ratios, significance values were computed using the two-sided Fisher Exact Test. This test, a form of the Chi-square evaluation, is appropriate for sparse datasets and evaluates whether the tested variables are independent or associated (Faraway 2006).

Geochemical Modeling of Precipitation in ZVI and FeS Systems

The geochemical modeling software packages MINEQL+ (Environmental Research Software 2001) and PHREEQC (Parkhurst and Appelo 1999) were used to model both FeS and ZVI systems. MINEQL+ models the equilibrium aquatic chemistry of systems, but requires that redox conditions be fixed. PHREEQC, on the other hand, allows for calculation of redox conditions based on other system parameters. Although PHREEQC has kinetic modeling capabilities, all simulations assumed equilibrium chemistry, since equilibrium predictions of, for example, precipitation will provide a conservative estimate of the parameter of interest (such as quantity of precipitates).

Results and Discussion

Statistical Analysis of ZVI Field PRBs

Identifying information for the 16 PRBs with sufficient available geochemical data reported in the literature is shown in Table 4.1. Geochemical data, both reported and calculated, are shown in Table 4.2 and Table 4.3.

Graphical and statistical (logistic regression and odds ratio maximization) analyses of geochemical and hydraulic data from 16 ZVI PRBs indicated that parameters often assumed to be closely tied to PRB longevity (saturation indices, dissolved oxygen and total dissolved solids) were not strongly correlated with "at risk" PRBs. In contrast, internal EH, influent pH and influent concentrations of alkalinity, NO_3^- and Cl^- were the geochemical parameters most strongly correlated to indicators of reduced PRB longevity. These results are shown graphically in Figure 4.1 and numerically in Table 4.4. In Figure 4.1, PRBs are graphed by geochemical parameter and grouped by "at risk" classification. Those variables identified as important are

able to divide geochemical spaces into regions into which "at risk" PRBs are likely to occur. In Table 4.4, low significance values indicate a strong likelihood of that parameter being important. A given parameter, such as nitrate, may have widely different significance in the two statistical tests; this difference is a result of the nature of the distribution of the data.

Table 4.1. ZVI PRBs analyzed for correlations between geochemical parameters and performance.

Name & Location	Contaminants	Performance Notes	Reference
Beka Site; Tubingen, Germany	TCE; cDCE; VC	Despite the precipitation of calcium, iron, and magnesium carbonates, no changes in hydraulics were observed.	(Klein and Schad 2000)
Canadian Forces Base, Borden; Borden, Ontario	TCE; PCE	Lower contaminant concentrations could have been achieved with higher Fe:sand ratio, or a more reactive Fe. Observed half-lives were ~6 times larger than those in bench tests, and rate constants decreased over time. Observations with time: 1 yr - no visual or microbial fouling; 2 yrs - no precipitates or cementation; 4 yrs - precipitates observed; 5 yrs - no decline in performance.	(Nicholson et al. 1983; O'Hannesin 1993; O'Hannesin and Gillham 1998; RTDF 2001)
Chlorinated Solvent Manufacturing; Syndey, Australia	PCE; CTC	Estimated 1.3% porosity loss/yr (based only on precipitation of FeS)	(Duran et al. 2000)
Copenhagen Freight Yard; Copenhagen, Denmark	TCE; cDCE; tDCE; VC	Failure due to poor hydraulic characterization (1/5 of plume migrates around PRB) & precipitates. H_2 production equiv to 5% of pore space/day. TDS reduced by 600 mg/L through wall; most precipitates are in the upgradient part of wall. Precipitates reduced hydraulic conductivity from 5.2 m/d to 0.7 m/d during 1st year; loss stabilized after 1 year.	(Kiilerich et al. 2000; Kjeldsen and Fulgsang 2000; RTDF 2001)
Denver Federal Center; Denver (Lakewood), CO	TCE; cDCE; 1,1-DCA; 1,1,1-TCA; 1,1-DCE	Hydraulic mounding and bypassing observed. Estimates of 0.35% - 0.5% porosity loss/yr due to calcite and siderite -- most at upgradient interface. Some cemented areas after 5 years; effects on hydraulic conductivity are expected. After 4 years, 10-50 μm layer of precip. at the upgradient interface (<20 cm into barrier). After 5 years, 50% of upgradient interface pore space is lost. H_2 production decreases with time in gate 2.	(McMahon et al. 1999; RTDF 2001; FRTR 2002; Wilkin and Puls 2003; Wilkin et al. 2003)
Dover Air Force Base, Area 5; Dover, DE	PCE; TCE; DCE	Little precipitation observed after 18 months; no conclusions about long-term performance drawn. pH increases were not controlled by the pyrite-Fe mix, and the pyrite-Fe mix was not as effective at removing DO as pure Fe.	(Gavaskar et al. 2000; Yoon et al. 2000; Liang et al. 2001; RTDF 2001; FRTR 2002)

Name & Location	Contaminants	Performance Notes	Reference
Haardkrom Site; Kolding, Denmark	Cr	Failure attributed to heterogeneous loading of PRB, which has created "exhaustion of iron-chromate removal capacity in the wall" (RTDF 2001)	(Kjeldsen and Fulgsang 2000; RTDF 2001; Kjeldsen 2006)
Industrial Facility; Upstate New York	TCE; cDCE; VC	Expect 10% porosity loss over 2 years. 6% (wt) $CaCO_3$ at upgradient interface; < 1% 15cm into barrier. Calcite & aragonite dominate at upgradient interface. No adverse effects of precip noted: VOC removal constant; hydraulic conductivity close to fresh iron; water velocity constant. Expect H_2-utilizing and sulfate reducing bacteria, but no microbial films observed. Suggest periodic scarification of upgradient face if necessary.	(Vogan et al. 1998; Vogan et al. 1999)
Intersil Semiconductor Site; Sunnyvale, CA	TCE; cDCE; VC	Pea gravel PTZ has resulted in precipitation of minerals and pretreatment of contaminants, and is therefore expected to increase life. Production of H_2(g) (to near saturation) taken as indication of continued PRB operation (i.e., Fe corrosion continues).	(Warner et al. 1998; RTDF 2001; Sorel et al. 2003)
Lowry Air Force Base; CO	TCE	Estimate 9.7% porosity loss over 18 months. Groundwater flow has probably not been affected by porosity changes. "During a clogging study performed in May 1997, 18 months after installation, calcite, aragonite, "green rusts", amorphous iron hydroxides, and magnetite were observed. A porosity loss of 9.7% for the 18-month operational period was estimated from the investigation." (RTDF 2001)	(Vogan et al. 1998; EPA 1999; Jain et al. 1999; RTDF 2001; FRTR 2002; ESTCP 2003)
Moffett Field; Mountain View, CA	TCE; cDCE; PCE	Aragonite, calcite, iron carbonate hydroxide found at upgradient interface. Some precipitates found in well silt traps.	(Sass et al. 1998; EPA 1999; RTDF 2001; Yabusaki et al. 2001; FRTR 2002; Gavaskar et al. 2005)
Monticello Mill Tailing Site; Monticello, Utah	U; Mn; Mo; NO_3^-; As; Se; V	Postulated that PTZ of gravel mix allows precipitation to occur upgradient of the reactive media. In contrast to column tests, effluent Fe concentrations are kept low by precipitation of $Fe(OH)_2$. 1 foot of upgradient mounding caused by 3 orders of magnitude hydraulic conductivity loss in pure ZVI; PTZ hydraulic conductivity remains unchanged.	(Ott 2000; US DOE - Subsurface Contaminants Focus Area 2000; Morrison et al. 2001; RTDF 2001; Morrison et al. 2002; Purdy et al. 2002)
Somersworth, NH Landfill Superfund	PCE; TCE; 1,2-DCE; VC	Initial decrease in hydraulic conductivity due to settling.	(Sivavec et al. 2003; O'Hara 2006)
USCG Support Center; Elizabeth City, NC	Cr; TCE	Estimate 1-2% porosity loss per year, but this should not affect the PRB permeability for 10 years. No hydraulic performance changes observed over 5 years.	(Puls et al. 1999; RTDF 2001; FRTR 2002; Wilkin et al. 2003 ; Wilkin et al. 2005)

Name & Location	Contaminants	Performance Notes	Reference
Vapokon Site, Denmark	PCE, TCE, cis-DCE, VC, other chlorinated organics	No "pronounced" deterioration of chlorinated organic removal. Expect hydraulics change in future - limiting lifespan to 10 years. Tracer study reveals zones of low permeability and clogging that change flow path. 0.88% porosity loss per year between March 2000 and August 2003	(Lai et al. 2005; Lai et al. 2006)
Y-12 Plant; pathway 2; Oak Ridge, TN	U, NO_3^-	Oxidation, precipitation, and cementation increased from 15 to 30 months (depends on depth). Akagenite transforms to goethite, and amorphous FeS into mackinawite. Fe oxy(hydr)oxides dominate precipitates; calcite not observed until 30 months. 30-80% of Fe filings are replaced by FeOOH corrosion rinds in cemented zones; Fe reactivity decreases. Based on corrosion, estimate lifespan of 5-10 years.	(Ott 2000; Phillips et al. 2000; Liang et al. 2001; FRTR 2002; Gu et al. 2002; Phillips et al. 2003)

Table 4.2. Reported geochemical data for ZVI PRBs.

Name	Run Time (yr)	Flow Rate (m/d)	pH influent	pH internal	Eh internal (mV)	TDS influent (mg/L)	DO influent (mg/L)	Ca^{2+} influent (mg/L)	Ca^{2+} internal (mg/L)	Alk influent (mg/L as CaCO3)	Alk internal (mg/L as CaCO3)	CO3T influent (mg/L as CO3)	Fe(T) internal (mg/L)	SO_4^{2-} influent (mg/L)	NO_3^- influent (mg/L)	Cl^- influent (mg/L)	PTZ	Δ hydr.	Δ perf.	failure	at risk
Beka Site, Germany	2	0.015	7.1	10.1	-310	800	1.0	150	20	338	711	464	0.25	88	7	75	1	0	0	0	0
Canadian Forces Base, Borden, Canada	10	0.082	8.1	8.7	-330	1065	3.4	278	102	140	82.0	170	7.5	609	0.6	2	0	0	0	0	0
Chlorinated Solvent Manufacturing, Australia	1	0.60	4.6	7.0	-217	1907	0.0	-	-	15.3	185	941	201	159	-	-	0	0	0	0	0
Copenhagen Freight Yard, Denmark	3	0.11	7.7	9.4	-	1222	0.2	130	3.6	503	299	625	0.2	110	0.2	180	1	1	0	0	1
Denver Federal Center, CO	7	0.07	7.5	9.7	-190	1100	0.61	107	2.7	440	350	560	0.04	260	2	64.5	1	1	0	0	1
Dover Air Force Base, Area 5, DE	4	2.5	5.1	10.8	-320	106	4.2	4.5	7.0	6	41.9	129	0.06	19.5	8	30	1	0	0	0	0
Haardkrom Site, Denmark	2	0.061	8.7	10.5	-	322	5.2	53.5	5	121	188	143	0.2	85.5	34.4	-	0	0	1	1	1
Industrial Facility, Upstate NY	4	0.45	7.4	9.5	-459	489	-	90.6	9.6	239	61.1	310	0.16	17.2	0.31	47.4	1	0	0	0	0
Intersil Semiconductor Site, CA	8	0.23	7.8	10.5	-350	686	2.0	-	-	235	7.4	291	0.05	400	-	-	1	0	0	0	0
Lowry Air Force Base, CO	8	0.30	6.9	10.0	-725	2900	0.66	290	-	530	-	795	-	1000	4	100	0	0	0	0	0
Moffett Field, CA	9	0.054	7.1	10.5	-372	820	0.1	158	10.9	288	20.2	400	0.02	350	2.4	40.9	1	0	0	0	0

Name	Run Time (yr)	Flow Rate (m/d)	pH influent	pH internal	Eh internal (mV)	TDS influent (mg/L)	DO influent (mg/L)	Ca^{2+} influent (mg/L)	Ca^{2+} internal (mg/L)	Alk influent (mg/L as CaCO3)	Alk internal (mg/L as CaCO3)	CO3T influent (mg/L as CO3)	Fe(T) internal (mg/L)	SO_4^{2-} influent (mg/L)	NO_3^- influent (mg/L)	Cl^- influent (mg/L)	PTZ	Δ hydr.	Δ perf.	failure	at risk
Monticello Mill Tailing Site, UT	3	5.7	6.5	9.0	-388	1300	0.44	339	211	237	22.0	460	0.17	1170	118	123	1	1	1	1	1
Somersworth Landfill, NH	4	0.09	6.5	10.0	-750	400	2.0	82.7	37.5	338	175	660	0.0	13.7	0.5	84.3	0	0	0	0	0
USCG Support Center, NC	8	4.5	6.1	9.8	-400	290	1.1	12.5	5.3	50	38.0	155	0.05	49	1.1	40	0	0	0	0	0
Vapokon Petrochem. Works, Denmark	7	0.27	7.2	9.8	-133	754	3.4	179	42.7	314	64.5	422	2.5	120	-	46.0	1	1	0	0	1
Y-12 Plant; pathway 2, TN	6	2.2	6.7	9.0	-166	887	2.8	190	93	360	868	604	14.9	92.5	85	50.5	1	1	1	0	1

"inf" and "int" indicate influent and values, respectively; "Run Time" is the time from a PRB's construction to the most recently published information regarding that PRB; "CO3T" indicates total carbonate (the sum of carbonate, bicarbonate, and carbonic acid); "PTZ" stands for Pre-Treatment Zone; "Δ hydr." and "Δ perf." indicate reported changes in hydraulics and performance, respectively; "at risk" indicates a PRB for which either a hydraulic change, a performance change, or failure has been reported.

Table 4.3. Calculated geochemical data for ZVI PRBs.

Name	Legend	Ca Flux ($g\ m^{-2}\ d^{-1}$)	Alk Flux ($g\ m^{-2}\ d^{-1}$)	CO3T Flux ($g\ m^{-2}\ d^{-1}$)	SO_4^{2-} Flux ($g\ m^{-2}\ d^{-1}$)	NO_3^- Flux ($g\ m^{-2}\ d^{-1}$)	Cl^- Flux ($g\ m^{-2}\ d^{-1}$)	Ca^{2+} Cumul. Flux ($kg\ m^{-2}$)	Alk Cumul. Flux ($kg\ m^{-2}$)	CO3T Cumul. Flux ($kg\ m^{-2}$)	SO_4^{2-} Cumul. Flux ($kg\ m^{-2}$)	NO_3^- Cumul. Flux ($kg\ m^{-2}$)	Cl^- Cumul. Flux ($kg\ m^{-2}$)	SI Calcite	SI Aragonite	SI Siderite	SI $Fe(OH)_2$	SI Magnetite	SI Hematite	SI Ferrihydrite	SI Goethite	at risk
Beka Site, Germany	Beka	2.2	5.0	6.8	1.3	0.10	1.1	1.6	3.6	5.0	0.94	0.075	0.80	2.8	2.6	1.1	0.23	2.5	2.0	0.66	1.7	0
Canadian Forces Base, Borden, Canada	Borden	22.8	11.5	13.9	49.9	0.049	0.16	83.2	42.0	50.9	182	0.18	0.60	1.5	1.3	1.9	0.27	2.1	1.4	0.11	1.2	0
Chlorinated Solvent Manufacturing, Australia	CSM	-	9.2	564	95.4	-	-	-	3.4	206	34.8	-	-	-	-	2.1	-0.72	1.4	0.80	-0.50	0.57	0
Copenhagen Freight Yard, Denmark	Copen	14.3	55.3	68.8	12.1	0.022	19.8	15.7	60.5	75.3	13.2	0.024	21.7	1.2	1.1	-	-	-	-	-	-	1
Denver Federal Center, CO	DFC	7.5	30.8	39.2	18.2	0.14	4.5	19.1	78.7	100	46.5	0.36	11.5	1.4	1.2	0.027	-0.42	2.5	2.1	0.78	1.8	1
Dover Air Force Base, Area 5, DE	Dover	11.0	14.7	317	47.8	19.6	73.5	16.1	21.5	463	69.8	28.6	107	1.3	1.1	-2.6	-0.42	2.2	1.7	0.40	1.5	0
Haardkrom Site, Denmark	Haard	3.3	7.4	8.7	5.2	2.1	-	2.4	5.4	6.4	3.8	1.5	-	1.7	1.6	-	-	-	-	-	-	1
Industrial Facility, NY	IF_NY	40.8	108	139	7.7	0.14	21.3	59.5	157	204	11.3	0.20	31.1	1.00	0.85	0.50	0.043	1.6	0.78	-0.52	0.55	0
Intersil Semiconductor Site, CA	Inter	-	52.8	65.4	90.0	-	-	-	154	191	263	-	-	-	-	-2.6	-0.26	2.1	1.5	0.24	1.3	0

Name	Legend	Ca Flux ($g\ m^{-2}\ d^{-1}$)	Alk Flux ($g\ m^{-2}\ d^{-1}$)	CO3T Flux ($g\ m^{-2}\ d^{-1}$)	SO_4^{2-} Flux ($g\ m^{-2}\ d^{-1}$)	NO_3^- Flux ($g\ m^{-2}\ d^{-1}$)	Cl^- Flux ($g\ m^{-2}\ d^{-1}$)	Ca^{2+} Cumul. Flux ($kg\ m^{-2}$)	Alk Cumul. Flux ($kg\ m^{-2}$)	CO3T Cumul. Flux ($kg\ m^{-2}$)	SO_4^{2-} Cumul. Flux ($kg\ m^{-2}$)	NO_3^- Cumul. Flux ($kg\ m^{-2}$)	Cl^- Cumul. Flux ($kg\ m^{-2}$)	SI Calcite	SI Aragonite	SI Siderite	SI $Fe(OH)_2$	SI Magnetite	SI Hematite	SI Ferrihydrite	SI Goethite	at risk
Lowry Air Force Base, CO	Lowry	87.0	159	239	300	1.2	30.0	254	464	697	876	3.5	87.6	-	-	-	-	-	-	-	-	0
Moffett Field, CA	Moffett	8.5	15.6	21.6	18.9	0.13	2.2	28.0	51.1	71.0	62.1	0.43	7.3	1.1	0.95	-2.5	-0.45	1.9	1.3	-0.006	1.1	0
Monticello Mill Tailing Site, UT	Mont	1932	1351	2620	6669	673	701	2116	1479	2869	7303	736	768	1.5	1.4	-0.065	-0.28	1.5	0.81	-0.49	0.58	1
Somersworth Landfill, NH	Somer	7.4	30.4	59.4	1.2	0.045	7.6	10.9	44.4	86.8	1.8	0.066	11.1	2.4	2.2	-	-	-	-	-	-	0
USCG Support Center, NC	USCG	55.6	223	690	218	4.7	178	162	650	2015	637	13.6	520	0.77	0.62	-0.37	-0.071	1.9	1.2	-0.15	0.92	0
Vapokon Petrochem. Works, Denmark	Vapok	48.9	85.7	115	32.8	-	12.5	125	219	294	83.9	-	32.0	1.9	1.8	-0.12	-0.050	3.0	2.7	1.4	2.4	1
Y-12 Plant; pathway 2, TN	Y-12	418	792	1328	204	187	111	915	1735	2909	446	410	243	2.7	2.6	3.1	0.53	3.4	3.0	1.7	2.8	1

"SI" stands for Saturation Index; "CO3T" indicates total carbonate (i.e., the sum of the carbonate species: carbonate, bicarbonate, and carbonic acid).

Table 4.4. Logistic regression and odds ratio maximization results.

	Logistic Regression				Odds Ratio		
Parameter	**β_1**	**Standard Error**	**Wald**	**Significance**	**Max. Odds Ratio**	**Cutoff Value**	**Fisher Exact Test Significance**
Run Time (yr)	-0.1470	0.200	0.54	0.461	1.33	2.5	1.000
Flow Rate (m/d)	0.1806	0.302	0.36	0.550	2	1	0.604
pH influent	0.8910	0.700	1.62	0.203	4.67	7.2	0.302
pH internal	-0.1315	0.564	0.05	0.816	3	8.9	0.500
Eh internal (mV)	0.0161	0.009	3.32	0.069	60	-200	0.011
TDS influent (mg/L)	0.0000	0.001	0.00	0.965	5	700	0.307
DO influent (mg/L)	0.2015	0.334	0.36	0.547	3.6	5	0.400
Ca influent (mg/L)	0.0035	0.006	0.39	0.534	5	100	0.301
Ca internal (mg/L)	0.0106	0.012	0.84	0.359	6	40	0.266
Alk influent (mg/L as CaCO3)	0.0050	0.004	1.70	0.192	9	350	0.118
Alk internal (mg/L as CaCO3)	0.0025	0.002	1.15	0.284	8	200	0.235
CO3T influent (mg/L as CO3)	0.0007	0.002	0.09	0.759	7.5	410	0.145
Fe(T) internal (mg/L)	-0.0180	0.035	0.26	0.610	1.75	1.3	1.000
SO4 influent (mg/L)	0.0003	0.001	0.04	0.840	8	75	0.234
NO3 influent (mg/L)	0.1005	0.089	1.28	0.258	24	20	0.035
Cl influent (mg/L)	0.0246	0.018	1.93	0.165	10.67	110	0.128
Alk Flux (g/m2d)	0.0040	0.003	1.37	0.242	5	25	0.307
SI Calcite	0.5300	0.911	0.34	0.561	9	1.15	0.192
SI Siderite	0.3483	0.377	0.85	0.356	8	-0.2	0.208
SI Fe(OH)2	0.9669	1.806	0.29	0.592	5.33	0.35	0.333
PTZ	1.6094	1.265	1.62	0.203	5	1	0.307
media mix	-20.9	28421	0.00	0.999	3	1	0.500

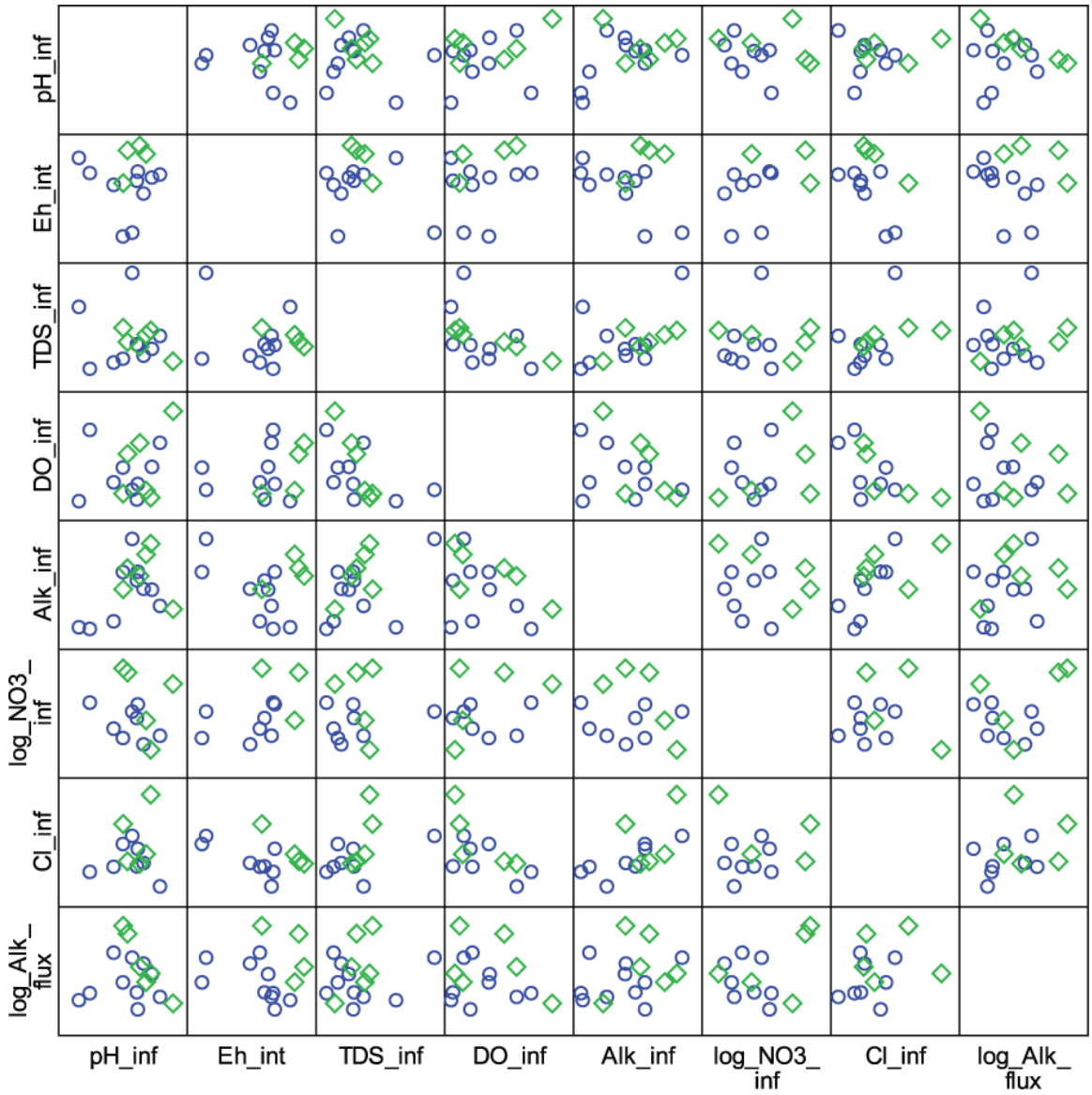

Figure 4.1. Matrix plot of selected variables for analysis of PRB geochemistry. "At risk" PRBs are indicated by green diamonds; "not at risk" by blue circles. (See Table 4.4 for units of measure).

Geochemical Modeling of Precipitation in ZVI and FeS Systems

FeS in Buffered Systems. It has been observed that the interaction of FeS with a non-buffered aqueous system causes a pH increase. Equilibria between unlimited amounts of FeS and varying amounts of calcium and carbonate (with various initial values of pH) were simulated using MINEQL+. The results, shown in Figure 4.2, indicate that the precipitation of $CaCO_3(s)$ is likely only for systems with initial pH > 7, and concentrations of calcium and total carbonate in excess of about 200 mg/L. Therefore, it appears that the buffering capacity of carbonate can mitigate the pH rise in FeS systems, preventing the precipitation of calcium carbonate which could cause a decrease in hydraulic conductivity.

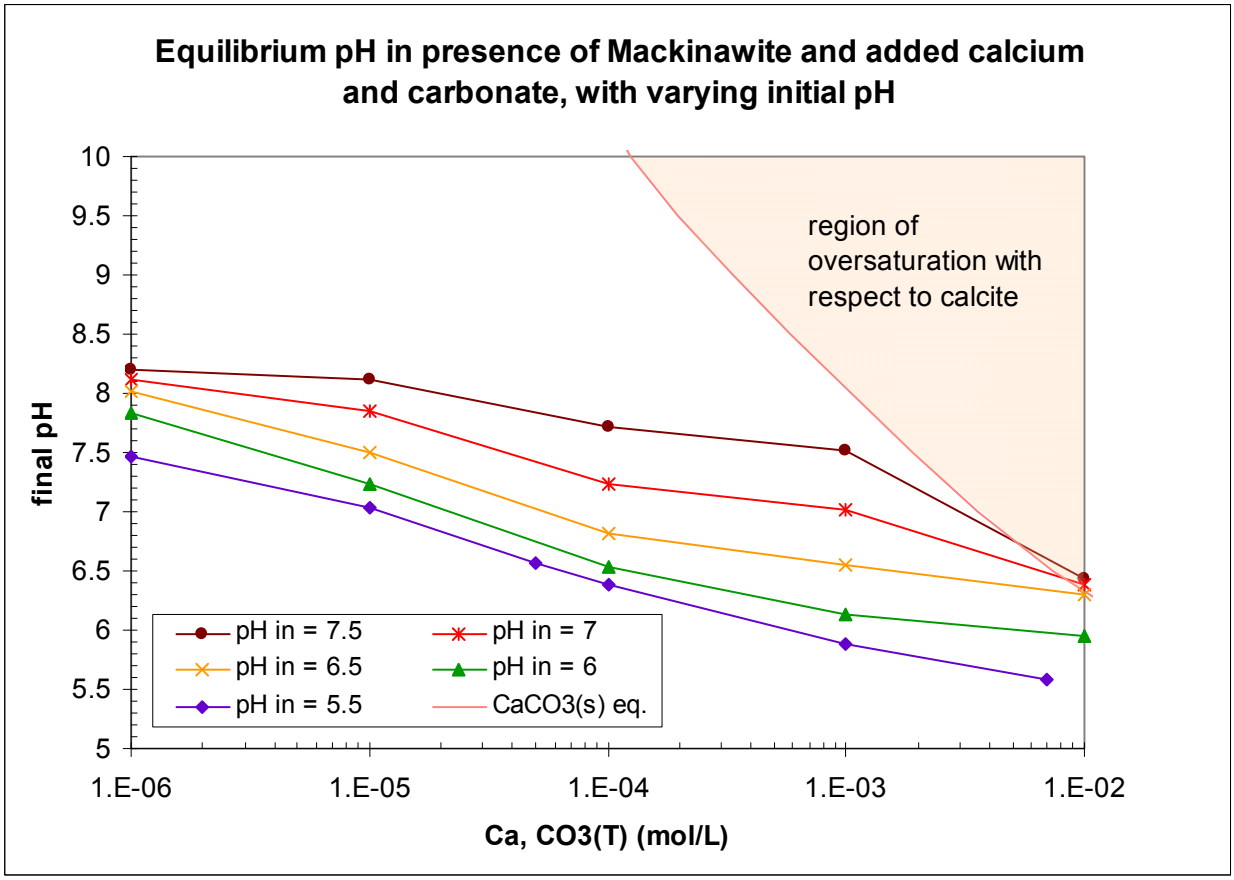

Figure 4.2. MINEQL+ simulations of the final pH in the FeS system as a function initial pH, carbonate and calcium concentrations. Increasing carbonate provides buffering (increasing values on the x axis) and prevents pH increase (values of final pH are close to initial pH), and thus precipitation is expected only with initial pH >7 and carbonate > 1 x 10^{-3} mole/L.

In the field sites included in the literature review of 16 ZVI PRBs that experienced operational problems (Henderson and Demond 2007), the average influent pH was about 6.8, and the average influent carbonate was about 450 mg/L. Therefore, it may be anticipated that in many systems, the buffer capacity of the carbonate system may be able to absorb the pH rise produced by FeS, thus preventing the precipitation of carbonate minerals that may reduce hydraulic conductivity.

ZVI and FeS with Dynamic Redox Conditions and Varying Reactive Media and Buffering. PHREEQC was used to simulate the equilibrium interaction of reactive media (ZVI or FeS) with water containing varying amounts of calcium and carbonate. Solids formation, pe, and pH were tracked in these simulations. Two classes of simulations were conducted. In the first, the amount of reactive media was varied in pure water. In the second class, the amount of reactive media was fixed, and the concentrations of calcium and carbonate were varied. The latter simulations were conducted with and without 100 mg/L (1.6 * 10^{-3} mole/L) nitrate in the system.

Varying Amounts of ZVI or FeS. For the first class of simulations, varying amounts (10^{-7} to 10^{-1} mole/L) of reactive media, either FeS or ZVI, were allowed to equilibrate with pure water. These simulations indicated that ZVI is thermodynamically unstable in water, and therefore – at equilibrium – will completely dissolve. This is in keeping with the iron-carbonate-sulfur pe-pH stability diagram, shown in Figure 4.3. In this diagram, ZVI sits entirely below the water stability line, while FeS exists on both sides of that line.

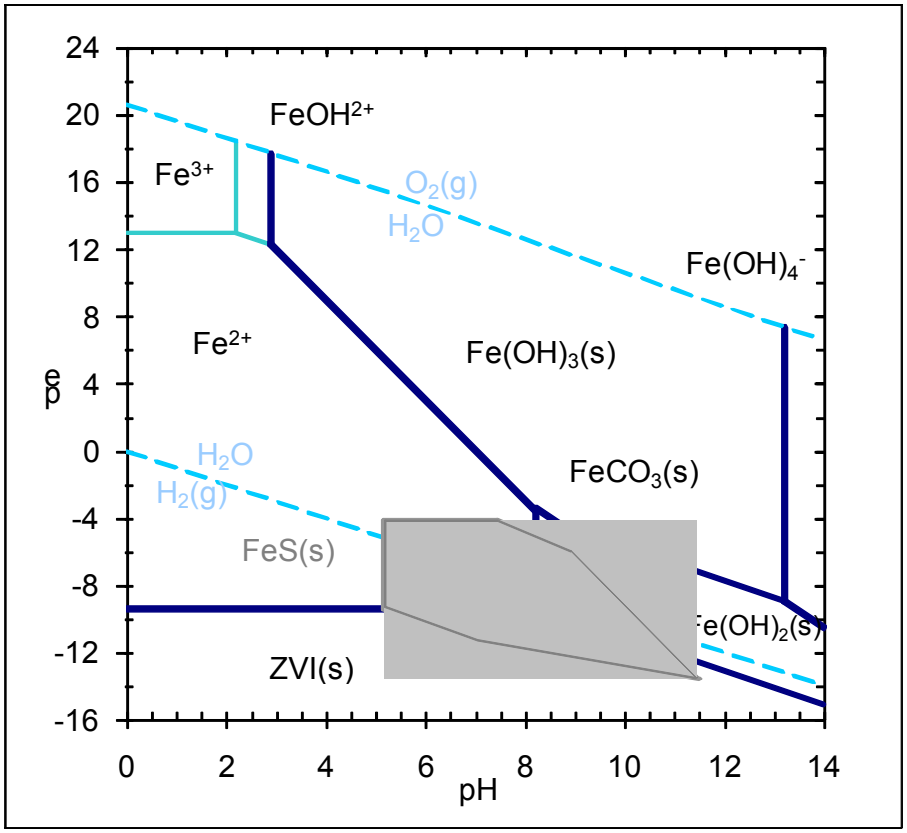

Figure 4.3. Stability diagram for ZVI and FeS system, assuming FeT = 10^{-5} M, ST = 10^{-3} M, and CO3T = 10^{-2} M.

As ZVI is oxidized to Fe(II), water is reduced to $H_2(g)$, resulting in a monotonic increase in pH and decrease in pe as the amount of ZVI is increased (Figure 4.4). The formation of solids, especially a hydroxy green rust, $Fe_2(OH)_5(s)$, sequestered much of the hydroxide produced and thus prevented the pH from increasing to values up to 11. (Solids production is discussed in more detail below, for simulations with carbonate present.) FeS, in contrast to ZVI, does not have the strong driving force for corrosion that ZVI does. Therefore, for equal amounts of reactive media, the pH increase with FeS is less than that with ZVI.

Varying Amounts of Calcium and Carbonate. In the second class of simulations, a fixed amount (5 mmol/L) of reactive media, again either ZVI or FeS, was allowed to equilibrate with solutions containing varying amounts (10^{-6} to 10^{-2} mole/L) of calcium and total carbonate (Figure 4.5). 5 mmol/L was chosen based on the work of Liang (2001), who noted that 0.5 mmol of aqueous Fe(II) has been measured at ZVI PRBs. This value was increased by a factor of 10 to

make a conservative estimate of geochemical changes. The results confirmed that the presence of carbonate, which acts as a buffer, mitigated the pH increase observed in the pure water systems (Figure 4.5). Again, the changes induced by FeS were either less severe or equal to the changes induced by ZVI.

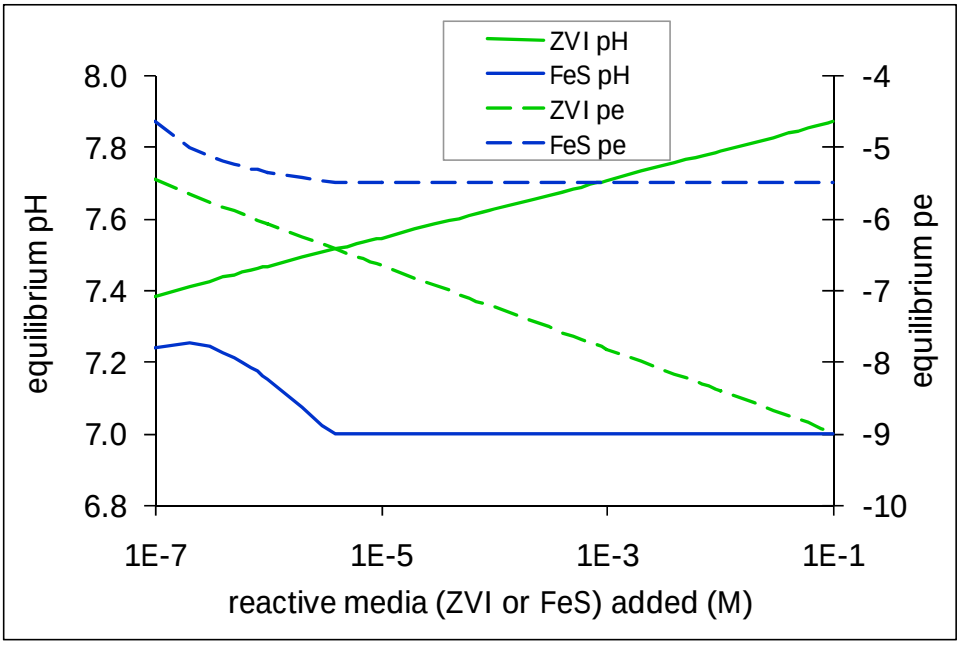

Figure 4.4. PHREEQC equilibrium simulation of addition of reactive media to pure water indicates the pH increase and pe decrease due to ZVI is greater than that due to FeS.

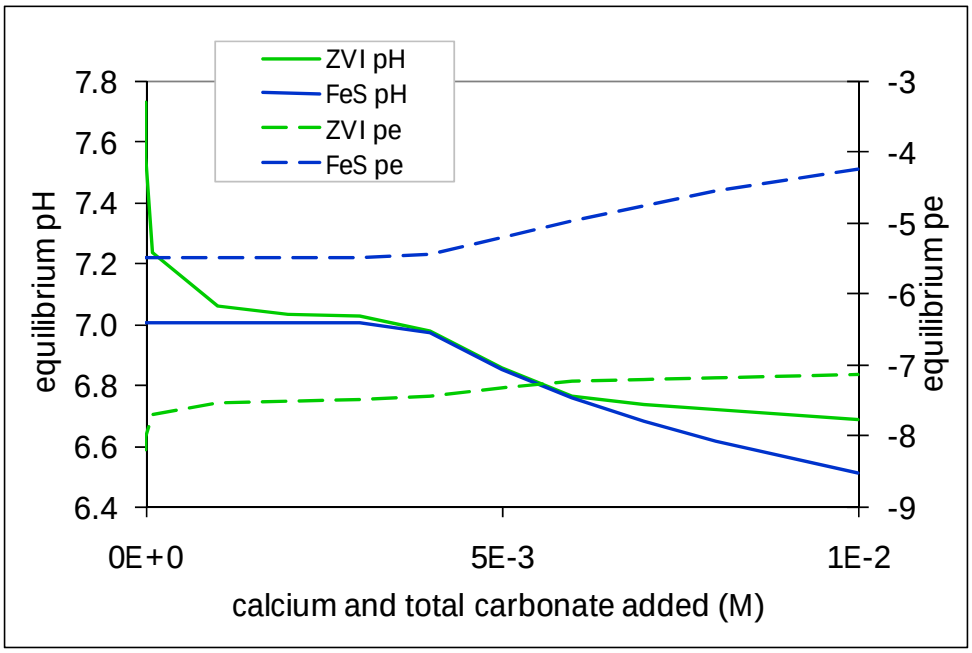

Figure 4.5. PHREEQC simulations indicate that carbonate mitigates the pH and pe changes caused by the presence of ZVI or FeS reactive media.

Furthermore, it was observed that total solids production (including both iron (oxy)hydroxides and carbonate-bearing minerals) was greater in the ZVI system than in the FeS system, as shown in Figure 4.6. Note that in the ZVI system, ZVI itself is not present, as it is thermodynamically unstable. However, the FeS added in the FeS simulations remains present as FeS. The number of moles of solids formed is shown in Figure 4.6, while the mass and volume of new solids produced in these two systems is shown in Figure 4.7. Figure 4.7 shows that the ZVI system gains mass because all of the iron in ZVI completely dissolves, and reprecipitates as less dense solids (the density of ZVI is 7 g/cm^3) which have incorporated ligands such as OH^- as in $Fe_2(OH)_5$. In the case of FeS, the initially added FeS remains present as FeS, and new mass is added to the system only when $CaCO_3$(s) precipitates.

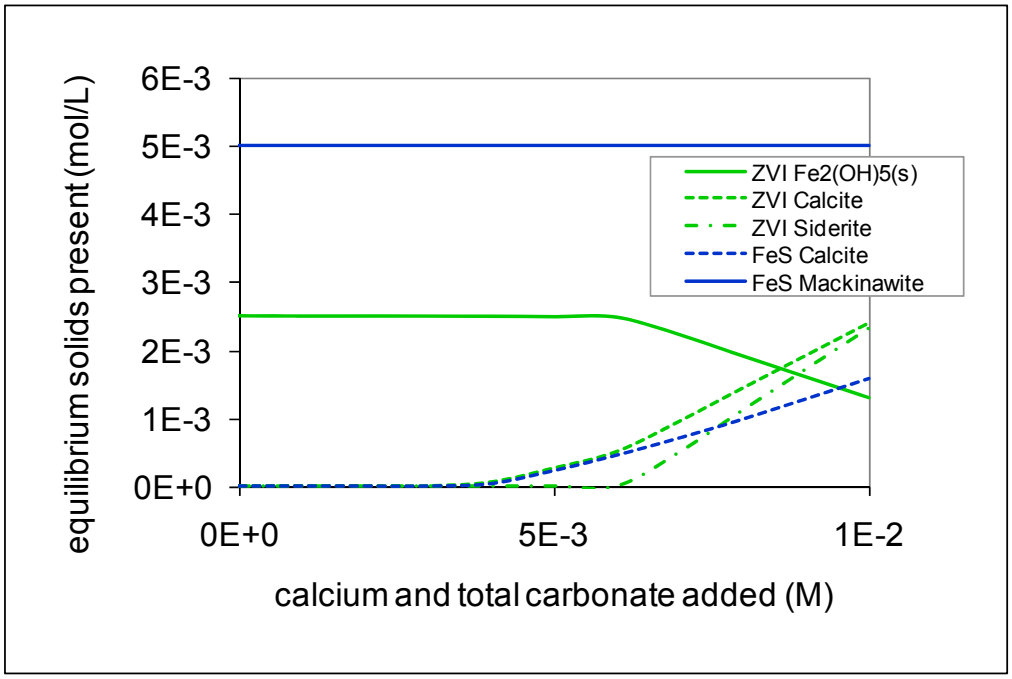

Figure 4.6. PHREEQC simulations showing the solids production due to the presence of 5 mmol/L of reactive media and calcium and carbonate in varying concentrations.

Additional simulations, identical to those described above with calcium and carbonate, and 0.005 mole/L of reactive media – but with the addition of nitrate – indicated that the presence of nitrate may increase the equilibrium pH in PRB systems. As the redox-active nitrate oxidizes ZVI (or FeS), pe changes in the system favor the conversion of aqueous ferrous iron (which forms strong complexes with hydroxide) to ferric iron, which exists largely in the solid phase. These changes affect the system pH, as shown in Figure 4.8: with no buffering, for example, ZVI reaches an equilibrium pH of 11 (as opposed to 7.8 with no nitrate [Figure 4.5]), and FeS reaches pH of about 9 (as opposed to 7 [Figure 4.5]). Therefore, it appears that nitrate may increase the equilibrium pH in ZVI and FeS systems.

As with the nitrate-free system, the pH increase observed with ZVI is greater than the increase with FeS. The majority of ZVI is transformed to $Fe_2(OH)_5$. However, the increased pH

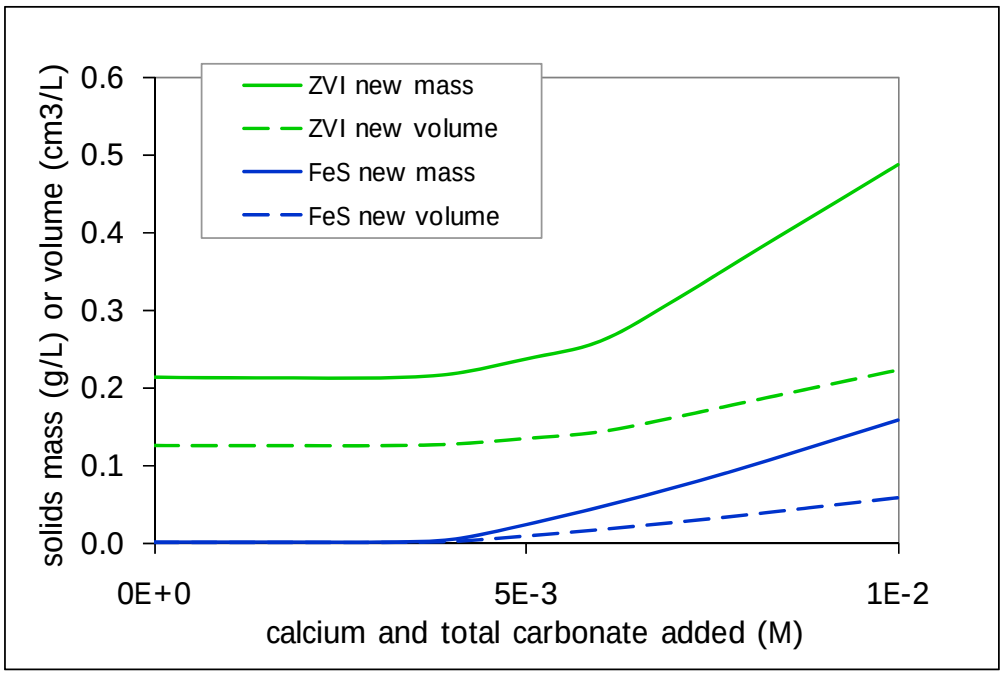

Figure 4.7. PHREEQC simulations showing mass and volume production of solids for the ZVI and FeS systems; ZVI consistently results in more solids mass and volume than FeS.

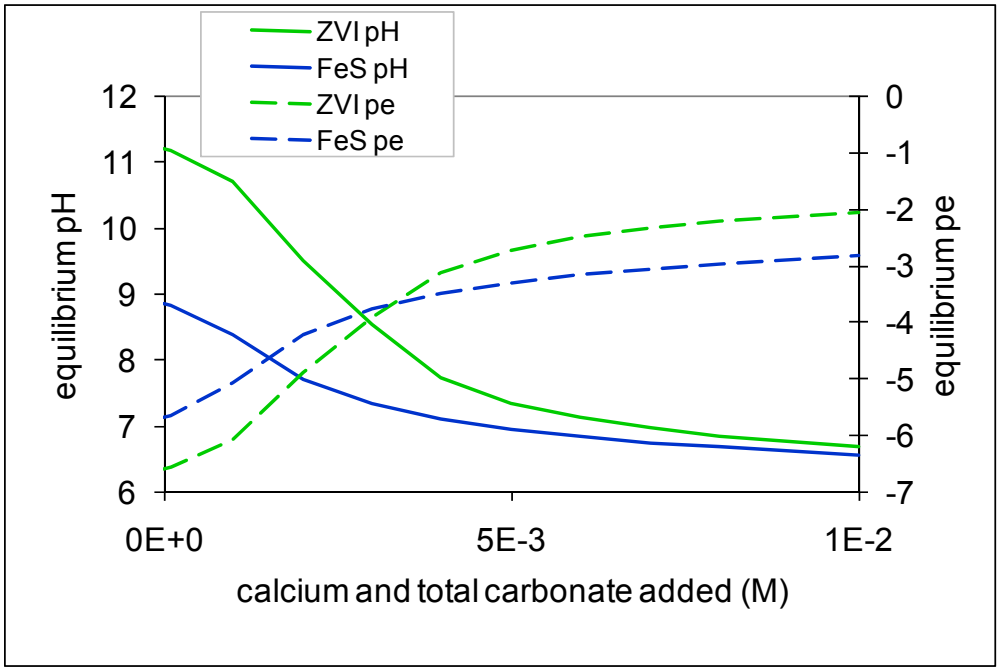

Figure 4.8. PHREEQC simulations with 5 mmol/L reactive media and 1.6mmol/L nitrate show that nitrate increases the equilibrium pH, and that the ZVI pH is consistently higher than the FeS system pH.

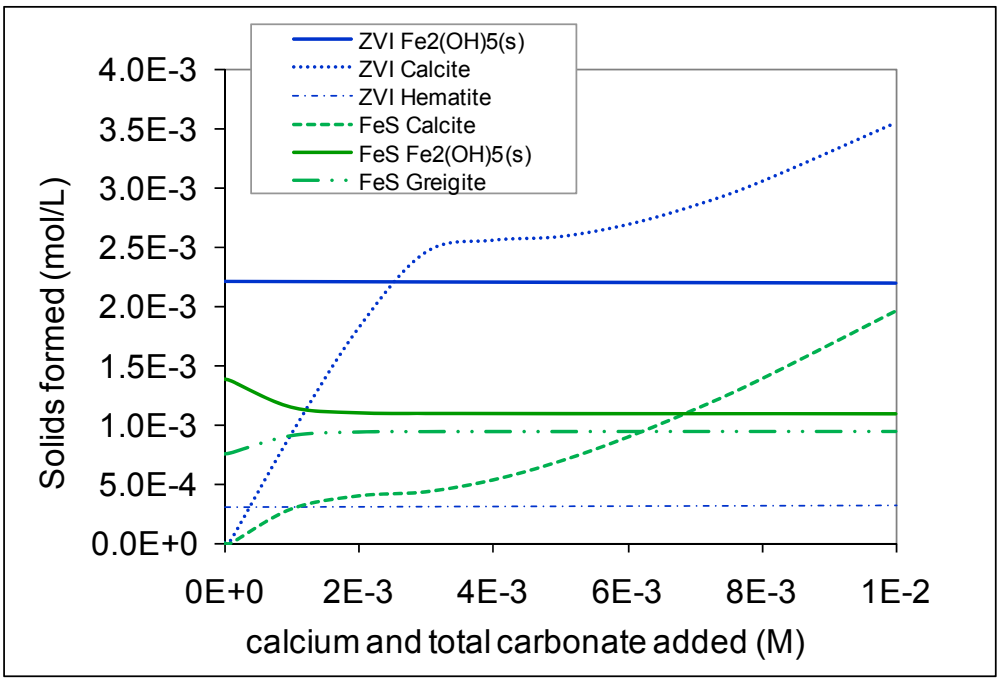

Figure 4.9. PHREEQC simulation show speciation of solids formed for the ZVI and FeS systems (5 mmol/L of reactive media) with 1.6mmol/L nitrate; ZVI consistently results in more solids mass and volume than FeS.

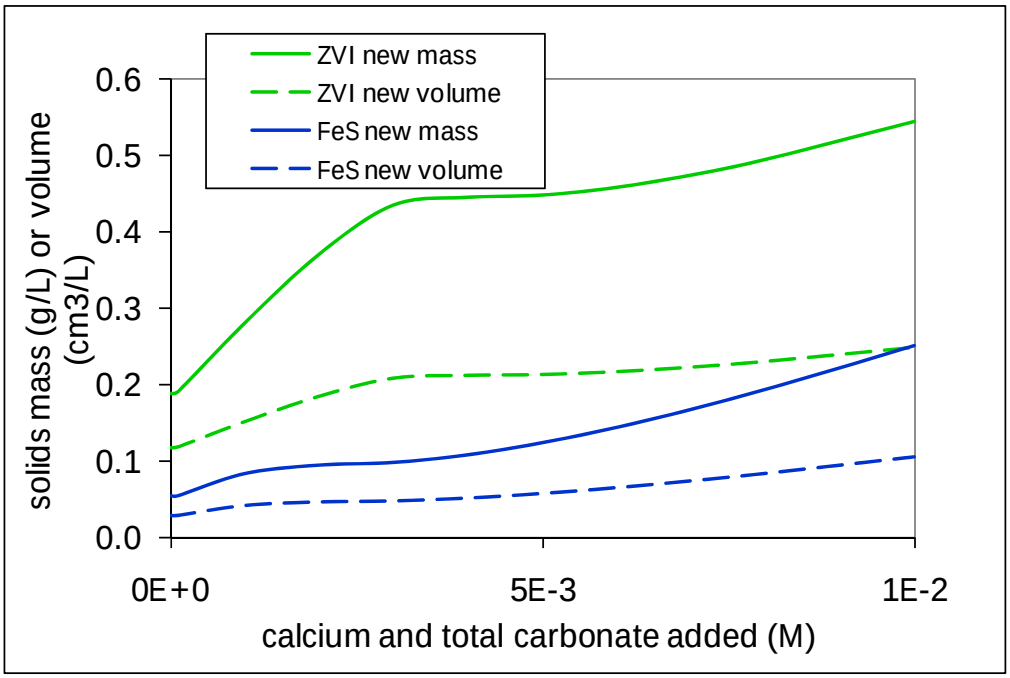

Figure 4.10. PHREEQC simulations showing mass and volume production of solids for the ZVI and FeS systems (5 mmol/L of reactive media) with 1.6mmol/L nitrate; ZVI consistently results in more solids mass and volume than FeS.

drives the precipitation of more $CaCO_3$(s). The latter is true for the FeS system, as seen in Figure 4.9. Overall, because solids accumulation is linked to pH increase, FeS systems may experience less solids accumulation than ZVI systems, as shown in Figure 4.10.

Summary and Conclusions and Implications for Future Research/Implementation

Literature Review and Statistical Analysis

In this subtask, a review of data from 16 ZVI PRBs was conducted in order to improve understanding about conditions that may be problematic for PRB longevity. These data were analyzed graphically and statistically to determine which geochemical factors are most associated with the potential for PRB failure. It was found that high influent pH or high internal E_H, as well as high nitrate, chloride, or alkalinity were correlated with a likelihood of failure. These results were used to select conditions in which to operate laboratory columns for Subtask 4.3.

The sparseness of available field data precluded the use of multivariate analysis, so it is crucial that future work expand the dataset. As many PRBs begin their second decade of operation, they may be nearing the end of their estimated life spans. Thus, it becomes critical that field PRBs are monitored more closely to determine the factors that control the time to failure. If it becomes apparent that precipitation is a key reaction controlling PRB longevity, then FeS-based PRBs will have a significant advantage over ZVI systems.

Geochemical Modeling

A variety of MINEQL+ and PHREEQC geochemical simulations have been carried out. Both ZVI and FeS have been modeled, the amount of reactive media has been varied, the amount of calcium and carbonate in the aqueous system has been changed, and nitrate has been included as an oxidant. These models have indicated potential benefits of FeS barriers as compared to ZVI barriers. MINEQL+ results show that the buffering capacity of carbonate is likely to negate potential pH changes due to FeS dissolution, thus making precipitation of $CaCO_3$(s) likely only when the influent solution contains high carbonate (>200 mg/L) and has a pH above 7. PHREEQC results indicate that the pH increase is greater, on a molar basis, for ZVI than for FeS. Furthermore, ZVI is thermodynamically favored to transform into new solids with higher mass and volume than the initial system. This indicates that FeS media may not be subject to the same clogging problems (due to high-pH precipitation of $CaCO_3$(s) and iron (oxy)hydroxides) that have affected ZVI systems in the field.

Literature Cited

Duran, J. M., Vogan, J. L., and Stening, J. R. 2000. Reactive barrier performance in a complex contaminant and geochemical environment. In *Chemical oxidation and reactive barriers: Remediation of chlorinated and recalcitrant compounds* (eds. G. B. Wickramanayake, A. R. Gavaskar and A. S. C. Chen). Battelle Press, Columbus, Ohio: pp. 401-408.

Dwyer, B. P. 2000. *Design, construction and monitoring of a permeable reactive barrier technology for use at Rocky Flats Environmental Technology Site (RFETS)*. (Report No. SAND-2000-2702). Albuquerque, NM: Sandia National Laboratories.

Environmental Research Software. 2001. MINEQL+ version 4.5. Hallowell, ME.

EPA. 1999. *Field applications of in situ remediation technologies: Permeable reactive barriers*. (Report No. 542-R-99-002). Washington, D.C.: United States Environmental Protection Agency, Office of Solid Waste and Emergency Response.

ESTCP. 2003. *Evaluating the longevity and hydraulic performance of permeable reactive barriers at department of defense sites*. (Report No. CU-9907). Washington, DC: U.S. Department of Defense, Environmental Security Technology Certification Program.

Faraway, J. J. 2006. *Extending the linear model with R: Generalized linear, mixed effects and nonparametric regression models.* Boca Raton: Chapman & Hall/CRC.

FRTR. 2002. *Evaluation of permeable reactive barrier performance: Revised report*. Cincinnati, OH: Federal Remediation Technologies Roundtable; Tri-Agency Permeable Reactive Barrier Initiative.

Furukawa, Y., Kim, J. W., Watkins, J., and Wilkin, R. T. 2002. Formation of ferrihydrite and associated iron corrosion products in permeable reactive barriers of zero-valent iron. *Environ. Sci. Technol.* **36**, 5469-5475.

Gavaskar, A., Yoon, W. S., Sminchack, J., Sass, B., Gupta, N., Hicks, J., et al. 2005. *Long term performance assessment of a permeable reactive barrier at Former Naval Air Station Moffett Field*. (Report No. CR 05-006-ENV). Port Hueneme, CA: Naval Facilities Engineering Command.

Gu, B., Watson, D. B., Phillips, D. H., and Liang, L. Y. 2002. Biogeochemical, mineralogical, hydrological characteristics of an iron reactive barrier used for treatment of uranium and nitrate. In *Handbook of groundwater remediation using permeable reactive barriers: Applications to radionuclides, trace metals, and nutrients* (eds. D. L. Naftz, S. J. Morrison, J. A. Davis and C. C. Fuller). Academic Press, San Diego, CA: pp. 305-342.

Henderson, A. D. and Demond, A. H. 2007. Long-term performance of zero-valent iron permeable reactive barriers: A critical review. *Environ. Eng. Sci.* **24**, 401-423.

Hosmer, D. W. and Lemeshow, S. 1989. *Applied logistic regression.* New York: Wiley.

ITRC. 2005. *Permeable reactive barriers: Lessons Learned/New directions*. (Report No. PRB-4). Washington, D.C.: Interstate Technology & Regulatory Council, Permeable Reactive Barriers Team.

Jain, A., Raven, K. P., and Loeppert, R. H. 1999. Arsenite and arsenate adsorption on ferrihydrite: Surface charge reduction and net OH- release stoichiometry. *Environ. Sci. Technol.* **33**, 1179-1184.

Jambor, J. L., Raudsepp, M., and Mountjoy, K. 2005. Mineralogy of permeable reactive barriers for the attenuation of subsurface contaminants. *Can. Mineral.* **43**, 2117-2140.

Kiilerich, O., Larsen, J. W., Nielsen, C., and Deigaard, L. D. 2000. Field results from the use of a permeable reactive wall. Paper presented at the *Chemical Oxidation and Reactive Barriers: Remediation of Chlorinated and Recalcitrant Compounds: The Second International Conference on Remediation of Chlorinated and Recalcitrant Compounds,* Monterey, CA. pp. 377-384.

Kjeldsen, P., & Fulgsang, I. A. 2000. Demonstration program on reactive barrier technologies using zero-valent iron. Paper presented at *ConSoil 2000,* Leipzig, Germany. pp. 943-950.

Klein, R., & Schad, H. 2000. Results from a full-scale funnel-and-gate system at the BEKA site in Tubingen (Germany) using zero-valent iron. Paper presented at *ConSoil 2000,* Leipzig, Germany. pp. 917-923.

Lai, K. C. K., Lo, I. M. C., and Kjeldsen, P. 2005. Remediation of chlorinated aliphatic hydrocarbons in groundwater using Fe^0 PRB. *IAHS-AISH Publication.* **298**, 12-22.

Lai, K. C. K., Lo, I. M. C., Birkelund, V., and Kjeldsen, P. 2006. Field monitoring of a permeable reactive barrier for removal of chlorinated organics. *J. Environ. Eng.* **132**, 199-210.

Lennie, A. R., Redfern, S. A. T., Champness, P. E., Stoddart, C. P., Schofield, P. F., and Vaughan, D. J. 1997. Transformation of mackinawite to greigite; an in situ X-ray powder diffraction and transmission electron microscope study. *Am. Mineral.* **82**, 302-309.

Liang, L. Y., Korte, N. E., Moline, G. R., and West, O. R. 2001. *Long-term monitoring of permeable reactive barriers: Progress report*. (Report No. ORNL/TM-2001/1). Oak Ridge National Laboratory.

Liang, L. Y., Sullivan, A. B., West, O. R., Moline, G. R., and Kamolpornwijit, W. 2003. Predicting the precipitation of mineral phases in permeable reactive barriers. *Environ. Eng. Sci.* **20**, 635-653.

Matheson, L. J., W. C. Goldberg, W. D. Bostick, and L. Harris. 2002. Analysis of uranium-contaminated zero valent iron media sampled from permeable reactive barriers installed at U.S. Department of Energy sites in Oak Ridge, Tennessee, and Durango, Colorado. In *Handbook of groundwater remediation using permeable reactive barriers: Applications to radionuclides, trace metals, and nutrients* (eds. D. L. Naftz, S. J. Morrison, J. A. Davis and C. C. Fuller). Academic Press, San Diego, CA: pp. 343-367.

McMahon, P. B., Dennehy, K. F., and Sandstrom, M. W. 1999. Hydraulic and geochemical performance of a permeable reactive barrier containing zero-valent iron, Denver Federal Center. *Ground Water.* **37**, 396-404.

Morrison, S. J., Carpenter, C. E., Metzler, D. R., Bartlett, T. R., and Morris, S. A. 2002. Design and performance of a permeable reactive barrier for containment of uranium, arsenic, selenium, vanadium, molybdenum, and nitrate at Monticello, Utah. In *Handbook of groundwater remediation using permeable reactive barriers: Applications to radionuclides, trace metals, and nutrients* (eds. D. L. Naftz, S. J. Morrison, J. A. Davis and C. C. Fuller). Academic Press, San Diego, CA: pp. 371-399.

Morrison, S. J., Metzler, D. R., and Carpenter, C. E. 2001. Uranium precipitation in a permeable reactive barrier by progressive irreversible dissolution of zerovalent iron. *Environ. Sci. Technol.* **35**, 385-390.

Mushovic, P., Bartlett, T., and Morrison, S. 2006. Hydraulic conductivity loss at the Monticello PRB leads to trial use of ex-situ treatment cell. *Tech. News & Trends.* **23**, 1-3.

Nicholson, R. V., Cherry, J. A., and Reardon, E. J. 1983. Migration of contaminants in ground water at a landfill: A case study. 6. hydrogeochemistry. *J. Hydrol. (Amst.).* **63**, 131-176.

O'Hannesin, S. F. 1993. Field demonstration of a permeable reaction wall for the in situ abiotic degradation of halogenated aliphatic organic compounds. (Ph.D. Dissertation, University of Waterloo).

O'Hannesin, S. F. and Gillham, R. W. 1998. Long-term performance of an in situ "iron wall" for remediation of VOCs. *Ground Water.* **36**, 164-170.

Suzanne O'Hara. 2006. Pers. Comm.

Oliviera, I. B., Demond, A. H., and Salehzadeh, A. 1996. Packing of sands for the production of homogeneous porous media. *Soil Sci. Soc. Am. J.* **60**, 49-53.

Ott, N. 2000. *Permeable reactive barriers for inorganics*. Washington, D.C.: United States Environmental Protection Agency.

Parkhurst, D. L., & Appelo, C. A. J. 1999. *User's guide to PHREEQC (version 2): A computer program for speciation, batch reaction, one-dimensional transport, and inverse geochemical calculations*. (Report No. WRI-99-4259). Lakewood, CO: U.S. Geological Survey, Water Resources Investigation.

Phillips, D. H., Gu, B., Watson, D. B., Roh, Y., Liang, L. Y., and Lee, S. Y. 2000. Performance evaluation of a zerovalent iron reactive barrier: Mineralogical characteristics. *Environ. Sci. Technol.* **34**, 4169-4176.

Phillips, D. H., Watson, D. B., Roh, Y., and Gu, B. 2003. Mineralogical characteristics and transformations during long-term operation of a zerovalent iron reactive barrier. *J. Environ. Qual.* **32**, 2033-2045.

Puls, R. W., Blowes, D. W., and Gillham, R. W. 1999. Long-term performance monitoring for a permeable reactive barrier at the US Coast Guard Support Center, Elizabeth City, North Carolina. *J. Hazard. Mater.* **68**, 109-124.

Purdy, C., Gerdes, K., Aljayoushi, J., Kaback, D., and Ivory, T. 2002. Examples of department of energy successes for remediation of contaminated groundwater: Permeable reactive barrier and dynamic underground stripping ASTD projects. Paper presented at the *28th Annual Waste Management Conference,* Tucson, AZ.

RTDF. 2001. *Permeable reactive barrier installation profiles.* Retrieved March 1, 2005, from http://www.rtdf.org/public/permbarr/prbsumms/default.cfm.

Sarr, D. 2001. Zero-valent-iron permeable reactive barriers - how long will they last? *Remed. J.* **11**, 1-18.

Sass, B. M., Gavaskar, A. R., Gupta, N., Yoon, S. W., Hicks, J. E., O'Dwyer, D., et al. 1998. Evaluating the Moffett Field permeable barrier using groundwater monitoring and geochemical modeling. Paper presented at the *Designing and Applying Treatment Technologies: Remediation of Chlorinated and Recalcitrant Compounds: The First International Conference on Remediation of Chlorinated and Recalcitrant Compounds,* Monterey, CA. pp. 169-175.

Sivavec, T., Krug, T., Berry-Spark, K., and Focht, R. 2003. Performance monitoring of a permeable reactive barrier at the Somersworth, New Hampshire landfill superfund site. *Chlor. Solv. and DNAPL Remed.* **837**, 259-277.

Sorel, D., Warner, S. D., Longino, B. L., Honniball, J. H., and Hamilton, L. A. 2003. Performance monitoring and dissolved hydrogen measurements at a permeable zero valent iron reactive barrier. In *Chlorinated solvent and DNAPL remediation: Innovative strategies for subsurface cleanup* (eds. S. M. Henryand S. D. Warner). American Chemical Society / Oxford University Press, Washington, DC: pp. 278-285.

Su, C. and Puls, R. W. 2001. Arsenate and arsenite removal by zerovalent iron: Kinetics, redox transformation, and implications for in situ groundwater remediation. *Environ. Sci. Technol.* **35**, 1487-1492.

US DOE - Subsurface Contaminants Focus Area. 2000. *Permeable reactive treatment (PeRT) wall for rads and metals*. (Report No. OST/TMS ID 2155; DOE/EM-0557). United States Department of Energy.

Vogan, J. L., Butler, B. J., Odziemkowski, M. S., Friday, G., and Gillham, R. W. 1998. Inorganic and biological evaluation of cores from permeable iron reactive barriers. Paper presented at the *Designing and Applying Treatment Technologies: Remediation of Chlorinated and Recalcitrant Compounds: The First International Conference on Remediation of Chlorinated and Recalcitrant Compounds,* Monterey, CA. pp. 163-168.

Vogan, J. L., Focht, R. M., Clark, D. K., and Graham, S. L. 1999. Performance evaluation of a permeable reactive barrier for remediation of dissolved chlorinated solvents in groundwater. *J. Hazard. Mater.* **68**, 97-108.

Warner, S. D.and Sorel, D. 2003. Ten years of permeable reactive barriers: Lessons learned and future expectations. In *Chlorinated solvent and DNAPL remediation: Innovative strategies for subsurface cleanup* (eds. S. M. Henryand S. D. Warner). American Chemical Society, Washington, DC: pp. 36-50.

Warner, S. D., Yamane, C. L., Bice, N. T., Szerdy, F. S., Vogan, J. L., Major, D. W., et al. 1998. Technical update: The first commercial subsurface permeable reactive treatment zone composed of granular zero-valent iron. Paper presented at the *Designing and Applying Treatment Technologies: Remediation of Chlorinated and Recalcitrant Compounds: The First International Conference on Remediation of Chlorinated and Recalcitrant Compounds,* Monterey, CA. pp. 145-150.

Wilkin, R. T., Jacobsen, L., and Coombe, E. 2005. Zero-valent iron PRB application expands to arsenic removal. *Tech. News & Trends.* **21**, 1-2.

Wilkin, R. T., & Puls, R. W. 2003. *Capstone report on the application, monitoring, and performance of permeable reactive barriers from ground-water remediation; volume 1, performance evaluations at two sites*. (Report No. EPA/600/R-03/045A). Washington, DC: United States Environmental Protection Agency.

Wilkin, R. T., Puls, R. W., and Sewell, G. W. 2003. Long-term performance of permeable reactive barriers using zero-valent iron: Geochemical and microbiological effects. *Ground Water.* **41**, 493-503.

Yabusaki, S., Cantrell, K. J., Sass, B. M., and Steefel, C. 2001. Multicomponent reactive transport in an in situ zero-valent iron cell. *Environ. Sci. Technol.* **35**, 1493-1503.

Yoon, S. W., Gavaskar, A. R., Sass, B. M., Gupta, N., Janosy, R., Drescher, E., et al. 2000. Innovative construction and performance monitoring of a permeable reactive barrier at Dover Air Force Base. In *Chemical oxidation and reactive barriers: Remediation of chlorinated and recalcitrant compounds* (eds. G. B. Wickramanayake, A. R. Gavaskar and A. S. C. Chen). Battelle Press, Columbus, Ohio: pp. 409-416.

Subtask 4.2. Analyze and Measure the Patterns of Permeability and Porosity Reduction

Objective

One component of the mitigation of permeability reduction (Subtask 4.1) is an understanding of changes in hydraulic conductivity in FeS systems. Consequently, this subtask aimed to experimentally characterize the nature of precipitation observed in PRB systems as the basis of the change in hydraulic conductivity. These experiments investigated the hypothesis suggested by the modeling reported in Subtask 4.1, that greater precipitation results in greater permeability reduction in the ZVI system than in the FeS system, and that the presence of oxidants, such as nitrate, increases this effect.

Background

The current state of knowledge, based on column experiments, suggests that precipitation of mineral solids can have a significant impact on the hydraulic and reactive performance of ZVI columns. To date, it is believed that no column experiments using FeS as mackinawite have been reported in the literature.

Most column work with ZVI, both in the laboratory and in the field, has found significant precipitation of solids, often with accompanying changes in permeability. In the field, for example, an ex situ reactor at the Portsmouth Gaseous Diffusion Plant near Piketown, OH accumulated iron sulfide, iron oxyhydroxides, and carbonates, causing a reduction in flow (Liang et al., 1997). An on-site ZVI column at the Backnang site in Germany experienced a loss of reactivity towards chlorinated ethylenes (Kober et al., 2002). Although hydraulic conductivity was not reported, the loss of reactivity was attributed to the precipitation of iron and calcium carbonates, with some hydrogen gas also passivating the reactive media. At the Y-12 site in Oak Ridge, TN, a column study using site groundwater estimated a 45% porosity loss at the influent end of the column, mainly due to the formation of mineral solids in the reactive media, rather than gas accumulation (Kamolpornwijit et al., 2003). This groundwater was characterized by high calcium, alkalinity, and nitrate. The presence of nitrate was argued to be a major factor in controlling the solution chemistry of the columns, as nitrate was thought to be responsible for the majority of ZVI oxidation (Kamolpornwijit et al., 2006). Another set of field columns, receiving an oxic site groundwater with explosives from the Umatilla Chemical Storage Depot near Hermiston, OR, lost conductivity as well, causing the authors to suggest a pre-treatment step to remove oxygen (Johnson et al., 2005).

Work in the laboratory also shows evidence of solids accumulation and permeability loss in ZVI media. For example, Gu et al. (1999) demonstrated that bicarbonate and sulfate promoted ZVI corrosion such that columns receiving high concentrations of these anions accumulated more iron carbonate and produced more hydrogen gas than columns receiving control solutions. The solids formed in these columns, including iron carbonate, iron oxyhydroxide, and iron sulfide were calculated to reduce porosity by up to 10%. The column experiments of Gu et al. used a constant hydraulic head and did not measure a change in flow rate. Other researchers, however, have demonstrated a loss in hydraulic conductivity. Mackenzie et al. (1999) found a significant loss of permeability in a column receiving aerated water over a period of about 50 hours (the flow rate for this column was not reported). In the same study, a groundwater with 4-6 mg/L of oxygen also demonstrated permeability loss. The loss of porosity was attributed

mainly to a film of hydrogen gas at the iron surfaces, with the buildup of ferrous hydroxide (and other carbonate-bearing solids expected at longer flow times) accounting for the remainder. Similarly, Johnson et al. (2005) showed a column receiving 8mg/L of oxygen lost 2 orders of magnitude of hydraulic conductivity over a one month period.

Columns without oxygenated influent have generally been observed to accumulate solids but not to plug due to a loss of hydraulic conductivity. For example, Johnson et al. (2005) did not report hydraulic conductivity loss in a column receiving 10 mg/L TNT. Columns receiving various concentrations of $NaHCO_3$ and NaCl showed between 6 and 24% decrease in porosity, but the changes in hydraulic conductivity were estimated to be minor in comparison to passivation effects (Vikesland et al., 2003). Jeen et al. (2006) operated columns with de-oxygenated influent solutions containing 0, 100, or 500 mg/L CaCO3. This work showed that porosity loss was a function of the influent carbonate concentration, but that the precipitation of solids passivated the reactive media, thus moving the zone of precipitation to areas with non-passivated media. This result suggested that significant hydraulic conductivity loss due to mineral precipitation is unlikely.

The literature therefore suggested that oxygen, carbonate, and oxidants such as nitrate could be important players in controlling the porosity and permeability of ZVI. As far as is known, work with FeS reactive media has not been reported in the literature. Therefore, column experiments were conducted to assess the effects of oxygen, carbonate, and nitrate on ZVI and FeS columns.

Materials and Methods

Development of Column System

Mixing of ZVI and Sand Particles. Tests were conducted to determine the porosity achieved through mixing of sand and ZVI particles. It is expected that FeS-coated sand will pack similarly to uncoated sand; so the results here are applicable to FeS-coated sand and ZVI mixtures, as well. The sand utilized had a median grain diameter of 0.5mm and concavity and uniformity indices of 1.2 and 1.7, respectively. The ZVI utilized was -8 + 50 mesh ZVI from Peerless Metals and Abrasives (Detroit, MI), and was angular and irregularly shaped, with a median grain size of 0.7mm, with concavity and uniformity indices of 0.9 and 3.8, respectively.

Packing Techniques. Packing of porous media may have a strong impact on the distribution of flow across the cross-sectional area of the column. Because creating 1-D flow conditions is paramount to the decoupling of packing heterogeneities from permeability reduction, considerable effort was devoted to developing techniques for the homogeneous packing of sand to prevent the uneven distribution of flow in the lab columns.

Column and System Setup. The columns used were Plexiglas, with length = 25 cm and inner diameter = 5 cm. The fluid handling components were 316 stainless steel tubing with stainless steel connections from Swagelok (Solon, OH). The pumps used in the study were Varian Dynamax SD-200 pumps (Varian, Palo Alto, CA), with flow rate 0.1 – 10 mL/min. A flow rate of 0.7 mL/min was used; this rate corresponds to a Darcy flow rate of 0.5 m/d and a true flow velocity of 1.5 m/d. Two column experiments, intended to provide a high mass flux of oxygen to the column, used flow rates of 8 mL/min.

Sand Particle Sizes. The sand used in this study was Wedron 510 silica sand (Fairmount Mineral, Wedron, IL). The three size fractions of this sand used for the column studies correspond to sieve sizes -80/+100 (finer than sieve #80, retained on sieve #100), -70/+80, and -40/+50, with grain diameters 149, 177, 297µm and specific surface areas 152, 128, and 75 cm^2/g, respectively. These three particle sizes were used to yield two different particle size distributions. The first was a combination of -70/+80 and -80/+100 sieve sizes. This combination matches the porous media used in Subtask 1.2 and is herein referred to as "fine". The second particle size distribution is -45/+50 mesh, which is the largest size fraction available in the silica sand in this study. This size distribution is referred to as "coarse". Once packed into columns, these size fractions are expected to have hydraulic conductivities of 9 and 30 m/d, respectively (as predicted by the Carman Kozeny equation). It was anticipated that the difference in hydraulic conductivity between these two sands would result in different hydraulic responses to mass flux of calcium and carbonate.

Reactive Media. ZVI and FeS-coated sand systems were studied. ZVI, as the most commonly used PRB material in the field, was chosen to provide a baseline against which to compare the performance of FeS-coated sands. The ZVI was manufactured by Peerless Metals (Detroit, MI), with grain size -8/+50 mesh and median grain size = 720 µm. FeS-coated sands were prepared according to the procedures described in Task 1. Iron extraction of the FeS-coated sands yielded a mean coating of $1.47 * 10^{-5}$ mole Fe / g sand ($1.42 * 10^{-3}$ mole Fe / m^2 sand).

All FeS columns were packed in an anaerobic chamber. Because ZVI was shipped in ambient air, the ZVI column was not packed in the anaerobic chamber. To simulate field conditions, with native aquifer materials up and downgradient of the PRB, some columns contained 2 cm of sand at the column influent and effluent.

Influent Solutions. Several types of influent solutions were used for these column studies. To establish a base case, oxygenated de-ionized (DI) water was used in two columns. The remainder of the column experiments used influent solutions designed to mimic properties of groundwater that Subtask 4.1 identified as problematic for PRBs. It was found that high alkalinity was correlated with impaired PRB performance, and therefore the remainder of the column experiments used deoxygenated water bearing high levels of calcium and carbonate.

This influent solution was prepared by adding $CaCO_3(s)$ and HCl to deoxygenated, distilled water. The influent calcium and carbonate concentrations were Ca^{2+} = 280 mg/L and CO_3^{2-} = 420 mg/L (0.007 moles/L of each species), based on a reported concentration of Ca^{2+} = 275 mg/L and CO_3^{2-} = 460 mg/L at the PRB at Monticello, UT, which experienced a hydraulic conductivity loss of three orders of magnitude (Mushovic et al. 2006). The PRB at Monticello also had high nitrate levels (118 mg/L), so some column experiments included 100 mg/L (0.0016 moles/L) of nitrate. Off-gassing of carbon dioxide from the influent solution was prevented by storing the influent in a zero headspace Tedlar bag. The solution pH was set to 6 by the addition of HCl, to ensure that $CaCO_3(s)$ remains undersaturated in the influent vessel, pump, and feed lines.

Geochemical Characterization. The columns were equipped with ports for hydrostatic pressure measurement at six points (1.9, 3.8, 6.35, 10.15, 15.25, and 20.3 cm from the inlet). Pressure transducers (Validyne, Northridge, CA) were used to continuously monitor pressure at these

ports. A UPC-607 computer interface card (Validyne) was used for datalogging of pressure transducer data.

Calcium, iron, pH and oxygen were also measured in the columns. pH and dissolved oxygen (DO) were measured at the influent and effluent of the columns with a Ross Ultra #8102 electrode (ThermoFisher, Waltham, MA), a pH meter (EA 920, Mettler-Toledo, Columbus, OH), and a dissolved oxygen electrode and meter (YSI-58, YSI Inc., Yellow Springs, OH). pH and DO samples were collected from the column and measured quickly (within seconds of the end of sample collection) in the ambient lab atmosphere. Aqueous calcium and total iron were measured using an ICP-MS. Samples for these two parameters were also collected from the column influent and effluent; these samples were acidified with 20uL of 70% nitric acid.

Results and Discussion

Development of Column System

Mixing of ZVI and Sand Particles. Mixtures of ZVI and sand were packing into columns and measured for porosity. The mass fraction of ZVI was varied from 0-100% mass fractions of ZVI; in these mixtures, porosities varied linearly from 0.37, for pure sand to 0.6, for pure ZVI (Figure 4.11).

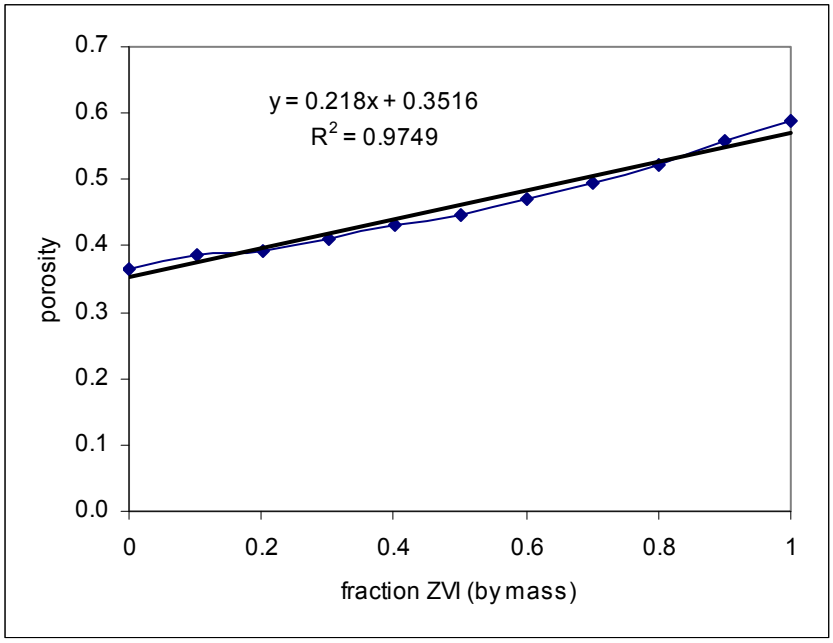

Figure 4.11. Porosity of mixtures of sand and ZVI is shown to vary linearly by mass fraction.

The results of packed porosities for mixtures of spherical sand (or FeS-coated sand) and platy, irregular ZVI particles indicates that porosity increases as the ZVI fraction is increased. Since greater precipitation is expected to occur in regions of high reactivity, the greater porosity of these regions may prove advantageous, since the adverse effects of precipitates will be mitigated in high porosity regions.

Packing Techniques. To be able to attribute the development of preferential flow pathways to precipitation, the packing of the lab columns must be initially homogeneous. Figure 4.12 compares the flow distribution, which has been visualized with a dye, in two columns: column A has been packed in 2-cm lofts compacted manually, while column B has been packed in 0.2-cm lofts compacted with the use of a vibrating table (FMC Technologies, Homer City, PA) as recommended in Oliviera and Demond (1996). This figure shows that the packing procedure utilized in B ensures a uniform distribution of flow across the column.

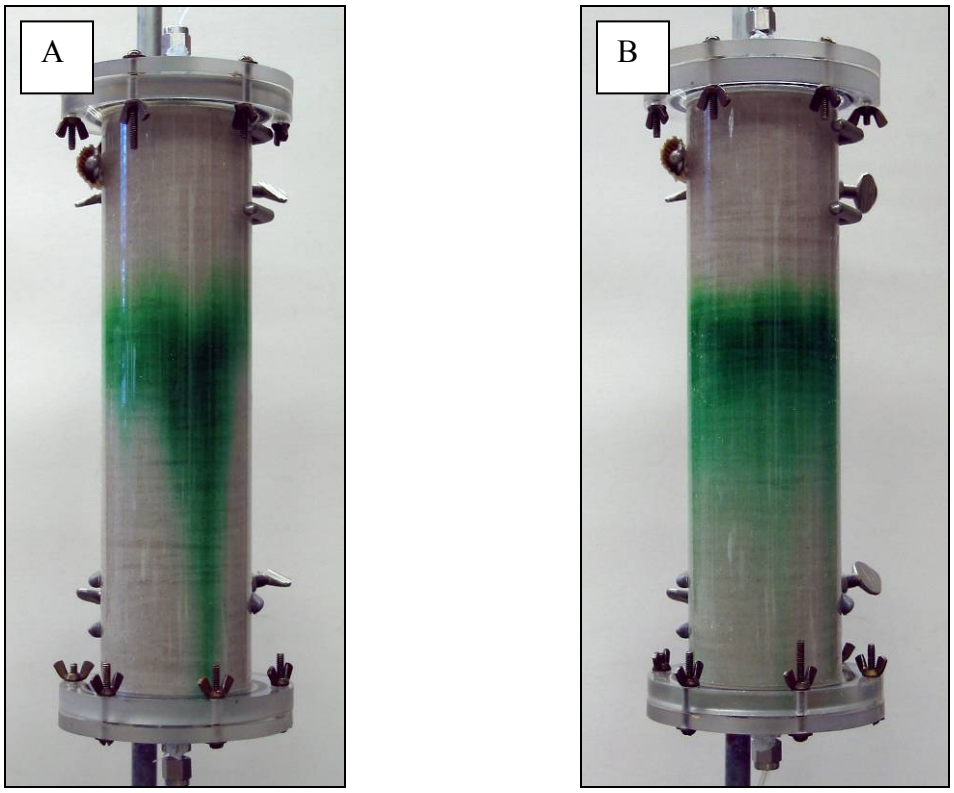

Figure 4.12. A) uneven flow distribution across the cross-sectional area of the column, and B) 1-D flow created by proper column packing and fitting assembly.

Beginning with ZVI and oxygenated conditions to establish a base case, seven column experiments were conducted. These columns are summarized in Table 4.5, and the individual experiments are described in detail in the following sections.

Columns with Oxygenated Influent Solution

ZVI-oxygen. This column experiment was meant to establish a baseline for permeability loss, against which FeS column experiments could be compared. A high flow rate was selected to maximize the mass flux of oxygen into the column. 250 pore volumes were injected, resulting in a loss of permeability of 89%. The changes in DO and pH over the length of the column were a decrease of 5.7 mg/L DO, and an increase of 0.9 pH units. Based on the changes in these parameters, it was estimated that up to 20 mg/cm^3 (of the column) of ferrihydrite, $Fe(OH)_3$, a

Table 4.5. Summary of column experiments.

Column Name	Reactive Media	Grain Size	Media Mixture	Influent Solution	Flow Rate (mL/min)	Porosity
ZVI-oxygen	ZVI	as-received (-8/+50 mesh)	pure	oxygenated	8	0.60
FeS-oxygen	FeS	coarse (-45/+50 mesh)	pure	oxygenated	8	0.32
ZVI	ZVI	as-received (-8/+50 mesh)	pure	deoxygenated, with Ca^{2+} and CO_3^{2-}	0.7	0.60
FeS-fine	FeS	fine (-70/+100 mesh)	50:50 FeS-coated sand: uncoated sand	deoxygenated, with Ca^{2+} and CO_3^{2-}	0.7	0.34
FeS-coarse	FeS	coarse (-45/+50 mesh)	50:50 FeS-coated sand: uncoated sand	deoxygenated, with Ca^{2+} and CO_3^{2-}	0.7	0.33
ZVI-nitrate	ZVI	as-received (-8/+50 mesh)	pure	deoxygenated, with Ca^{2+}, CO_3^{2-}, and NO_3^-	0.7	0.60
FeS-nitrate	FeS	fine (-70/+100 mesh)	pure	deoxygenated, with Ca^{2+}, CO^{32-}, and NO_3^-	0.7	0.33

frequent corrosion product from ZVI oxidation, was deposited. The increasing pressure drop across the column is shown in Figure 4.13.

After the conclusion of the ZVI-oxygen experiment, the column was dissected for study using SEM. Precipitation in the interstitial pore space was observed (Figure 4.14), supporting the hypothesis that precipitates accumulated in the column, contributing to permeability loss. The precipitates were observed to have a needle structure, possibly indicating the presence of goethite, a ferric iron solid (Figure 4.15).

FeS-oxygen. Experimental conditions for this column were chosen to match those of the ZVI-oxygen column. Unlike the ZVI-oxygen column, the FeS-oxygen column experiment conducted in 2007 showed no change in permeability or pH. Because the column received a significant amount of oxygen, FeS was observed to quickly (within 100 PV) change from black to a rust color. This shift in color can be seen in Figure 4.16. The lack of permeability loss appears to be consistent with the geochemical modeling efforts discussed in Subtask 4.1.

Columns with Calcium and Carbonate

ZVI. This column received an influent solution adjusted to pH = 6, with Ca^{2+} = 280 mg/L and CO_3^{2-} = 420 mg/L (0.007 moles/L of each species), selected to match conditions of the failed

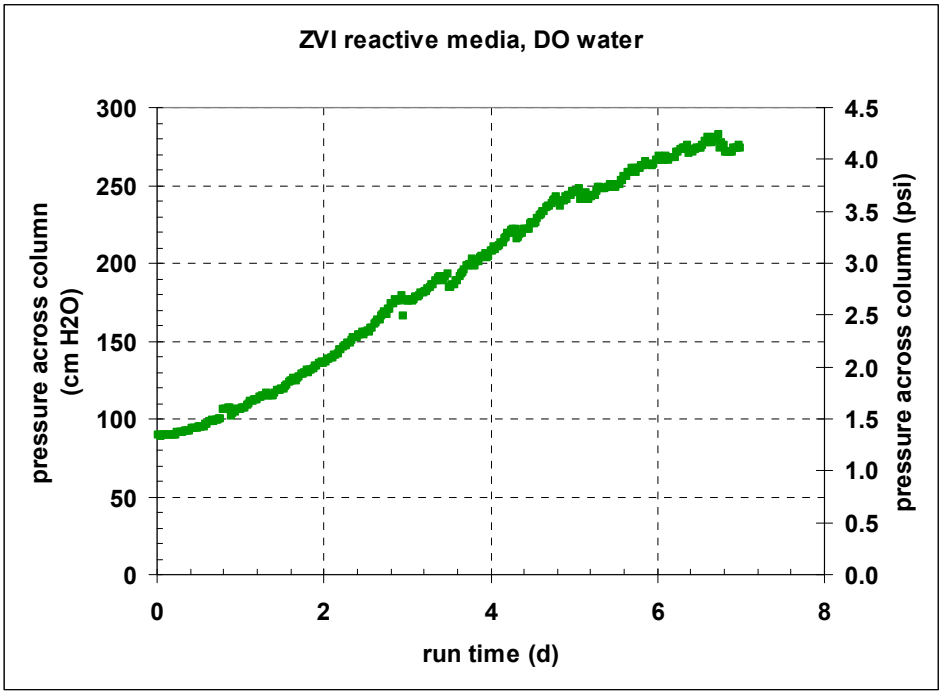

Figure 4.13. Increasing pressure to maintain flow caused by permeability loss in the ZVI-oxygen column.

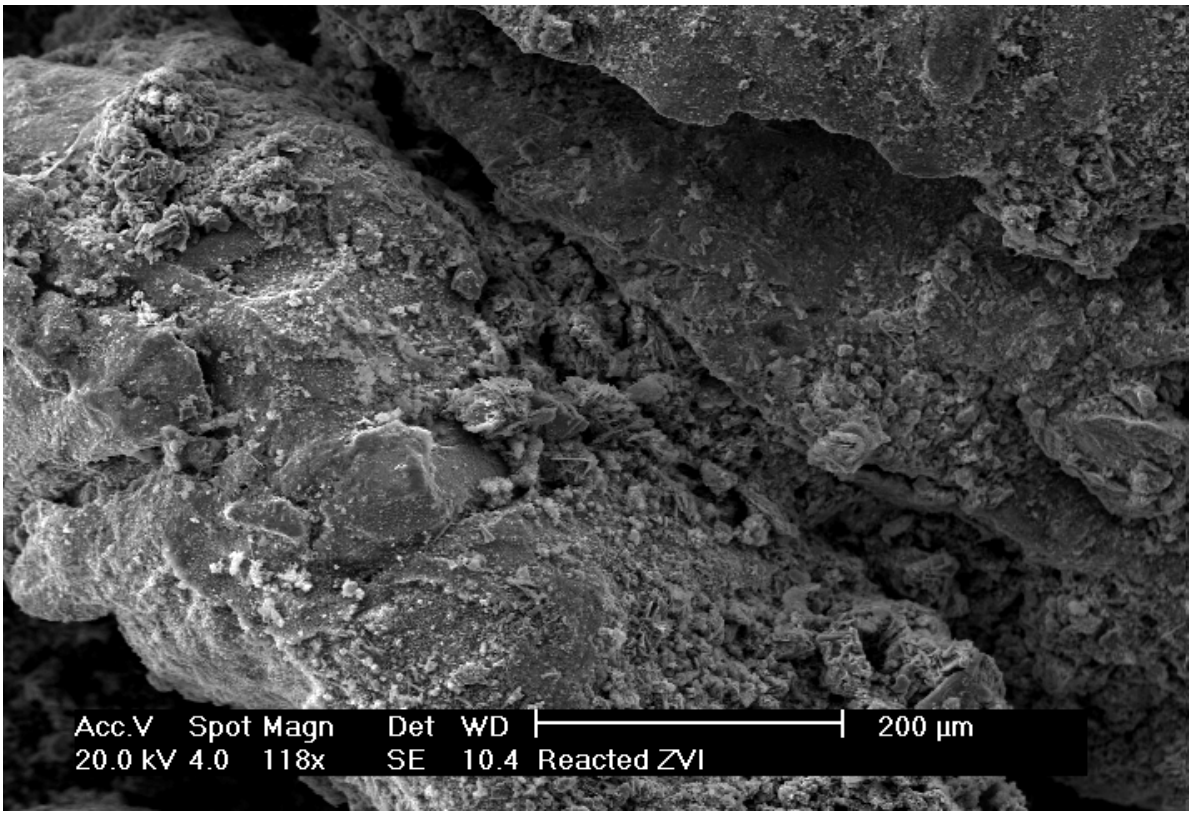

Figure 4.14. SEM of ZVI-oxygen grains shows precipitation. ZVI particles are lower left and upper right; precipitates are seen in the pore space running from upper left to lower right.

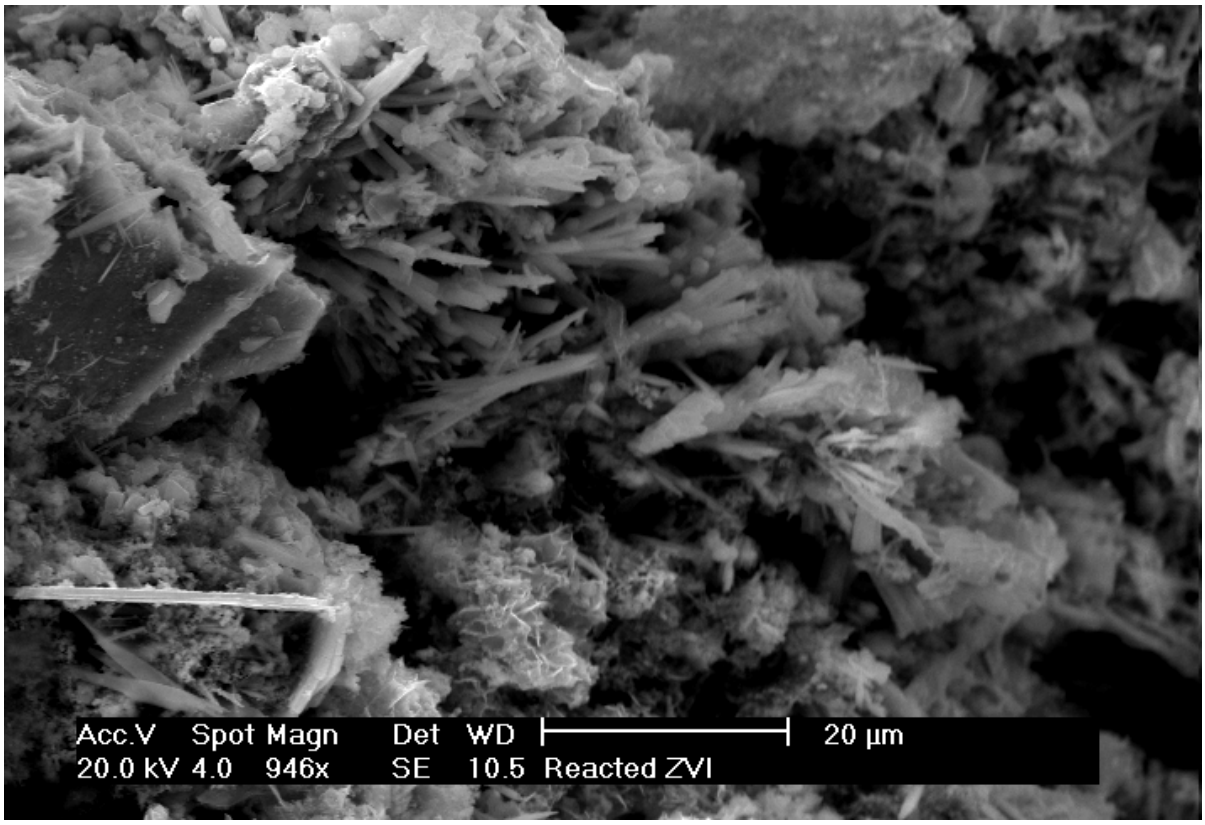

Figure 4.15. Needle structure of precipitates in the ZVI-oxygen column.

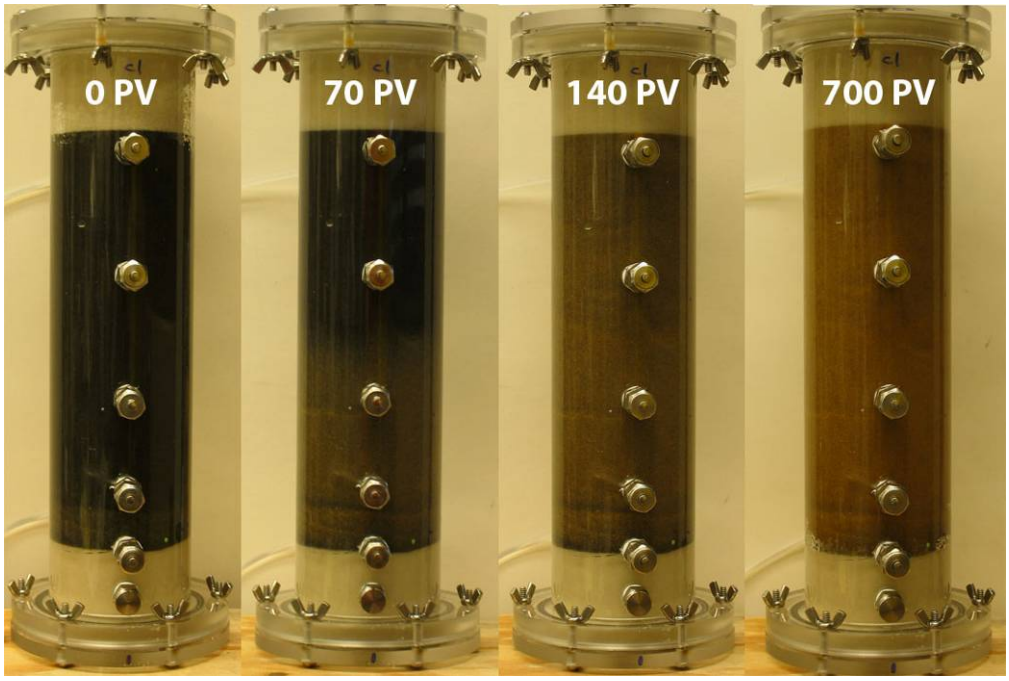

Figure 4.16. FeS-oxygen column changes color as it is oxidized.

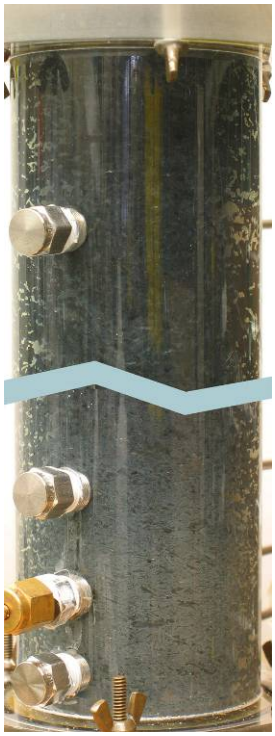

Figure 4.17. Change in color in the ZVI column influent end (bottom) relative to effluent end suggests accumulation of calcium carbonate.

PRB at Monticello, UT. This column was operated for 58 PV, or 17 days. On average, pH increased from 6.0 to 6.6 between the influent and effluent of the column, and Ca^{2+} decreased from 280 mg/L to 245 mg/L. Visually, the influent end of the column turned a whitish color, indicative of the accumulation of $CaCO_3$(s). The accumulation of $CaCO_3$(s) can be seen in Figure 4.17, which shows a color difference between the influent and effluent ends of the ZVI column. Unfortunately, failure of the computer interface equipment prevented the measurement of changes in hydrostatic pressure in this column.

FeS-fine and FeS-coarse. These columns received deoxygenated influent solution with the same amount of calcium and carbonate (0.007 M of each) as the ZVI column. It was anticipated that their different particle size distributions would lead to different permeability changes. However, no differences in their hydraulic response were observed over the 150 pore volume duration of the experiment. Furthermore, there were few geochemical changes.

During the entire course of both column experiments, the difference in influent and effluent pH at a given sampling time was minimal: the effluent was, at most, 0.3 pH units above the influent. There was, furthermore, little or no consistent change in the concentration of calcium. pH and calcium results for both the FeS-fine and FeS-coarse columns are shown in Figure 4.18.

It was observed that the color of the FeS-fine column (which was initially black) changed to a whitish sand color at the influent end of the columns; this whitish area was observed to move towards the effluent end of the columns as time passed (Figure 4.19). The color change is most

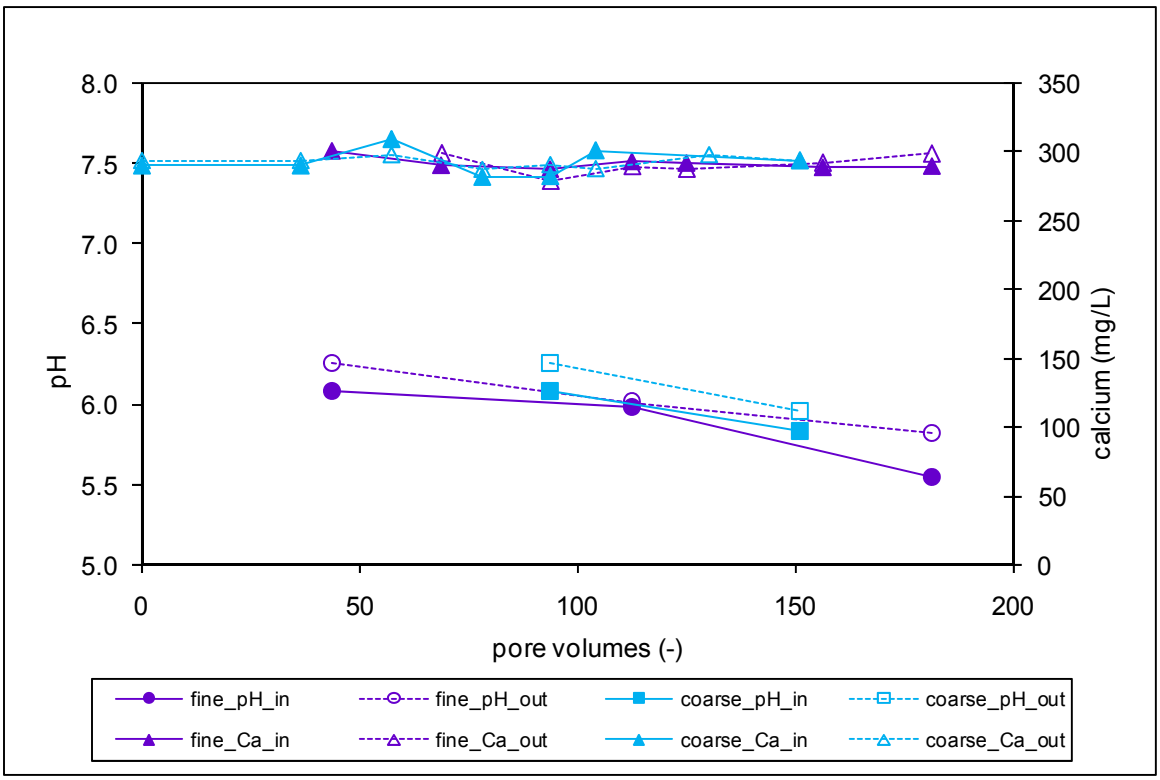

Figure 4.18. pH and calcium data for both the FeS-fine and FeS-coarse columns; minimal changes in either parameter are observed.

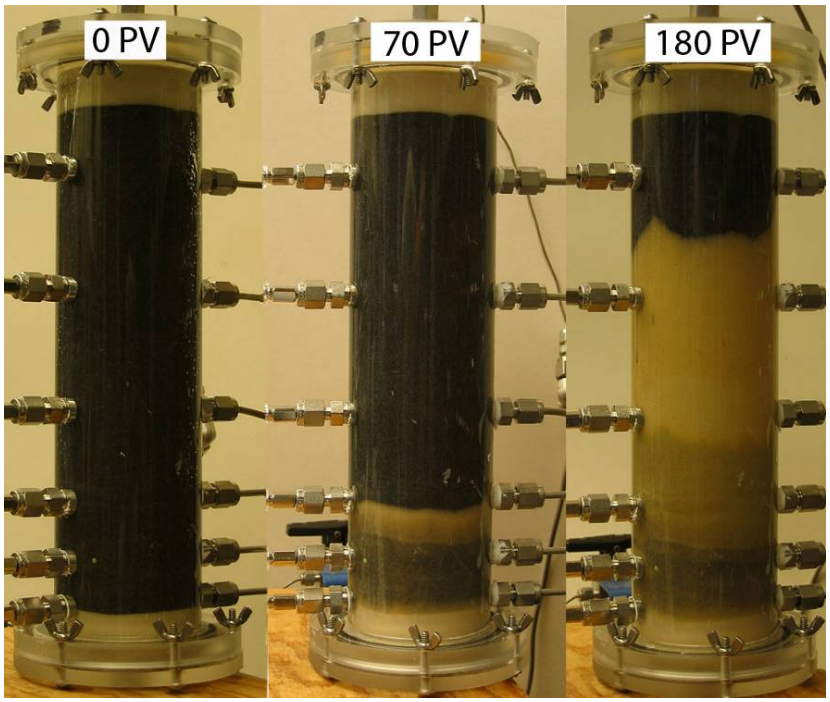

Figure 4.19. The appearance of the FeS-fine column changed with time, moving from the influent (bottom end) to the effluent.

likely due to the slow dissolution of FeS: since the aqueous phase is undersaturated with respect to calcite ($CaCO_3(s)$) (based on the low pH and unchanging calcium values), precipitation of calcite cannot account for the observed color change.

Hydrostatic pressure was monitored at 6 points along each column using pressure transducers. However, the hydrostatic pressure measurements did not indicate any change in the hydraulic conductivity of the porous media in either column (data not shown). This is consistent with pH measurements that show conditions are not favorable for precipitation of calcium carbonate.

The FeS-fine and FeS-coarse columns were destructively sampled at the end of the experiment (examples shown in Figure 4.20). These sections all showed uniform FeS coating (or lack thereof, in cases where the FeS had dissolved) perpendicular to flow, indicating that preferential flow paths were not significant. In the fine column, average iron content decreased from 0.84 to 0.66 mg Fe / g sand; in the coarse column, no decrease was measured. This was corroborated by visual observations of the column, as the fine column's color changed, while the coarse column, in contrast, did not show a visible color change. Loss of FeS, such as that observed in the fine column, has not been observed in other work in this task or in Task 1. The cause remains to be determined.

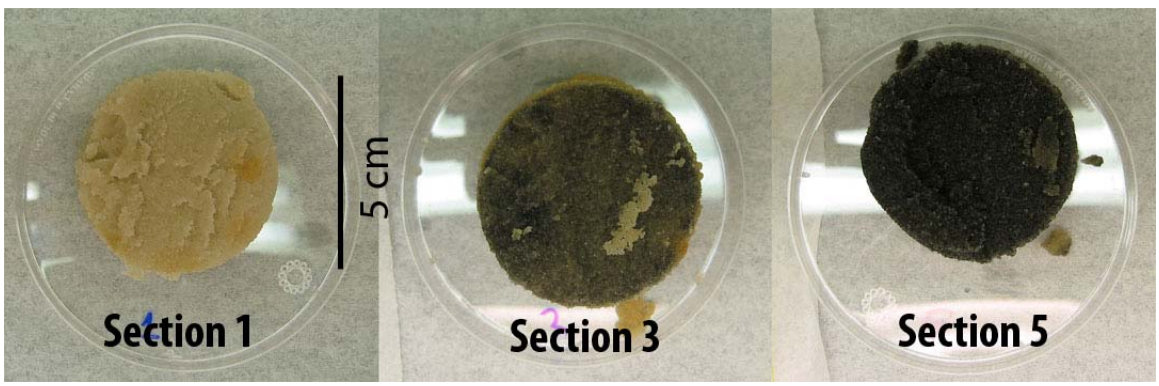

Figure 4.20. Sections taken from the FeS-coarse column indicate dissolution of FeS, but no preferential flow paths. Each section is 2.5 cm thick, and section 1 is the influent end of the column.

Columns with Calcium, Carbonate, and Nitrate

Based on the statistical analysis of PRB longevity (Henderson and Demond, 2007) and geochemical modeling (see Subtask 4.1), it was hypothesized that nitrate could alter geochemical conditions such that hydraulic conductivity losses would be detectable in FeS columns. The influent solution used for these columns was identical to the other columns, with the addition of 100 mg/L NO_3^- (0.0016 mole/L). This addition was meant to mimic conditions at the failed Monticello PRB, where 118 mg/L nitrate was reported (Mushovic et al., 2006).

ZVI-nitrate. The presence of nitrate produced a marked difference in the effluent pH in the ZVI column, as shown in Figure 4.21. The pH rapidly increased from pH 6 to pH 9.2 after 10 pore volumes. During the course of the 70 pore volume experiment, the effluent pH slowly decreased from above 9 to less than 8, which is two pH units above the influent pH. A whitish substance

was observed to accumulate at the influent end of the column, possibly indicative of the accumulation of $CaCO_3$(s).

The analysis of aqueous calcium in the effluent indicated that calcium was being removed in the ZVI column. As shown in Figure 4.22, about 80 mg/L of calcium was removed by the column on average. Consistent with the pH and calcium observations, the pressure gradient along the column increased, indicating a decrease in permeability by a factor of 10.

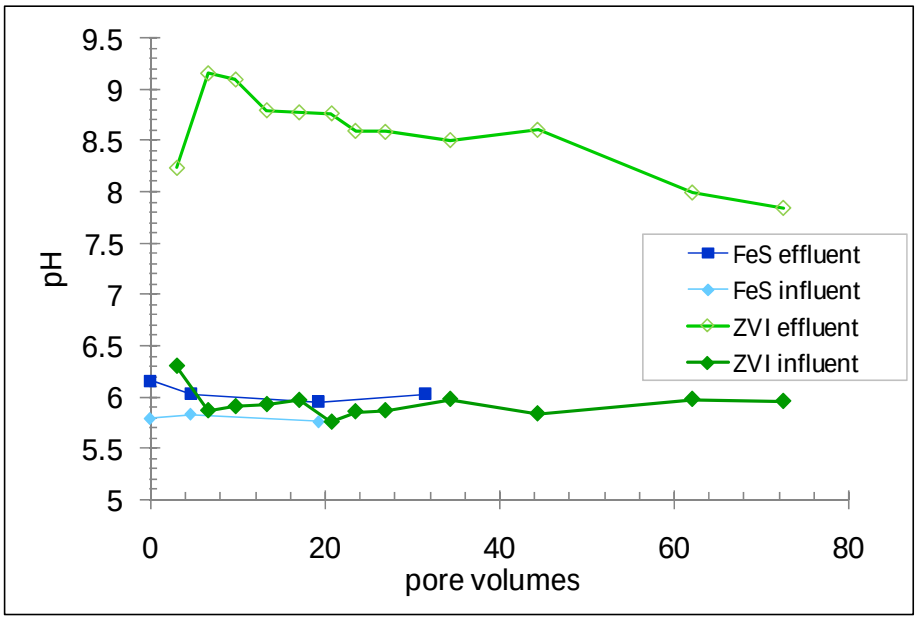

Figure 4.21. pH increase in ZVI-nitrate column; minimal increase in FeS-nitrate column.

FeS-nitrate. Pump failure after about 30 pore volumes caused a significant intrusion of oxygen into the FeS-nitrate column, at which point the experiment was terminated. However, initial data allows for comparison to ZVI, for trends observed in ZVI were visible within 30 pore volumes. In contrast to the ZVI column, the FeS column showed a pH increase of only about 0.4-0.6 pH unit (see Figure 4.21), which is insufficient to promote the formation of carbonate or iron oxide or hydroxide solids.

Because the pH increase was insufficient for the formation of calcium carbonate, there is no discernable difference between the influent and effluent calcium values (Figure 4.22). Therefore, it appears that the presence of a strong oxidant (either oxygen or nitrate, for example) is necessary for appreciable pH increase in ZVI.

Summary and Conclusions and Implications for Future Research/Implementation

Column Method Development. In order to determine that hydraulic conductivity changes are due to precipitate buildup, it is essential to ensure the starting conditions for bench-scale columns is 1-D and homogeneous. Therefore, tests were conducted to determine a suitable method for packing. It was found that columns must be packed in small, 0.2 cm lofts. If precipitation in FeS systems is an issue for PRB longevity, then lifetimes may be extended by more carefully engineered particle size distributions. Work in this task has also demonstrated control of porosity through the mixing of sand and ZVI particles.

Column Experiments. A suite of column experiments was conducted, both with ZVI and FeS-coated sands, in which influent solutions were chosen to match the conditions expected, based on work in Subtask 4.1 to promote permeability reduction. As a baseline, oxygenated solutions were also used.

It was found that in all columns, ZVI was prone to permeability reduction; however, no

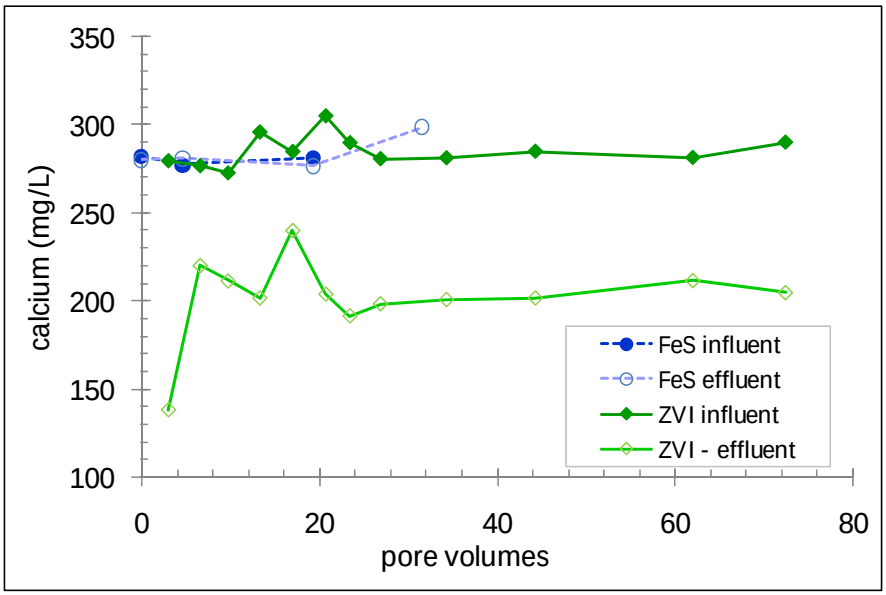

Figure 4.22. Calcium removal in ZVI-nitrate column; no removal in FeS-nitrate column.

permeability reduction was detectable in FeS column. In the case of the oxygenated column, the FeS column showed no permeability reduction, while the ZVI column lost nearly 90% of its permeability. In columns receiving water containing high calcium and carbonate, ZVI appeared to remove some calcium (about 40 mg/L), which was coupled with a pH increase of about 0.6 pH units. In contrast, the FeS columns which received identical water showed no calcium removal and no pH increase. When nitrate was added to the influent solution, increased pH and calcium removal were observed in the ZVI column. The FeS columns, on the other hand, showed a pH increase of about 0.5 pH units and no appreciable calcium removal.

Although permeability loss was observed in ZVI columns, permeability loss was not observed in columns packed with FeS-coated sands. Indeed, regardless of influent conditions, the FeS columns did not show evidence of any permeability reduction. These findings were in keeping with the geochemical modeling results from Subtask 4.1. Based on these results, it appears that permeability-reducing precipitation should not occur in FeS-based PRBs to the same extent that it does in ZVI PRBs. If these results are indicative of long-term behavior of FeS PRBs, pretreatment zones, with a gradation of particle size distributions or mixtures of reactive and non-reactive sand, may not be necessary.

Literature Cited

Gu, B., Phelps, T. J., Liang, L. Y., Dickey, M. J., Roh, Y., Kinsall, B. L., et al. 1999. Biogeochemical dynamics in zero-valent iron columns: Implications for permeable reactive barriers. *Environ. Sci. Technol.* **33**, 2170-2177.

Jeen, S. W., Gillham, R. W., and Blowes, D. W. 2006. Effects of carbonate precipitates on long-term performance of granular iron for reductive dechlorination of TCE. *Environ. Sci. Technol.* **40**, 6432-6437.

Johnson, R. L., Tratnyek, P. G., Miehr, R., Thoms, R. B., and Bandstra, J. Z. 2005. Reduction of hydraulic conductivity and reactivity in zero-valent iron columns by oxygen and TNT. *Ground Water Monit.Remediat.* **25**, 129-136.

Kamolpornwijit, W., Liang, L. Y., West, O. R., Moline, G. R., and Sullivan, A. B. 2003. Preferential flow path development and its influence on long-term PRB performance: Column study. *J. Contam. Hydrol.* **66**, 161-178.

Kamolpornwijit, W. and Liang, L. 2006. Investigation of gas production and entrapment in granular iron medium. *J. Contam. Hydrol.* **82**, 338-356.

Köber, R., Schlicker, O., Ebert, M., and Dahmke, A. 2002. Degradation of chlorinated ethylenes by Fe^0: Inhibition processes and mineral precipitation. *Environ.Geol.* **41**, 644-652.

Liang, L. Y., Korte, N. E., Gu, B., Puls, R., and Reeter, C. 2000. Geochemical and microbial reactions affecting the long-term performance of in situ 'iron barriers'. *Adv. Environ. Res.* **4**, 273-286.

Liang, L. Y., West, O. R., Korte, N. E., Goodlaxson, J. D., Pickering, D. A., Zutman, J. L., et al. 1997. *The X-625 groundwater treatment facility: A field-scale test of trichloroethylene dechlorination using iron filings for the X-120/X-749 groundwater plume*. (Report No. ORNL/TM--13410). Oak Ridge, TN: Oak Ridge National Laboratory.

Mackenzie, P. D., Horney, D. P., and Sivavec, T. M. 1999. Mineral precipitation and porosity losses in granular iron columns. *J. Hazard. Mater.* **68**, 1-17.

Roberts, L. R., Ball, W. P., Searson, P., Fairbrother, H., Vikesland, P. J., Klausen, J., et al. 2002. *Final report for the SERDP project CU-1125: Influence of groundwater constituents on longevity of iron-based permeable barriers*. (Report No. CU-1125). Baltimore, MD: John Hopkins University.

Vikesland, P. J., Klausen, J., Zimmermann, H. J., Roberts, A. L., and Ball, W. P. 2003. Longevity of granular iron in groundwater treatment processes: Changes in solute transport properties over time. *J. Contam. Hydrol.* **64**, 3-33.

Task 5. DEVELOPMENT AND LABORATORY-VALIDATION OF A MULTI-COMPONENT REACTIVE TRANSPORT MODEL FOR PRB PERFORMANCE PREDICTIONS AND FIELD-SCALE DESIGN APPLICATIONS (TUFTS UNIVERSITY-ABRIOLA)

The primary goal of this task is to develop a laboratory-validated numerical simulator that can predict the performance of FeS-coated sand based PRBs for the treatment of As contaminated groundwater. To achieve this goal, research was organized around three subtasks, associated with the following specific sub-objectives: 5.1 develop a conceptual reaction model for As(III) interaction with FeS-coated sand and validate it using laboratory batch data; 5.2 investigate rate limited processes in transport systems using 1-D reactive transport modeling; and 5.3 extend the model to 2-D and perform example simulations of field-scale reactor performance.

Subtask 5.1 Conceptual Reaction Model Development and Validation

Objective

The objective of this subtask is to develop a geochemical model to simulate equilibrium chemical reactions in systems consisting of As(III) and FeS-coated sand and to validate the model with data from batch experiments.

Background

Results from Subtask 1.3c suggested that in the batch system consisting of FeS-coated sand and As(III), formation of orpiment (As_2S_3) is one of the major mechanisms for removing As(III) from aqueous solution at acidic conditions, while under neutral to alkaline conditions, As(III) is primarily adsorbed on the FeS-coated sand surface. Based upon this information, a geochemical reaction model was developed using PHREEQC version 2 (Parkhurst and Appelo, 1999) with the embedded MINTEQA2 database version 4.0 (Allison et al., 1991) to simulate the equilibrium behavior of As(III) retention by FeS-coated sand as a function of pH in batch systems. The model developed in this subtask provides a quantitative tool for evaluating the fate of As(III) in FeS-controlled reducing environments as a function of pH and pe, and will be useful for designing and operating groundwater remediation systems targeting As(III) removal using FeS based systems.

Materials and Methods

A geochemical reaction model was developed to simulate As(III) retention by FeS-coated sand under different pH conditions in batch systems. The modeled chemical reactions included aqueous speciation, redox reactions, mineral dissolution/precipitation, and a non-electrostatic surface complexation model (SCM) to account for pH dependent As(III) sorption. Also considered was the oxidative transformation of mackinawite (FeS) to magnetite (Fe_3O_4) on the coated sand surface. A component additivity approach was adopted to simulate As(III) sorption through surface complexation onto both mackinawite and magnetite, which transform to each other with changing pH conditions.

Geochemical modeling was conducted with PHREEQC version 2, a general purpose, geochemical reaction simulator that is supported and distributed by the US Geological Survey

and designed to perform a variety of low-temperature aqueous geochemical calculations. The current version of PHREEQC can model both equilibrium and kinetically controlled reactions, precipitation/dissolution of binary solid solutions, fixed volume or fixed pressure gas phases, evolving surface or exchange sites, and diffusional reaction or mass-transfer limitations. Some well-known and widely-used geochemical reaction databases are distributed with the program, but the user can also add elements and reactions to these databases or create a database with new reactions, surfaces, or elements. Here the popular MINTEQA2 version 4 database was used in all simulations. Some customized reactions were added to the model database where necessary.

A nonlinear parameter estimation package PEST (Doherty, 2004) was used to estimate the initial amount of each mineral on the coated sand surface and SCM parameters based on data from batch experiments. PEST is a unique software package that can be used with any pre-existing model for model-independent parameter estimation and uncertainty analysis and has been widely used in geochemical and hydrological researches. Here PEST was used to "take control" of PHREEQC, running it as many times as necessary while adjusting specified model parameters until the discrepancies between model predictions and experimental data are reduced to a minimum in the weighted least squares sense.

Results and Discussion

Model Formulation. A conceptual reaction model was formulated to describe all possible reactions in the system initially consisting of FeS-coated sand and As(III) (Figure 5.1). Solid phase mackinawite on the FeS-coated surface will dissolve under acidic conditions and release S(-II) and Fe(II) to the aqueous solution. Fe(II) can lose one electron and be converted to

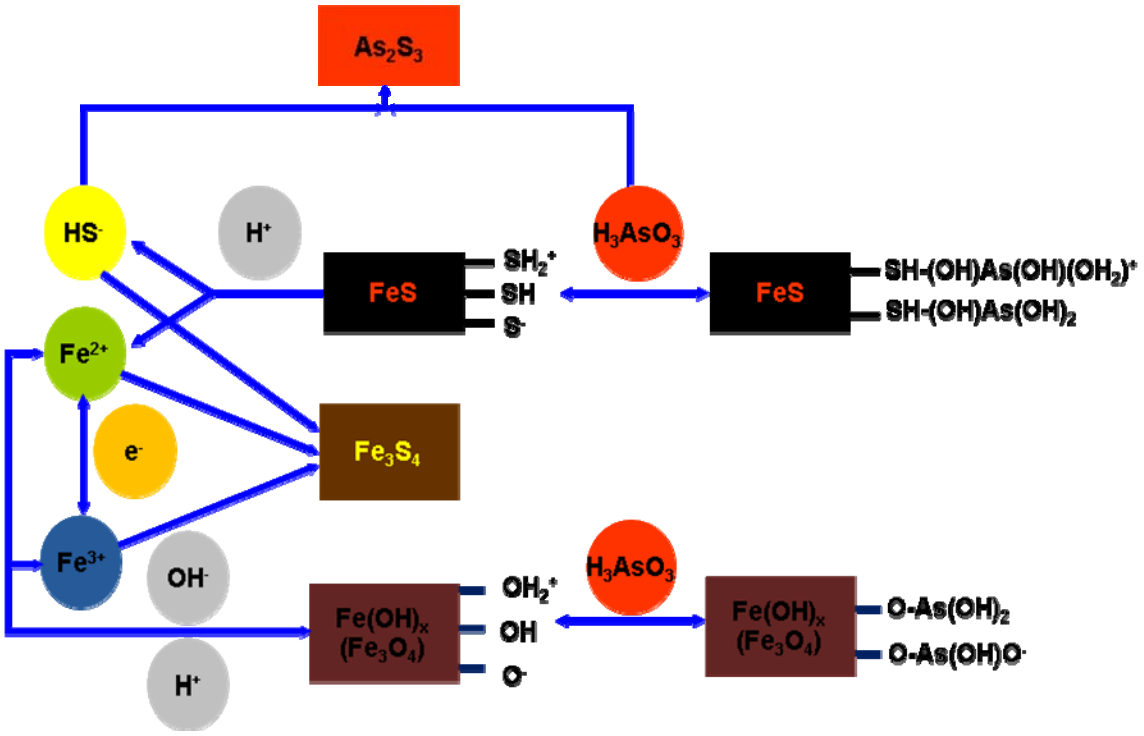

Figure 5.1. Conceptual reaction model of FeS-coated sand–As(III) system.

Fe(III) under certain redox conditions and subsequently cause the formation of solid phase greigite (Fe_3S_4), which was identified as a possible oxidation product on the surface of reacted FeS-coated sand in the XPS measurements made in Subtask 1.1. Gregite is an intermediate iron sulfide mineral, which can transform to more stable iron sulfides, such as pyrite, over very long time periods, but in this simplified conceptual model, iron sulfide minerals other than mackinawite and greigite were not included.

During the preparation and storage of FeS-coated sand, partial oxidation of mackinawite can occur and iron (hydr)oxide minerals such as magnetite can be formed on the FeS-coated sand surface. Once in contact with alkaline solutions, iron (hydr)oxide minerals will also precipitate out. These iron (hydr)oxide minerals can provide extra sorption capacity for As(III), which becomes very important at high pH conditions. Based on the dissolved total iron concentration data from a set of FeS-coated sand dissolution experiments (Subtask 1.4c), and XPS data (Subtask 1.1) it was determined that magnetite is the most likely iron (hydr)oxide mineral formed in the system. To account for this, magnetite was included to represent the possible oxidative product of mackinawite in the FeS-coated sand -As(III) system.

Orpiment (As_2S_3) will precipitate out when saturated at high S(II) concentrations due to mackinawite dissolution at low pHs. This is the dominant mechanism for removing As(III) from solution by FeS-coated sand at acidic conditions. Electron transfer can also occur between Fe(II) and As(III), causing reduction of As(III) to As(II) and precipitation as solid phase realgar (AsS). Based on observations from Subtask 1.3c, only orpiment was identified on reacted FeS-coated sand surfaces. Therefore formation of realgar was not included in the reaction model.

At neutral to alkaline conditions, it is believed that As(III) is primarily removed by FeS-coated sand through adsorption. A non-electrostatic surface complexation model was developed with a component additivity approach (Davis et al., 1998) to explicitly describe the pH-dependent adsorption behavior of As(III) by both mackinawite and iron (hydr)oxide on the FeS-coated sand surface. This simplified non-electrostatic model was employed due to the difficulty in distinguishing the impacts of surface potential associated with different minerals. A non-electrostatic surface complexation model is also easier to apply in reactive transport modeling to predict the fate and transport of arsenic in the subsurface environment.

The surface sites associated with mackinawite are hypothesized to be sulfhydryl sites, ≡S-H, which can undergo protonation or deprotonation to form positively or negatively charged surface sites. Two types of outer-sphere surface complexes are assumed to form between H_3AsO_3 and ≡S-H, a neutrally charged species $\equiv S\text{-}H\text{-}H_3AsO_3$ and a positively charged species $\equiv S\text{-}H\text{-}H_4AsO_3^+$. The latter one might be very important at low to mid pH values in a reactive transport system in which the dissolution of mackinawite becomes rate limited.

Iron hydroxyl sites, ≡Fe-OH, are assumed to exist on the surface of iron (hydr)oxide and can take or release one proton to form positively or negatively charged surface sites. Two types of inner-sphere surface complexes are hypothesized to form between H_3AsO_3 and ≡Fe-OH, a neutrally charged species $\equiv Fe\text{-}O\text{-}H_2AsO_2$ and a negatively charged species $\equiv Fe\text{-}O\text{-}HAsO_2^-$. The latter complex behaves as extra sorption capacity for As(III) at very high pH conditions.

The total amount of surface sites associated with each mineral is related to the actual amount of the minerals in the system so that dissolution or precipitation of the minerals will change the total amount of available surface sites proportionally. In the case of mineral dissolution, adsorbed As(III) will also be released proportionally. This is a unique feature in PHREEQC for geochemical simulations combining mineral dissolution/precipitation and surface complexation.

Table 5.1 summarizes the important chemical reactions included in the conceptual model for the FeS-coated sand-As(III) system. Associated thermodynamic constants used in the equilibrium simulations are also listed. The mineral solubility constants are derived from the databases distributed with PHREEQC. The surface complexation constants are determined from the literature or obtained by fitting the batch experimental data of Task 1.

Table 5.1. Important chemical reactions in the FeS-coated sand-As(III) system.

	Reactions	lgK
Minerals		
Mackinawite	$FeS + H^+ = Fe^{2+} + HS^-$	-3.6[a]
Greigite	$Fe_3S_4 + 4H^+ = Fe^{2+} + 2Fe^{3+} + 4HS^-$	-45.035[a]
Magnetite	$Fe_3O_4 + 8H^+ = 2Fe^{3+} + Fe^{2+} + 4H_2O$	3.4028[a]
Orpiment	$As_2S_3 + 6H_2O = 2H_3AsO_3 + 3HS^- + 3H^+$	-46.3[b]
Surface Complexation – Mackinawite (Qmax_FeS = 0.0292[c] mol sites/mol FeS)		
	$\equiv S\text{-}H + H^+ = \equiv S\text{-}H_2^+$	lgKS1 = 8.8[c]
	$\equiv S\text{-}H = \equiv S^- + H^+$	lgKS2 = -7.2[c]
	$\equiv S\text{-}H + H_3AsO_3 = \equiv S\text{-}H\text{-}H_3AsO_3$	lgKS3 = 6.1[d]
	$\equiv S\text{-}H + H_3AsO_3 + H^+ = \equiv S\text{-}H\text{-}H_4AsO_3^+$	lgKS4 = 13.3[d]
Surface Complexation – Magnetite (Qmax_Fe_3O_4 = 0.0116[f] mol sites/mol Fe_3O_4)		
	$\equiv Fe\text{-}OH + H+ = \equiv Fe\text{-}OH_2^+$	lgKFe1 = 3.5[e]
	$\equiv Fe\text{-}OH + \equiv Fe\text{-}O^- + H^+$	lgKFe2 = -9.6[e]
	$\equiv Fe\text{-}OH + H_3AsO_3 = \equiv Fe\text{-}O\text{-}H_2AsO_2 + H_2O$	lgKFe3 = 5.41[d]
	$\equiv Fe\text{-}OH + H_2AsO_3^- = \equiv Fe\text{-}O\text{-}HAsO_2^- + H_2O$	lgKFe4 = 7.3[d]

[a] MINTEQ2 version 4 database
[b] WATEQ4F database
[c] Obtained by fitting the FeS-coated sand batch acid/base titration data without As(III) added
[d] Obtained by fitting the FeS-coated sand batch acid/base titration data with As(III) added
[e] (Marmier and Fromage, 2000)
[f] (Missana et al., 2003)

Estimation of Mineral Composition on FeS-Coated Sand Surface. Partial oxidation of mackinawite can occur on FeS-coated sand surfaces during storage or sample preparation for X-ray analysis. The mackinawite on the FeS-coated sand surface can also transform to iron (hydr)oxide minerals in alkaline solutions. In Task 1 (Subtask 1.1), XPS analysis of the FeS-coated sand surface identified two types of FeS-coated sand surface characteristics, one associated with FeS and another with Fe(III). The latter clearly suggested the presence of iron (hydr)oxides, which could be attributed to partial oxidation of mackinawite or iron (hydr)oxides in the natural sand. However, current surface analysis techniques could not differentiate between these or determine the exact type of iron (hydr)oxide mineral.

Fortunately, indirect evidence can be found from aqueous concentration measurements in batch experiments. In Subtask 1.4c, a set of batch experiments was conducted to measure the dissolved total iron concentration at different pH values by adding acid or base to vials containing 1g FeS-coated sand and 10 ml aqueous solution, assuming an equilibrium condition was reached after mixing for 24 hours. A subset of the chemical reaction model for the FeS-coated sand-As(III) system developed above was used to simulate the pH-dependent dissolution and precipitation behavior of the mineral mixture on the FeS coated sand surface in these experiments. It was assumed that the mineral mixture initially consists of mackinawite and one possible iron (hydr)oxide. Greigite was allowed to precipitate out when saturated. The measured iron concentration data were used to determine the most likely type of iron (hydr)oxide and estimate the initial amount of each mineral on the FeS-coated sand surface.

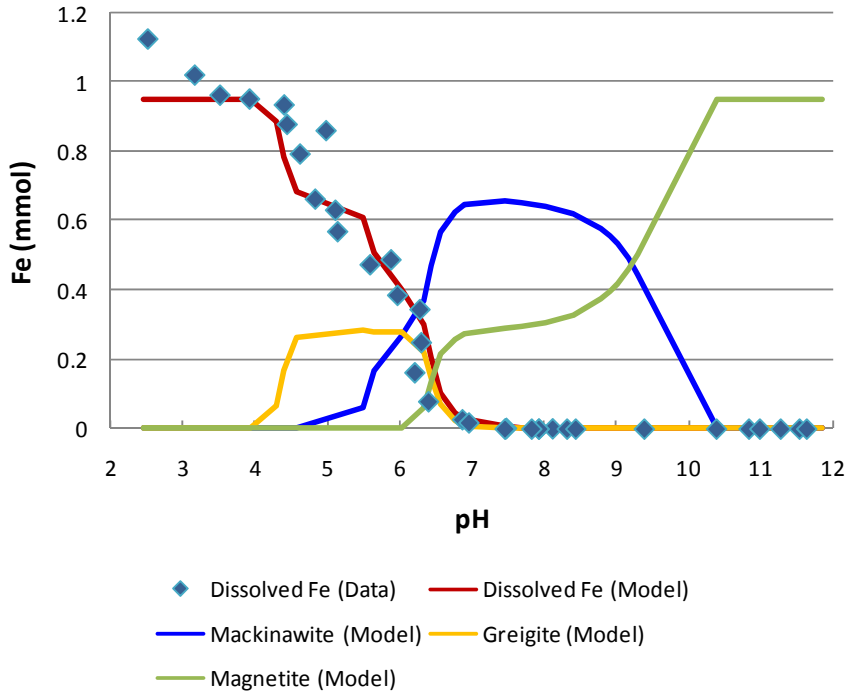

Figure 5.2. Distribution of iron in different phases in batch systems (1g FeS-coated sand in 10 ml solution).

A series of commonly observed iron (hydr)oxides, including goethite, lepidocrocite, ferrihydrite, hematite, magnetite, and maghemite, were used in equilibrium simulations to test against the experimental data. It was found that magnetite gave the best match to the dissolved iron concentration data consistent with the earlier analysis that indicated its presence. Figure 5.2 plots the model predicted distribution of iron in different phases, along with the measured concentrations of iron in the aqueous phase, when magnetite is assumed to be the iron (hydr)oxide on the FeS coated sand surface. The initial amounts of mackinawite and magnetite were estimated to be 6.7×10^{-6} mol/g FeS coated sand and 9.3×10^{-7} mol/g FeS-coated sand, with mackinawite accounting for approximately 70% of the total dissolvable iron on the FeS-coated sand surface.

Modeling pH-Dependent As(III) Removal by FeS-Coated Sand. The pH-dependent As(III) retention behavior by FeS-coated sand in batch systems was simulated by considering

precipitation as orpiment at low pH and sorption onto the FeS-coated sand surface at mid to high pH (see details above in the Model Formulation discussion). The sorption part was modeled as a non-electrostatic surface complexation process. A component additivity approach was adopted to explicitly simulate As(III) sorption onto both mackinawite and magnetite on the FeS-coated sand surface. The reactions and their thermodynamic constants for the SCM were listed in Table 5.1. For each mineral, the number of available surface sites (Qmax: mol sites/mol mineral), two thermodynamic constants for surface protonation and deprotonation, and two thermodynamic constants for formation of different As(III) surface species need to be determined.

Ideally, the number of available surface sites associated with each mineral can be estimated independently from surface analysis, and the surface protonation and deprotonation constants can be estimated independently from acid/base titration data of each pure mineral. However, due to the limitations of the analysis techniques used in this research and the difficulties in distinguishing the relative amounts of different minerals on the FeS coated sand surface, there was insufficient information to determine the Qmax of each mineral on FeS-coated sand. Therefore, to minimize the number of fitted parameters, the Qmax of mackinawite was estimated, together with the protonation and deprotonation constants (lgKS1 and lgKS2) of surface sites associated with mackinawite, based on the acid/base titration data of FeS-coated sand. The Qmax and protonation and deprotonation constants (lgKFe1 and lgKFe2) of magnetite were taken from literature (Marmier and Fromage, 2000; Missana et al., 2003), where the surface properties of pure magnetite had been studied in detail. The fitting parameter values were optimized by minimizing the difference between the measured pH and dissolved Fe concentration data and model predictions (see Figure 5.3A and Figure 5.3B).

Figure 5.4 presents the model predicted speciation of surface sites associated with mackinawite and magnetite on the FeS-coated sand surface under different pH conditions. Note that the amount of surface sites associated with mackinawite and magnetite dropped to zero with the complete dissolution of these minerals below certain pH levels (see Figure 5.2). However, for a flowing system in which mineral dissolution is not at equilibrium, there could still be significant amounts of mackinawite and magnetite at early times even at very low pH. Thus, adsorption to these mineral surfaces could be very important in controlling the reactive transport behavior of contaminants such as As(III) (detailed discussions can be found in Subtask 5.2).

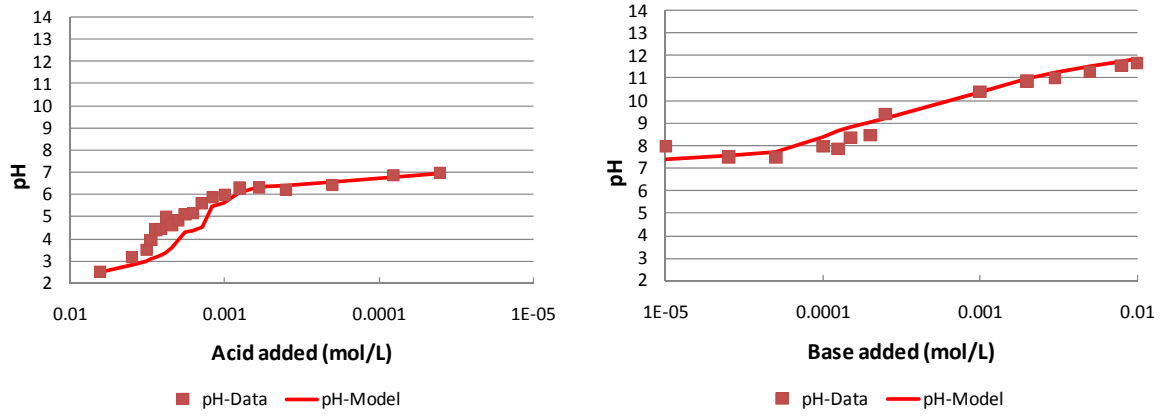

Figure 5.3A. Comparison of model predictions with measured pH data in the FeS-coated sand acid/base titration experiments (1g FeS-coated sand in 10 ml solution with no As(III) added).

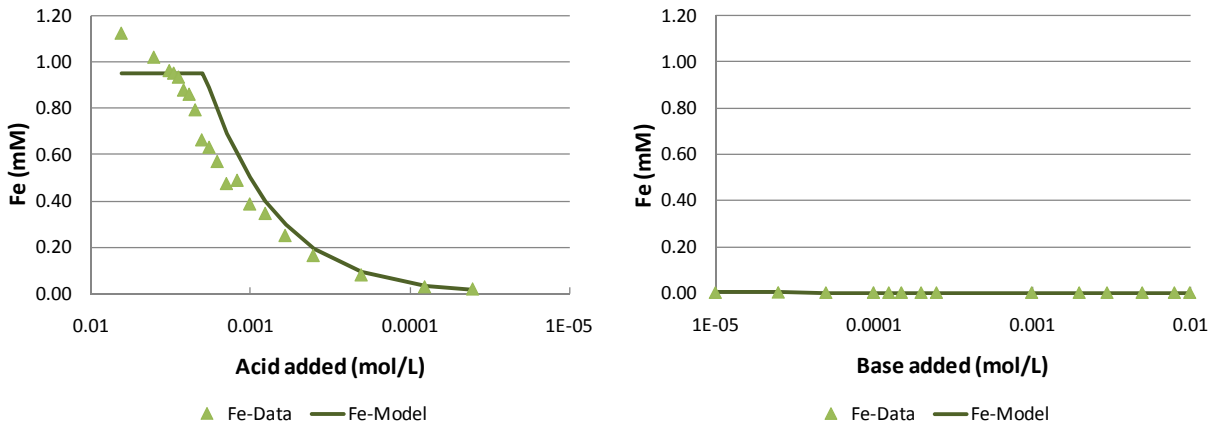

Figure 5.3B. Comparison of model predictions with measured dissolved Fe concentration data in the FeS-coated sand acid/base titration experiments (1g FeS-coated sand in 10 ml solution with no As(III) added).

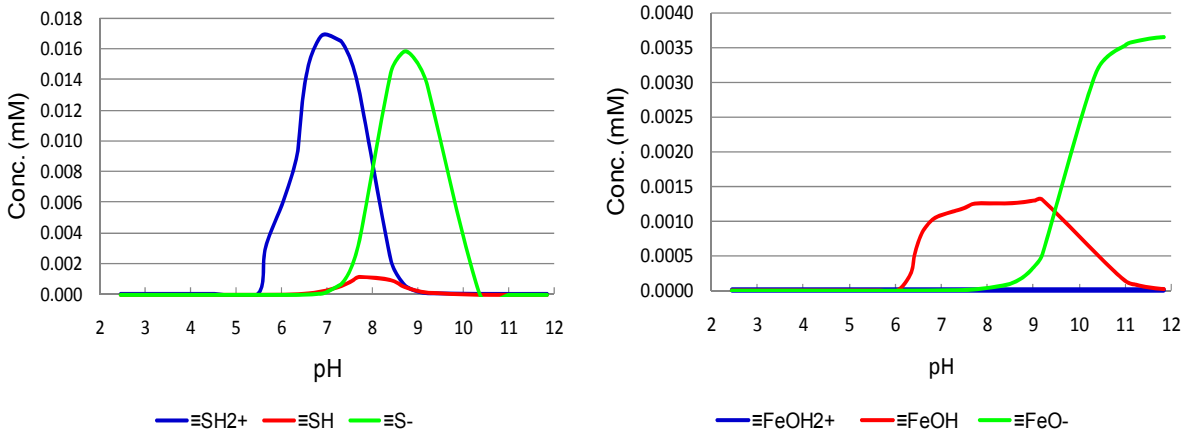

Figure 5.4. Model predicted pH-dependent speciation of surface sites associated with mackinawite and magnetite on the FeS-coated sand surface (1g FeS-coated sand in 10 ml solution with no As(III) added).

Similarly, another series of acid/base titration data with 1 ppm As(III) added to the batch system was used to estimate the thermodynamic constants for As(III) association to ≡S-H and ≡Fe-OH sites (see Table 5.1 for the parameter values). Figure 5.5 compares the measured data of As(III) concentrations remaining in the aqueous phase under different pH conditions with model predictions using the estimated FeS-coated sand parameters. Figure 5.6 plots the model-predicted As distribution in the aqueous, solid and adsorbed phases under different pH conditions in batch systems initially consisting of 1g FeS-coated sand and 10 ml of 1 ppm As(III) solution. The modeling results using estimated initial mineral amounts and SCM parameters were consistent with the hypothesis that As(III) can be removed by FeS-coated sand through precipitation as orpiment at low pH and adsorption at mid to high pH in batch systems.

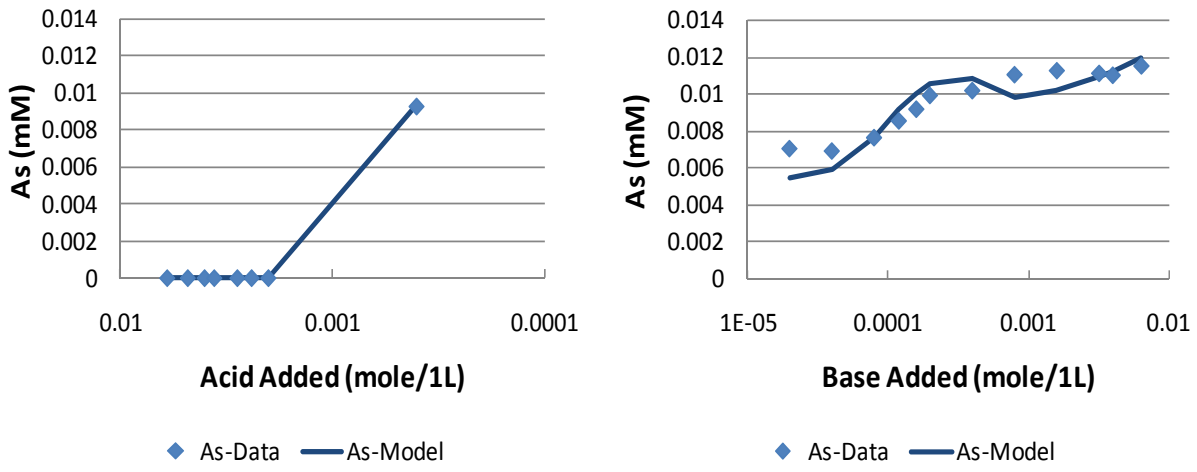

Figure 5.5. Comparison of model predictions with measured As concentration data in the FeS-coated sand acid/base titration experiments (1g FeS-coated sand in 10 ml solution with 1 ppm As(III) added).

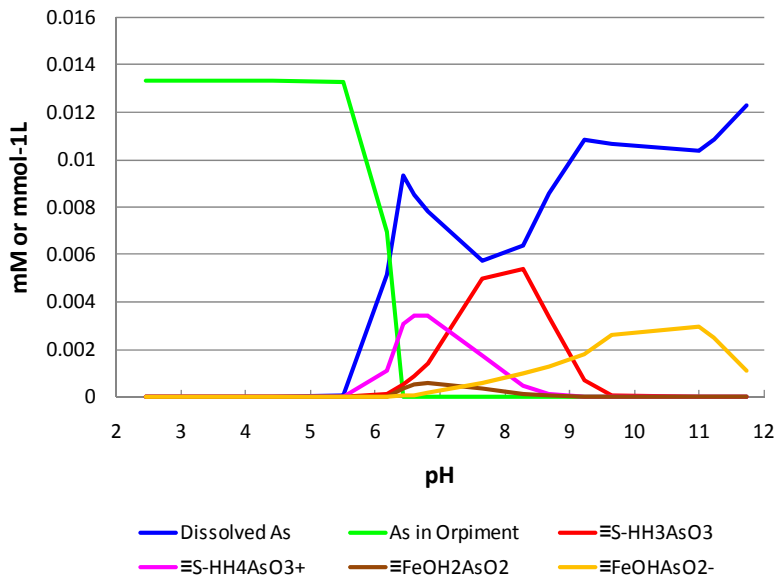

Figure 5.6. Model predictions of pH-dependent As distribution in different phases (1g FeS-coated sand in 10 ml solution with 1 ppm As(III) added).

Summary and Conclusions and Implications for Future Research/Implementation

In this study, a geochemical model was developed using PHREEQC to simulate As(III) retention by FeS-coated sand as a function of pH in batch systems. It was hypothesized that As(III) can be removed through precipitation as arsenic sulfide minerals at low pH, while at neutral to alkaline conditions, arsenite is primarily adsorbed to the MCS surface. The modeled chemical reactions in the Fe-As-S system included aqueous speciation, redox reactions, mineral dissolution/ precipitation, and a non-electrostatic SCM to account for pH dependent As(III) sorption. Also

considered was the oxidative transformation of mackinawite (FeS) to magnetite (Fe_3O_4) on the coated sand surface. A component additivity approach was adopted to simulate As(III) sorption through surface complexation onto both mackinawite and magnetite, which transform to each other with changing pH conditions. A nonlinear parameter estimation package PEST was used to estimate the initial amount of each mineral on the coated sand surface and SCM parameters based on data from batch experiments. Equilibrium modeling results with estimated parameters matched the batch reactor data well, suggesting that the proposed reaction mechanisms can satisfactorily explain the equilibrium retention behavior of As(III) by FeS-coated sand in batch systems.

The model developed in this study provides a quantitative tool for evaluating As(III) retention in FeS-controlled reducing environments as a function of pH and pe, and will be useful for designing and operating groundwater remediation systems targeting As(III) removal using FeS based systems. However, when applied in reactive transport modeling, rate limited processes such as kinetic mineral dissolution or kinetic sorption need to be considered and the related rate coefficients need to be derived from time series data of bench-scale column experiments or field measurements.

Literature Cited

Allison, J. D., et al., 1991. MINTEQA2/PRODEFA2, A Geochemical Assessment Model for Environmental Systems: Version 3.0 User's Manual, U.S. Environmental Protection Agency.

Davis, J. A., et al., 1998. Application of the Surface Complexation Concept to Complex Mineral Assemblages, *Environmental Science & Technology*, *32*(19), 2820-2828.

Doherty, J., 2004. PEST: Model-Independent Parameter Estimation User Manual: 5th Edition, Watermark Numerical Computing.

Marmier, N., and F. Fromage, 2000. Sorption of Cs(I) on Magnetite in the Presence of Silicates, *Journal of Colloid and Interface Science*, *223*(1), 83-88.

Missana, T., et al., 2003. Uranium (VI) sorption on colloidal magnetite under anoxic environment: experimental study and surface complexation modelling, *Geochimica et Cosmochimica Acta*, *67*, 2543-2550.

Parkhurst, D. L., and C. A. J. Appelo, 1999. PHREEQC (Version 2) - A Computer Program for Speciation, Batch-reaction, One-dimensional Transport, and Inverse Geochemical Calculations, U.S. Geological Survey.

Subtask 5.2. Investigation of Rate-limited Processes in Transport Systems

Objective

The objective of this subtask was to incorporate the reaction model developed in Subtask 5.1 into a 1-D multi-component reactive transport model to simulate the breakthrough of As(III) in FeS-coated sand column experiments and investigate rate-limited processes in the FeS-coated-As(III) system under flowing conditions.

Background

In this subtask, a 1-D multi-component reactive transport model was developed to simulate the advection, diffusion/dispersion, and reactions of As(III) in FeS-coated columns operated under different pH conditions (see Subtask 1.6 for details about the column experiments). The reaction model developed in Subtask 5.1 was incorporated into the reactive transport model to account for the interactions between As(III) and FeS-coated. Some of these reactions were modeled as kinetic reactions. The As(III) breakthrough data were used to estimate the rate coefficients. This 1-D model is a useful tool to study rate-limited processes in FeS-coated column systems. With calibrated parameters based on batch and column experiments, it can be further applied to larger scale simulations to study the long-term performance of FeS-coated based PRBs for remediation of arsenic contaminated groundwater under realistic field conditions.

Materials and Methods

1-D reactive transport modeling was conducted using the transport module in PHREEQC (Parkhurst and Appelo, 1999). In this module, the one dimensional governing equation for reactive solute transport under constant velocity and saturated groundwater flow conditions is solved by an operator splitting scheme. This scheme sequentially computes terms for advective and dispersive transport, and then callskinetic and equilibrium modules for evaluation of the reactions in each cell. The transport part is solved with an explicit finite difference scheme that is forward in time, central in space for dispersion, and upwind for advective transport. This transport module was coupled to the reaction model developed in Subtask 5.1, where dissolution of mackinawite, dissolution/precipitation of magnetite, and sorption of As(III) on mackinawite were modeled as rate limited processes. PEST (Doherty, 2004) was used with PHREEQC to estimate the rate coefficients in these kinetic reactions, based on the breakthrough data of As(III) in the FeS-coated column experiments operated at different pH conditions. Dispersivities used in the reactive transport simulations were obtained by fitting the analytical solution of the 1-D advective-dispersion equation to the conservative tracer data using CXTFIT (Toride et al., 1995).

Results and Discussion

Model Formulation. A 1-D reactive transport model was formulated using PHREEQC to simulate the column experiments conducted in Subtask 1.6. In a transport system where the local equilibrium assumption may not hold, kinetic expressions are needed for some rate-limited processes. For the FeS-coated-As(III) system, it was assumed that dissolution of mackinawite, dissolution/precipitation of magnetite and sorption of As(III) onto mackinawite are rate limited

under the flowing conditions in the columns (Figure 5.7). The precipitation of orpiment and greigite could also be rate-limited. However, due to the slow dissolution of mackinawite, the saturation of these two minerals was never reached in model simulations. In addition, there was a lack of evidence pointing to their formation in column experiments conducted in Subtask 1.6. Therefore, mineral equilibrium was assumed for greigite and orpiment, although these were never formed in model predictions of the FeS-coated column experiments.

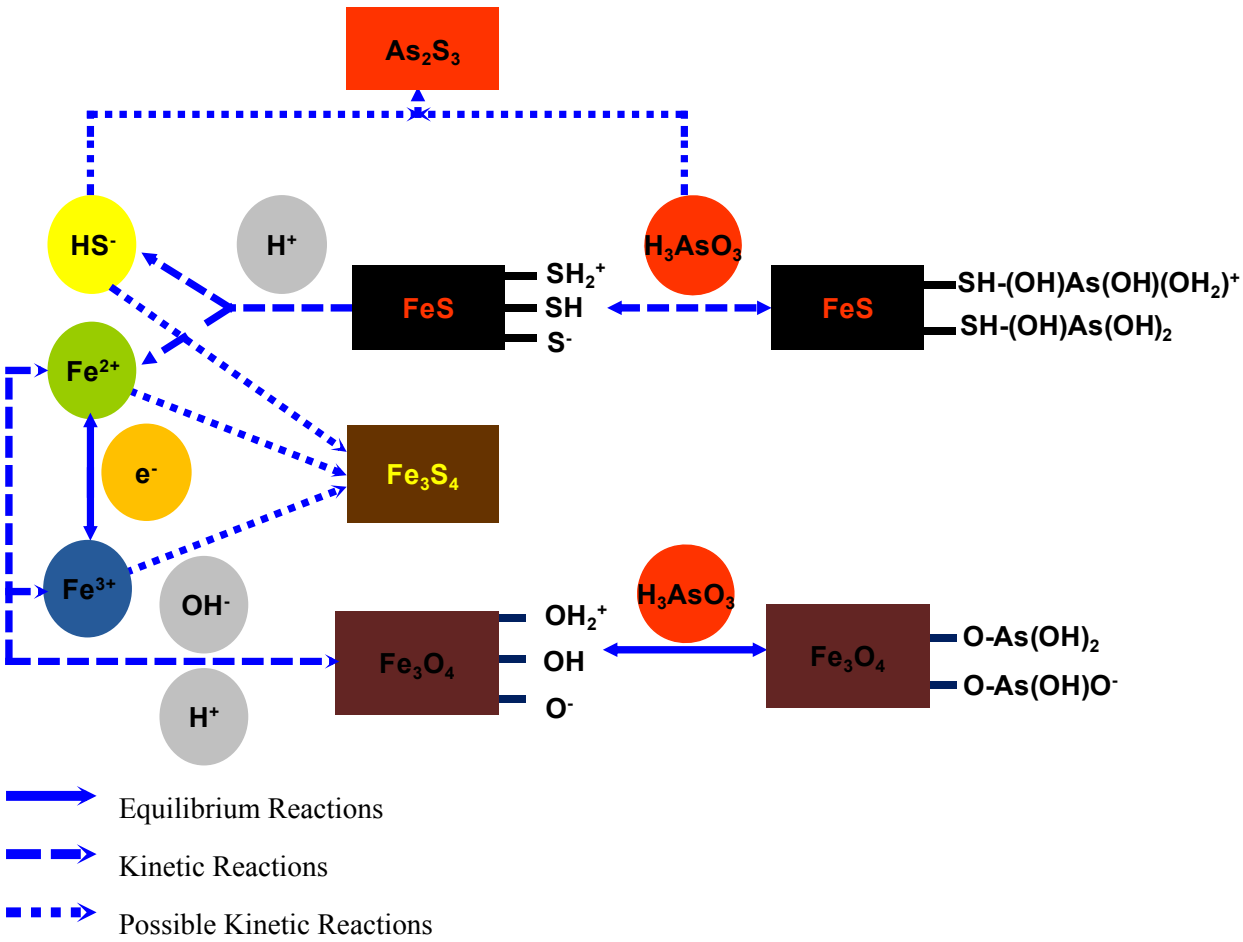

Figure 5.7. Reaction part of the reactive transport model for columns.

The rate expression employed for for kinetic mineral dissolution or precipitation in the model is:

$$r = -k_{eff}\left(1 - \frac{IAP}{K_{eq}}\right) \tag{5.1}$$

where r is the rate of the mineral dissolution/precipitation, k_{eff} (mol/L/s) is an effective rate coefficient, IAP and K_{eq} are the ion activity product and the solubility constant of the mineral, respectively. The ratio of IAP and K_{eq} represents the mineral saturation status. An advantage of this expression is that it applies for both supersaturation and undersaturation, and the rate is zero at equilibrium. The rate is relatively constant over a large range of conditions, whenever the

reaction is far from equilibrium (e.g., IAP/Keq<0.1), and the rate approaches zero when IAP/Keq approaches 1.0 (equilibrium).

An equilibrium-kinetic two-site model (Selim and Amacher, 1988) was used to simulate the rate-limited adsorption of As(III) onto mackinawite in FeS-coated sand columns. It was assumed that surface sorption sites associated with mackinawite on FeS-coated sand can be divided evenly into two types, i.e. fast equilibrium sorption sites and slow kinetic sorption sites, and that the equilibrium As(III) sorption behavior for both types of sites can be described by the same surface complexation constants derived from the batch data. For the kinetic sorption part, e.g., the formation of neutrally charged surface As(III) species (equation 5.2), the net reaction rate was modeled as:

$$rate = k_{f1} \times [\equiv FeSH] \times [H_3AsO_3] - k_{b1} \times [\equiv FeSH_4AsO_3] \qquad (5.2)$$

where [≡FeSH], [H_3AsO_3], and [≡$FeSH_4AsO_3$] are the concentration of aqueous and surface species, k_{f1} (L/mol/s) and k_{b1} (1/s) are the forward and backward rate coefficients, and the ratio of k_{f1} and k_{b1} is determined by the thermodynamic constant KS3 of this surface complexation reaction, i.e.

$$KS3 = \frac{k_{f1}}{k_{b1}} \qquad (5.3)$$

A local equilibrium assumption was applied to As(III) sorption onto surface sites associated with Fe_3O_4 on MCS.

Determination of Dispersivities. Bromide was used as a conservative tracer in all column experiments before injecting As(III)-containing solutions (see Subtask 1.6 for details). CXTFIT was used to fit the dispersivity to the Bromide breakthrough data in each column (Table 5.2). The obtained dispersivity values were consistent among the different columns.

Table 5.2 Dispersivities in Column Experiments

	Col#1	Col#4	Col#2	Col#3	Col#6	Col#5
pH	5	5	7	9	9	9
Length (cm)	15	4.8	15	15	4.8	4.8
Inner Diameter (cm)	4.8	4.8	4.8	4.8	4.8	4.8
Mass of MCS (g)	271.43	86.86	271.43	271.43	86.86	86.86
Porosity[a]	0.35	0.35	0.34	0.34	0.35	0.35
Flow Rate (ml/hr)	28	26	28	28	8.8	26
Dispersivity[b] (cm)	0.09	0.08	0.06	0.08	0.14	0.08

[a] Estimated based on MCS mass assuming the density of MCS is 2.65g/cm3
[b] Fitted to Br- tracer data

Simulation of As(III) Breakthrough in MCS Columns. Although 7 column experiments were conducted under different conditions in Task 1, only the two short, fast flow rate columns at pH 5 and 9 (i.e., Col#4 and Col#5) were used to estimate the rate coefficients for the kinetic

reactions described above. These experiments were selected, based upon the consistency of their flow and initial chemical conditions.

Figure 5.8 presents a comparison of the model simulated As(III) breakthrough curve with experimental data in the in Col#5, where adsorption onto the MCS surface is believed to be the primary mechanism for As(III) retention. At pH 9, the dominant As(III) surface species on mackinawite is the neutrally charged $\equiv$S-H-H_3AsO_3. The rate coefficient for $\equiv$S-H-H_3AsO_3 desorption (k_{b1}) was estimated to be 1.5×10^{-5} s^{-1}, based on the As(III) breakthrough data, and the forward reaction rate coefficient k_{f1} was calculated to be 18.88 L/mol/s, based on equation 5.3 above. The estimated mineral dissolution/precipitation rate for mackinawite and magnetite were 1×10^{-12} mol/L/s and 1×10^{-14} mol/L/s.

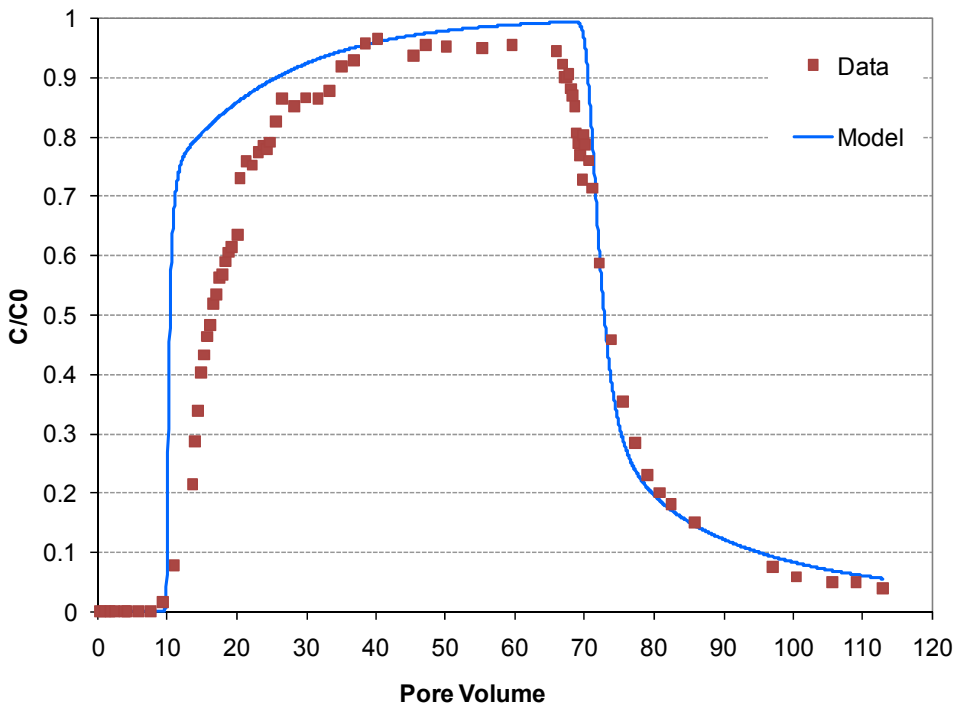

Figure 5.8. Comparison of As(III) breakthrough data with model predictions in Col#5.

In low pH columns, the rate-limited processes are much more complicated. For Col#4, the formation of orpiment was not predicted because the concentration of HS^- released to the aqueous phase due to slow dissolution of mackinawite was not high enough to reach its solubility. Increasing the assumed mackinawite dissolution rate caused orpiment formation near the end of the column, but the predicted breakthrough curve had a much lower plateau and much earlier breakthrough in comparison with the data.

In fact, due to the slow dissolution rate, a significant amount of mackinawite can remain in the column for quite a long time. Therefore, formation of positively charged As(III) species ($\equiv$S-H-$H_4AsO_3^+$) on mackinawite becomes very important, which was also clearly indicated by the shape of the breakthrough data. However, application of the batch model parameters derived in Subtask 5.1 in the two-site sorption model was unable to match the delayed breakthrough of As(III) in Col#4.

During the Col#4 experiment, pH 5 buffer solution without As(III) was flushed through the column for a period of time to allow the flow conditions in the column to reach a steady state before switching to As(III) containing solution. It is hypothesized that during this conditioning period the surface properties of FeS-coated sand might have been modified. For example, more surface sites might have been activated on mackinawite. The thermodynamic constant of ≡S-H-$H_4AsO_3^+$ (lgKS4) might also be different from what was obtained from batch equilibrium experiments. Using a larger fitted value for lgKS4 (15.3) and fitted rate coefficients for the formation of ≡S-H-$H_4AsO_3^+$ (k_{f2} = 3.0x10^8 L^2/mol^2/s, k_{b2} = 1.5x10^{-7} s^{-1}), the simulated As(III) breakthrough curve in Col#4 matched the data almost perfectly (Figure 5.9).

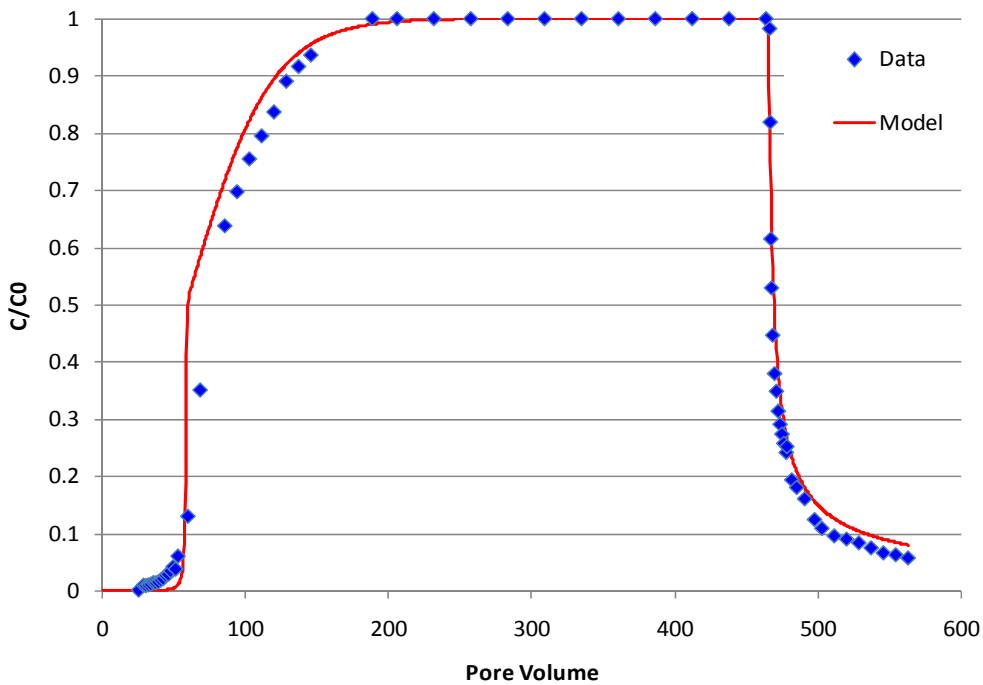

Figure 5.9. Comparison of As(III) breakthrough data with model predictions in Col#4.

<u>Summary and Conclusions and Implications for Future Research/Implementation</u>

A 1-D multi-component reactive transport model was developed in this subtask to simulate column experiments conducted under different pH conditions and to investigate rate-limited processes, such as kinetic mineral dissolution/precipitation and kinetic sorption in the FeS-coated sand-As(III) system under flowing conditions. Rate coefficients were fit to the column breakthrough data.

Simulation of As(III) breakthrough in the column experiments met with mixed success. For high pH columns, sorption onto MCS is the primary As(III) retention mechanism. By applying a kinetic-equilibrium 2-site model for As(III) sorption onto mackinawite and assuming equilibrium for all other surface complexation reactions, the As(III) breakthrough in Col#5 was successfully reproduced. For low pH columns, the association constant for ≡S-H-$H_4AsO_3^+$ had to be changed to obtain a good match to the Col#4 breakthrough data. To explain this discrepancy, it was hypothesized that the surface properties of MCS might have been modified during the conditioning period.

It is evident from this study that rate-limited processes are very important in a reactive transport system and that kinetic sorption tends to be the controlling mechanism for As(III) retention by FeS-coated sand under low pH conditions. More information on the reacted FeS-coated sand in the column experiments is needed to further constrain the components and rate expressions in the model.

The reactive transport model with estimated equilibrium and kinetic parameters based on batch and column experiments can be used in larger-scale simulations for performance evaluation of FeS coated sand-based PRBs for remediation of arsenic contaminated groundwater under field conditions (see Subtask 5.3 for details).

Literature Cited

Doherty, J., 2004. PEST: Model-Independent Parameter Estimation User Manual: 5th Edition, Watermark Numerical Computing.

Parkhurst, D. L., and C. A. J. Appelo, 1999. PHREEQC (Version 2) - A Computer Program for Speciation, Batch-reaction, One-dimensional Transport, and Inverse Geochemical Calculations, U.S. Geological Survey.

Selim, H. M., and M. C. Amacher, 1988. A second-order kinetic approach for modeling solute retention and transport in soils, *Water Resources Research*, *24*(12), 2061-2075.

Toride, N., et al., 1995. The CXTFIT code for estimating transport parameters from laboratory or field tracer experiments (Version 2), U. S. Salinity Laboratory, USDA, ARS, Riverside, CA.

Subtask 5.3 Field-scale Simulation for Long-term Performance Evaluation of FeS-coated Sand Based PRBs

Objective

The objective of this subtask is to develop a 2-D/3-D field-scale multi-component reactive transport model to evaluate the long-term performance of FeS-coated sand based PRBs for remediation of a realistic arsenic plume in groundwater.

Background

In this subtask, the model developed and validated in Subtasks 5.1 and 5.2 was implemented in 2-D simulations to evaluate the long-term performance of field-scale PRBs. A 2-D/3-D reactive transport model is an important and necessary extension of the established batch and 1-D models for design and field-scale application of the proposed FeS-coated sand PRB. A typical subsurface environment is highly heterogeneous in chemical and physical characteristics. These heterogeneities will lead to uneven contaminant flux loading along the barrier. Furthermore, barrier emplacement will inevitably be imperfect, leading to some variations in the initial physical and, possibly, geochemical conditions within the barrier. It is also anticipated that precipitation/dissolution reactions will further likely lead to preferential flow behavior and change of barrier reactivity. The application of a 2-D/3-D model can facilitate the examination of these effects under site-specific hydrogeological and geochemical settings and help in the design of more robust barrier configurations.

Materials and Methods

Modeling Tools. PHAST (Parkhurst et al., 2005), a modeling tool for multi-component, reactive solute transport in three-dimensional saturated ground-water flow systems developed by U.S. Geological Survey, was used for the 2-D field-scale simulations in this subtask. PHAST uses a non-iterative operator-splitting scheme to solve reactive transport problems by coupling HST3D (Kipp, 1987; 1997), a three-dimensional heat and solute transport code, and PHREEQC-2 (Parkhurst and Appelo, 1999), a general-purpose, comprehensive geochemical model for thermodynamics-based equilibrium reactions and programmable kinetic reactions.

Numerical simulation of ground-water flow and solute transport with geochemical reactions is often computationally intensive. The geochemical calculations usually require 90 to 99 percent of the CPU time. Therefore, a parallel version of PHAST developed by USGS was compiled using GNU Fortran Compiler with Open MPI (Message Passing Interface) on the Tufts Linux Research Cluster. The cluster is comprised of 49 identical IBM Linux systems (compute nodes) interconnected via an Infiniband network. Each cluster node has eight 2.8Ghz Intel Xeon CPUs and 16 or 32 gigabytes of memory for a total of 392 compute cores. The computational efficiency was greatly improved by running simulations with the parallel version of PHAST on the cluster.

PHAST assumes time-invariant material properties, including porosity and hydraulic conductivity, based upon the specified initial conditions in the model domain. This assumption of time invariance may not be valid if there is significant change in the volume of non-aqueous phases, due to such processes as mineral dissolution/precipitation or gas generation. To address

this concern, the source code of PHAST was modified to account for time-varying porosity and permeability. The data structures of both equilibrium and kinetic reactants were modified to facilitate tracking of the volume changes of related non-aqueous phases during each time-step. Based upon these volume changes, the porosity and permeability fields are then updated according to a user-specified model (e.g. the Carman-Kozeny equation). The kinetic module was also modified so that spatial and temporal changes of pore velocity and porosity can be accounted for in the calculation of some of the rate coefficients (e.g. mass transfer coefficient for NAPL dissolution).

In addition, the output option for the scientific data storage format, the Hierarchical Data Format (HDF) adopted in PHAST was enabled by compiling the source code with the current HDF5 package (Version 1.8.2). The source code was further modified to allow selective porosity and hydraulic conductivity output at specified time steps in HDF format.

Simulation Scenarios. To introduce realistic arsenic contamination features to the numerical study, the Saco Municipal Landfill Site in Maine (Nielsen et al., 1995; Stollenwerk and Coleman, 2003; 2004) was used as a reference site. Naturally occurring arsenic is often strongly bonded to mineral oxides such as iron hydroxides in soil and bedrocks in the New England area. Leachate seeping from the Area 4 at the site had formed a plume rich in dissolved organic compounds. Natural degradation of the dissolved organic compounds by microorganisms using iron hydroxides as electron acceptors had resulted in the release of arsenic into groundwater. A two-dimensional profile (cross-sectional) model domain was created based on the geological profile in Area 4. The flow and reactive transport of solutes in groundwater were modeled using PHAST so that the process of reductive dissolution of iron hydroxides and subsequent release of arsenic can be simulated numerically. A FeS coated sand-based PRB was then inserted downstream to intercept and treat the arsenic plume. Note that the purpose of this modeling study was not to exactly reproduce the site in a numerical model, but rather to use the features of a typical site that has arsenic contamination problems to create realistic field conditions for evaluation of the long-term performance of PRBs.

Factors that might negatively affect PRB performance were studied through model simulations of different scenarios, including aquifer heterogeneity, non-uniform distribution of iron hydroxides, desorption of organic compounds from aquifer materials, and non-ideal packing conditions in the barrier. Geostatistical methods were used to generate the heterogeneous permeability field and non-uniform distribution of minerals for the model domain.

Results and Discussion

Code Modification & Validation for Time-Varying Porosity and Permeability Change. The versatile capabilities of the embedded geochemical algorithms in PHREEQC suggest that PHAST may be more suitable for modeling systems of complex reactions in FeS coated sand-PRBs than the all-kinetic-approach of RT3D or a fully-implicit reactive transport code such as MIN3P. However, as a single-phase flow simulator, PHAST is not appropriate for unsaturated-zone flow, multiphase flow, density-dependent flow, or solutions with high ionic strength. More importantly, PHAST, like most other computer programs, does not account for the potential changes of porosity and hydraulic conductivity due to chemical reactions involving mineral phases. Therefore, the source code of PHAST was modified so that time-varying porosity and permeability can be calculated based on equilibrium or kinetic reactions.

As illustrated in Figure 5.10, three major steps were involved to accomplish this goal. First, the simulation sequence of PHAST was modified to allow re-calculation of the flow field using the updated porosity and hydraulic conductivity fields. Second, volume changes of mineral phases were incorporated into the geochemical reaction part (i.e., PHREEQC) by modifying the data structures of both equilibrium and kinetic reactants. Third, extra subroutines were added to optionally update the porosity field based on the volume changes of mineral phases. The porosity change information was then employed to update hydraulic conductivity values based on porosity-hydraulic conductivity relationships.

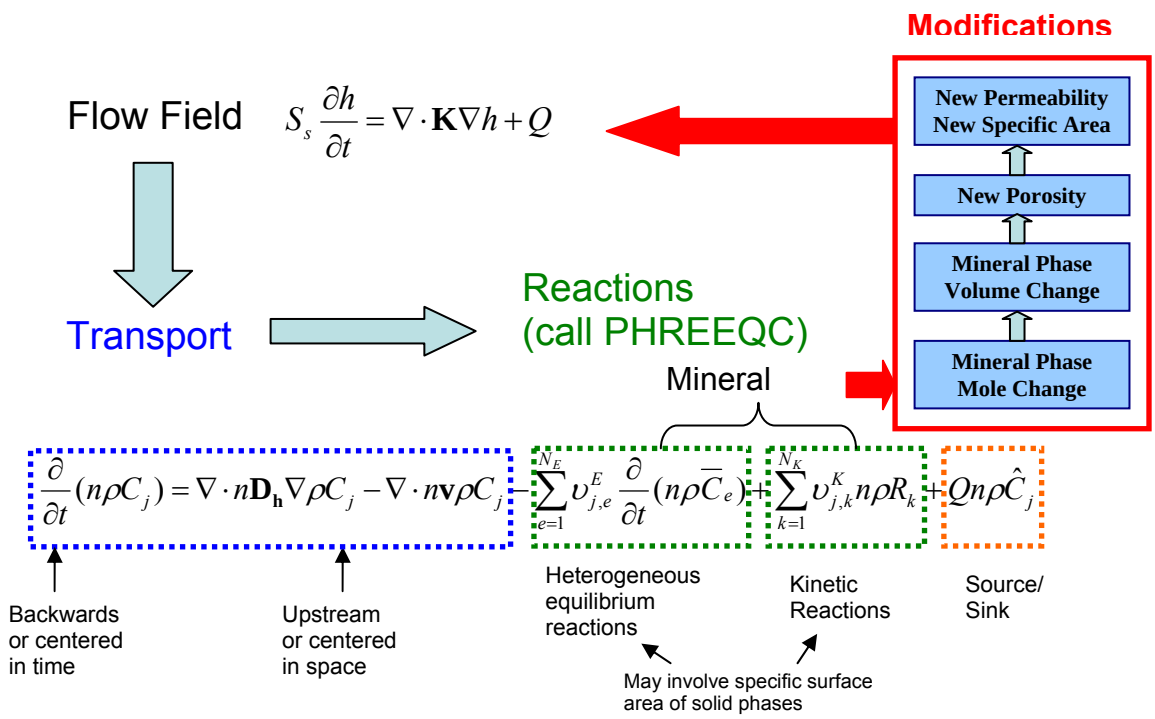

Figure 5.10. Flowchart of PHAST algorithm and modifications.

Assuming the porous medium is comprised of only solid minerals and pore space, the porosity can be calculated from the volume fractions of minerals

$$n = 1 - \sum_{m=1}^{nm} fr_m - fr_u \tag{5.4}$$

where n is porosity, fr_m is the volume fraction of reactive minerals m, fr_u is the total volume fraction of unreactive minerals and nm is the number of reactive minerals. The porosity change can then be obtained from the volume fraction change of reacted minerals

$$\Delta n = -\sum_{m=1}^{nm} \Delta fr_m \tag{5.5}$$

Ignoring changes in grain size, tortuosity and specific surface area, the change of hydraulic conductivity can be derived from the porosity change using a modified Carman-Kozeny equation and as:

$$K_t = K_0 \frac{n_t^{\ 3}}{n_0^{\ 3}} \frac{(1-n_0)^2}{(1-n_t)^2} \tag{5.6}$$

where subscripts *0* and *t* represent initial and changed hydraulic conductivities and porosities. A critical value of porosity n_c, at which hydraulic conductivity reduces to zero, can be incorporated into the hydraulic conductivity-porosity relationship to account for the complex effects of pore size distribution, pore space geometry, distribution of mineral precipitates in the pore space, and pore connectivity:

$$\frac{K_t}{K_0} = \left(\frac{n_t - n_c}{n_0 - n_c} \right)^{\varphi} \tag{5.7}$$

where the power law exponent φ and the critical porosity n_c are system dependent.

The modified PHAST code was validated using data from a field ZVI PRB site, Moffett Federal Airfield in Mountain View, CA (Li et al., 2006). The changes of inorganic chemistry and porosity/permeability caused by iron corrosion and subsequent mineral precipitation were simulated in one dimension, using a mixed equilibrium and kinetic reaction model. The simulated profiles of pH and major inorganic component concentration in groundwater were in good agreement with the field observed data (Figure 5.11). Predictions of the extent and distribution of mineral precipitation along the ZVI PRB were also consistent with the field observations, where most mineral precipitation concentrated near the influent and iron oxide

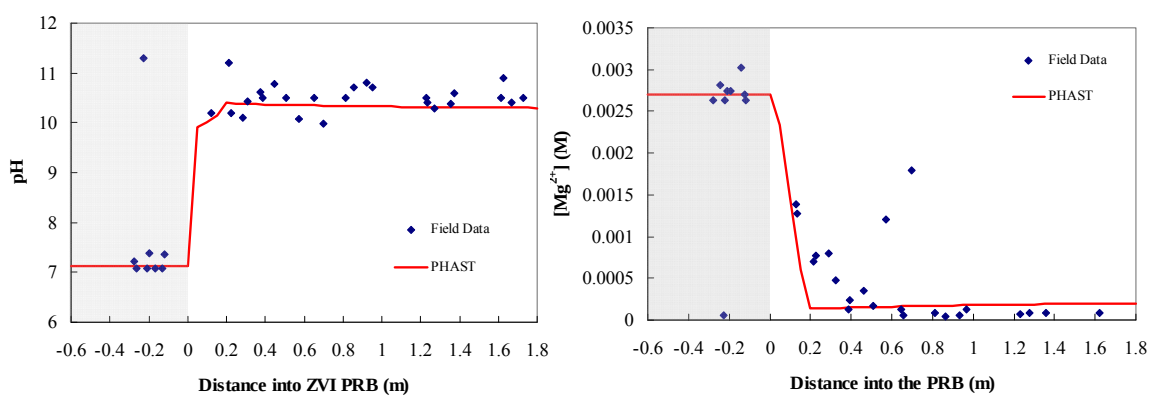

Figure 5.11. 1-D Simulation using data from a field ZVI PRB Site (Moffett Federal Airfield in Mountain View, CA) using a mixed equilibrium and kinetic reaction model for iron corrosion and subsequent mineral precipitation.

minerals were distributed along the entire length (in the direction of flow) of the PRB. The greatest porosity reduction was predicted to be approximately 0.02 near the PRB inlet after 1 year of operation, which was within the estimated range of 0.015-0.03 per year based on field core samples. Good agreement was also obtained when the modified program was applied to simulate a ZVI column experiment using field groundwater at the site of Y-12 National Security Complex in Oak Ridge, TN (Yabusaki et al., 2001).

The modified PHAST simulator was also applied to investigate the reactivity change in granular ZVI materials used in PRBs. A new ZVI reactivity model was used to account for both reactivity reduction, due to surface passivation caused by mineral coating, and initial enhancement by iron corrosion products such as amorphous iron oxides. The model was validated by simulation of the ZVI column experiments conducted by (Jeen et al., 2007). The simulated trichloroethylene profiles were in good agreement with the published data (Figure 5.12).

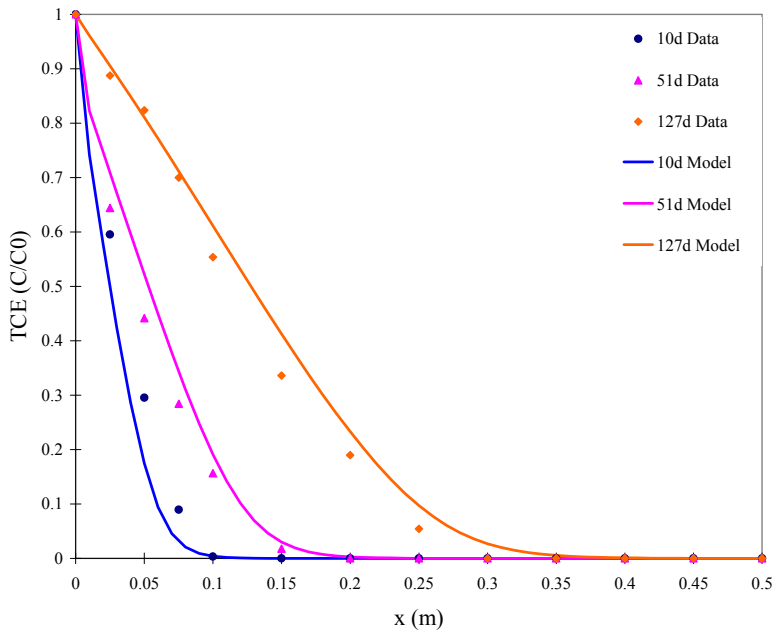

Figure 5.12. Comparisons of model predictions with measured trichloroethylene profiles in a ZVI column experiment conducted by Jeen et al. (2007).

Numerical Simulation of FeS-coated sand-based PRBs for Long-Term Performance Evaluation. A two-dimensional (cross-sectional) model was formulated based on the hydrogeological and geochemical features in Area 4 of Saco Municipal Landfill Site, Maine. Reductive dissolution of iron hydroxides and subsequent release of arsenic was simulated so that an arsenic plume was numerically generated. Then a FeS coated sand-based PRB was inserted downstream in the model. Numerical studies of its long-term performance in different scenarios are still in progress.

Summary and Conclusions and Implications for Future Research/Implementation

With the capabilities of the modified PHAST code, the treatment efficiency and long-term performance of FeS-coated sand-based PRBs can be simulated numerically based on realistic

arsenic contamination scenarios and mechanisms described from laboratory experiments. Results from this study can also provide guidance for the design and maintenance of FeS-coated sand PRBs under site-specific hydrogeological and geochemical conditions. Questions such as the risk of releasing immobilized arsenic from the barrier after the plume is treated and when to excavate the depleted reactive material can also be answered from the numerical studies.

Literature Cited

Jeen, S. W., et al., 2007. Reactive transport modeling of trichloroethene treatment with declining reactivity of iron, *Environmental Science and Technology*, **41**, 1432-1438.

Kipp, K. L., 1987. HST3D—A computer code for simulation of heat and solute transport in three-dimensional ground-water flow systems, 517 pp, U.S. Geological Survey, Denver, Colorado.

Kipp, K. L., 1997. Guide to the revised heat and solute transport simulator HST3D - Version 2, 149 pp, U.S. Geological Survey, Denver, Colorado.

Li, L., et al., 2006. Modeling porosity reductions caused by mineral fouling in continuous-wall permeable reactive barriers, *J. Contam. Hydrol.*, **83**, 89-121.

Nielsen, M. G., et al., 1995. Geohydrology, Water Quality, and Conceptual Model of the Hydrologic System, Saco Landfill Area, Saco, Maine, 94 pp, U.S. Geological Survey.

Parkhurst, D. L., and C. A. J. Appelo, 1999. PHREEQC (Version 2) - A Computer Program for Speciation, Batch-reaction, One-dimensional Transport, and Inverse Geochemical Calculations, U.S. Geological Survey.

Parkhurst, D. L., et al., 2005. PHAST—A program for simulating ground-water flow, solute transport, and multicomponent geochemical reactions, 154 pp, U.S. Geol. Surv.

Stollenwerk, K. G., and J. A. Coleman, 2003. Natural remediation potential of arsenic-contaminated ground water, in *Arsenic in Ground Water: Geochemistry and Occurrence*, edited by A. H. Welch, Stollenwerk, K. G, pp. 351-379, Kluwer Academic Publishers, Boston, MA.

Stollenwerk, K. G., and J. A. Coleman, 2004. Natural Remediation of Arsenic Contaminated Ground Water Associated With Landfill Leachate, 4 pp, U.S. Geological Survey.

Yabusaki, S., et al. (2001), Multicomponent reactive transport in an in situ zero-valent iron cell, *Environmental Science & Technology*, **35**, 1493-1503.

Appendix A. Supporting Data

All data contained in this report (Figures and Tables) were deemed sufficient for archiving the results of this project.

Appendix B. List of Scientific/Technical Publications

Dissertations:

Gallegos, T.J., "Sequestration of As(III) by Synthetic Mackinawite under Anoxic Conditions," Ph.D. Dissertation, Department of Civil and Engineering, University of Michigan, August 2007.

Lee, Jun Hee, "Chemical Optimization of in situ emplacement of nano-particulate iron sulfide in porous media, Ph.D. Dissertation, Department of Civil and Engineering, University of Michigan, December 2008.

Han, Y.-S., "Iron-Coated Sand for Remediation of Arsenic(III)-Contaminated Anoxic Groundwater," Ph.D. Dissertation, Department of Civil and Engineering, University of Michigan, expected August 2009.

Wang, Li., "Long-term Performance Evaluation of FeS-coated Sand Based Permeable Reactive Barriers for Remediation of Arsenic Contaminated Groundwater Using Reactive Transport Modeling," Ph.D. Dissertation, Department of Civil and Engineering, Tufts University, expected August 2009.

Henderson, A., "Extending Long Term Performance of Permeable Reactive Barriers with Modified Reative Media Material," Ph.D. Dissertation, Department of Civil and Engineering, University of Michigan, expected December 2009.

Journal Papers:

1. Gallegos, T.J., S.P. Hyun, and K.F. Hayes, "Spectroscopic and Macroscopic Investigation of the Uptake of Arsenic from Solution by Mackinawite," *Environmental Science and Technology*, 41, 7781-7786, 2007.
2. Henderson, A.D., and A. H. Demond, "Long-term performance of zero-valent iron permeable reactive barriers: A critical review," *Environmental Engineering Science* 24, (4): 401-423, 2007.
3. Jeong, H.Y., J.H. Lee, and K.F. Hayes, "Characterization of Synthetic Nanocrystalline Mackinawite: Crystal Structure, Surface Area, and Particle Size Determination," *Geochimica et Cosmochimica Acta*, 72, 493-505, 2008.
4. Gallegos, T.J., Y.-S. Han, and K.F. Hayes, "Model Predictions of Realgar Precipitation by Reaction of As(III) with Synthetic Mackinawite Under Anoxic Conditions," *Environmental Science and Technology*, 42, 9338-9343, 2008.
5. Renock, D., T.J. Gallegos, S. Utsunomiya, K.F. Hayes, R.C. Ewing, and U. Becker, "Chemical and Structural Characterization of As Immobilization by Nanoparticles of Mackinawite (FeS_m)," *Chemical Geology*, accepted, 2009.
6. Han, Y.-S., T.J. Gallegos, A.H. Demond, and K.F. Hayes, "FeS Coated-Sand for Removal of Arsenic(III) Under Anaerobic Conditions: Coating Method and Characterization," *Water Research*, in review, 2009.
7. Jeong, H.Y., S.W. Park, and K. F. Hayes, "Impact of aerobic oxidation of mackinawite (FeS) on sorbed arsenic mobilization," *Environmental Science and Technology*, in review, 2009.
8. Jeong, H.Y., and K.F. Hayes, "An x-ray absorption spectroscopy (XAS) study of arsenic mobilization during mackinawite (FeS) oxidation," *Environmental Science and Technology*, in review, 2009.

Conference Proceedings, Abstracts, and Poster Presentations

1. Gallegos, T.J. (invited), Hayes, K.F.; L.M. Abriola, "Reactive Ferrous Sulfide/Ferric Oxide Multilayer Films for Remediation of Arsenic Contaminated Groundwater," *Society of Hispanic Professional Engineers National Technical and Career Conference*, Dallas, TX, January 2005 (2nd Prize Graduate Student Paper Award).
2. Gallegos, T.J., K.F., Hayes, and L.M. Abriola, "Sorption of Arsenite onto Mackinawite Coated Sand," *EGS-AGU-EUG Joint Assembly*, May 17, 2005, Montreal, Canada.
3. Gallegos, T.J., K.F. Hayes, and L.M. Abriola, "Deposition and characterization of nanoparticulate FeS on quartz surfaces for remediation of As(III) contaminated groundwater," *79th American Chemical Society Colloid and Surface Science Symposium*, Potsdam, NY, June 12-15, 2005.
4. Gallegos, T.J., K.F. Hayes, and L.M. Abriola, "Uptake of As(III) by nanoparticulate mackinawite," *230th American Chemical Society National Meeting*, Washington DC, August 28-September 1, 2005 (Certificate of Merit Award).
5. Gallegos, T.J., K.F. Hayes, L. M. Abriola, "Remediation of As(III) contaminated groundwater by nanoscale FeS," *Partners in Environmental Science and Technology Technical Symposium and Workshop*, Washington, D.C., Nov. 29-30, 2005 (Poster).
6. Lee, J.H.; Olson, T.M. "Optimization of colloidal injection methods for effective introduction and dispersal of nanoscale FeS in porous media," *Partners in Environmental Science and Technology Technical Symposium and Workshop*, Washington, D.C., Nov. 29-30, 2005 (Poster).
7. Vannela, R., P. Adriaens and K. F. Hayes, "Geomicrobiological Regeneration of Iron Sulfides in Engineered barrier Systems," *American Geophysical Union Fall Conference*, 5–9 Dec 2005, San Francisco, CA.
8. Gallegos, T. J., K. F. Hayes, L.M. Abriola, and K. Baldwin "Mackinawite-Coated Sand for Remediation of Arsenite Contaminated Groundwater," *231st American Chemical Society National Meeting,* Atlanta GA, March 26 – 30, 2006.
9. Renock, D., T. J. Gallegos, U. Becker, K. F. Hayes, S. Utsunomoyia, R. Ewing, "STEM and SFM Characterization of As-Containing nanoscale phases on iron sulfides," *231st American Chemical Society National Meeting,* March 26 – 30, 2006. Atlanta GA.
10. Gallegos, T. J., and K. F. Hayes "Modeling As(III) Uptake by Synthetic Mackinawite," *231st American Chemical Society National Meeting,* Atlanta GA, March 26 – 30, 2006.
11. Henderson, A. D.; Demond, A.H. "Long-term performance of permeable reactive barriers," *231st American Chemical Society National Meeting,* Atlanta GA, March 26 – 30, 2006.
12. Lee, J. H., and T.M. Olson, "In situ emplacement of nano-sized FeS in porous media: Chemical optimization," *231st American Chemical Society National Meeting,* Atlanta GA, March 26 – 30, 2006.
13. Gallegos, T.J., K.F. Hayes, and L.M. Abriola, "Mackinawite-Ferrihydrite Coated Sand for Remediation of Arsenite Contaminated Groundwater," *The Battelle Fifth International Conference on Remediation of Chlorinated and Recalcitrant Compounds*, Monterey, California, May 2006 (Graduate Student Paper Award).
14. Henderson, A. D.; Demond, A. H. "Long-term performance of permeable reactive barriers," *The Battelle Fifth International Conference on Remediation of Chlorinated and Recalcitrant Compounds,* Monterey, California, May 2006.

15. Hayes, K.F., CH2M-Hill Distinguished Lecture, "Reduced Iron Sulfide Systems for Sequestration of Metals and Transformation of Chlorinated Pollutants," Auburn University, May 2006.
16. Olson, T.M. and Lee J.H, "Optimization of *in situ* emplacement of nano-sized FeS for permeable reactive barrier construction," *Proceedings of Waste Managements 2006 Conference*, Malta, June 21-23, 2006, WIT Press.
17. Henderson, A. D. and A. H. Demond. "Long-Term Performance of Zero-Valent Iron Permeable Reactive Barriers." *2006 EPA Graduate Fellowship Conference "From Discovery to Solutions: Generation Y Scientists Lead the Way*" Hyatt Regency Washington On Capitol Hill, September 24-26, 2006 (Poster).
18. Henderson, A. D. and A. H. Demond. "Geochemical Indicators of Impaired Performance and Reduced Longevity of ZVI PRBs." *Remediation Technologies Development Forum (RTDF) Permeable Reactive Barriers (PRB) Action Team Meeting*, Marriott Courtyard, Charleston, South Carolina, October 11-12, 2006 (Poster).
19. Renock, D., S. Utsunomiya, U. Becker, R.C. Ewing, T. Gallegos, K. Hayes "Arsenic Uptake on Synthetic Mackinawite" *Slovenia and US workshop on Environmental Science and Engineering*, Ljubljana, Slovenia, September 27-30, 2006 (Poster).
20. Gallegos, T.J., K.F. Hayes, and L.M. Abriola, "Sequestration of As(III) by Nanoparticulate Mackinawite Under Anoxic Conditions," *Partners in Environmental Technology Symposium*, Washington DC , November 28–30, 2006 (Poster).
21. Olson, T.M. and Lee J.H., "In situ emplacement and optimization of colloidal FeS for permeable reactive barrier construction," *Partners in Environmental Technology Technical Symposium*, Washington, D.C., Nov. 28-30, 2006 (Poster).
22. Vannela, R. P. Adriaens, and K.F., Hayes, "Geomicrobiological Regeneration of Iron Sulfide Minerals in Engineered Barrier Systems," *Partners in Environmental Technology Symposium*, Washington DC, November 28–30, 2006 (Poster).
23. Henderson, A.D. and A. H. Demond, "Interaction of ZVI and FeS with Carbonate: Implications for PRB Longevity," *Partners in Environmental Technology Symposium*, Washington DC, December 4-6 2007 (Poster).
24. Henderson, A. D.; Demond, A. H. "Comparison of Iron Sulfide and Zero-Valent Iron as Reactive Materials for the Removal of Arsenic from Groundwater," *American Geophysical Union Fall Meeting,* San Francisco*,* California, December 2007 (Poster).
25. Vannela, R., P. Adriaens, and K.F. Hayes, "Sulfate-Reducing Bacterial Iron-Sulfur Metabolism in Biogenic Formation of FeS Minerals," *American Society for Microbiology (ASM)*, April 30th – May 4th, 2007, Montreal, Canada.
26. Han, Y-S., T.J. Gallegos, A.H. Demond, and K.F. Hayes, "FeS-Coated Sand for Remediation of As(III) Contaminated Groundwater," *2007 Spring Conference of the Korean Society of Soil and Groundwater Environment*, Gangneung, S. Korea, April 12-13, 2007.
27. Renock, D., S. Utsunomiya, T.J. Gallegos, K.F. Hayes, R.C. Ewing, U. Becker, "Arsenic Uptake and Release on Sulfide Nanoparticles," *2007 Goldschmidt Conference*, Cologne University, Germany, August 19th-24th 2007.
28. Jeong, H.Y., K.F. Hayes, S.W. Park, and C.W. Kim, "Remobilization of Arsenic(III) Sorbed by Mackinawite (FeS) under Oxic Conditions," *235th National American Chemical Society Meeting*, Division of Geochemistry, Special Symposium on Advanced Approaches to Investigating Adsorption at the Solid-Water Interface, New Orleans, April 6 -10, 2008.

29. Henderson, A. D.; Demond, A. H. "Interaction of FeS PRBs and Carbonate: Implications for PRB Longevity," *The Battelle Sixth International Conference on Remediation of Chlorinated and Recalcitrant Compounds,* Monterey, California, May 2008.
30. Wang, L., L.M. Abriola, Y.S. Han, K.F. Hayes and A.H. Demond, "Modelling As(III) Removal by Synthesized FeS Coated Sand in Batch and Column Systems," *2008 Goldschmidt Conference*, Vancouver, Canada, July 13 – 18, 2008.
31. Hayes, K.F. (invited), T.G. Gallegos, H.Y. Jeong, and S.P. Hyun, "Sorption of As(III), Cd(II), and Hg(II) by Nanoparticulate Iron Sulfide: Uptake Mechanisms and Modeling," *235th National American Chemical Society Meeting*, Division of Geochemistry, Special Symposium on Advanced Approaches to Investigating Adsorption at the Solid-Water Interface, New Orleans, April 6 -10, 2008.
32. Henderson, A.D. and A.H. Demond, "Interaction of FeS and ZVI PRBs with Calcium, Carbonate, and Nitrate," *Partners in Environmental Technology Symposium*, Washington DC, December 2-4 2008 (Poster).
33. Wang, L. L.M. Abriola, Y.-S. Han, K.F. Hayes, and A.H. Demond, "Interaction of FeS and ZVI PRBs with Calcium, Carbonate, and Nitrate," *Partners in Environmental Technology Symposium*, Washington DC, December 2-4 2008 (Poster).
34. Jeong, H.Y., and K.F. Hayes (invited), "Arsenic mobilization during mackinawite (FeS) oxidation," *237th American Chemical S National Meeting*, Salt Lake City, UT, March 22-26, 2009.
35. Han, Y.-S., A.H. Demond, K.F. Hayes, "FeS-coated sand for removal of arsenic(III) under Anaerobic Conditions: Comparison of Batch and Column Experiments," *237th American Chemical S National Meeting*, Salt Lake City, UT, March 22-26, 2009.

Appendix C. Other Supporting Material

Honors and Awards

1. **Certificate of Merit Award to T.J. Gallegos and co-authors**, from the American Chemical Society for the paper and presentation "Uptake of As(III) by nanoparticulate mackinawite," *230th American Chemical Society National Meeting*, Washington DC, August 28-September 1, 2005.
2. **2nd Prize for T.J. Gallegos**, *Technical Paper Competition at Society of Hispanic Professional Engineers*, Dallas, TX, January 5-9, 2005, for paper entitled: "Reactive Ferrous Sulfide/Ferric Oxide Multilayer Films for Remediation of Arsenic Contaminated Groundwater." Co-authors L. M. Abriola and K. F. Hayes.
3. **Paper Award for T. J. Gallegos** "Mackinawite-Ferrihydrite Coated Sand for Remediation of Arsenite Contaminated Groundwater," *The Battelle Fifth International Conference on Remediation of Chlorinated and Recalcitrant Compounds, Monterey,* California, May 22-25, 2006. Co-authors: K. F. Hayes and L. M. Abriola.
4. **CH2M-Hill Distinguished Lecture for K.F. Hayes**, ""Reduced Iron Sulfide Systems for Sequestration of Metals and Transformation of Chlorinated Pollutants," Auburn University, May 2006.